ICFA International Committee for Future Accelerators

Sponsored by the Particles and Fields Division of IUPAP

Beam Dynamics Newsletter

No. 76

Issue Editor:
Christopher Prior, STFC/RAL

Editor-in-Chief:
Ingo Hofmann, GSI/TUD

April 2019

CONTENTS

1. FOREWORD

1.1 From the Chair

Ingo Hofmann, GSI/TUD

The sudden passing of Prof. Yong Ho Chin on January 8 came as a shock to us, and it is a big loss to the accelerator community and the ICFA Beam Dynamics Panel. Yong Ho Chin had served as a dedicated Panel Chair since 2016. In his memory, this newsletter offers tributes from several colleagues who have closely interacted with him. Newsletter #77 (August 2019) will be prepared and edited by Dr. Yoshihiro Shobuda from JPARC as a scientific dedication to Yong Ho Chin's achievements and related topics.

A short note about ICFA itself: The "International Committee for Future Accelerators" held its last meeting (usually twice a year) at the University of Tokyo on March 6-8, 2019. A central topic was the future of the International Linear Collider (ILC) project – in its new version with a total collision energy reduced to 250 GeV from originally 500 GeV for cost and time saving reasons. A press conference about this project was held announcing that currently an "Update of the European Strategy for Particle Physics" is being collected, which will be presented and discussed at an "Open Symposium" in 2020.

On behalf of the beam dynamics panel we are glad to announce the following ICFA meetings in 2019:

- The 63rd ICFA Advanced Beam Dynamics Workshop on Energy Recovery Linacs (ERL2019), September 15-20, 2019, in Berlin, Germany, is the eighth in the series of international workshops covering accelerator physics and technology of energy recovery linacs. See https://www.helmholtz-berlin.de/events/erl19/index_en.html
- An ICFA Mini-Workshop on Slow Extraction, July 22-24, 2019 at FNAL, USA, in continuation of successful previous meetings on the same topic held at GSI (2016) and CERN (2017). See https://indico.fnal.gov/event/20260/
- An ICFA Mini-Workshop on Mitigation of Coherent Beam Instabilities in Particle Accelerators (MCBI), September 23-27, 2019, in Zermatt, Switzerland.
  See https://indico.cern.ch/event/775147/

For 2020 ICFA has now endorsed the choice of time and location of the 64th Advanced Beam Dynamics Workshop on High-Intensity and High-Brightness Hadron Beams (HB2020), which will be held at FNAL September 28–October 2, 2020. It is the follow-up to HB2018 in Daejeon, Korea, and the 10th event of this series – started also at FNAL in 2002 – and considered the primary conference for the international community of high intensity beam dynamics. The Workshop and LOC chair of HB2020 is Eliana Gianfelice-Wendt, FNAL.

The present Newsletter #76 focuses on the exciting subject of Fixed-Field alternating gradient Accelerators (now abbreviated to FFAs). An impressive number of 18 articles reflects the worldwide status of activities in this area. Our thanks go to Chris Prior who took responsibility and made this comprehensive survey possible as editor. It should become a highly valued and up-to-date document covering the whole field of FFAs and their prospects of application!

Along with this we also owe Chris thanks for having taken the initiative to realise for our Newsletter the optional use of Microsoft Word (used so far) and LaTeX (now the preferred choice) – thus responding to the preference of many actual and potential authors. In §7.1.3 details are found how to prepare manuscripts.

We welcome Suzie Sheehy as new Regular Correspondent for Australasia, who offers insight into hadron-therapy plans in Melbourne (section 4, also with reports on Middle East activities including the latest development at SESAME in Jordan by our correspondent Sameen Ahmed Khan). The Panel hopes that further Regular Correspondents can be encouraged to join in!

From time to time, it appears necessary to draw attention to the guidelines for the different types of ICFA workshops:

- ICFA Advanced Beam Dynamics Workshops are a long-established and prestigious series and need approval by ICFA itself; we recommend submitting an application to the ICFA Beam Dynamics Panel as early as possible to attain the required ICFA sponsorship.
- ICFA Mini-Workshops are sponsored by the ICFA Beam Dynamics Panel itself; Panel approval takes usually two weeks and must in all cases precede public announcement. Approval post publication cannot be accepted.

For both types of workshop the organizers are required to submit a summary report after the workshop for publication in the ICFA Beam Dynamics Newsletter. For further important details please see our website.

1.2 From the Editor

Chris Prior, Rutherford Appleton Laboratory, UK

It is over ten years since the ICFA Beam Dynamics Newsletter was last published on the theme of Fixed-Field alternating gradient Accelerators (now known as FFAs). Back in 2007, FFAs were enjoying a revival led by the demand for rapid acceleration of unstable particles and robust, reliable accelerators for high power applications. I wrote at the time of the interest in EMMA, the world's first-ever non-scaling FFA under construction at the Daresbury Laboratory. A small (16.6 m circumference) electron FFA designed as a test model of a larger muon accelerator, EMMA was a proof-of-principle machine, used to show that resonances could be crossed sufficiently rapidly to avoid emittance growth and particle loss, and also gave the first verification of what became known as "serpentine" (or 'out-of-bucket') acceleration. The latter discovery featured as the cover article in Nature Physics and it was expected that EMMA would go on to become a useful tool for exploring beam dynamics. But financial constraints and budgetary cuts reared their ugly heads and EMMA's life was short-lived. Now, the only FFAs in an operational state are those in Japan.

Looking back, it is easy to see how the outlook has changed with time. In 2007, there were ideas that FFAs could be used for large-scale projects like the neutrino factory or muon collider, as drivers for ADS, or to generate high-power, multi-megawatt proton beams for, say, spallation neutron sources. These were all highly expensive projects and in that respect nothing has changed. But, as design reports were completed and projects progressively shelved, research has become more detailed and focused on specific aspects. Other possible benefits and applications of FFAs have been identified. Suzie Sheehy gives a wide-ranging overview of the possibilities in her article on FFA applications. The small FFAs in Japan have been used to study beam dynamics in some depth: tune variation, resonances, chromaticity effects, orbit correction, errors, fringe fields. Compact FFAs might be used, say, to generate radio-isotopes. The advantages of FFAs in hadron therapy for cancer treatment are becoming increasingly recognised, and there are proposals for FFA-based proton and ion accelerators small enough to fit in hospitals, with relatively light, flexible gantries using FFA-type magnets that can handle a wide range of energies.

The main FFA-related construction project at the moment is CBETA, a joint initiative between Cornell University and BNL in the United States for a proto-type ERL that features a single FFA return loop capable of transporting accelerated and decelerated beams at four different energies in the same beam pipe. The project is part of the development programme for a future electron-ion collider, such as eRHIC.

In Europe, most of the FFA work is in the U.K. At the Rutherford Appleon Laboratory a long-term study is exploring ideas for a future spallation neutron source. A possible candidate is an accelerator using fixed-field magnets, possibly arranged in a DF-spiral configuration and conceivably designed so that the orbit moves in a vertical, rather than radial, direction as the beam is accelerated. This would reduce the footprint but present constructional challenges. A small prototype ring is planned, using RAL's existing 3 MeV injector.

Most of these projects (and more) are included in this issue of the Newsletter. We also include details of the announcement of the first successful nuclear transmutation of minor actinides carried out at Kyoto University's research reactor with a beam accelerated by an FFA. This is reported in Yoshihiro Ishi's comprehensive article on the experimental FFA programme in Japan.

Understandably, codes to model the beam dynamics in such complicated machines are also important. Traditional synchrotron codes, with the same central orbit at all energies, are not suitable when a beam is accelerating in an FFA structure, and paraxial approximations are

seldom valid in this context. The two main codes used in FFA studies, OPAL and Zgoubi, are featured here.

Theme articles aside, I was delighted to receive contributions from our 'Regular Correspondents', describing accelerator-related activities in Australia and the Middle East. There are announcements of eleven recent PhD awards in accelerator physics - which may well be a record for the Newsletter. Two have been awarded prizes for the quality of their theses. It is encouraging to see such interest in young people joining the field and good to know that we are investing in training the next generation of accelerator physicists. The Newsletter provides a good opportunity for them to bring their ideas and results to the attention of the beam dynamics community at large.

Finally, the change of acronym to FFA (referring to Fixed-Field alternating gradient Accelerators). The original acronym brought to mind a perjorative term used against members of the LGBT+ community. We have acknowledged this and followed organisations at SLAC and CERN and possibly elsewhere, that have changed their acronyms. Our Japanese colleagues have led the way in the accelerator world by labelling last year's workshop FFA'18. I have accordingly tried to use "FFA" only throughout this Newsletter; of course, there should be no attempt to re-write history, so references to published works containing the old acronym remain unaltered. We have found it quite easy to make the change and if we can avoid causing offence at little or no cost to ourselves, there is no reason why we should not do it.

2. TRIBUTE TO YONG HO CHIN

Yong Ho Chin, the Chair of the ICFA Beam Dynamics Panel, passed away quite unexpectedly early in January 2019.

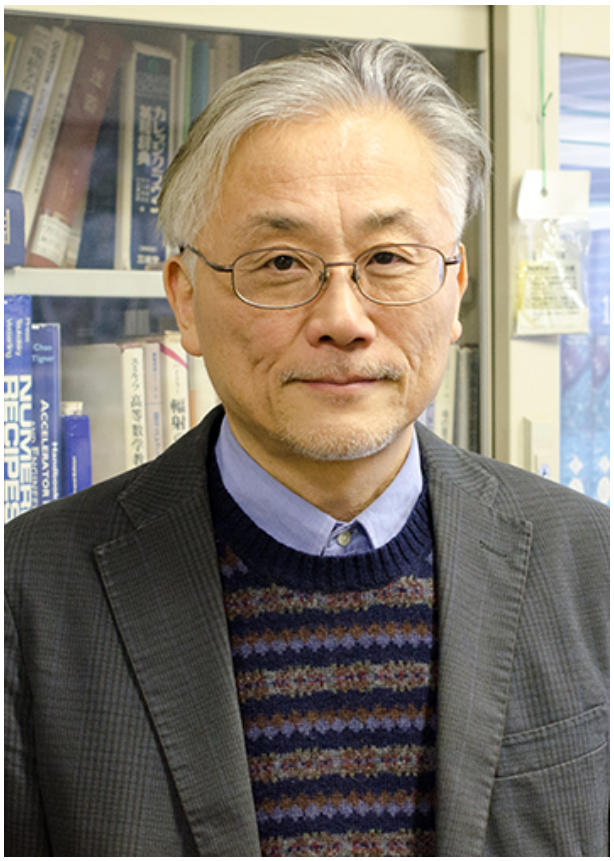

Most of the members of the Panel remember him for his quiet but firm leadership, his clear thinking, and his remarkable ability to absorb but not create controversy. He was clearly good at managing people and making them feel their efforts were appreciated. He was good company, good to talk to, intelligent and very knowledgeable, with amusing snippets of stories drawn from experiences in his past life.

His natural talent for resolving issues, always in a warm, respectful manner, spilled over into his physics. He was able to combine two different points of view into one and at the same time generalize the results of both. His technical ability was widely recognised but so too was his generosity of mind.

Yong Ho had been hoping to develop the activities of the Panel further, making it more pro-active in encouraging initiatives and collaborations in those areas of beam dynamics most important for future accelerator physics. It is a huge blow to us all that he was unable to achieve

his vision and see through the vital role he was expecting to play.

The editor asked a selection of people to contribute their memories of Yong Ho to try to bring out the character of the man.

Swapan Chattopadhyay, who was involved with Yong Ho from the earliest days of his career, writes:

In remembering Yong-Ho, I have the singular distinction of having been in a position to have secured a permanent career position for him as a staff scientist at Berkeley Lab in my accelerator center in the 1980s. Young-Ho was at CERN at that time and it was non-trivial to secure him, as CERN kept offering him extended short-term contracts with attractive tax-free CERN-style salaries. In my negotiations and interactions with him, I was most impressed and struck by Yong-Ho's desire to understand his scientific research portfolio in his future appointment in detail, without ever raising any questions of substance about salaries, compensations etc. He decided to join my group at Berkeley based purely on the scientific canvas that he envisioned and the relative stability/permanence of the position, allowing him to do his research unimpeded and not wowed by financial packages.

Second, after a few years at Berkeley when Yong-Ho joined KEK in Japan as a junior accelerator professor and scientist, he had an unusually keen sense of humor, being very aware of his special status as a Japanese citizen in his own right, but with also a special status as one with a Korean heritage, with all its implications as a citizen. There were many exchanges between him and our mutual mentor and colleague Dr Kimura-san and myself about the pros and cons of this status, sociologically, culturally and scientifically. Yong-Ho never focused on some of the negative aspects of this as I have heard from many others, but kept on focusing that he could serve as a scientific ambassador of collaboration with Korean and Chinese universities, laboratories and institute in matters of international and pan-Asian collaboration on Linear Collider research and design etc. – and this he did in an exemplary way later in his career for all to behold.

Third, his integrity on the face of personal tragedy is worth mentioning. When he found out and shared with me the terminal nature of illness of his intelligent and beautiful wife, whom he stood to lose in a short order of time, he continued to attend to her while burying himself unusually deep into long hours of work and research via tele-commmuting, and no one knew how intense a personal life he was living at that point in time judging by his prodigious productivity.

Yong-Ho was a quiet and substantial scientist in his research. I could get him to the point when he would drop his guard and boast about his wake-field and electromagnetic code being superior to all others etc. But he was always very polite when dealing with colleagues, though I have heard that he stood his ground when some senior scientists kept on questioning his formulation of the code in Europe, which actually had left a scar with him, eventually healed by its own merits.

We were personal friends and he introduced me to Japanese and Korean food, culture and many historical tid-bits. I will miss him dearly, professionally and personally.

Swapan Chattopadhyay, Fermilab, USA

Weiren Chou, former chair of the ICFA Beam Dynamics Panel, writes:

Yong Ho was a long-time friend and colleague of mine. We got to know each other about 30 years ago in 1989 when I was at ANL. Yong Ho, then at LBL, came to a workshop and made an elegant presentation on a longitudinal mode-coupling instability model for bunch lengthening. This was subsequently published in the workshop proceedings ANL/APS/TM-5, April 1990.

We then began a collaboration on impedance and instability studies. An example of this work was a comparison of three impedance codes: TBCI (by Thomas Weiland), ABCI (by Yong Ho) and BPERM (a boundary perturbation method code by me). For an insertion device, the three codes gave nearly identical wakefield curves, one of a few successful examples of code benchmarking.

In 2002, Yong Ho, several colleagues and myself started a new ICFA Advanced Beam Dynamics Workshop (ABDW) series on high intensity, high brightness hadron beams (the HB series). The first three workshops in the series took place in the US (2002, Fermilab), Europe (GSI, 2004), and Asia (KEK, 2006). The 2006 workshop was chaired by Yong Ho. These workshops were well received by the community and this biennial series continues today, and the 3-continent rotation pattern has become a tradition.

In 2016, Yong Ho was appointed by ICFA to be the new Beam Dynamics Panel Chair and succeeded me in that role. The transition went smoothly and Yong Ho did an excellent job as Chair. His sudden passing was totally unexpected and a shock to me.

Yong Ho was an excellent accelerator physicist. His contributions will be remembered for a long time. He will be deeply missed as a friend, a colleague, and a wonderful person.

Weiren Chou, Fermilab, USA

Yoshishige Yamazaki, formerly of KEK, now at FRIB, gives his thoughts on "Missing Yong Ho":

At the news that he passed away, I was so embarrassed and shocked, since I had lunch together with him last November. He looked so healthy and strong. He himself proposed and planned the special lunch to celebrate that our common KEK supervisor, Prof. Koji Takata, had been awarded a very honorable medal from the Japanese government for his great accomplishments on RF technologies. Yong-Ho scheduled the lunch that prompted my visit to Japan. He also encouraged me very much, since I was so depressed that my wife got sick, and I paid the visit to discuss with a doctor on my wife's case.

Then, early January he would have come to Michigan to serve as a scientific program coordination committee member for NAPAC 2019, that I am chairing. He has been always a great help to me for this kind of occasion.

When I first met him, he was just 22 or 23 years old, a young boy, very good looking, and of course, very smart. He was a master course student of the University of Tokyo and staying at KEK in order to work on accelerator physics. At that time, I was fabricating accelerating RF cavities on my design for the KEK Photon Factory. I was also investigating possible coupled bunch instabilities by these cavities both theoretically and empirically. He came to my office, and asked me several questions on modes in cavities. I explained these, showing my own note book. I made this note book for my own purpose, summarizing all possible modes and their longitudinal or transverse impedances in a pill box cavity, including the relations to the growth rates of the coupled bunch instabilities. After he became a world expert on this field it has been my great pride that he learned these physics at first using my note book.

Ever after, he was one of my best friends, and helped me both technically and privately. Beam instabilities and related problems at the J-PARC accelerators was his responsibility. On my request, he chaired HB2006 held for the first time in Japan, and was SPC chair of Linac 2010. He had a very good sense of coordination of international affairs. Thus, he gave me many good suggestions and advice whenever I was organizing international conferences and collaborations. I believe that this is not only for me, but for many people. His passing away is thus a really great loss to our world-wide accelerator community.

Yoshishige Yamazaki, Facility for Rare Isotope Beams (FRIB), Michigan USA

The next edition of the Newsletter will contain articles highlighting Yong Ho Chin's work and scientific achievements.

3. FIXED FIELD ALTERNATING GRADIENT ACCELERATORS (FFA)

3.1 Current and Future Applications of Fixed-Field Alternating Gradient (FFA) Accelerators

Suzanne Sheehy, University of Oxford, United Kingdom, and University of Melbourne, Australia

Introduction

The Fixed Field Alternating Gradient accelerator is a flexible accelerator type, which can be used for leptons or hadrons over a wide energy range. To understand where FFAs fit in the landscape of applications, we first need to look at how accelerators are used worldwide and which properties are required in terms of particle type, energy, intensity, size, flexibility and so on. Then, we can identify areas where FFAs may have advantages over existing cyclotron, synchrotron, LINAC and electrostatic accelerator technologies.

Of course, the applications of particle accelerators are incredibly broad. There are estimated to be between 35,000 and 45,000 of them in the world and their use can be roughly divided into 50% industrial application and 50% medical, with just a few large machines for scientific applications and particle physics [1]. Some of these applications are well established, with machines produced and developed almost exclusively in industry. These include machines in the medical domain including radioisotope production cyclotrons and short 3GHz linacs for electron and X-ray radiotherapy (radiotherapy alone accounts for around 15,000 accelerators worldwide, although a shortage exists in low and middle-income countries [2]).

Machines for ion implantation in the semiconductor industry, electron beam processing and irradiation are key commercial applications. Other commercial applications are rapidly growing. These include proton and ion (hadron) therapy machines, neutron generators, accelerators for security applications, inspection using ion beam analysis, non-destructive testing and compact synchrotron radiation sources. Other applications cross over into cultural and heritage areas, such as the established techniques of ion beam analysis in art and ceramics, accelerator mass spectrometry in radiocarbon dating, through to the much newer muon tomography currently performed using cosmic rays.

A revival of interest since the 1990s has seen a number of FFAs constructed, including scaling and linear non-scaling variants for protons [3, 4] and electrons [8] respectively. Since this time, the range of FFA designs has rapidly diversified and there are now designs with non-linear field profiles and non-radial edge angles, racetrack shapes and other super-periodic structures, dispersion suppression sections, vertical orbit movement and other innovations. While it would be impossible to give an exhaustive review of such developments here, I will highlight some examples to outline general direction of travel in this constantly evolving field. The purpose of this article is to outline which applications FFAs have been used for, which areas are active in R&D but have not yet been realised and which may have potential in the future.

3.1.1 Science and Particle Physics

FFA accelerators have been considered in particle physics projects for their large energy and dynamic acceptance. The primary work in this application was undertaken in the context of the muon collider and neutrino factory programmes [5–7]. That work has now evolved into potential nearer-term muon and neutrino projects. For instance, the NuSTORM project which aims to create a high flux of neutrinos in order to measure neutrino couplings precisely, an FFA option may be able to store an enhanced number of muons compared to a conventional storage ring [9]. The PRISM project (Phase Rotated Intense Slow Muon source) [10], aims to study charged lepton flavour violation by creating a facility which reduces the muon beam energy spread by phase rotation and purifies the muon beam in the storage ring. A 6-cell FFA ring was constructed and tested using alpha particles in Osaka, demonstrating phase rotation. The PRISM task force continues to address the challenges in realising an FFA based muon-to-electron conversion experiment [11].

A large amount of R&D work has also gone into the development of recirculating non-scaling FFA arcs for the eRHIC project [12]. The most recently developed, constructed and commissioned FFA is the non-scaling FFA arcs of the CBETA project at Cornell, demonstrating the capacity of one FFA arc to enable a 4-turn Energy Recovery Linac (ERL with superconducting injector LINAC [13, 14]. The layout and magnet girder are shown in Fig. 1.

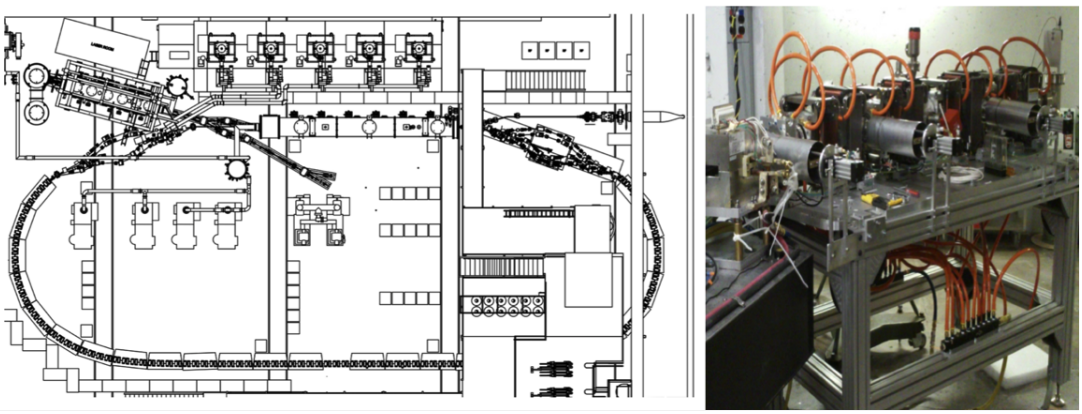

Figure 1: The CBETA layout (left) and first magnet girder (right) where the permanent halbach magnets are small magnets close to the beampipe, embedded within the more visible corrector coils.

Looking forward, one current R&D project which is pushing forward the development of high intensity hadron FFAs is the consideration of this technology for a novel short pulse spallation neutron source, under the auspices of the ISIS-II study [15]. In the present design, a novel 'FD Spiral' configuration [16] is employed. Advantages of the FFA method over the alternative rapid cycling synchrotron option include; flexibility in the pulse rate up to 100 Hz, lower power requirements for DC operation of magnets, and potential for high intensity operation. However, the technology is less mature than the rapid cycling synchrotron, so detailed studies and ideas for prototyping are currently underway.

A number of projects are looking to combine the large energy-acceptance capability of FFA optics with novel accelerator techniques which (at present) produce beams with a large energy spread. One such application, discussed at the 2018 FFA workshop, was the idea of a FFA-based Free Electron Laser system with a laser-plasma wakefield injector. The challenge of course would be to utilise all of the beam created in a LPWA source to generate radiation at a single wavelength in a relatively compact setup. Meanwhile, the Centre for Clinical Application of Particles (CCAP) at Imperial College, London, are discussing ideas for a laser-plasma injected

beamline for radiobiology facility, with long term plans for an FFA as part of the facility [18].

3.1.2 Medical Applications

Hadron therapy designs

FFAs are considered a promising future option for medical applications due to their capability of high repetition rate and variable energy extraction operation with no limitation on top energy. This appears to be an advantage over synchrotrons in terms of repetition rate and achievable intensity, and also over cyclotrons as FFAs should be able to accelerate heavier ions for therapy, with clean variable energy fast extraction and no need for a degrader system.

FFAs in the right energy range for hadron therapy have been designed and realised in Japan with a 150 MeV radial sector scaling FFA [19] for protons, with versions at Kyoto University (shown in Fig. 2) and Kyushu University. Prototype magnets were also produced for the spiral scaling machine RACCAM (Recherche en ACCélérateurs et Applications Médicales) which took a multi-room delivery approach to optimise treatment time [21, 22][1].

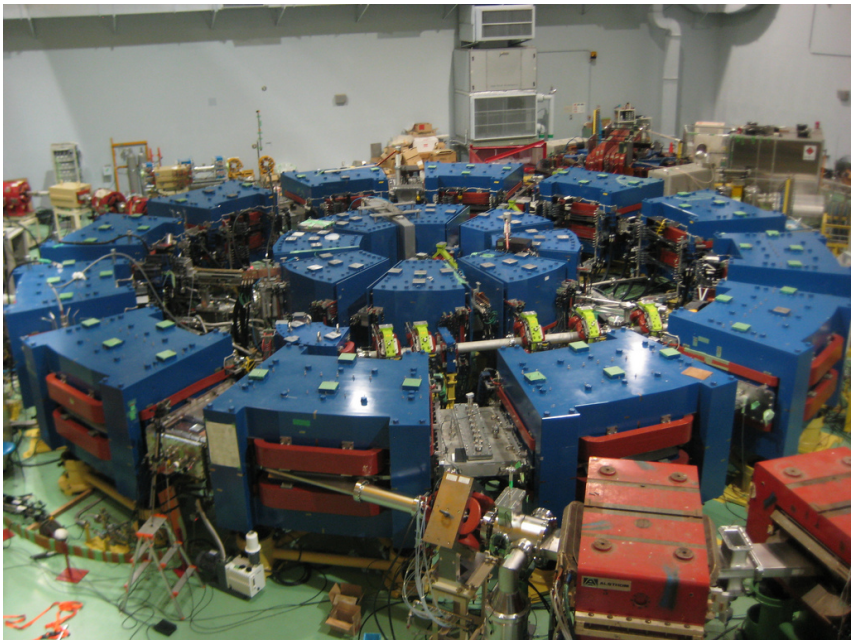

Figure 2: The 150 MeV FFA at Kyoto University.

A review of accelerators for hadron therapy in 2014 [20] gives a convenient overview of the many different approaches and designs of FFA accelerators for hadron therapy facilities, which was a very active research area particulary from around 2004 - 2012. Designs for linear non-scaling FFA based hadron therapy facilities [23] emerged in the early 2000's. However, integer resonance crossing was highlighted as a potential issue in a hadron ns-FFA accelerator with realistic acceleration over thousands of turns [24]. Note that this is due to the limited acceleration rate achievable in a hadron machine of this type, whereas there was no beam degradation observed in the fast-accelerating EMMA demonstrator machine [8], where serpentine acceleration is used.

To overcome the resonance crossing issue, non-scaling variants with small orbit excursion and incorporating non-linear magnetic fields emerged, primarily as part of the PAMELA (Particle Accelerators for MEdicaL Applications) project [25] shown in Fig. 3. The fields were configured

[1] A full facility based on this design was not part of the original funded project.

to stabilise the betatron tune and ensure that no integer or half-integer resonances were crossed during acceleration [26].

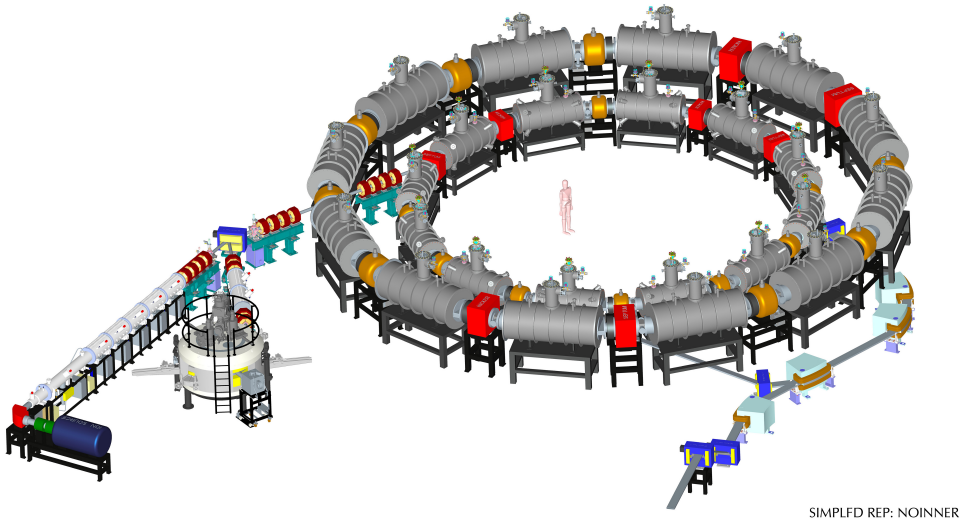

Figure 3: Rendered 3D drawing of the PAMELA hadron therapy FFA design, where two rings are used to cover the full energy of protons to 250 MeV (inner ring) and low energy C6+ ions, which would be transferred to the outer ring and further accelerated up to 400 MeV/u.

An alternative method to stabilise tunes using magnet edge angles and arbitrary functions of field with radius was also developed [28]. Continued work in this direction for non-scaling arbitrary field FFA designs now includes a concept for ions including helium and carbon from 70/90 to 430 MeV/u [29,30]. The design is based on a racetrack configuration which allows long straight sections, where an extraction system based on a bipolar field is located. While this has not yet been demonstrated in an operating machine, it would allow a fast variable energy extraction system with no degrader. The design is near to isochronous for CW operation, which leads to a large cyclotron-like radial aperture for both the magnets and rf system.

In recent years, the PAMELA work was taken forward to develop normal-conducting designs in a racetrack configuration [27], removing the seemingly complicated superconducting magnets of the PAMELA design and increasing the energy range in one ring to 350 MeV with proton CT in mind. A microtron-like FFA has also been proposed for Carbon Ions, and a patent application is in process [31]. At the time of writing, none of these designs have been realised in operating facilities.

Gantries and beamlines

In addition to the accelerator, a clinical hadron therapy centre also requires transport lines and gantries which can focus, scan and deliver the beam to the patient at any angle. The potential advantage of FFA optics in this domain is the large energy acceptance with relatively compact magnets to enable fast variable energy delivery all the way to the patient, and the potential to use permanent or superconducting magnets to reduce the size and weight of existing gantries. The key R&D work on non-scaling FFA gantries has been carried out by Trbojevic *et al.* [32], and a number of patents now exist in this area although no clinical gantries of this type have yet been realised.

With the advent of linear accelerators such as that made by ADAM/AVO [33] which can change energy at a high repetition rate around 100 Hz, interest may well emerge in the use of FFA optics to deliver beams in a large energy acceptance design, even if the accelerator itself

is not an FFA. Further work toward this including approaches using adiabatic matching have recently been studied [34].

A major step toward the realisation of permanent magnet beamlines applicable to hadron therapy gantries was made recently at Brookhaven National Laboratory (Fig. 4), where a linear non-scaling permanent magnet arc bending through 40 degrees was demonstrated with electrons over the energy range of 17-80 MeV kinetic energy, highlighting the efficacy of using ns-FFA technology over a factor of 4 in momentum [35].

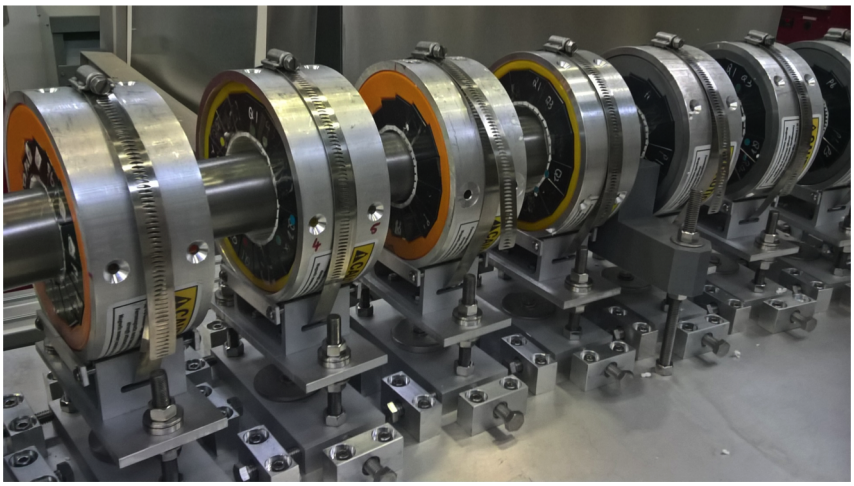

Figure 4: The Brookhaven ns-FFA test arc, made from permanent magnets with 3D printed holders and correction scheme. Image from [35].

Radioisotope production

Compact high current FFAs may be applied to radio-isotope production. One such design is the Proton Isotope Production (PIP) design [36] shown in Fig.5. This is a cyclotron-like FFA being studied for proton energies up to 26 MeV for the production of radioisotopes, in particular ^{99m}Tc. The magnetic field varies from 0.99 to 1.03 T up to a 1.5 m radius and the gradient is optimised by adjusting the magnet geometry to stabilise the tunes and enhance beam focusing whilst maintaining isochronicity. The use of a thin internal target and recycled beam is being investigated as it could greatly improve production efficiency. At present, simulations with a 20 mA beam in OPAL show good transmission through the acceleration cycle of over 98%.

3.1.3 Industrial Applications

Electron beam processing

The design and implementation of an electron FFA with serpentine acceleration for industrial applications has now been realised with NHV Corp in Japan [37]. The primary requirements were for fixed frequency RF and fixed magnetic field, providing roughly 10 MeV electrons at a high current. The design built on earlier work on serpentine acceleration in a scaling FFA [38].

Energy Applications and Accelerator Driven Systems

A substantial amount of work has been undertaken in designing and understanding how an FFA could act as a high power proton driver for ADS. Of paramount importance here is providing a CW beam; fixed field and fixed rf frequency at the same time. This was achieved in the lower energy electron machines in the previous section, but is substantially more challenging

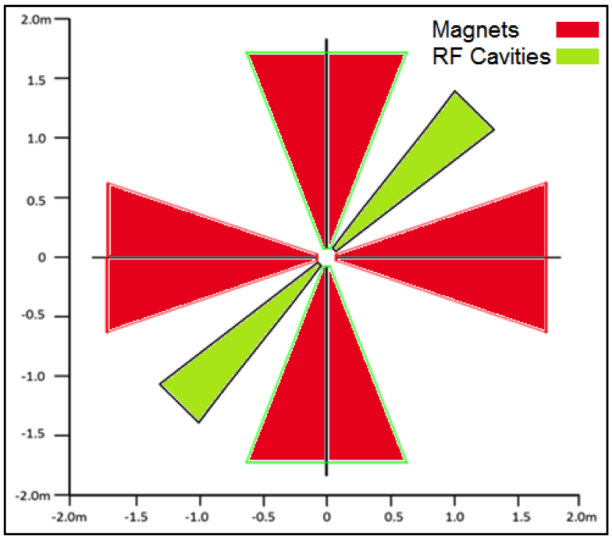

Figure 5: A view of the PIP ring. The internal target would be located in one long gap between sectors.

when taking protons up to the 1 GeV energy range required for accelerator driven transmutation systems.

Designs have included a scaling racetrack FFA [39], which requires challenging levels of RF to open up the serpentine acceleration channel at 20 MV/turn. Similar studies were carried out on a 'nearly' isochronous ring using a non-scaling approach [40], which were again found to be challenging in terms of high RF voltage requirements, although a further iteration toward better isochronicity would be needed to progress the design. Further questions remain in terms of the effect of space charge in an accelerator which uses serpentine acceleration, as there is no longitudinal focusing of the bunch in the serpentine channel. However, a lot of progress has been made on simulation tools, particularly OPAL [41], which will help answer these questions.

Additional ideas include a vertical excursion FFA with harmonic number jump, the 'harmonytron' concept [42]. Machine parameters have been studied for this type of vertical scaling FFA which accelerates proton from 50 MeV to 500 MeV. This concept aims to accelerate protons or ions over a wide range of non-relativistic energies with a fixed frequency rf acceleration and fixed magnetic field, while overcoming the lack of longitudinal focusing in normal isochronous rings (such as cyclotrons).

At Kyoto University (KURNS), an experimental programme is underway which has modified the existing Energy Recovery Internal Target FFA (ERIT) to a demonstrator for muon production, MERIT. The primary changes include a lower energy injection, the introduction of a wedge-shaped target for muon production, and the reduction in k-value of the focusing system of the accelerator. The long-term idea is to create an intense negative muon source for muon nuclear transformation, which is aimed at the mitigation of long lived fission products in existing nuclear waste. MERIT stands for Multiplex Energy Recovery Internal Target. Studies estimate that roughly $10^{16}\,\mu$/sec could be achieved [43].

Conclusions

The recent developments in FFA accelerators have moved on from just paper design studies to the realisation of FFAs for real world use. Of particular note is the compact electron FFA for electron processing. A number of different types of FFA are now in prototype and commissioning stage for applications ranging from fundamental science through to medical and industrial use. Many

design studies have now been completed, particularly in the medical domain. The practical realisation and then commercialisation of medical FFAs, particularly in the domain of beam delivery systems and gantries, is now needed. In all domains but particularly in high power proton applications, creative and novel FFA designs and ideas continue to emerge and evolve. This dynamic activity in the field makes this a particularly exciting time to review the rapid pace of progress. A positive and exciting future lies ahead for the applications of FFAs.

References

[1] R. Hamm, presented at Accelerator Industry Co-Innovation Workshop, Brussels, Belgium, 2018. https://indico.cern.ch/event/682411/contributions/2798415/

[2] E.H. Zubizarreta *et al.*, Need for radiotherapy in low and middle income countries; the silent crisis continues. Clin. Oncol. (2015), 27(2):107-114.

[3] M. Aiba *et al.*, Development of a FFAG Proton Synchrotron, in Proceedings of EPAC2000, Vienna, Austria, pp. 581–583.

[4] Y. Mori, Present Status of FFAG Proton Accelerators at KURRI, in Proc. 2nd International Particle Accelerator Conference, IPAC'11, San Sebastian, Spain, 2011, paper WEPS077, pp. 2685–2687.

[5] G.H. Rees, FFAG Studies for Neutrino Factory Accelerators,‖ Nucl. Phys. B (Proc. Suppl.) 155 (2006) 301–304.

[6] Muon colliders and Neutrino Factories, ICFA Beam Dynamics Newsletter No. 55, August 2011, http://www-bd.fnal.gov/icfabd/Newsletter55.pdf

[7] M. Bogomilov *et al.* Phys. Rev. ST Accel. Beams 17 (2014), 121002.

[8] S. Machida *et al.*, Acceleration in the linear non-scaling fixed-field alternating-gradient accelerator EMMA, Electron Model for Many Applications, Nat. Phys. 8 (2012), pp. 243–247.

[9] J.-B. Lagrange *et al.*, Racetrack FFAG muon decay ring for nuSTORM with triplet focusing, J.INST. **13**, P09013, September 2018. See also article in this issue of the Newsletter.

[10] J. Pasternak and the PRISM Task Force 2013 J. Phys.: Conf. Ser. 408 012080.

[11] J. Pasternak, presented at the FFA'18 workshop, Kyoto, Japan, 2018. https://indico.rcnp.osaka-u.ac.jp/event/1143/

[12] D. Trbojevic, Linear Fixed Field return arcs ERL's for Electron Colliders, presented at the FFA'18 workshop, Kyoto, Japan, 2018. https://indico.rcnp.osaka-u.ac.jp/event/1143/

[13] C. Guillford *et al.*, Beam commissioning results from the CBETA fractional arc test, 2019. arXiv:1902.03370[physics.acc-ph]

[14] G.H. Hoffstaetter *et al.*, "CBETA, the 4-Turn ERL with SRF and Single Return Loop", in Proc. 9th Int. Particle Accelerator Conf. (IPAC'18), Vancouver, Canada, 2018. TUYGBE2

[15] S. Machida, FFA based ISIS upgrade option, article in this volume.

[16] S. Machida, Scaling Fixed-Field Alternating-Gradient Accelerators with Reverse Bend and Spiral Edge Angle, Phys. Rev. Lett. (2017), 119, 064802.

[17] K. Dewhurst, presented at the FFA'18 workshop, Kyoto, Japan, 2018. https://indico.rcnp.osaka-u.ac.jp/event/1143/

[18] A. Kurup, LARA: a Laser-based Beam Line for Clinical Applications, presented at the JAI Fest, December 2018. https://indico.cern.ch/event/776077/

[19] T. Uesugi *et al.*, FFAGs for the ERIT and ADS Projects at KURRI, in Proceedings of 8th European Particle Accelerator Conference (EPAC02), Genoa, 2008.

[20] Hywel Owen, Ranald MacKay, Ken Peach & Susan Smith, Hadron accelerators for radiotherapy, Contemporary Physics (2014) 55:2, 55-74, DOI:10.1080/00107514.2014.891313

[21] S. Antoine *et al.*, Principle design of a proton therapy, rapid-cycling, variable energy spiral FFAG, Nucl. Instrum. Methods Phys. Res. A 602 (2009), pp. 293–305.

[22] F. Méot *et al.*, Nucl. Instr. Meth., A602(3), pp.293-305(2009).

[23] E. Keil, A. Sessler, and D. Trbojevic, Hadron cancer therapy complex using nonscaling fixed field alternating gradient accelerator and gantry design, Phys. Res. S.T. Accel. Beams 10 (2007), p. 054701.

[24] S.L. Sheehy and D.J. Kelliher, Effects of alignment errors in proton on-scaling FFAG accelerators, Int. J. Mod Phys. A (2011), Vol. 26, No. 10n11, pp. 1842-1851.

[25] K. Peach *et al.*, Conceptual design of a nonscaling fixed field alternating gradient accelerator for protons and carbon ions for charged particle therapy, Phys. Rev. S.T. Accel. Beams (2013) 16, 030101.

[26] S.L. Sheehy *et al.*, Fixed field alternating gradient accelerator with small orbit shift and tune excursion, Phys. Rev. S.T. Accel. Beams 13 (2010), p. 040101.

[27] J.M. Garland, R.B. Appleby, H. Owen, and S. Tygier, Normal-conducting scaling fixed field alternating gradient accelerator for proton therapy, Phys. Rev. ST Accel. Beams (2015) 18, 094701.

[28] C. Johnstone *et al.*, Nonscaling FFAG variants for HEP and medical applications, in Proceedings of PAC09, Vancouver, BC, Canada, 2009. TU6PFP080.

[29] C. Johnstone, Compact CW nonscaling FFAGs for medical applications, in *FFAG Workshop 2016*, London, Sept., 2016.

[30] J. Taylor, HEATHER - HElium ion Accelerator for radioTHERapy, in *FFAG Workshop 2016*, London, Sept., 2016.

[31] M.H. Tahar, Fixed field alternating gradient ion accelerator for variable energy extraction, US Patent App. 16/122,190, 2019.

[32] D. Trbojevic, FFAG gantries, in *FFAG Workshop 2016*, London, Sept., 2016.

[33] A. Degiovanni *et al.*, LIGHT: A linear accelerator for proton therapy, in Proceedings of NAPAC2016, Chicago, USA (2016), FRB1IO02.

[34] S.T. Descalu, MPhys Report, University of Oxford, 2019.

[35] S. Brooks, Test of Linear-Field Non-Scaling FFAG Arc with a Wide Energy Range, presented at the FFAG'17 workshop, Cornell, USA, 2017.

[36] D. Bruton *et al.*, A compact and high current FFAG for the production of radioisotopes for medical application, in *Proc. International Particle Accelerator Conference, IPAC'16*, Busan, Korea, 2016. TUPOY023, pp. 1957–1959.

[37] T. Baba *et al.*, A new type of electron accelerator for industrial applications, presented at IMRP, London, 2008. http://iiaglobal.com/uploads/documents/imrp2008/Takashi%20Baba.pdf

[38] E. Yamakawa *et al.*, Serpentine Acceleration in Scaling FFAG, in Proc. 3rd Int. Particle Accelerator Conf. (IPAC'12), New Orleans, LA, USA, May 2012, paper WEPPR006, pp. 2946-2948.

[39] E. Yamakawa *et al.*, High Intensity Proton FFAG Ring with Serpentine Acceleration for ADS, in Proc. 52nd ICFA Advanced Beam Dynamics Workshop on High-Intensity and High-Brightness Hadron Beams (HB'12), Beijing, China, Sep. 2012, paper MOP209, pp. 60-63.

[40] S.L. Sheehy, The potential for a high power FFAG proton driver for ADS, 2013. arXiv:1310.3588[physics.acc-ph]

[41] S.L. Sheehy *et al.*, "Progress on Simulation of Fixed Field Alternating Gradient Accelerators", in Proc. 6th Int. Particle Accelerator Conf. (IPAC'15), Richmond, VA, USA, May 2015, pp. 495-498.

[42] Y. Mori, Experience and Perspective of FFAG Accelerator, in Proc. 61st ICFA Advanced Beam Dynamics Workshop on High-Intensity and High-Brightness Hadron Beams (HB'18), Daejeon, Korea, June 2018, pp. 342-346.

[43] Y. Mori *et al.*, Intense Negative Muon Facility with MERIT Ring for Nuclear Transmutation, Proceedings of the 14th International Conference on Muon Spin Rotation, Relaxation and Resonance (μSR2017), 2017 https://doi.org/10.7566/JPSCP.21.011063.

3.2 Overview of Fixed Field Alternating Gradient Accelerators

Grahame H. Rees (RAL, U.K., retired)

Non-linear magnetic field FFAs were invented by Ohkawa [1] in 1953 and subsequently prototyped at MURA (Mid-western Universities Research Association), Wisconsin [2]. The combined function gradient magnets had either spiral edges, or formed F(+) O D(-) O type lattice cells, where (±) indicates magnet bend directions. Field profiles were defined by $B_{y=0} = B = B_0(1 + x/r_0)^K$, where K is the constant field index, x is the radial offset from a B_0 reference orbit, at a distance r_0 from the FFA ring's centre, and $r = r_0 + x$. Local, normalized field gradients are: $B'/B\rho = K_v = K/\rho r$, where ρ_0 and ρ are the local magnet bend radii. Beam orbits are said to be scaling if different momenta orbits are scaled replicas of one another. Conditions for F D lattice scaling are that the beam orbits follow arcs at a constant field level and magnet edges are aligned with radial lines drawn to the ring centre ($\rho/\rho_0 = r/r_0$). In most practical cases, these conditions are not met.

Interest in FFAs returned in the 1990s [3], mainly in Japan, employing spiral or {D(-) o F(+) o D(-) O} triplet cell designs (with short o and longer O drift lengths). A 150 MeV proton triplet FFA was built at KEK [4]. A chain of three proton FFAs was built at KURRI[1] [5], to allow ADSR studies at KURRI's research reactor. There is a 0.1-2.5 MeV spiral ring and 2.5-20 MeV and 20-150 MeV triplet rings. The output energy of the first ring is adjustable and fields may be lowered in the other rings to provide scaled momentum ranges. The first ring uses induction acceleration, while the other two use broadband magnetic alloy (MA) Ohmori-type cavities [6] for the acceleration.

A FFA may use an internal emittance recovery target (ERIT) for an intense source of secondary particles (neutrons, pions etc.) [7]. A 10 MeV proton FFA has been developed for a KURRI neutron source since 2005, using a 5 micron thick beryllium target and a 200 kV, ionisation cooling cavity. Cooling limits transverse and longitudinal emittance growth due to multiple scattering and energy loss in the target. ERIT has been modified recently into a POP-MERIT (multiplex energy recovery internal target), with a reduction of the field index to allow simultaneous fixed frequency acceleration and storage [8], and the studies are to continue.

Traditional doublet or triplet FFAs have wide magnets and so are costly for higher intensities; studies at ANL, Chicago and Jülich, Germany were discontinued after low loss H^- injection proved to be a problem area. Scaling pumplet cells [9], {O d(-) o F(+) o D(-) o F(+) o d(-) O} and {O f(+) o D(-) o F(+) o D(-) o f(+) O} both allow reduced apertures, but H^- injection remains a problem for high powers. An alternative of direct, two plane multi-turn injection of protons [10] allows a higher current, lower emittance injector linac and an insertion-free FFA ring. A novel proposal is that of a vertical orbit excursion, superconducting magnet FFA [11], using a vertical field component to yield a skew quadrupole focusing action.

FFA rings may operate at a high repetition rate or, possibly, in a cw mode, to reach high power. Schemes appeared in the late 1990s to reduce the orbit separations and hence the radial apertures. Different arrangements of magnets were considered which were far removed from the scaling designs. Orbit bend radii were allowed to alter for each orbit, with continuously changing orbit beam dynamics. Designs were obtained for non-isochronous or nearly, or fully isochronous rings. A design using linear focusing magnets was proposed in 1999 for the rapid acceleration of high energy, $\mu^{\pm}$ beams [12].

Another type of non-scaling FFA accelerator [13] was proposed in 2004 by A.G. Ruggiero (BNL), for use in proton or heavy ion, high power driver applications. It again employed linear focusing gradient magnets [14]. Beam dynamics is different from that of the muons, however,

[1]Kyoto University Research Reactor Institute. The name has recently been changed to the Kyoto University Institute of Integrated Radiation and Nuclear Science, KURNS.

as the normalised beam emittances are smaller, space charge issues are involved, acceleration is always in the stable region, and operation is far away from isochronism. Both designs are similar, though, in that the negative chromaticities give large variations of tune with momentum, so that integer and half integer, betatron resonances are crossed in the ten to a hundred turns of acceleration and yet give only a small growth of the emittances.

An electron ring, EMMA, was built and commissioned at Daresbury Laboratory to study beam dynamic issues that occur in accelerators similar to those of references [12–14]. EMMA operated over the energy range 10 to 20 MeV and had 42 F D doublet cells and 19 rf cavities operating at 1.3 GHz. Studies were made of rapid acceleration, with large variations of the ring tunes, and the machine was able to demonstrate a new type of out-of-bucket acceleration called serpentine [15]. EMMA was the only FFA to have been built in Europe and the world's first non-scaling fixed field alternating gradient accelerator; however, it has since been dismantled. Despite all the studies that have been made, no high power FFA has yet been built.

Some of the design issues listed were previously reviewed in reference [16].

References

[1] T. Ohkawa, Proceedings of the annual meeting of the JPS, Japanese Physical Society (1953).

[2] K.R. Syman *et al.*, (MURA), Phys. Rev., p. 1837, 103 (1956).

[3] M.K. Craddock, The Rebirth of the FFAG, CERN Courier, 44-6, (2004).

[4] M. Aiba *et al.*, Status of 150 MeV Proton FFAG, Proceedings of International Workshop on FFAG Accelerators, KURRI (2005).

[5] Y. Mori, Development of FFAG Accelerators at KURRI, Proceedings of International Workshop on FFAG Accelerators, KURRI (2006).

[6] C. Ohmori *et al.*, High Field-gradient Cavities Loaded With Magnetic Alloys for Synchrotrons, Proceedings of PAC99, p413-417, New York (1999).

[7] Y. Mori, Secondary source by FFAG–ERIT scheme, Proceedings of International Workshop on FFAG Accelerators, KURRI (2005).

[8] Y. Mori, Beam study of MERIT-FFAG, Proceedings of International Workshop on FFAG Accelerators, KURRI (2018).

[9] G.H. Rees, FFAG Studies for Neutrino Factory Accelerators, Neutrino Factory Workshop, (2005).

[10] G.H. Rees, Direct Proton Injection for Spallation Source Rings, RAL internal note GHR1/ASTeC/Nov. (2016).

[11] S.J. Brooks, Vertical orbit excursion, fixed field alternating gradient accelerators, Phys. Rev. Vol. 16, Issue 8, Aug (2013).

[12] C.J. Johnstone *et al.*, Fixed field circular accelerator designs, Proceedings of PAC99, p3068-3070 (1999).

[13] A.G. Ruggiero, FFAG-based high intensity proton drivers, Proceedings of ICFA-HB2004, 324 (2004).

[14] A.G. Ruggiero, FFAG-based proton and ion drivers, ICFA Beam Dynamics Newsletter No. 43, 84 (2007)

[15] S. Machida, *et al.*, Nature Physics 8, 243 (2012).

[16] C.R. Prior, issue editor, FFAG accelerators, ICFA Beam Dynamics Newsletter No. 43, p12-126 (2007).

3.3 The Jülich SNQ-FFA Study 1983 to 1986

Godehard Wüstefeld, Guest Scientist, Helmholtz-Zentrum, Berlin, Germany

During the years 1980 to 1986 a feasibility study was carried out for the German spallation neutron source, Spallations Neutronen Quelle or SNQ [1]. Different methods for proton bunch compression for the SNQ were explored at the Kernforschungsanlage (KFA) Jülich (now Forschungszentrum (FZ) Jülich, Germany); among these, was an FFA, studied during the years 1983 to 1986. This machine combines acceleration and bunch compression for a pulsed neutron source. The study covered only a short time period, but it is worth recalling it in the context of this Newsletter. The work took place partly in Jülich and partly at the Argonne National Laboratory (ANL, Chicago, USA), in close collaboration with the ANL ASPUN team headed by R. Kustom. ANL pioneered the accelerator based spallation with their synchrotron-based "Intense Pulsed Neutron Source" [2]. During our visit there, we benefited from the expertise on FFAs of this group, where some veterans of the MURA group were still active [3]. In this note mostly the results of the FFA work done by the Jülich SNQ group are summarized.

FFA studies were abandoned after the MURA project ended until the nineteen eighties when the concept was revived by Tat K. Khoe (ANL) and Phil F. Meads jr. (Oakland, USA, a former MURA scientist). They independently suggested that an FFA would be an ideal high current proton accelerator for an intense spallation neutron source. A first proposal of a machine, satisfying the required beam parameters, was presented by the ASPUN team [4, 5]. Typical beam requirements for these machines were 1.5 GeV beam energy, average beam current of 5 mA, and a repetition rate of the extracted beam of less than 100 Hz.

The Jülich FFA study group was small: the author and Ph. Meads as an external consultant, spending about 3 years on this subject. Two international workshops were organized in Jülich to explore the potential of FFAs as a driver for a spallation neutron source [6, 7]. As a first attempt for an SNQ-FFA proposal, we simply scaled the ASPUN machine parameters to the quite similar SNQ demands. Both proposals where based on spiral-sector FFAs. We came up, for example, with huge but feasible magnets, comparable with the SIN cyclotron magnets [8].

During our ANL stay we started to re-evaluate a radial-sector FFA. This type of FFA was not really considered as a serious option. Its reverse bending magnets require larger integrated magnet length around the machine circumference. This leads to a less compact design than a spiral-sector machine. We used simple approximations to better understand the conditions for the required magnet length; the results are summarized in [9, 10].

We found, for example, that the integrated magnetic length scales with the inverse square of the applied field strength, which favours solutions with high magnetic fields. A superconducting (SC) coil, as suggested for the SuSe cyclotron [11] with 4.8 T peak field and was under construction at that time was our guide line. By applying such a SC magnet compared to a normal conducting magnet one could drastically reduce the magnet length.

Additionally, we proposed a new layout of the magnets. Up to this point, all radial-sector FFA designs had separate focusing and defocusing magnets in a type of FODO cell. The magnets are designed like classical C-shaped magnets, where the return flux of the field is guided backwards out of the beam area. We came up with a new scheme, to combine the F and D magnet types into a single magnet, as a DFD triplet. Here the return flux of the main F field is shared with the adjacent D magnets and shaped in such a way, that the required defocusing D field scaling is satisfied, see inset in Fig. 1. This complex field shape needs to fulfil the FFA scaling conditions for gradient and flutter. The advantage of this scheme was a very compact design of the magnets, yielding what today is called the triplet focusing DFD of the FFA. A comparison of the spiral- and radial-scaled FFA for nearly equal beam target values is presented in Fig. 1. This estimate was based on crude approximations of the magnetic field. A careful design of the

required SC magnet shape confirmed the feasibility of this concept [12, 13].

This radial-sector machine shows several promising advantages, such as longer and better usable drift spaces between the magnets, i.e. the radio-frequency cavities become well separated from the magnets, injection and extraction can be done easier, the beam passes the fringing field regions at less critical, smaller angle. However, the SC magnets, if required, are more complicated to build, need more care for operation and cooling and are sensitive to radiation damage.

For beam dynamic studies we used the newly developed code "ORBIT" [14]. This code generates the linear machine optics, like Twiss parameters, produces a fast scan of various working points and performs multi-turn tracking. For tracking an 8th order Runge-Kutta integration routine was applied. The magnetic field input requires a user supplied azimuthal field profile along the reference orbit, the k index and the spiral angle, which is then completed analytically to obtain the correct scaling three dimensional FFA field.

The tracking integration routine was non-symplectic. A correct symplectic integration routine was possible, but to simulate the multi-turn beam dynamics in such a time consuming way was beyond the scope of computer performances at that time. To overcome this limitation and to speed up the tracking we developed the method of numerical generating functions. A set of tracking results of particle coordinates of one FFA magnet sector were fitted to a numerical generating function, approximated by higher order power series expansions. This generating function could be repeatedly iterated for many turns, leading to a fast and symplectic tracking. A first attempt of this method for fixed particle energy is shown in [15][1].

An FFA of this size would be a major technological challenge compared to the small electron prototypes built during MURA times. The ANL group suggested therefore, to build a smaller machine, "Mini-ASPUN", to evaluate its feasibility. Mini-ASPUN was designed already as a powerful spallation source and could be used later as an injector for the larger ASPUN FFA. A comparison of the main FFA parameters of these two spiral-sector machines, together with the radial-sector SNQ-FFA are shown in Table 1. Figure 1 compares the footprint of the spiral- and the radial-sector FFAs. The target values for the beams of the two larger machines where very similar. For the Mini-ASPUN a technical design report was produced by the ASPUN team [17]; a few parameters are presented in [18].

In summer 1986 the SNQ project and the FFA work were terminated prematurely. However, two more results can be mentioned. Radial- and spiral-scaling FFAs represent two limiting cases: a smooth transition between these types is possible and could relax some of the design parameters, like the edge angle. A radial-scaling FFA combined with a modest spiral angle of 30° was suggested in [19]. A non-scaling FFA with achromatic arcs was studied by Ph. Meads [20]. The achromatic straight could be used, i.e. to place rf cavities of smaller radial extension or injection and extraction elements.

After the shutdown of the SNQ project, some FFA activity still continues on an informal level, headed by S. Martin (FZ Jülich) and K. Ziegler (Hahn-Meitner Institut, now Helmholtz-Zentrum Berlin, Germany). Several papers were published from this collaboration, e.g. [21, 22]. The goal was to establish this machine as a European or a National spallation source.

It is a pleasure to thank my former colleagues R.L. Kustom, S.A. Martin and Ph.F. Meads for a productive collaboration on FFAs about 35 years ago and for proofreading this note.

References

[1] G.S. Bauer, H. Sebening, J.-E. Vetter, H. Willax (Herausgeber), "Realisierungsstudie zur Spallations-Neutronenquelle", JÜL-SPEZ-113, KfK 3175, Jülich und Karlsruhe, Germany

[1] This method was later further developed and adopted to track complex, helical electron orbits in undulators, resulting in a flexible, fast and symplectic tracking routine [16].

Table 1: Comparison of the main FFA parameters, suitable as a neutron spallation source, Mini-ASPUN (spiral), ASPUN (spiral) and the SNQ-FFA (radial).

Parameter	**Unit**	**Mini-ASPUN**	**ASPUN**	**SNQ-FFA**
injection energy	MeV	50	200	350
extraction energy	MeV	500	1500	1500
injection orbit length	m	8.41	25.89	26.37
extraction orbit length	m	9.67	28.14	28.14
number of sectors		16	20	20
field index k		8	14	13.4
spiral angle	degrees	57	61	0
magnetic field at injection	T	0.49	0.41	
magnetic field at extraction	T	1.5	1.33	4.1
radial, vertical tunes		3.15, 2.3	4.25, 3.3	4.25, 3.3
max. rf voltage per turn	kV	60	400	200
extracted beam repetition rate	Hz	30	50	100
average beam current	mA	0.1	3.8	5

(1981). https://publikationen.bibliothek.kit.edu/270016054/3812274

[2] J.M. Carpenter, D.L. Price, "An Intense Pulsed Neutron Source for Argonne National Laboratory", Proceedings of the 1975 Particle Accelerator Conference, Washington, DC, USA (1975). http://accelconf.web.cern.ch/AccelConf/p75/PDF/PAC1975_1768.PDF

[3] F.T. Cole, "O Camelot! A Memoir of the MURA Years", Proceedings of the 16th International Conference on Cyclotrons, 2001, Supplementary Materials, East Lansing, USA (2001). http://accelconf.web.cern.ch/AccelConf/c01/cyc2001/extra/Cole.pdf

[4] T.K. Khoe, R.L. Kustom, "ASPUN, Design for an Argonne Super Intense Pulsed Neutron Source", Proceedings of the 1983 Particle Accelerator Conference, Santa Fe, New Mexico, USA (1983). http://accelconf.web.cern.ch/AccelConf/p83/PDF/PAC1983_2086.PDF

[5] R.L. Kustom, E.A. Crosbie, T.K. Khoe, "A 1500 MeV Fixed-Field Alternating-Gradient Synchrotron for a Pulsed-Spallation Neutron Source", Proceedings of the 1985 Particle Accelerator Conference, Vancouver, BC, Canada (1985). http://accelconf.web.cern.ch/AccelConf/p85/PDF/PAC1985_2672.PDF

[6] S. Martin, G. Wüstefeld, editors, "Jülich Seminar on Fixed Field Alternating Gradient Accelerators (FFAG)", March, 1983, Kernforschungsanlage, SNQ 2 MZ / BS 99 1 8, Jülich, Germany (1983). http://cds.cern.ch/record/406922?ln=de

[7] G. Wüstefeld, editor, "2nd Jülich Seminar on Fixed Field Alternating Gradient Accelerators (FFAG)", May, 1984, Kernforschungsanlage, SNQ 2 MV. / CY 03 07 84, Jülich, Germany (1984). http://cds.cern.ch/record/406923?ln=de

[8] H. Willax, "Status report on SIN", Proceedings of the 5$^{\text{th}}$ International Cyclotron Conference, Oxford, UK (1969). http://accelconf.web.cern.ch/AccelConf/c69/papers/cyc69a07.pdf

[9] G. Wüstefeld, "Conceptual design of a radial FFAG type lattice", unpublished note, ASPUN Note-10 (4/18/85), Argonne, USA (1985).

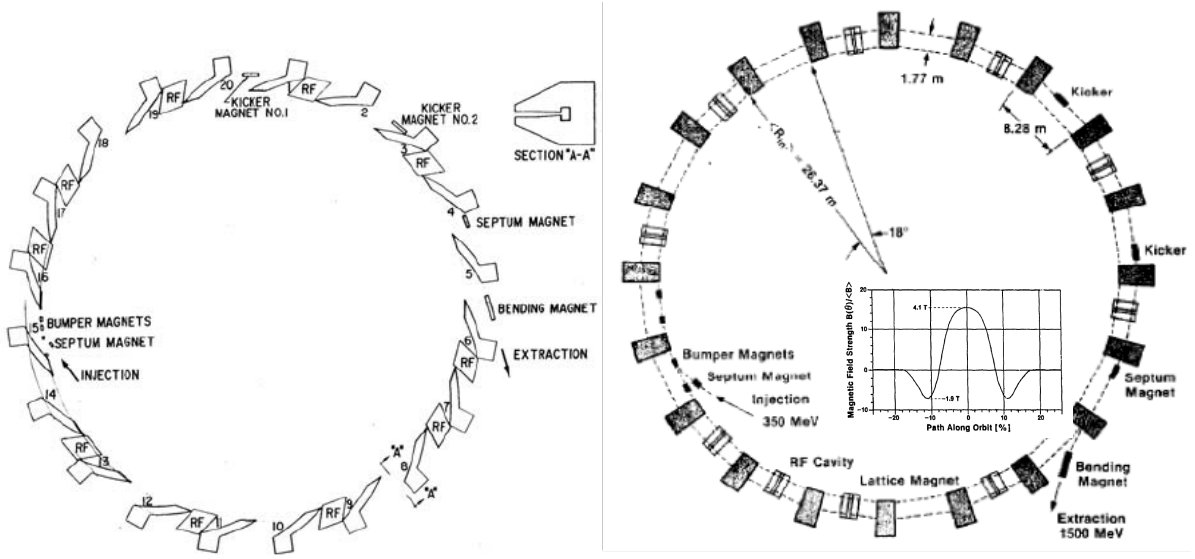

Figure 1: Scheme of the spiral-scaling ASPUN-FFA [5] and the radial-scaling SNQ-FFA [10]. The small inset in the left figure shows the C-shaped, normal conducting magnet, the inset right shows the longitudinal dependence of the SC magnetic field of one of the DFD magnets.

[10] Ph.F. Meads jr., G. Wüstefeld, "An FFAG Compressor and Accelerator Ring Studied for the German Spallation Neutron Source", Proceedings of the 1985 Particle Accelerator Conference, Vancouver, BC, Canada (1985). http://accelconf.web.cern.ch/AccelConf/p85/HTML/AUTHORS.HTM

[11] U. Trinks et al., "Design Status of the Munich Cyclotron SuSe", Proceedings of the 1983 Particle Accelerator Conference, Santa Fe, New Mexico, USA (1983). http://accelconf.web.cern.ch/AccelConf/p91/PDF/PAC1991_2254.PDF

[12] M. Abdelsalam, R. Kustom, "Superconducting Magnet Design for Fixed-Field Alternating-Gradient (FFAG) Accelerator", IEEE Transactions on Magnetics, Vol. 30 No. 4, July 1994. https://ieeexplore.ieee.org/document/305816

[13] S. Martin, priv. communication

[14] Ph.F. Meads, "A New FFAG Orbit Code", Proceedings of the 1985 Particle Accelerator Conference, Vancouver, BC, Canada (1985). http://accelconf.web.cern.ch/AccelConf/p85/PDF/PAC1985_2243.PDF

[15] H. Lustfeld, G. Wüstefeld, Ph. F. Meads, et al., "A Proper Canonical Mapping Transformation", Proceedings of the 1984 Linear Accelerator Conference, Seeheim, Germany (1984). https://accelconf.web.cern.ch/accelconf/l84/papers/tup0016.pdf

[16] J. Bahrdt, G. Wüstefeld, "Symplectic tracking and compensation of dynamic field integrals in complex undulator structures", Phys. Rev. ST Accel. Beams 14, 040703, 2011. https://journals.aps.org/prab/pdf/10.1103/PhysRevSTAB.14.040703

[17] R. Kustom, Mini-ASPUN, private communication

[18] R. Kustom, "Overview of ASPUN and Prototype Projects, Appendix: The ASPUN / Mini-ASPUN-Projects", in [7].

[19] Ph. Meads, G. Wüstefeld, "FFAG Synchrotrons for Heavy Ion Acceleration", Proceedings of the 1987 Particle Accelerator Conference, Washington, D.C., USA (1987). http://accelconf.web.cern.ch/AccelConf/p87/PDF/PAC1987_0842.PDF

[20] Ph.F. Meads jr., "A Compensated Dispersion-free Long Insertion for an FFAG Synchrotron", Proceedings of the 1993 Particle Accelerator Conference, Washington, D. C., USA (1993). http://accelconf.web.cern.ch/AccelConf/p93/PDF/PAC1993_3825.PDF

[21] S.A. Martin, E. Zaplatin et al., "Study of an FFAG Synchrocyclotron for a Pulsed Neutron Source", Proceedings of the 13$^{\text{th}}$ International Conference on Cyclotrons and their Applications, Vancouver, BC, Canada (1992). http://accelconf.web.cern.ch/AccelConf/c92/papers/xii-02.pdf

[22] R.L. Kustom, S. Martin, Ph.F. Meads jr., E. Zaplatin, K. Ziegler, "FFAG - Option for Spallation Neutron Sources", ICANS-XIII, 13$^{\text{th}}$ Meeting of International Collaboration on Advanced Neutron Sources, Paul Scherrer Institut, Villingen, Switzerland (1995). http://www.neutronresearch.com/parch/1995/01/199501007450.pdf

3.4 FFAs at KURRI

Yoshihiro Ishi, Tomonori Uesugi, Yasutoshi Kuriyama and Yoshiharu Mori,
Institute for Integrated Radiation and Nuclear Science, Kyoto University, Japan.

3.4.1 Proton Driver for ADS

An accelerator complex at Kyoto University Research Reactor Institute (KURRI[1]) has been designed as a proton driver for an accelerator driven system (ADS) which is a hybrid system composed of a nuclear reactor facility and an accelerator facility. It sustains a nuclear fission chain reaction induced by a large number of spallation neutrons obtained by irradiation of a heavy metal target using high energy proton beams generated by accelerators. The nuclear reactor plays the role of neutron booster which amplifies the neutron flux from the target.

Nowadays, especially after the severe nuclear accident in Fukushima Japan, ADS is important not only as an energy production facility, but as a technique for transmuting long-lived radiative materials such as the minor actinide (MA) to others whose lifetimes are much shorter than the original ones. In the nuclear fuel cycle, MAs can be processed in a fast breeder. But in terms of the stability of the critical operation, the fraction of the MAs in the fuel system is limited to a few percent. On the other hand, in the ADS, MA can be loaded up to some 30% because the fuel system is operated at a sub-critical level.

At the Kyoto University Research Reactor Institute (KURRI), basic experimental studies about the ADS have been running since 2009 using one of research reactors, the Kyoto University Critical Assembly (KUCA) [1]. In these studies, the KUCA has been operated in sub-critical mode and FFA accelerators have been used as a proton driver.

3.4.2 FFA Accelerator Complex at KURRI

A schematic diagram of the KURRI FFA accelerator complex is shown in Fig. 1 [2]. The complex used to have three FFA rings: the ION-BETA, the BOOSTER and the MAIN RING. All three rings adopt an FFA focusing scheme. However, the original injector system composed of the ION-BETA and the BOOSTER has been replaced by the 11 MeV H^- linac in order to increase the beam intensity. Table 1 shows the basic parameters of the complex.

The new injector system consists of three linacs: RFQ, DTL1 and DTL2. and has been adopted as the injector to the ERIT ring [3]. The injection line is shown in Fig. 3. H^- beams are injected into the FFA MAIN RING through a charge stripping foil made of carbon. In this injection scheme, no pulse device is used. Even orbit merging magnets are not necessary because the H^- beams are merged inside the main magnet of the MAIN RING as shown in Fig. 4. The beam current extracted from the MAIN RING has been increased by a factor of 10 as a result of this replacement. A ring footprint of the KURRI FFA MAIN RING is shown in Fig. 5. The beta functions of this ring are shown in Fig. 6

3.4.3 Beam Users

The proton beams from the FFA complex are delivered to users of various experiments: ADS experiments[2], irradiation experiments on materials and biological experiments with irradiation to living animals (rats) for a basic study of BNCT[3].

[1] Although the name of the institute has been changed from KURRI to KURNS, which stands for "Institute for Integrated Radiation and Nuclear Science, Kyoto University", we use KURRI in this article.

[2] This work was supported by MEXT(the Ministry of Education, Culture, Sports, Science and Technology) of Japan as part of a task entitled "Research and Development for an Accelerator-Driven Sub-critical System Using an FFAG Accelerator".

[3] Boron Neutron Capture Therapy.

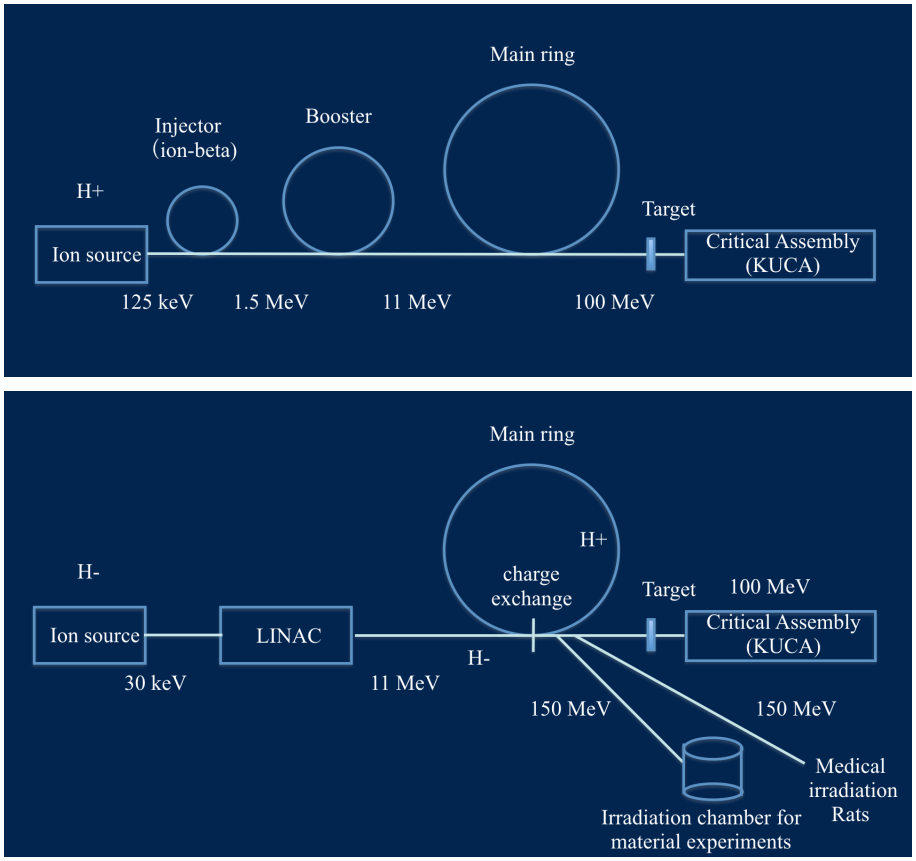

Figure 1: Schematic diagram of the KURRI FFA Accelerator Complex. The upper pictures shows the original configuration, the lower is the upgraded one. The injector system composed of the injector (ION-BETA) and the BOOSTER has been replaced by the H^- linac.

For the ADS experiments, the beam is transported from the accelerator facility to the subcritical fuel system located at one of the cores in the KUCA called "A-core" (Fig. 7). Two kinds of measurement are performed in the KUCA: dynamic characteristics measurements detecting prompt and delayed neutrons, and static measurements of neutron energy spectrum or reaction rate distributions using radio-activation of the indium (In). The result of dynamic measurements from the first experiment in the world is shown in Fig. 8. There are two components in the neutron counting rate: the fast component decaying exponentially and the slow component caused by delayed neutrons almost constant in time. The presence of the delayed neutrons indicates that neutrons are generated through the nuclear fission chain reaction inside the fuel system. This series of ADS experiments has been ongoing since 2009 with changing experimental conditions such as the material of the neutron production target, configuration of the fuel system and beam intensity. The results from these experiments can be seen in articles [4]- [8].

Reacently, on 14^{th} and 15^{th} February 2019, the first nuclear transmutation of minor actinides (^{237}Np and ^{241}Am) by the ADS process was successfully demonstrated [9] in a subcritical core at KUCA using FFA, as shown in Figs. 9-11.

3.4.4 Acceleration performance of the MAIN RING

MAIN RING Acceleration

The KURRI FFA synchrotron accelerates proton beams of 11 MeV up to 100 MeV or 150 MeV in ordinary operation. This machine is of the so-called *radial sector scaling FFA* type, where

Table 1: Basic Parameters of KURRI FFA Accelerator Complex

Linac	
Repetition rate	< 200 Hz
Peak current	< 5 µA
Pulse length	< 100 µs (uniform)
Energy	11 MeV
MAIN RING	
Field index k	7.5
Magnetic field	1.6 T (max.)
Energy	11 - 100 or 150 MeV
Revolution frequency	1.6 - 4.3 MHz
Rf voltage	4 kV

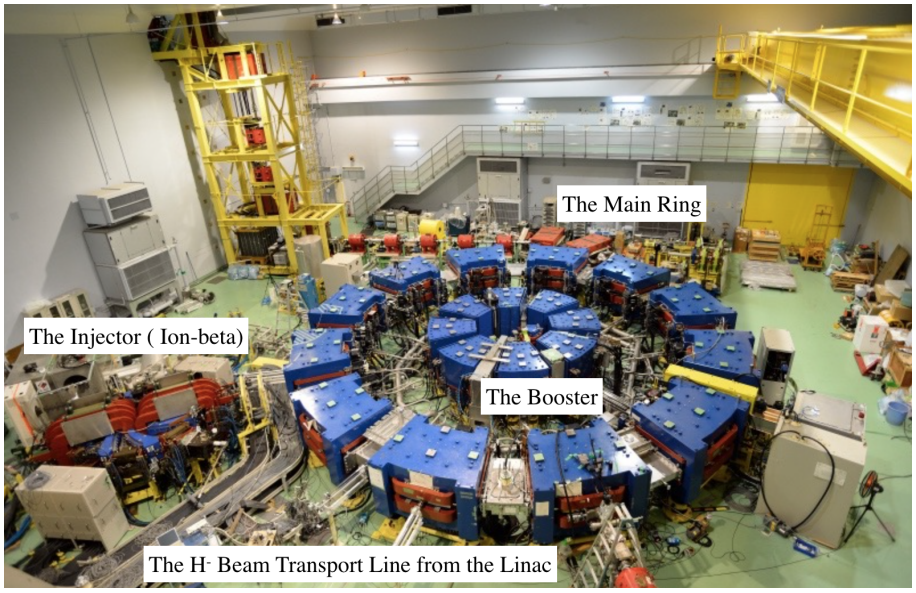

Figure 2: FFA Accelerator Complex at KURRI.

Table 2: Parameters of FFA MAIN RING and injector

Parameter	**Value**
Particle	Proton
Kinetic energy	11 – 150 MeV
Revolution frequency	1.58 – 3.85 MHz
Twiss (β_x, β_y)	(2.9 m, 2.5 m) at foil
Dispersion	24 mm/MeV
Acceleration speed	1.4 keV/turn

the field strength is designed such that $B(r)$ along a radius is proportional to r^k. The dispersion function is therefore $(k+1)r$, where r is the closed orbit radius. In reality, because of the scaling field imperfection, the field index k gradually shifts from 7.0 at the injection orbit to 7.7 at the extraction energy orbit, while the designed value was 7.5. The orbit shift due to the

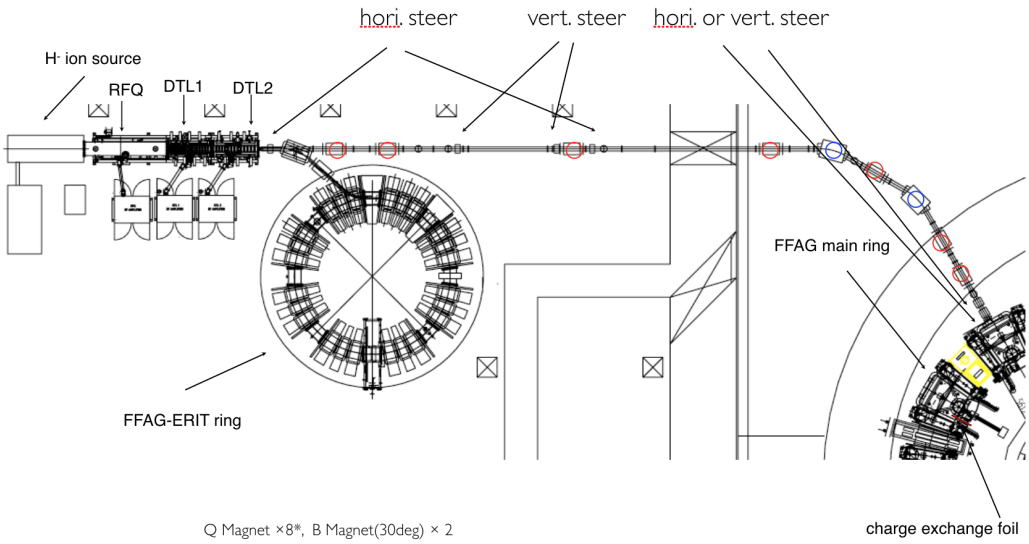

Figure 3: H^- beam transport line.

acceleration is 24 mm/MeV at the injection energy. The betatron tunes at the injection energy were measured to be $(3.63, 1.39)$ [10].

The emittance is typically assumed to be $5\,\pi$ mm-mrad in both transverse phase planes, which corresponds to 20 mm in real space. The measured dispersion of the beam line at the injection point was -0.54 m, while the dispersion function of the ring is $+0.59$ m. Injected beams are captured and accelerated by a moving rf bucket. The rf amplitude is fixed at 4 kV and the accelerating phase is 20 deg over the acceleration cycle. Thus the energy gain is 1.4 keV/turn and the orbit shift by the acceleration corresponds to 1 mm/30 turns, or, 50 mm/ms.

Stripping Foil

The stripping foil is made of carbon whose thickness is 10 μg/cm^2, and its dimensions are $25(\mathrm{H})\times30(\mathrm{V})$ mm^2. It is fixed at a three-sided holder at the tip of the rod, which limits the vertical aperture. The energy loss and scattering angle of an 11 MeV proton were simulated by GEANT4. Figures 12 and 13 show the distribution of lost energy and scattering angle, respectively. The stripping efficiency of H^- ion was $> 99\%$.

Simulation Studies

Multi-particle simulations in 6-dimensional space have been carried out. The stripping foil is defined as a rectangle in (r, y), and particles are injected only when they fall inside the foil (Fig. 14). A circulating particle undergoes scattering and energy loss when it hits the foil. Any particle that exceeds the vertical aperture is lost.

Emittance Growth without Acceleration

First, free emittance growth caused by the scattering was simulated without acceleration. A constant frequency rf was applied to maintain the beam energy. The results showed that the transverse emittances increased linearly at a constant rate of $70\,\pi$ mm-mrad/ms, as in Fig. 15, and the speed was independent of the initial distribution. Significant beam loss at the vertical

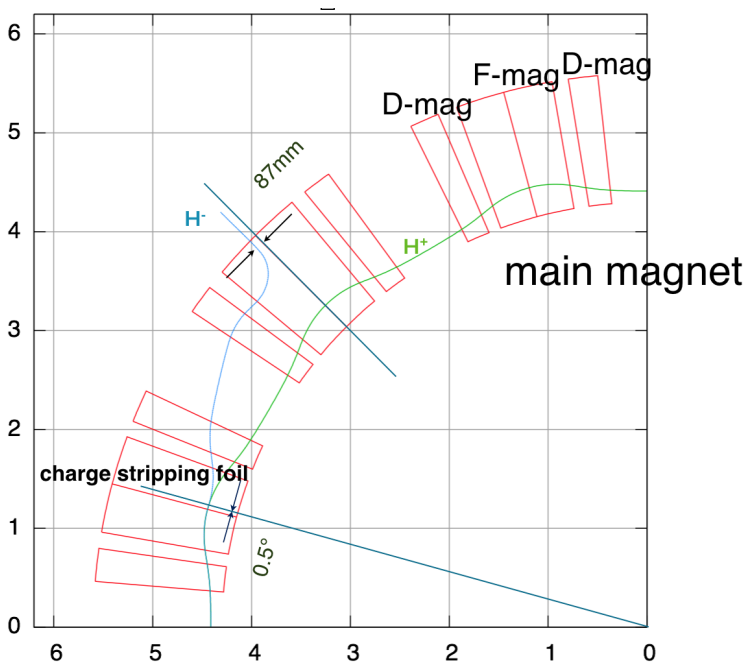

Figure 4: H^- beam injection using the charge stripping foil.

aperture started around 0.1 ms, which corresponds to 150 turns, and 90% of the beam was lost within 0.5 ms.

With Acceleration

With acceleration, the synchronous particle orbit is shifted at a rate of 50 mm/ms. Therefore a particle continues hitting the foil for 0.2 ms on average. This time is comparable to the emittance growth, as shown in Fig. 15. Simulation studies were carried out with acceleration, assuming the injected beam to be matched to the ring. Figure 16 shows the simulated emittance growth and beam loss. The capture efficiency was 25.7%. Each captured particle hits the foil 200 - 500 times.

The dependence on the momentum spread of the injected beam has also been studied (Fig. 18). The capture efficiency was reduced to 9% by increasing the momentum spread up to 1%.

Summary of Acceleration performance of the MAIN RING

Simulation studies of charge-exchange multi-turn injection have been performed including effects of scattering by the foil. The simulated capture efficiency was reduced to 25.7%, compared with 35% without scattering. However the efficiency is still higher than the experimental results show. Further studies, including experiments, such as injection mismatch, are necessary to understand this discrepancy.

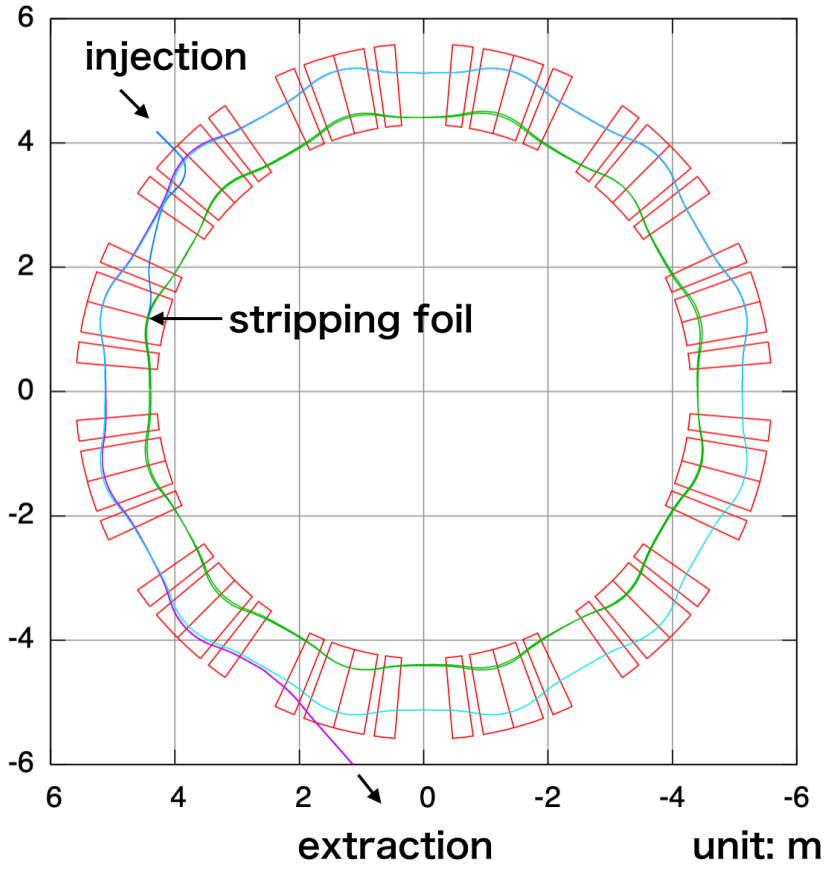

Figure 5: Footprint of the KURRI FFA MAIN RING.

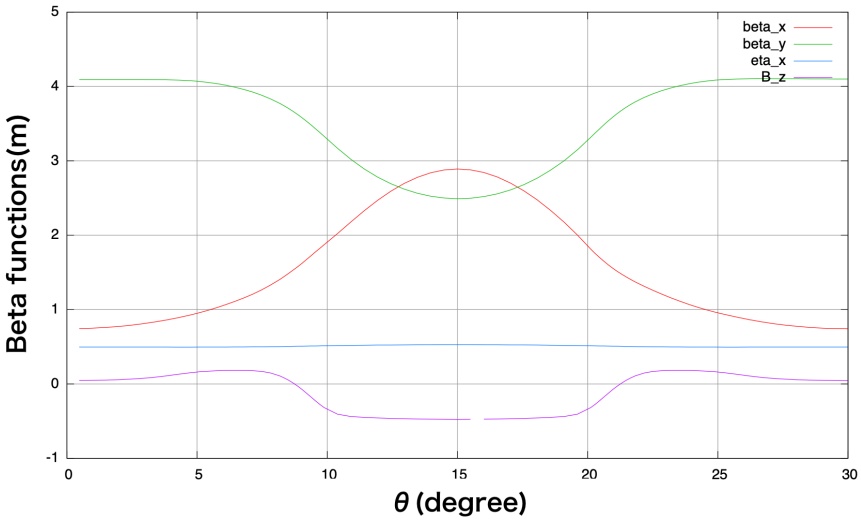

Figure 6: Beta functions of the KURRI FFA MAIN RING.

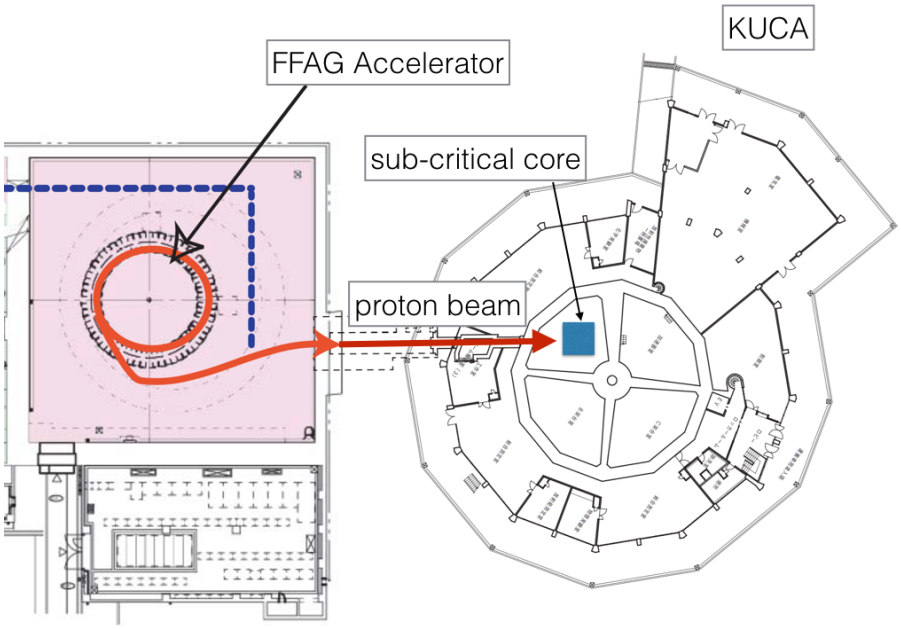

Figure 7: Connection between the FFA accelerator complex and KUCA.

3.4.5 Betatron Tune Behavior During Acceleration

Generally, a scaling FFA accelerator has zero-chromatic characteristics *i.e.* the betatron tunes are fixed during acceleration. This nature can be realized by orbit similarity for the different energy beams and an FFA magnetic field form

$$B(r,\theta) = B_0(\theta)\left(\frac{r}{r_0}\right)^k, \tag{1}$$

where θ is the azimuthal angle, r is the radius from the machine center and k is a constant number. If these scaling conditions are fulfilled, zero-chromatic operations can be carried out. However, in a practical machine, it is impossible to guarantee such a perfect zero-chromatic field configuration. One of major reasons for breaking the conditions is leakage of the magnetic field from the main body region to the straight section. If the leakage field distribution scales in the same manner as the main body field, zero chromaticity would be conserved. However, this is not the case for real machines. Since the gap of the FFA magnet becomes wider toward the inside, the influence of the leakage field becomes stronger in the inside without adjusted the field clamps.

There are two similar radial sector scaling FFA synchrotrons at KURRI: BOOSTER and MAIN RING. These rings adopt different types of magnets: one has no return yokes: the so-called 'yoke free type' adopted by MAIN RING, which has large tune variations causing non-negligible beam losses; the other has return yokes and field clamps adopted by BOOSTER, which has smaller tune variations compared with MAIN RING. We report the tune measurements and calculations based on 3-d magnetic field calculations for these two types of ring and discuss the scaling conditions in FFA accelerators [11].

Design parameters of the main magnets

The lattice structures of BOOSTER and MAIN RING are almost the same in that they are both DFD triplets. However, the basic design concepts of the main magnets are totally different. For

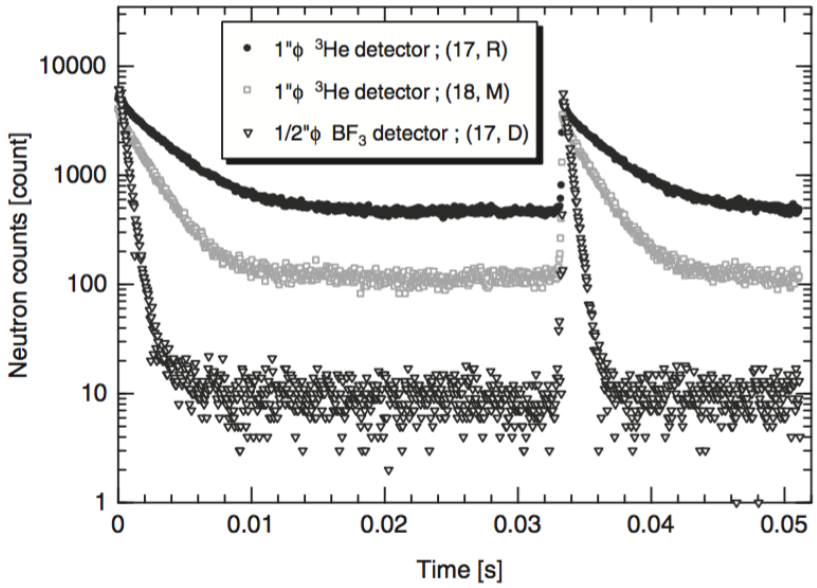

Figure 8: Measured prompt and delayed neutron behaviors obtained from different configurations of detectors.

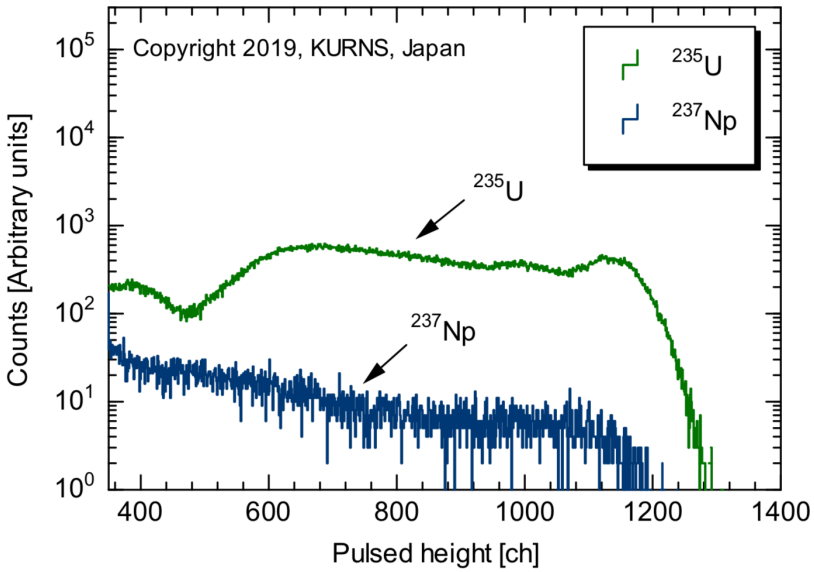

Figure 9: Measured pulsed heights of ^{237}Np and ^{235}U fission reaction rates at subcritical state.

MAIN RING, the different energy beam extraction is realized by changing the position of the extraction kicker and septum magnets. In this scheme, the beams with different energies are extracted through different trajectories. Therefore, we needed to expand the extraction channel which is located at the space for the return yoke. It is difficult to provide a wide channel inside the return yoke iron, eradicating the leakage field inside the channel. A novel idea to get around this difficulty is to get rid of return yokes. The input model of the main magnet in MAIN RING for the magnetic field calculation by TOSCA is shown in Fig. 19. Flux generated by the coil of

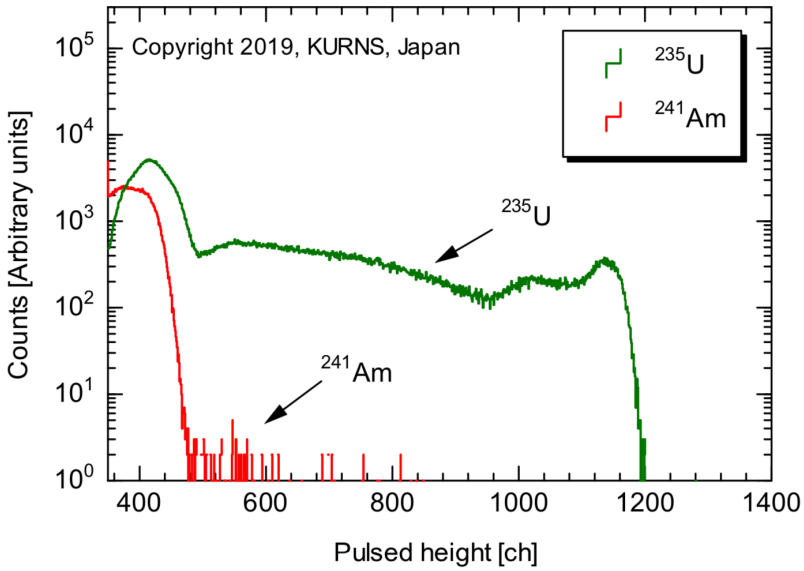

Figure 10: Measured pulsed heights of ^{241}Am and ^{235}U fission reaction rates at subcritical state.

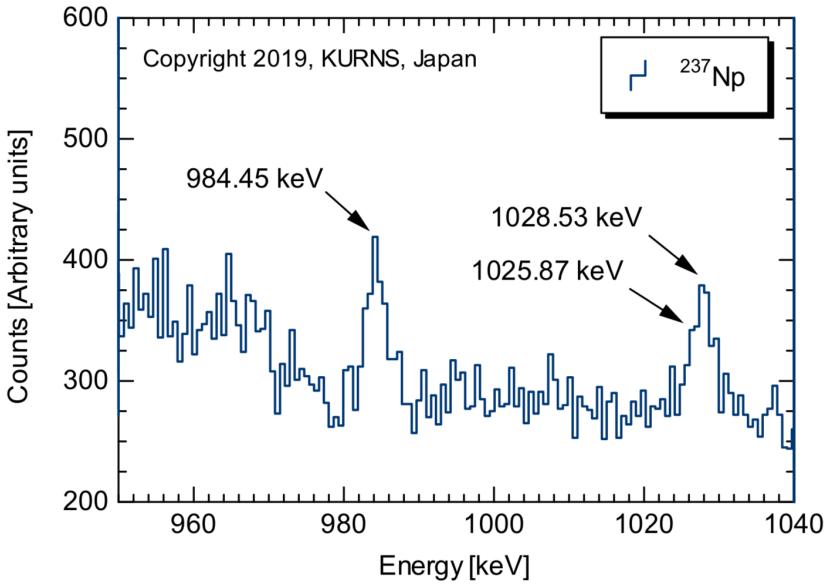

Figure 11: Measured γ-ray spectrum of ^{237}Np capture reaction rates at subcritical state

the F-pole returns through the D-poles, making the use of field clamps impractical. At the cost of an increase in leakage field in the straight section, we found a solution to the variable energy beam extraction. As shown in Fig. 20, there is leakage magnetic field more than a few 100 gauss at the center of the straight section.

Figure 21 shows the TOSCA input model of the BOOSTER main magnet, which has return yokes and field clamps to minimize the leakage field at the straight sections. As seen in Fig. 22, the leakage field at the center of the straight section is almost zero. In addition, the shape of $B_z(\theta)$ including leakage field scales with radius, which is desirable for zero chromaticity.

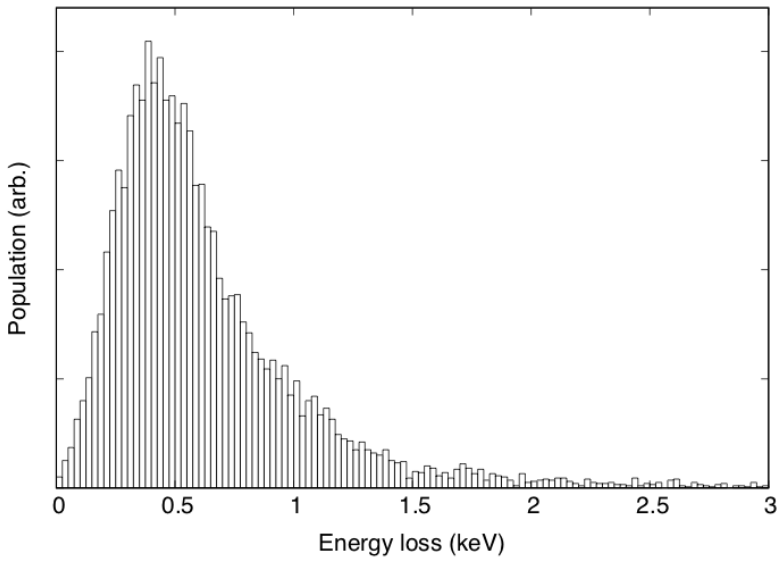

Figure 12: Energy loss on passage of the carbon foil (simulated with GEANT4).

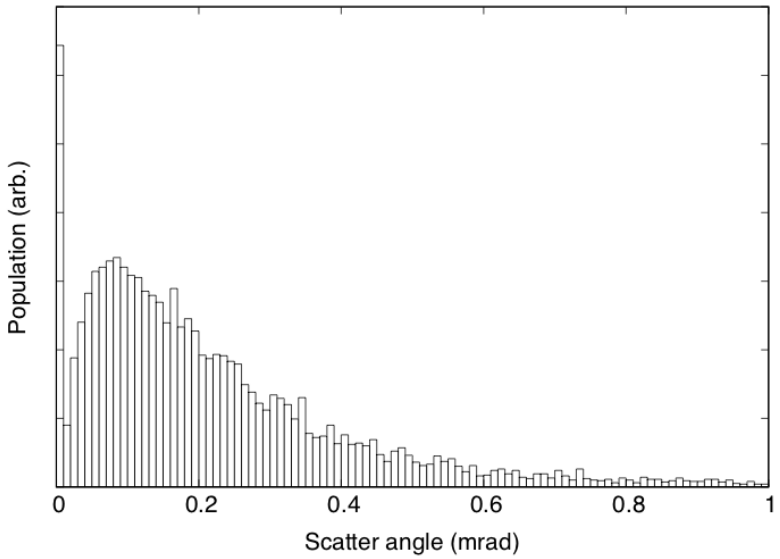

Figure 13: Scattering angle on passage of the carbon foil (simulated with GEANT4).

Tune spread, resonance crossing and beam losses

Betatron tunes for different energies have been measured in MAIN RING and BOOSTER. The measurements were performed at the flat top after acceleration for different energies. The tune footprint during acceleration in MAIN RING is shown in Fig. 23. Tunes from the simulations based on 3-d magnetic field maps are also shown in this figure. These are calculated from the transfer matrix determined in a small segment along the scalloped closed orbit,which is obtained by using a 4^{th} order Runge-Kutta solver. A simulation code named EARLIETIMES [12] has been used to calculate closed orbits, tunes and other features.

The tune spread during acceleration in MAIN RING is too large to avoid crossing resonance lines. Figure 24 shows the output signal from the bunch monitor. One can see some non-negligible beam losses around 1.0 ms, 2.7 ms, 4.3 ms and 20.1 ms from the start of acceleration.

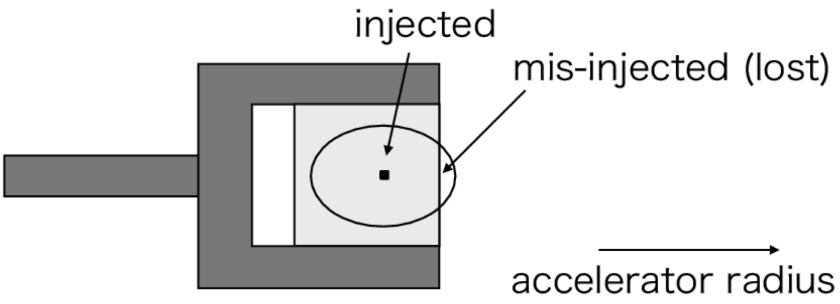

Figure 14: Stripping foil and its holder.

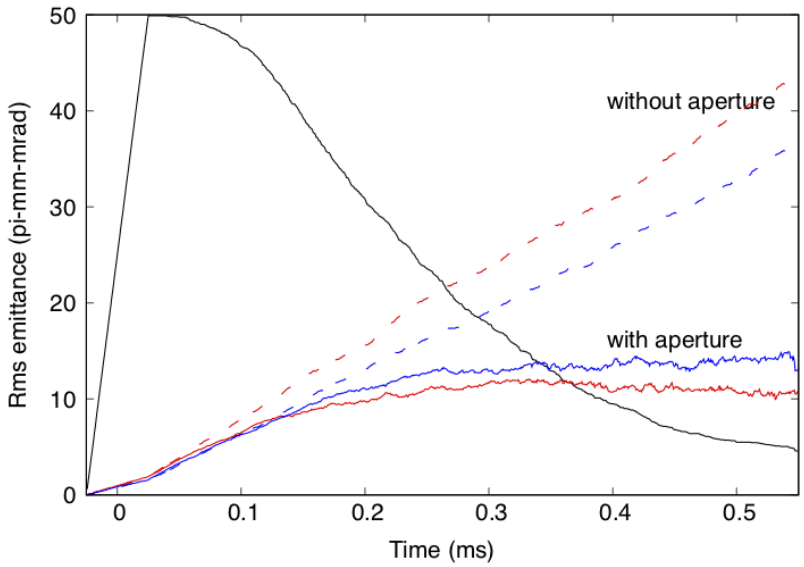

Figure 15: Horizontal (red) and vertical (blue) emittance growth caused by foil scattering. The number of surviving particles is plotted in black (full-span=100%). The dashed lines show the case with an infinitely large foil.

These loss timings could be related to the same timings as resonance crossing indicated in Fig. 23. In this case, the harmful resonance seems to be $Q_x - 2Q_y = 1$.

The tune footprint during acceleration in BOOSTER is shown in Fig. 25. The tune spread is small compared with MAIN RING, small enough to avoid crossing the resonances. In this case we need only be concerned with $Q_x + 2Q_y = 5$, but no obvious beam loss can be seen, as shown in Fig. 26.

Summary of Betatron Tune Behavior During Acceleration

As with the BOOSTER at KURNS, a scaling FFA accelerator, with magnets adopting flux return yokes and field clamps to suppress the leakage magnetic field at the straight section, considerably reduces the tune excursion during acceleration. In other words, it is scaled.

3.4.6 Upgrade Plans

In order to make the facility multi-capable, we are investigating two upgrade possibilities: (1) increasing the beam current up to the order of μA by increasing the repetition rate to the order

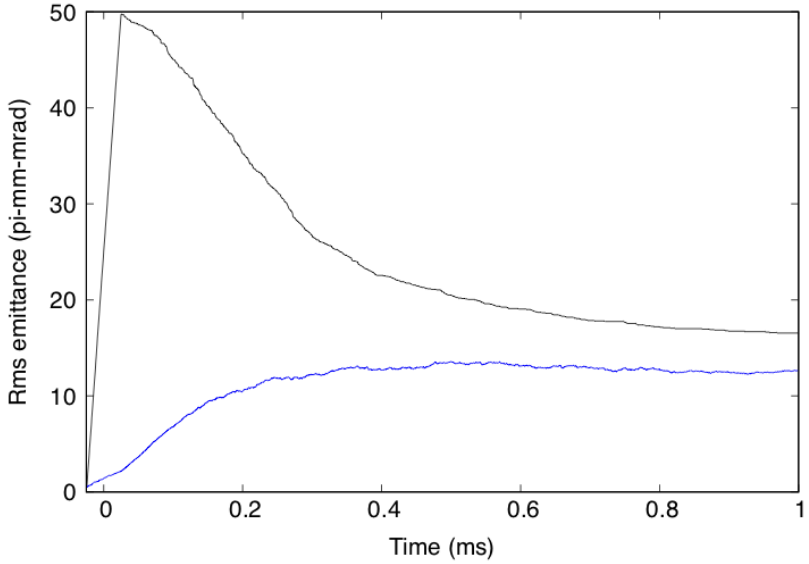

Figure 16: Vertical emittance growth (blue) and number of survived particles (black, full-span = 100%).

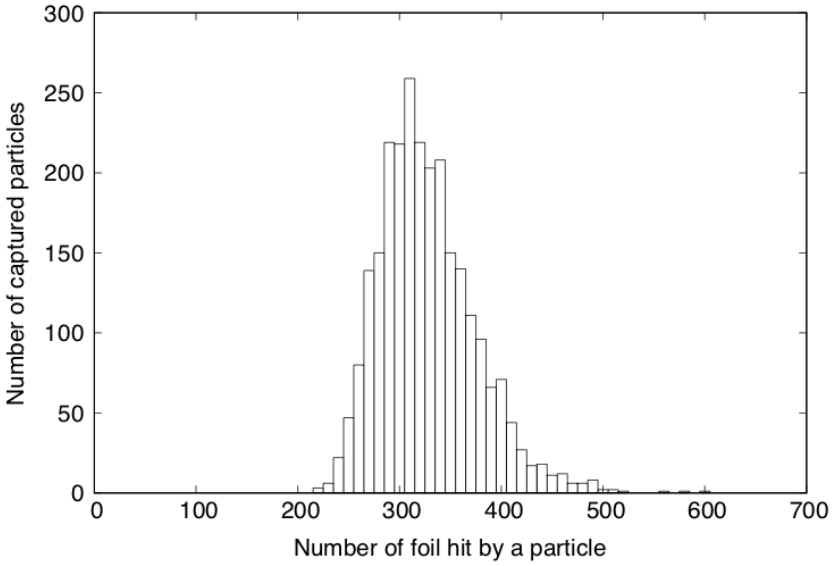

Figure 17: Histogram of number of foil traversals by a captured particle.

of 100 Hz; (2) upgrading the energy by adding a new ring outside the MAIN RING.

Beam Stacking at High Energy Orbit

As a potential candidate for a high intensity proton driver of a spallation neutron source, an FFA accelerator has advantages in terms of a high repetition rate such as 100-1000 Hz. However, some users desire a low spill rate (∼10 Hz) for their experiments *e.g.* neutron radiography using TOF which needs to get rid of contamination from a pulse of different timing. FFA rings can provide long interval pulses for users, while the machine operation itself is kept at a high repetition rate by using rf stacking after acceleration [13]. This scheme reduces space charge effects at the injection energy. For the machine, the charge in each bunch can be reduced by a high repetition rate. In the high energy region *i.e.* outer radius, accelerated beams are stacked and can continue

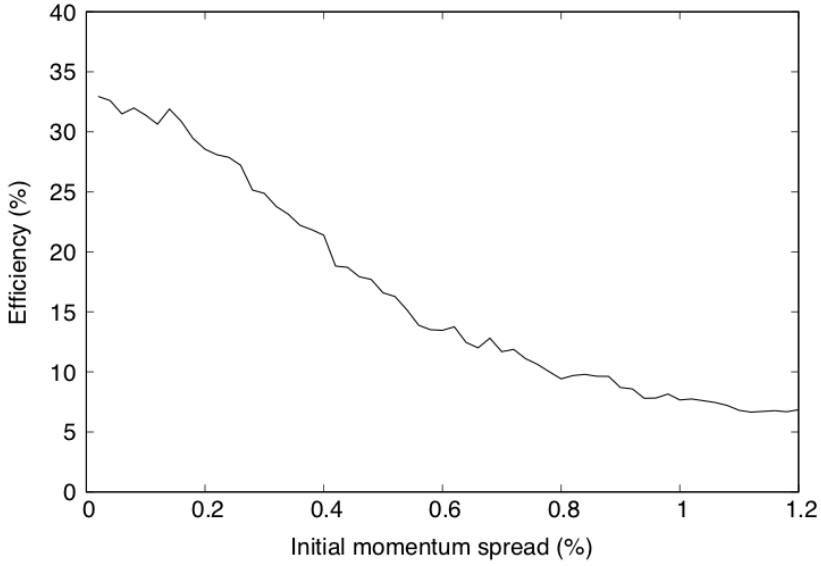

Figure 18: Capture efficiency dependence on initial momentum spread.

to circulate until the necessary amount of charge is accumulated. For users, highly compressed beams with a long time interval can be delivered.

To confirm the feasibility of rf stacking at extraction energy, simulation studies have been carried out. Figure 27 shows the results from the stacking simulations. In the upper plot, the longitudinal phase space structure is shown. The vertical axis is the momentum and the abscissa is the rf phase. The red points are stacked particle coasting around the extraction orbit, the green points represent accelerated particles landing on the extraction orbit and the blue lines are separatrices. In these simulations, the acceleration goes up to 150 MeV. While the landing process is happening, some stacked particles are already slipping below the bucket in the phase space. Eventually, beams have been stacked below the extraction momentum. In the lower plot, the momentum distribution is plotted. After first acceleration, the full width of momentum spread is about 0.5%, the final momentum spread after 10 stacks is 2.5% of the full width. This is much smaller than might be suggested by a naive guess based on the intrinsic momentum spread of each stacked beam multiplied by number of stacks *i.e.* $0.5\% \times 10$.

Although simulation studies showed that adiabatic landing, where the rf voltage is adiabatically reduced, is effective to suppress the momentum spread of the stacked beam, an experimental study is necessary.

An Additional Ring

The number of neutrons produced through the nuclear spallation process depends strongly on the beam energy of the primary protons. If the beam energy is increased from 100 MeV to 400 MeV, the number of neutrons corresponding to single primary proton is increased by a factor of 20. Therefore, an energy upgrade of the accelerator facility is an attarctive proposition to the reactor physicists.

Fortunately, there is an enough space to build an additional higher energy ring outside the MAIN RING. A basic design of the additional ring is now being carried out. The layout of the complex with a newly designed 400 MeV FFA ring is shown in Fig. 28. The basic parameters of the new ring are shown in Table 3. The ring consists of 16 cellsand the betatron functions for one cell are shown in Fig. 29.

The value of $k$is set to 0.672, which is rather small. This value makes *serpentine accelera-*

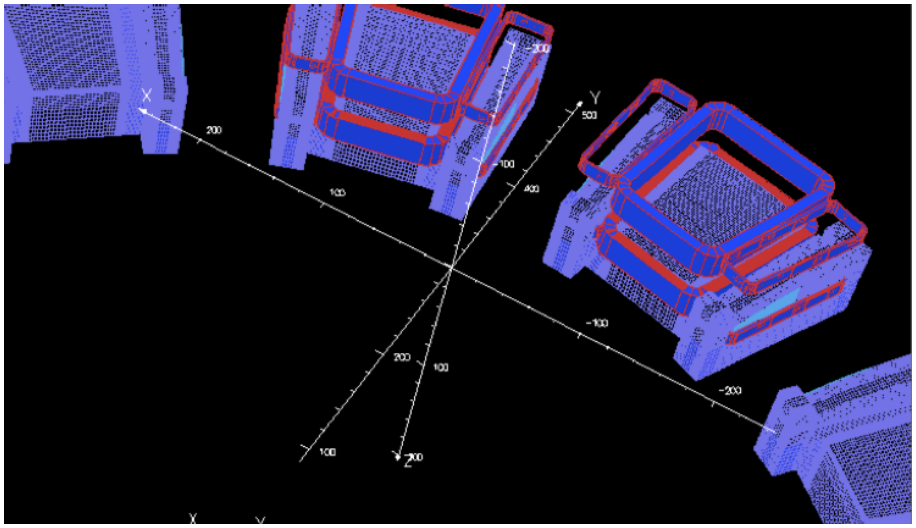

Figure 19: The input model of the main magnet in MAIN RING for the magnetic field calculation by TOSCA. Return yokes are not installed to make energy variable beam extractions easy. No field clamps are adopted.

Table 3: Parameters of the 400 MeV FFA Ring

Lattice	16-cell
Field index k	0.672
Energy	150 - 400 MeV
Average orbit radii	6.6 - 9.3 m
Magnetic field	1.3 T
Tune	(1.356, 2.248)

tion [14] possible. The longitudinal phase space structure in this acceleration scheme is shown in Fig. 30. Generally, the benefits of this scheme are follows:

- Since a fixed frequency is used, it is easy to get a high electric field in the acceleration cavity.
- Fast and continuous acceleration becomes possible.
- The ERIT mechanism [3] can be applied to generate secondary particles such as pions and their decay muons.

In the ordinary ERIT system as shown in Fig. 31, the ring is operated in a storage mode. However, in the extended ERIT system, the ring will operate in an acceleration mode. In this operation mode, since the beam hits the target at the maximum energy, the production efficiency of the secondary particles becomes high compared with the case of the storage mode.

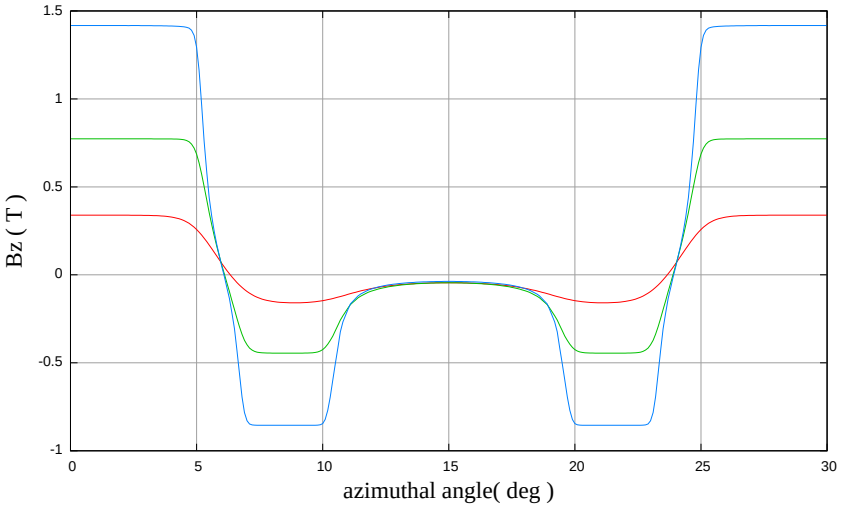

Figure 20: B_z vs θ along different radii for the unit cell in MAIN RING. Red, green and blue lines correspond to radii of 4.4 m, 4.9 m and 5.3 m, respectively.

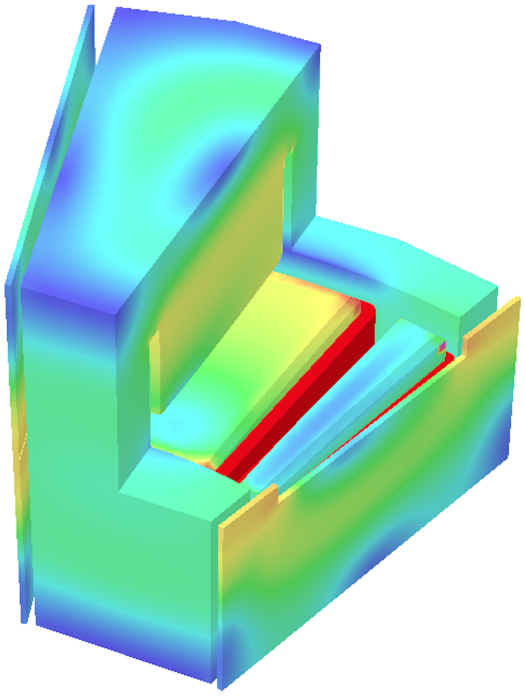

Figure 21: The input model of the main magnet in BOOSTER for the magnetic field calculation by TOSCA. Return yokes and field clamps are adopted.

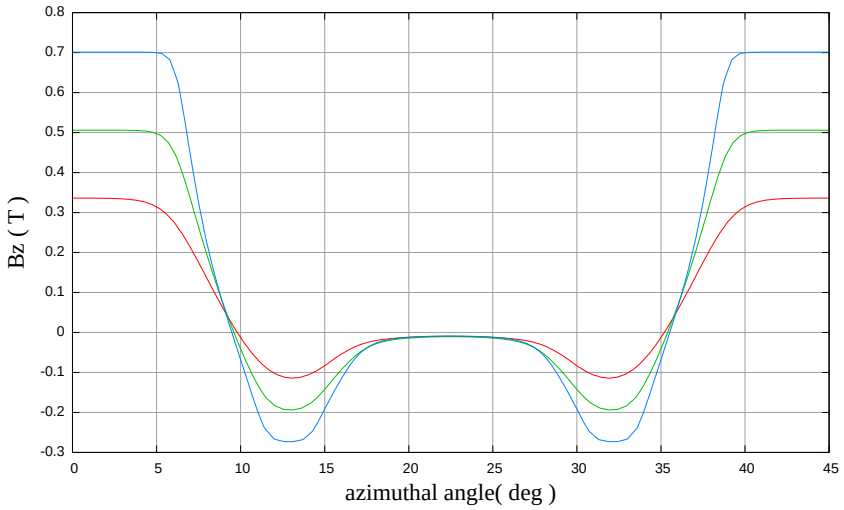

Figure 22: B_z vs θ along different radii for the unit cell in BOOSTER. Red, green and blue lines correspond to radius of 1.2 m, 1.4 m and 1.6 m, respectively.

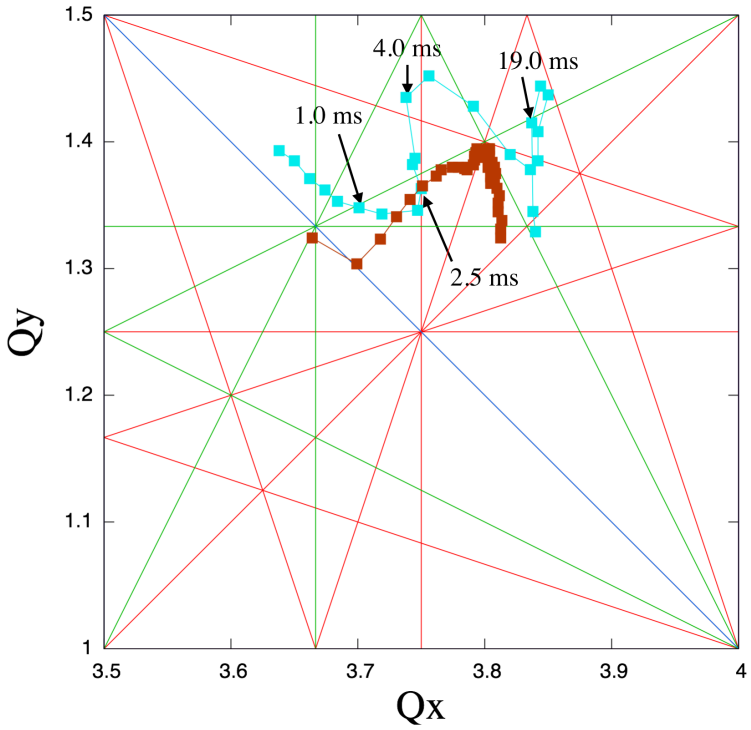

Figure 23: MAIN RING betatron tune footprints. Blue and brown squares indicate measurements and simulations, respectively.

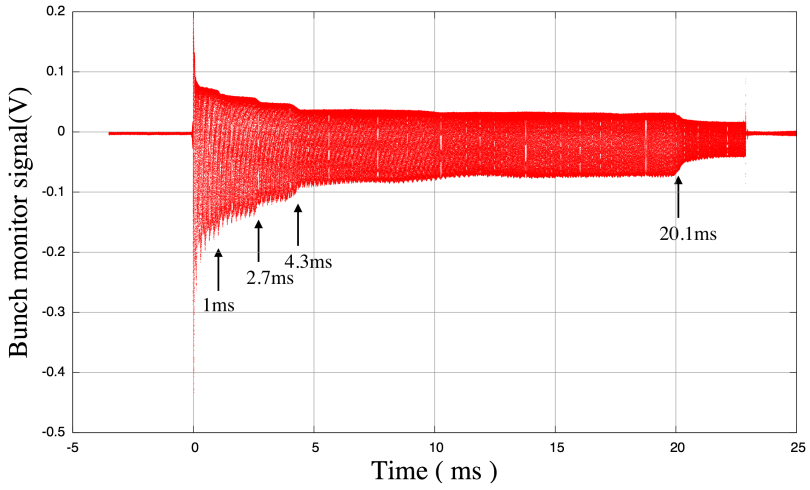

Figure 24: The output signal from the bunch monitor. There are some notable beam losses during acceleration.

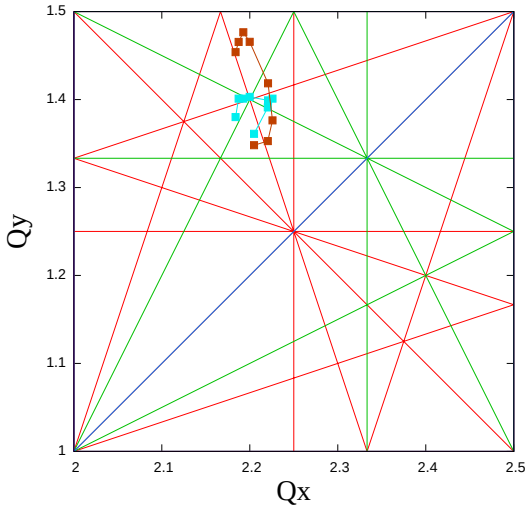

Figure 25: BOOSTER betatron tune footprints. Blue and brown squares indicate measurements and simulations, respectively.

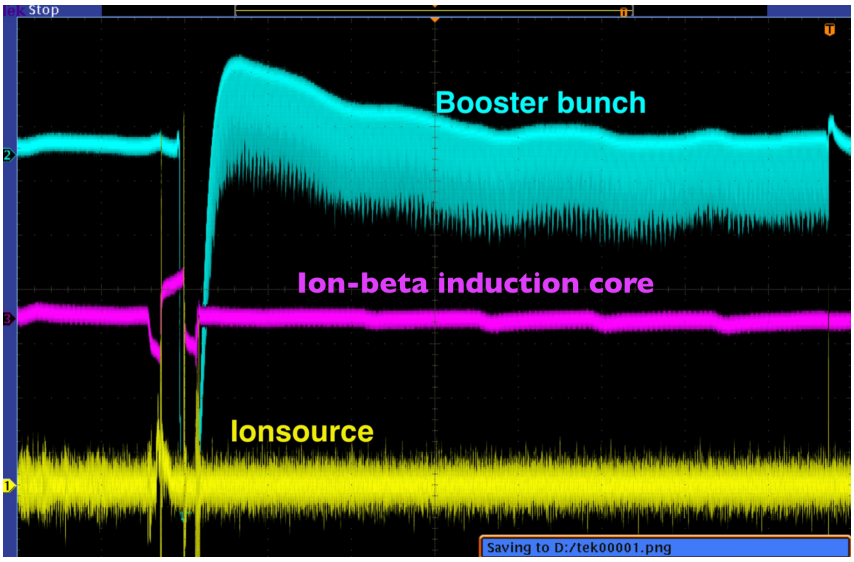

Figure 26: Output signal from the bunch monitor indicated by a blue line. There is no obvious beam loss during acceleration.

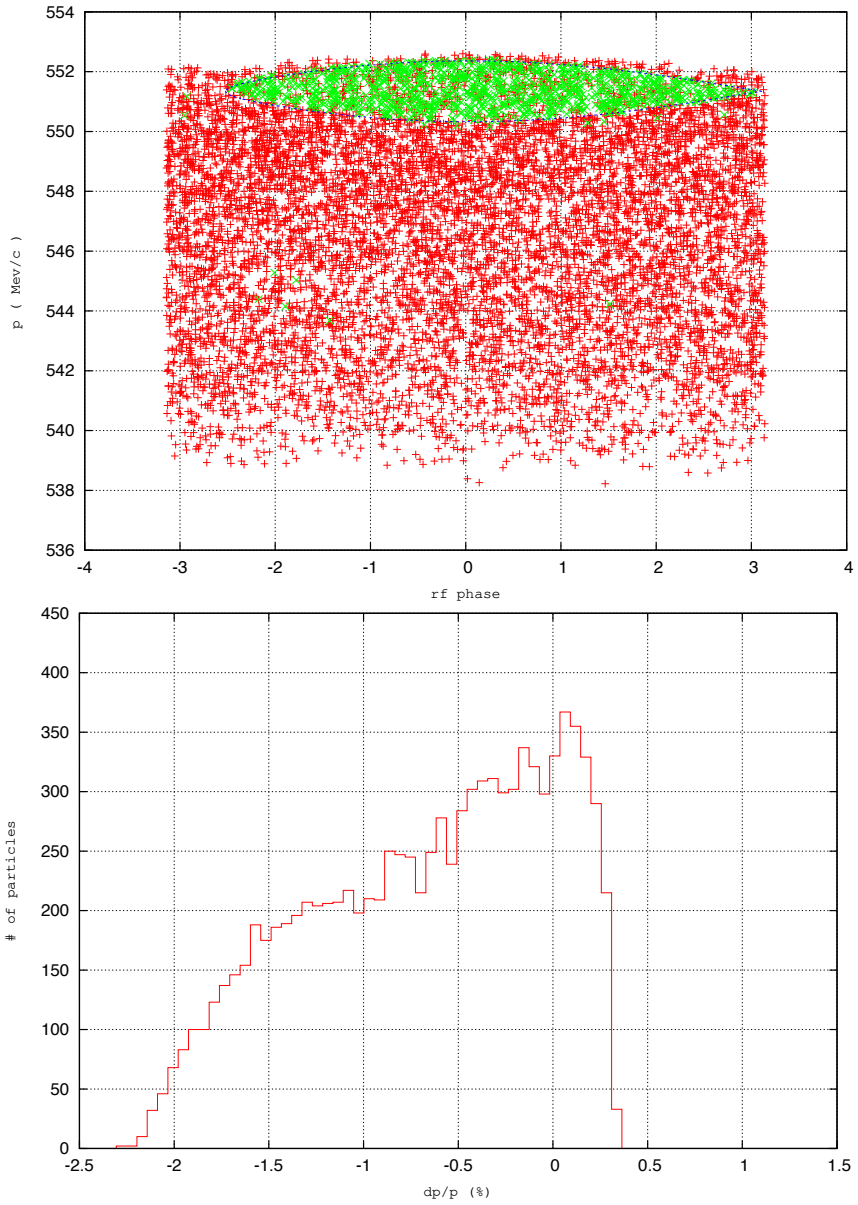

Figure 27: Results of the beam stacking simulation. The upper plot shows the phase space from the stacking simulations with adiabatic landing and the lower is the momentum distribution after the beam stacking.

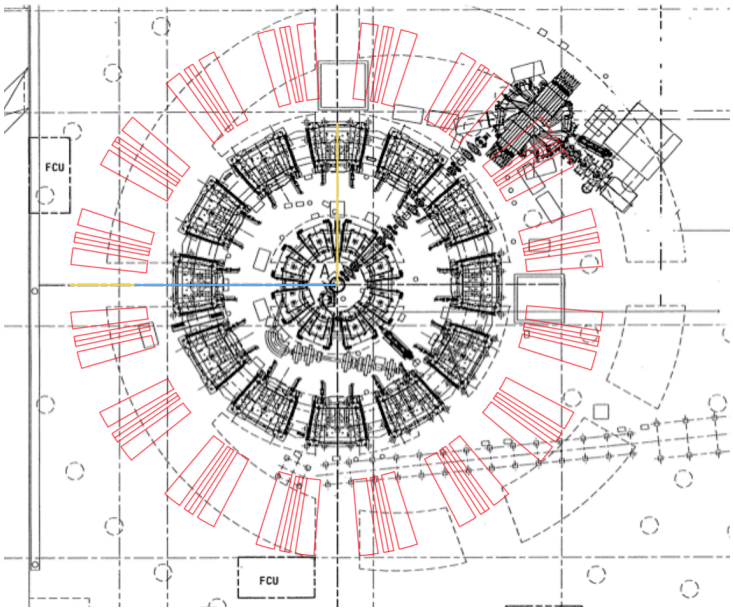

Figure 28: Layout of the complex with a newly designed 400 MeV FFA ring, which surrounds the MAIN RING.

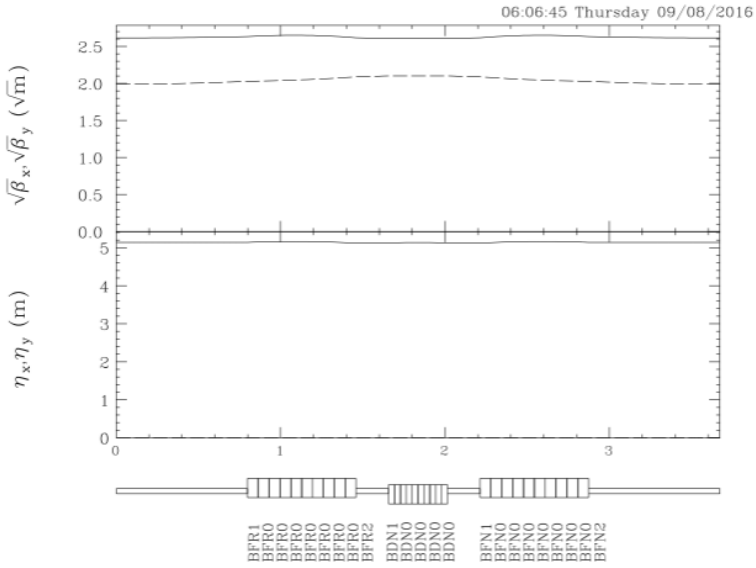

Figure 29: Betatron functions for a basic cell of the 400 MeV FFA ring.

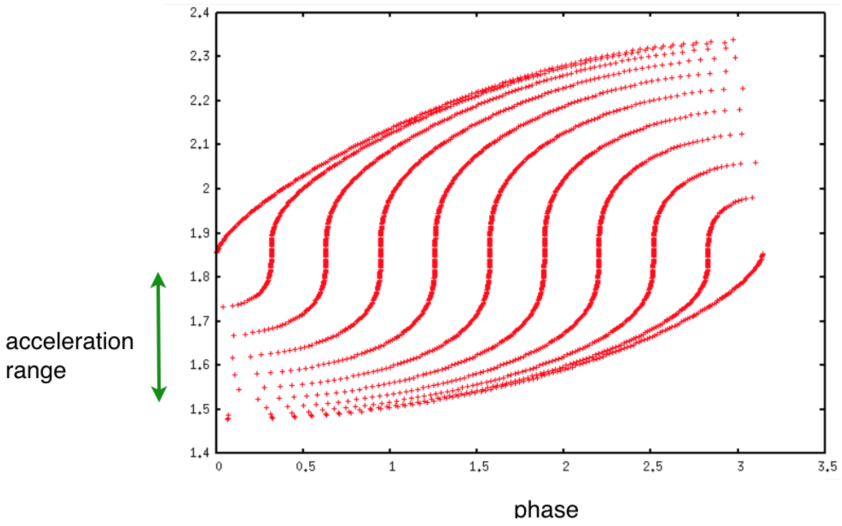

Figure 30: Phase space structure in the longitudinal direction for the serpentine acceleration.

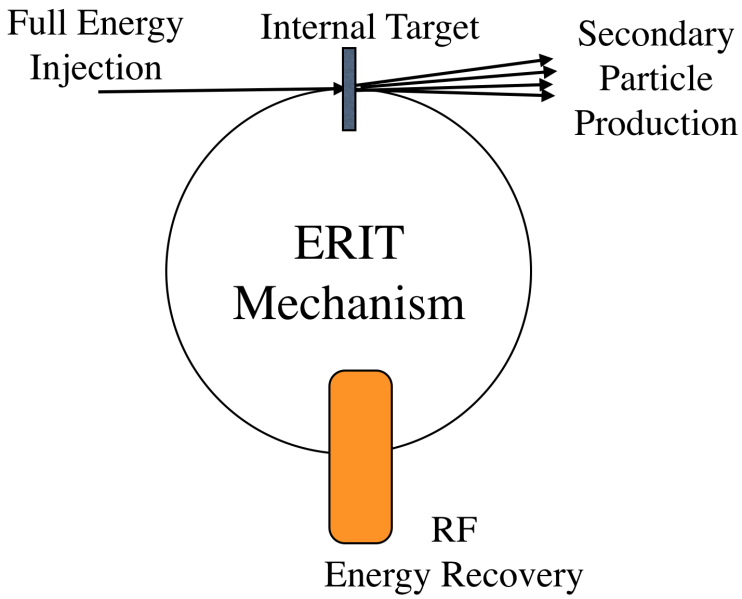

Figure 31: ERIT mechanism to produce secondary particles.

References

[1] C.H. Pyeon *et al.*, "First Injection of Spallation Neutrons Generated by High-Energy Protons into the Kyoto University Critical Assembly" *J. Nucl. Sci. Technol.*, vol. 46, no. 12, p. 1091(2009).

[2] Y. Ishi *et al.*, "Present Status and Future of FFAGs at KURRI and the First ADSR Experiment", in *Proc. 1st International Particle Accelerator Conference (IPAC'10)*, Kyoto, Japan, May 23-28 2010, paper TUOCRA03, p. 1327–1329.

[3] Y. Mori, *Nucl. Instr. Meth.*, A, vol. 536, p. 591(2006).

[4] C.H. Pyeon *et al.*, *Ann. Nucl. Energy.*, vol. 38, p. 2298 (2011).

[5] C.H. Pyeon *et al.*, *Nucl. Sci. Eng.*, vol. 117, p. 156 (2014).

[6] C.H. Pyeon *et al.*, *Nucl. Eng. Technol.*, vol. 45, p. 81 (2013).

[7] A. Sakon *et al.*, *Nucl. Eng. Technol.*, vol. 50, p. 481 (2013).

[8] A.Sakon *et al.*, *Nucl. Eng. Technol.*, vol. 51, p. 116 (2014).

[9] C. Pyeon, Rapid News,
`https://www.rri.kyoto-u.ac.jp/wp-content/uploads/Rapid_News_ADS-Transmutation_rev1_20190225.pdf`

[10] S.L. Sheehy *et al.*, "Characterization techniques for fixed-field alternating gradient accelerators and beam studies using the KURRI 150 MeV proton FFAG", Progress of theoretical and experimental physics, Oxford University Press, 7/2016, p. 73.

[11] Y. Ishi *et al.*, "Practical Betatron Tune Behavior During Acceleration in Scaling FFAG RINGS at KURNS", in *Proc. 9th International Particle Accelerator Conference (IPAC'18)*, Vancouver, Canada April 29 - May 4 2018, paper THPAK034, p. 3287–3289.

[12] S.L. Sheehy *et al.*, "Progress on Simulation of Fixed Field Alternating Gradient Accelerators", in *Proc. 6th International Particle Accelerator Conference (IPAC'15)*, Richmond, VA, USA, May 3-5 2015, paper MOPJE077, p. 495–498.

[13] Y. Ishi *et al.*, "Beam Stacking for High Intensity Pulsed Proton Beam with FFAG", in *Proc. 52nd ICFA Advanced Beam Dynamics Workshop on High-Intensity and High-Brightness Hadron Beams (HB2012)*, Beijing, China, Sep. 17 2012, paper MOP210, p. 64–67.

[14] E. Yamakawa *et al.*, "Serpentine Acceleration in Zero-Chromatic FFAG Accelerators" *Nucl. Instr. Meth.*, PRA, vol. 716,p. 46–53 (2013).

3.5 Status of the FFA at Kyushu University

Yujiro Yonemura, Hidehiko Arima, Nobuo Ikeda,
Faculty of Engineering of Kyushu University, Fukuoka, Japan.
Yoshiharu Mori, Kyoto University, Kyoto, Japan.

Introduction

A Center for Accelerator and Beam Applied Science has been established to promote activities in all the related scientific, medical, engineering and educational fields at Kyushu University [1]. To realize the purpose of the center, Kyushu University has decided to construct a new facility merging three institutes - the Cockcroft-Walton Accelerator Laboratory of Faculty of Engineering, the Institute for Irradiation and Analysis of Quantum Radiations and Kyushu University Tandem Accelerator Laboratory of Faculty of Sciences - on its new campus (Ito Campus) [1].

Figure 1 shows an overview of the new accelerator facility at Kyushu University. The facility consists mainly of a 10 MeV proton cyclotron, an 8 MV tandem accelerator and a 150 MeV FFA (150 MeV Fixed Field Alternating Gradient Accelerator) as a replacement for the Cockcroft-Walton accelerator.

The construction plan of the facility was divided into three stages. A building of the first stage was built in 2008, and the 150 MeV FFA was constructed between 2009 and 2011. In the second stage, the building was constructed as an extension to the first stage one, and construction of the tandem accelerator has been completed in 2014. A beam extraction line of the 150 MeV FFA and a beam injection line from the tandem accelerator to the 150 MeV FFA were constructed between 2015 and 2018. In third stage, we are planning to construct a new beam lines for experiments using beams from the 150 MeV FFA in the high energy experimental room.

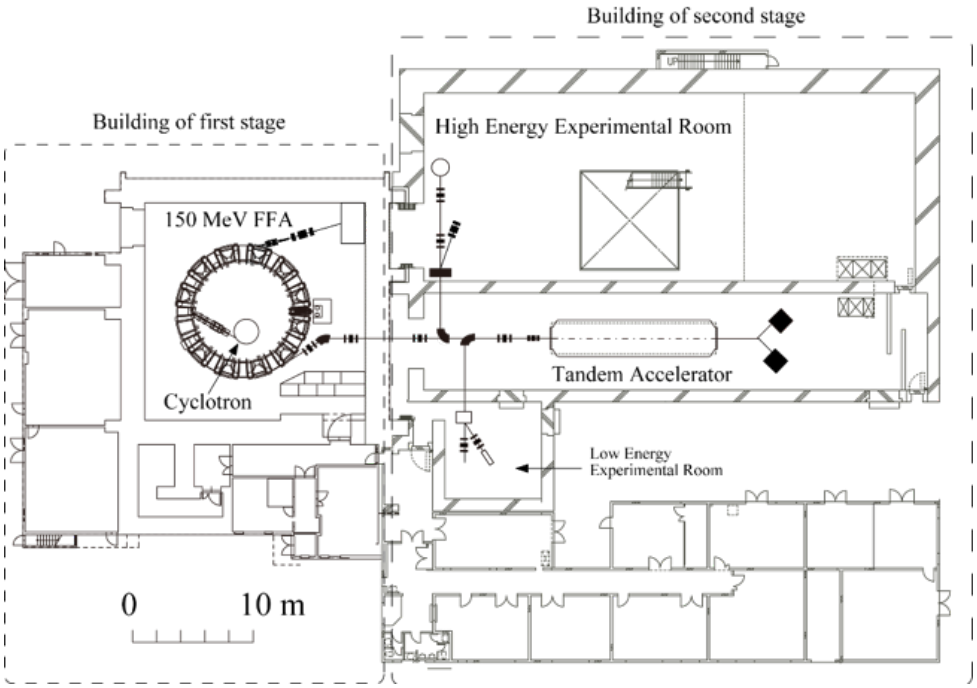

Figure 1: Overview of the accelerator facility at Kyushu University.

3.5.1 150 MeV FFA

The 150 MeV FFA was developed at High Energy Accelerator Research Organization (KEK) as a prototype of a proton FFA for various applications such as proton beam therapy. The construction of the 150 MeV FFA started in September 2002 at the east counter hall in KEK, and the beam extraction with 100 Hz operation was successfully demonstrated in November 2005 [2]. The FFA was disassembled in June 2006, transported by land from KEK to Ito Campus at Kyushu University in March 2008.

The re-construction of the FFA at the Center for Accelerator and Applied Beam Science at Kyushu University started in 2008. Beam commissioning started in December 2011, and beam acceleration was successfully demonstrated in 2013 [3]. The extraction kicker and the extraction magnetic septum were commissioned in 2017. The beam extraction line was constructed between 2016 and 2018. Figure 2 shows a schematic overview of the 150 MeV FFA. The main parameters of the 150 MeV FFA are summarized in Table 1.

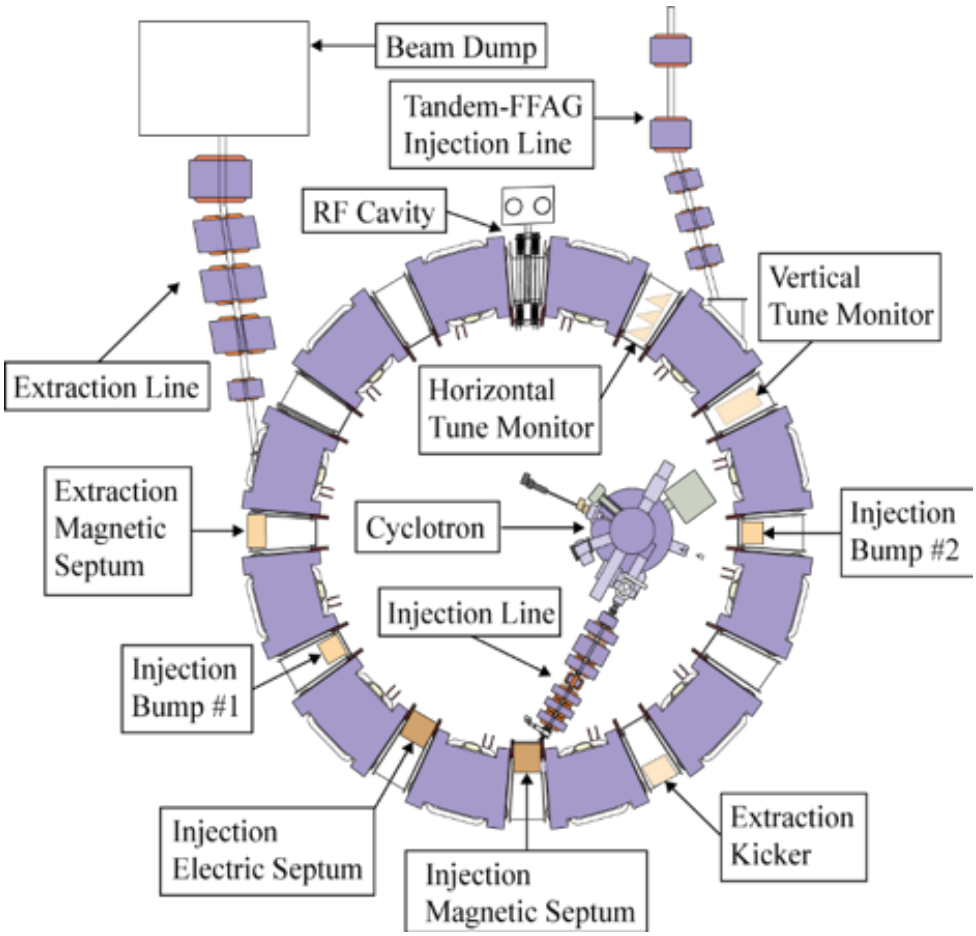

Figure 2: Overview of the 150 MeV FFAs.

Injectors

As an injector of the 150 MeV FFA, a cyclotron which accelerates protons to 10 MeV is employed. The cyclotron was originally developed by Japan Steel Works for positron emission tomography and material irradiation. The main parameters of the cyclotron are summarized in Table 2.

The tandem accelerator will be employed as a heavy ion injector to the 150 MeV FFA. The tandem accelerator has been employed independently for AMS, student experiments, RI

Table 1: Design parameters of the 150 MeV FFA

Energy	10 – 125 MeV (proton)
Type of magnet	Triplet radial (DFD)
Number of Cells	12
Average radius	4.47 – 5.20 m
Betatron tune (injection energy)	3.62 (Horizontal)
	1.42 (Vertical)
Magnetic field	Focus: 1.63 T
	Defocus: 0.78 T
Revolution frequency	1.5 – 4.2 MHz
Repetitionrate	100 Hz/ 2 Cavity
Beam current	1.5 nA (In the 1st stage)

Table 2: Cyclotron parameters

Energy	10 MeV (proton)
Type	AVF Cyclotron
Ion Source	Internal PIG (LaB6 cathode)
RF Dee voltage	40 kV
Extraction Radius	300 mm
Magnetic Field	Max. 1.54 T
RF Frequency	47 MHz (2nd hamonic acceleration)
Mean Beam Current	2 μA (In the 1st stage)

beam production and low-energy nuclear-physics experiments. The parameters of the tandem accelerator are summarized in Table 3.

Injection and Extraction Systems

The injection system consists of an injection magnetic septum, an injection electric septum and a pair of injection bump magnets. An injected beam is deflected by the injection magnetic septum, and its position and angle are adjusted by the injection electric septum. The bump magnets make o bump orbit in the septa. The extraction system consists of an extraction kicker magnet and an extraction septum magnet.

One of the technical difficulties in the operation of the 150 MeV FFA was the closed orbit distortion caused by a large fringing field of the magnets of the main ring [4]. The injection bump magnets and the extraction kicker magnet installed in the straight section couple to the fringing field, which distorts the closed orbit. In order to overcome the problem, a new type of bump magnet and kicker magnet have been developed.

The bump magnet consists of an air core coil to avoid coupling with the fringing field. The coil consists of 49 wires with a diameter of 0.6 mm to reduce the skin effect and heat generation. The measured inductance of the magnet is 5.6 μH. The switching power source supplies a half-sinusoidal pulse current to the bump magnet. The output peak current and pulse width are 2000 A and 10 μs, respectively [5].

The kicker magnet is composed of three air core coils. These coils are electronically connected in parallel in order to reduce the total inductance of the kicker magnet. The measured inductance of the magnet is 1.1 μH. The switching power supply consists of E2V CX1175 thyratron and PFN network. The voltage and current of the power supply are designed to be 40 kV and 5100 A, respectively, maximum. The rise time of the current is expected to be about 190 ns (0-96%) [6].

Table 3: Tandem accelerator parameters

Accelerator Type	Horizontal Tandem Van de Graaff
Model	NEC Pelletron (8UDH)
Terminal Voltage	8 MV
Accelerator Tank	Diameter: 3.0 m
	Length: 13.6 m
Insulation Gas	SF6 (pressure: 0.6 MPa)
Ion Source	Sputter Ion Source: NEC MC-SNICS
	RF Ion Source: NEC Alphatross
Injection Voltage	-70 kV
Beam	p, d, H.I.
Current	1 nA (in the first stage)
Terminal Stripper	C Foil and N2 gas
Charging Device	Double pellet Chains
	(Current: 150 μA $\times$ 2)

Acceleration System

The rapid cycling acceleration of the 150 MeV FFA was successfully achieved with the MA (Magnetic Alloy) cavity developed at KEK. However, the cooling system for the MA cores had a technical difficulty in terms of the thermomechanical reliability. Since the efficiency of the heat cooling was low, the temperature on the inner surface of the core reached over 150∘C [7].

To resolve this problem, a new type of the RF cavity with a high-efficiency cooling system has been developed [1]. The cavity consists of two MA cores, and the water cooled plates are attached to one side of the cores. Most part of the inside area of the cooling plate is covered by the coolant passage so as to significantly increase the contact area between the plate and cooling water. The measured maximum shunt impedance was 200 Ω. The measured resonance frequency and the quality factor of the cavity were 2.7 MHz and 0.43, respectively. The measured acceleration voltage is 4.0 kV, which was the voltage required to achieve the rapid acceleration of 100 Hz with two RF cavities [8].

Beam Monitor

Figure 3 shows the schematic layout of the beam diagnostic devices installed in the 150 MeV FFA. Beam probes are installed for the observation of the beam profile in a radial direction by the current detection with a picoammeter and controlled by PLC with LabVIEW [9]. Non-destructive beam monitoring based on an electrostatic pick-up is desirable to prevent radioactive contamination and it allows continuous measurement during acceleration. Therefore, a horizontal beam monitor with trapezoidal-shaped electrodes is used for detection of the horizontal beam position and tune measurement and a vertical one with a square plate for the vertical beam position and tune measurement. The radius of the beam orbit shifts from 4.47 m to 5.20 m during RF acceleration at a revolution frequency of 1.5 to 4.2 MHz. Therefore, beam monitors that cover a wide range of the horizontal area are required for the beam diagnostics. A new beam position monitor with five-segmented triangular electrodes has been developed [10]. The calibration test of the prototype monitor was performed before installation and the results have shown an excellent position linearity except for the edge regions.

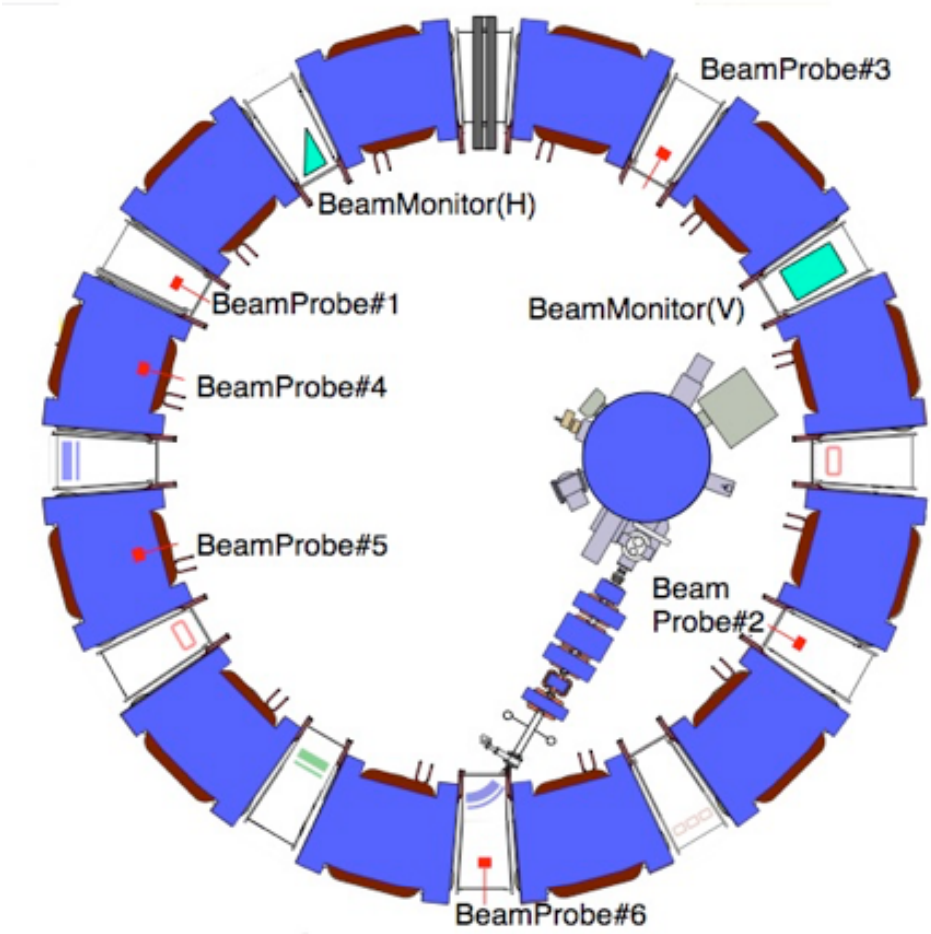

Figure 3: Schematic layout of beam diagnostics of the 150 MeV FFA.

Tune Correction

In the scaling FFA, the betatron tune is theoretically constant, but in actual ring it is not. Adjusting the focusing force is useful for avoiding resonances due to undesirable tune variation and allowing the FFA to have the required versatility. In the 150 MeV FFA, additional iron plates for adjustment of the vertical focusing force are attached on both outer sides of the defocusing magnets of the DFD triples and give the desired correction of the vertical tune compared with the case of no additional plates [11]. Furthermore, the procedure for adjustment of the horizontal focusing force by installing multi-stepped coils and/or changing the geometry of the pole surfaces has also been examined [12].

Summary

The construction of the new accelerator facility has been completed at the Center for Accelerator and Beam Applied Science at Kyushu University. Beam commissioning of the 150 MeV FFA has successfully been demonstrated. In parallel to the construction and the beam commissioning of the 150 MeV FFA, a new type of extraction kicker magnet, the injection bump magnet, beam monitors, the tune correction system and the RF cavity have been developed. The experiments with extracted beam are now in preparation.

References

[1] Y. Yonemura et al., "Status of Center for Accelerator and Beam Applied Science of Kyushu University", Proceedings of the 11$^{\text{th}}$ European Particle Accelerator Conference, Genoa, Italy (2008).

[2] M. Aiba et al., "Beam extraction of 150 MeV FFAG", Proceedings of the 10th European Particle Accelerator Conference, Edinburgh, Scotland (2006).

[3] Y. Yonemura, "Current status of beam commissioning of FFAG accelerator at Kyushu University", Int. FFA Workshop 2013 (2013).

[4] Y. Yonemura et al., "Commissioning of 150 MeV FFAG synchrotorn", Proceedings of 9$^{\text{th}}$ European Particle Accelerator Conference, Lucerne, Switzerland (2004).

[5] T. Matsunaga et al., "Development of the extraction kicker for FFAG accelerator at Kyushu University", Proceedings of the 7$^{\text{th}}$ Annual Meeting of Particle Accelerator Society of Japan, pp.593-595 (2010).

[6] S. Kuratomi et al., "Multi-turn injection the FFAG accelerator at Kyushu University", Proceedings of the 9$^{\text{th}}$ Annual Meeting of Particle Accelerator Society of Japan, pp.403-406 (2012).

[7] Y. Yonemura et al., "Development of RF acceleration system for 150 MeV FFAG accelerator", Nuclear Instruments and Methods in Physics Research, Section A, 576(2-3), 294-300 (2007).

[8] Y. Yonemura, "Beam commissioning of 150 MeV FFAG accelerator at Kyushu University", Int. FFA Workshop 2012 (2012).

[9] Y. Yonemura et al., "Present status of beam commissioning of FFAG accelerator at Kyushu University", Proceedings of the 10$^{\text{th}}$ Annual Meeting of Particle Accelerator Society of Japan, pp.852-854 (2013).

[10] S. Mochizuki et al., "Development of non-destructive large-aperture beam monitor", Progress in Nuclear Science and Technology Vol.1, pp.328-331 (2003).

[11] N. Motohashi, Int. FFAG Workshop 2015 (2015); Y. Waga, Int. FFA Workshop 2018 (2018).

[12] M. Ueda, "Correction of focusing force with pole surface coils for the radial sector type FFAG accelerator", Int. FFA Workshop 2017 (2017).

3.6 FFA-based ISIS Upgrade Options

Shinji Machida[1], STFC Rutherford Appleton Laboratory, United Kingdom.

Introduction

Among the various accelerator upgrade options being studied by the ISIS neutron and muon source group at RAL, the design of a Fixed Field alternating gradient (FFA) accelerator [1–3] is being developed. An FFA has several advantages for the proton driver of a spallation neutron source mainly because of the constant field of the main lattice magnets. First, it can deliver high average beam current. This is possible because the acceleration pattern is solely determined by the RF voltage and frequency, not by the kind of magnetic field ramping found in synchrotrons. Secondly, its energy efficiency can be high. DC magnets can easily be designed with superconducting technology or permanent magnets might even be used. Thirdly, an FFA allows a flexible time structure for neutron users. Depending on the type of experiment, the range of the neutron energy spectrum and therefore the time period for measurements are different. Some users prefer 10 Hz operation and others require 50 Hz. The possibility of a high repetition rate from an FFA accelerator could be used to advantage by delivering pulsed beams to multiple target stations at different rates so that neutrons could be generated with a variety of time structures.

The idea of using an FFA as a proton driver for spallation neutrons is not new [4–8]. In the 1980s, there was a proposal by Argonne National Laboratory (ANL) called ASPUN. A similar machine was considered as an afterburner of KENS at KEK. In the 1990s, as an option for a short pulse version of the European Spallation Source, an FFA was designed by Jülich. Unfortunately none of these proposals went further than paper studies.

A major revival of the FFA accelerator concept took place in 1999 when the first proton FFA was constructed in Japan and 1 ms acceleration was demonstrated [9]. This had a big impact on the high current proton accelerator community. Many advantages were foreseen for FFAs over conventional accelerator architectures for a range of projects, including future spallation neutron sources, and these were studied in detail in the projects that followed [10–12]. Traditionally, ever since the first generation of spallation facilities like IPNS at ANL, KENS at KEK, ISIS at RAL and LANSCE at Los Alamos, driving accelerators for neutron production have been based either on rapid cycling synchrotrons (RCS) or full energy linacs plus an accumulator ring (AR) to compress the long linac beam pulse to a microsecond. No one can deny that a great deal of R&D is needed if FFAs are to be used for these purposes, but there is certainly the potential for FFAs to make a breakthrough in this area of application, and in particular for an ISIS upgrade.

3.6.1 Accelerator choice

Discussions with the neutron user community indicate a requirement for a pulsed neutron source in the future to have a similar time structure to ISIS (10 and 50 Hz) but with higher beam power. Table 1 shows the minimum requirements requested.

Table 1: Neutron users' requirements.

Beam power	1.25	MW
Repetition rate	10 to 40	Hz
Number of target stations	preferably 3	

[1]On behalf of the FFA ISIS accelerator physics design team

The main parameters of the proton driver meeting these requirements are those shown in Table 2

Table 2: Main accelerator parameters.

Kinetic energy	1.2	GeV
Average beam current	1.04	mA
Repetition rate	90	Hz

Our first attempt is to design a new proton driver to fit into the existing ISIS tunnel even though it constrains the radius to around 24 m. The tunnel was initially constructed for the weak focusing synchrotron NIMROD, and there is plenty of width. As an injector, a 0.4-0.5 GeV superconducting linac is assumed. With 0.4 GeV injection energy, the momentum ratio, injection to extraction, will be a factor of 2. On the other hand, a beam energy of 0.5 GeV is known to be the optimum for muon production. A beamline from the injector to the muon target is likely therefore be considered if there is sufficient demand.

We have considered two options for the ring lattice: one is a horizontal orbit excursion FFA and the other is an FFA in which the orbit moves vertically (vFFA). The former is based on the so-called DF spiral design proposed by the author [13]. The latter is more challenging because this kind of FFA has never been built before although some proposals exist [14,15], most recently by Brooks [16]. Below we give details of both designs.

DF spiral

Using edge angles with respect to the beam orbits for focusing in one plane is a promising idea [17]. Designing a lattice with spiral FFA magnets with constant edge angle independent of the beam momentum eliminates reverse bending magnets and results in a smaller circumference. This means, however, that there is no means of adjusting focusing in the transverse plane. The field gradient of the main magnets could be adjusted if trim (correction) coils are attached, but this is not enough to explore the whole tune space. This could be a serious issue because it is hard to fix the transverse tune precisely at the design stage of an accelerator lattice, especially for high current proton accelerators where the tune depends on the beam current.

A DF spiral lattice incorporates normal as well as reverse bending magnets with a spiral edge angle. Compared with a conventional spiral sector FFA, the circumference tends to be larger due to the reverse bend magnets. However, the flexibility introduced by reverse bends cannot be overlooked. It is essential for the initial commissioning to find the best working point in tune space for day-to-day operation afterwards; this is a well known fact in synchrotron operation. More details on the design and dynamics are discussed in [13].

Table 3 shows the parameters identified for an upgrade lattice for ISIS.

The number of cells was chosen as 25 so that a systematic 5^{th} order resonance coincides with an integer. Space charge driven resonances at a quarter integer prohibit an operating tune just above a quarter integer. A cell number that is a multiple of 5 gives the largest resonance-free space between an integer and a quarter integer. As for cell tune, almost equal horizontal and vertical tunes are chosen because this is the choice of the high current accelerators built most recently, *e.g.* SNS and J-PARC. The spiral angle around 60 degrees approximates to the upper limit from an engineering point of view.

Figure 1 shows the top view of the DF spiral lattice. Figure 2 shows the beta function at the injection momentum and Fig. 3 shows the vertical magnetic field strength along the orbit at the injection and extraction momenta.

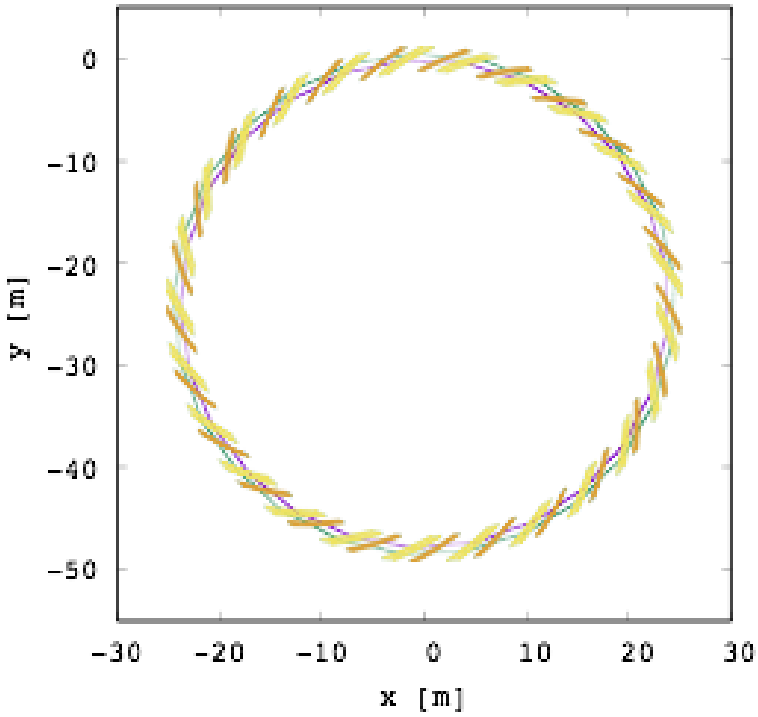

Figure 1: FFA-based ISIS upgrade lattice with 25 cells. Parameters are given in Table 3.

Table 3: Parameters of DF spiral 1.2 GeV FFA.

Kinetic energy	0.4 (0.5) - 1.2	GeV
Reference radius	24	m
Number of cell	25	
Magnet longitudinal length (Bd, Bf)	(0.60, 1.21)	m
Packing factor	0.35	
Straight section	3.58	m
Spiral angle	62	degrees
k index	20.6	
Ratio Bd/Bf strength	-0.47	
Orbit excursion	0.8	m
Cell tune (H, V)	(0.2076, 0.2096)	
Ring tune (H, V)	(5.19, 5.24)	
Transition gamma	4.6	

vFFA

With main magnets whose vertical field strength increases (or decreases) in a vertical direction with proper restoring forces in transverse directions, the equilibrium orbit for different beam momenta shifts vertically. One of the nice features of this arrangement is that the orbit radius is constant, like synchrotrons. Not only that, the horizontal dispersion function is zero and the momentum compaction factor becomes zero, meaning the transition energy is infinite. In that respect, it is like a linac where path length is independent of beam momentum. There is another advantage in the vFFA concept, and that is the separation of the scaling property from the geometrical arrangement of the lattice footprint. In principle, the ring could have any shape and it would still be possible to maintain a scaling property as long as the vertical magnetic field

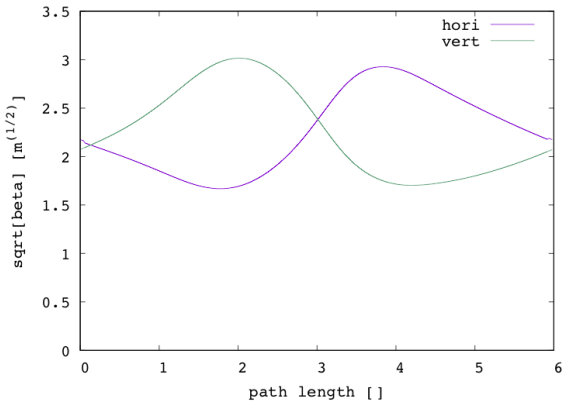

Figure 2: Beta functions at injection energy (0.4 GeV).

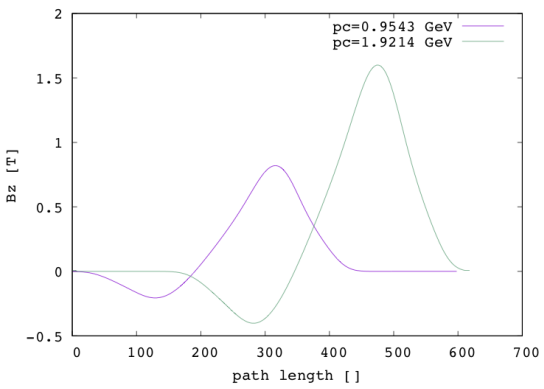

Figure 3: Vertical magnetic field along the orbit at injection and extraction momenta. The horizontal axis shifts depending on its momentum due to the spiral angle.

satisfies the design shape of scaling magnets, (*q.v.*). A simple rectangular shape for the main magnets and the coil geometry is another advantage. A negative curved coil, which is inevitable in the spiral magnet, can be avoided.

We have first examined a test ring lattice as a prototype of a larger vFFA ring designed for the ISIS upgrade. The test ring will take the 3 MeV beams from RAL's R&D injector, FETS, [18] and accelerate them to around 30 MeV. Our aim is to demonstrate the vFFA concept experimentally for the first time and establish a design procedure. The rest of the main parameters are given in Table 4.

Table 4: Parameters of test ring vFFA.

Kinetic energy	3 - 27	MeV
Reference radius	3.9789	m
Number of cells	10	
Magnet longitudinal length (Bd, Bf)	(0.5, 0.5)	m
Packing factor	0.40	
Straight section	0.75	m
m index	2.1	m^{-1}
Ratio Bd/Bf	-0.24	
Orbit excursion	0.6	m
Cell tune (H, V)	(0.17, 0.19)	
Ring tune (H, V)	(1.70, 1.90)	
Transition gamma	infinite	

Magnetic fields are expanded from the ideal mid-plane field (the mid-plane for a vFFA is a zero-displaced plane in the horizontal direction) so that the fields satisfy Maxwell's equations. The only assumption made here is that the shape of the fringe field and the length of fall-off are

of the form $g(x)$ as in the equations below:

$$B_z\left(z,x,y\right) = B_0 \sum_{i=0}^{\infty} B_{zi}\left(z,x\right) y^i\,,$$
$$B_x\left(z,x,y\right) = B_0 \sum_{i=0}^{\infty} B_{xi}\left(z,x\right) y^i\,,$$
$$B_y\left(z,x,y\right) = B_0 \sum_{i=0}^{\infty} B_{yi}\left(z,x\right) y^i\,,$$

where

$$B_{z0}(z,x) = \exp(mz)g(x),$$
$$B_{x0}(z,x) = \frac{1}{m}\exp(mz)\frac{\mathrm{d}g}{\mathrm{d}x}\,,$$
$$B_{y0}(z,x) = 0\,,$$

where x is longitudinal, y is horizontal and z is vertical. m is the field index, which is about equal to the field index k of a conventional FFA divided by the reference radius. B_0 is the reference field strength.

Figure 4 shows the magnetic fields obtained from the equations above. These correspond to a position slightly off mid-plane along the longitudinal direction to show the horizontal field.

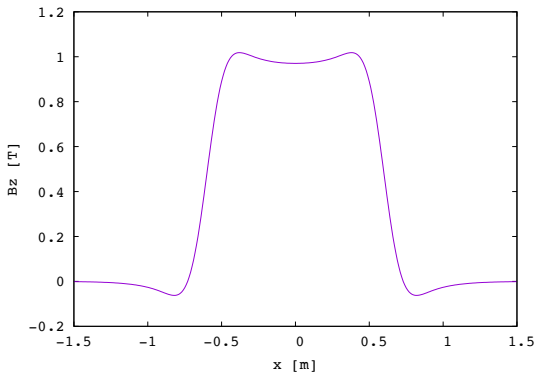

(a) Vertical field B_z

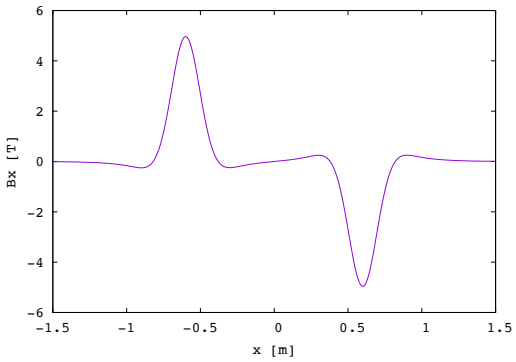

(b) Longitudinal field B_x

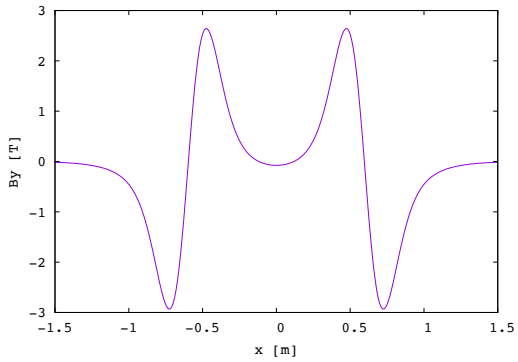

(c) Horizontal field B_y

Figure 4: Magnetic fields in the vFFA magnet. Values are given slightly off mid-plane ($y \neq 0$) to show the non-zero horizontal field.

Figures 5 and 6 show the closed orbits found for different momenta. As expected, the beam orbit is fixed in the horizontal plane, while it moves vertically with momentum. For a given momentum, the orbit shifts slightly along the magnets in the vertical direction because of the horizontal magnetic field which is non-zero off midplane. The vertical field along the orbit is shown in Fig. 7 which shows relatively higher fields compared with a conventional FFA.

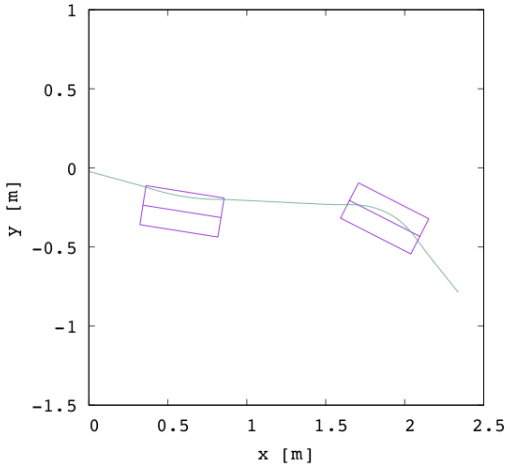

Figure 5: The orbit, seen from the top for a single cell, is independent of beam momentum. The rectangular blocks represent the Bd magnet (left), which bends the beams outward, and the Bf magnet (right), which bends the beams inward.

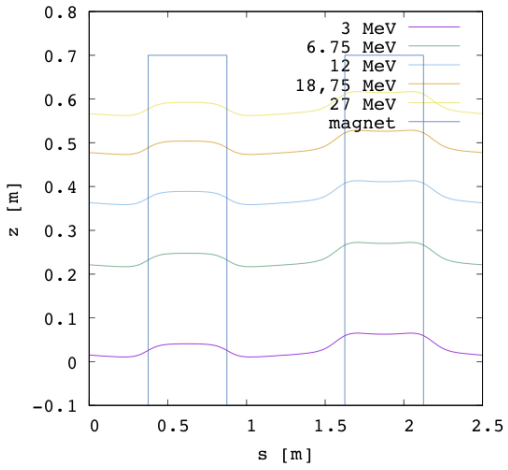

Figure 6: The orbit seen from the side for a single cell. As beams are accelerated, the orbit moves up. There is a slight shift in the vertical direction along the magnets due to the horizontal field.

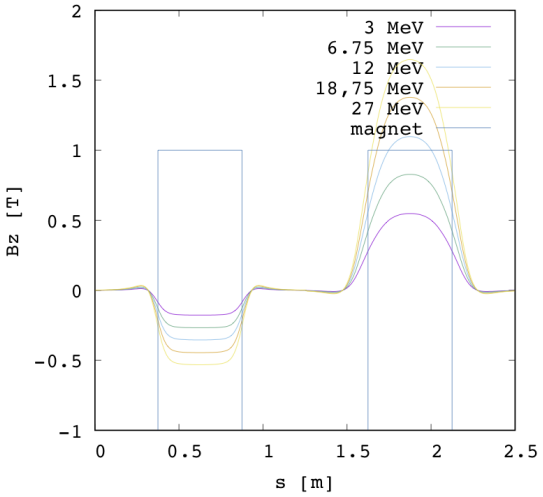

Figure 7: Vertical magnetic field along the orbit as a function of momentum.

For use as an accelerator at a user facility, easy operation with sufficient tuning knobs must be guaranteed. The transverse tune can be adjusted by the field index m and the magnetic field ratio, Bd/Bf. Additional control from the relative distance in the radial direction of Bd and Bf, together with m and Bd/Bf, give coverage of the whole range of cell tune-space from 0 to 0.5 in both decoupled tune spaces, as shown in Fig. 8.

Dynamic aperture is a particular concern in a vFFA because of intrinsic, relatively stronger nonlinearity in the lattice magnets. The optics are coupled in the two transverse planes, which creates another complexity in the dynamics. The dynamic aperture was investigated, first, by

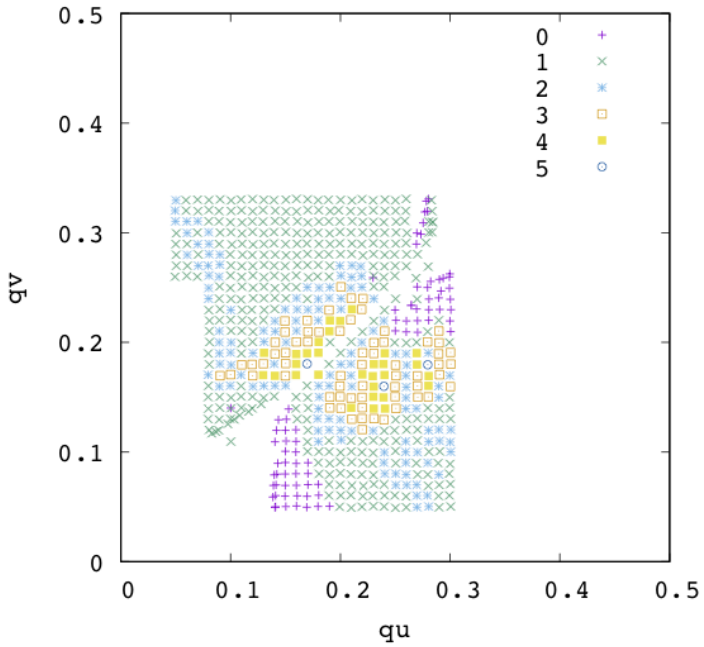

Figure 8: Tune-ability of the focusing in terms of cell tune. The field index m and magnetic field ratio Bd/Bf are the main parameters available for changing tune. Occasionally adjusting the displacement between Bd and Bf in the radial direction is necessary to explore the whole cell tune space from 0 to 0.5 in both directions. The colour scale indicates a rough idea of dynamic aperture, from 0 (the worst) to 5 (best).

looking at surviving particles from a random 4D distribution, as shown in Fig. 9, top row; and, secondly, by tracking particles positioned equally in one of the decoupled coordinates, as shown in Fig. 9, bottom row. Both results show a normalised dynamic aperture of around $30\,\pi$ mm.mrad for the test ring, which is more than enough considering the actual limitation from physical aperture.

Summary

Although any major upgrade to ISIS accelerators will not happen in the immediate future, the team has started looking at detailed options for accelerator designs. A FFA has several advantages over a conventional proton driver, such as an RCS or linac+AR. However, no large-scale facility using an FFA as part of the accelerator infrastructure exists and extensive physics design and hardware R&D in many areas are necessary before making a final choice. Accelerator designs based on DF spiral magnets and a vFFA have been explored. The vFFA in particular seems an interesting and promising option.

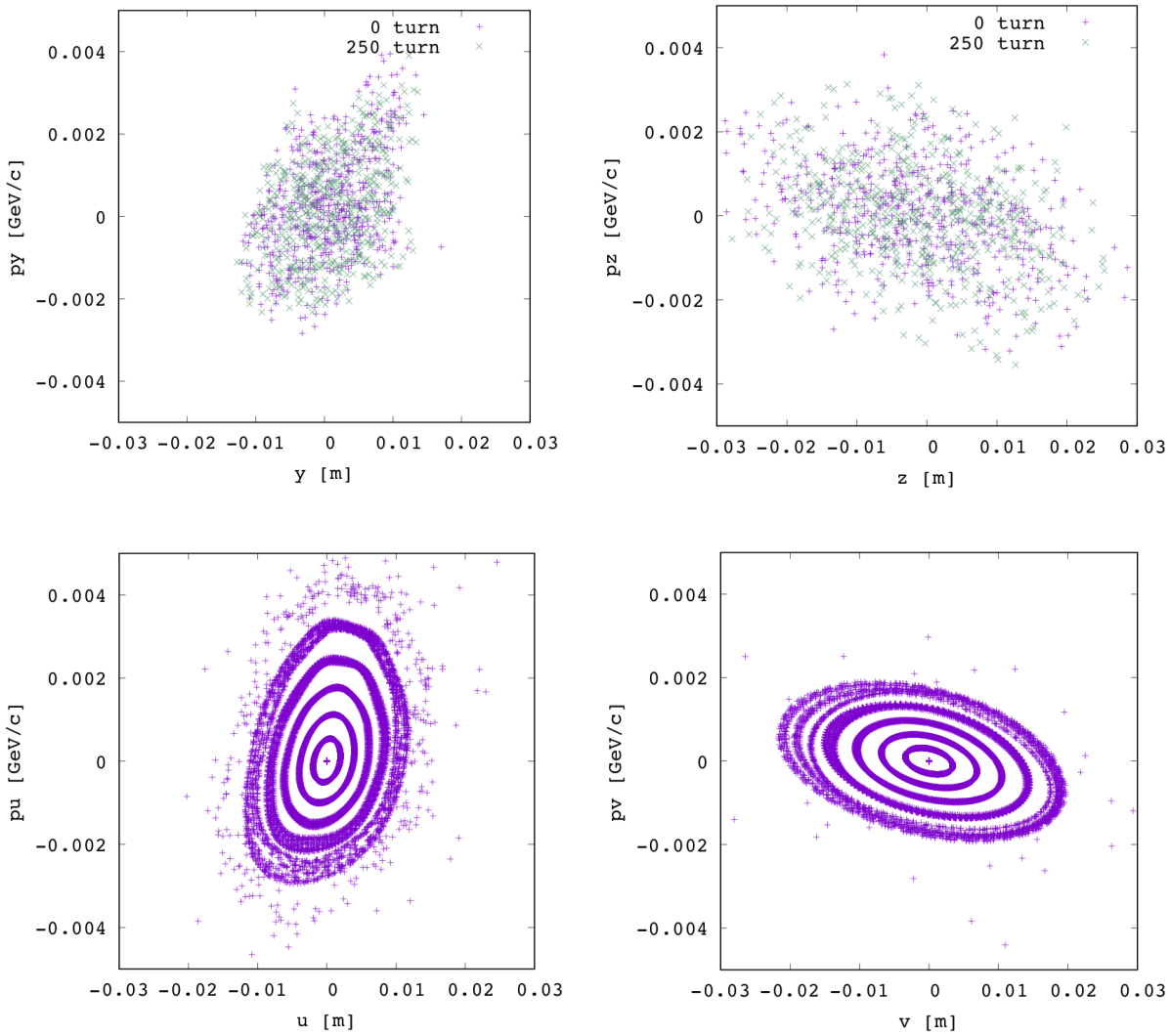

Figure 9: Dynamic aperture in the test ring. The survival of particles in 4D phase space is shown in the top row: horizontal in coupled coordinates on the top left, vertical in coupled coordinates on the top right. Decoupled, orthogonal space coordinates are used in the bottom row.

References

[1] T. Ohkawa, Proc. Annual meeting of JPS (1953).

[2] K.R. Symon, D.W. Kerst, L.W. Jones, L.J. Laslett, and K.M. Terwillinger, Phys. Rev. **103** (1956) 1837.

[3] A.A. Kolomensky and A.N. Lebedev, *Theory of Cyclic Accelerators* (North-Holland, Amsterdam, 1966), p. 332.

[4] Y. Ishikawa, *et. al.*, Proc. of the 8$^{\text{th}}$ meeting of the Int. Collaboration on Advanced Neutron Sources (1985) 17.

[5] R.L. Kustom, T.K. Khoe and E.A. Crosbie, IEEE Trans on Nuclear Science, Vol. **NS-32**, No. 5 (1985) 2672.

[6] P.F. Meads, Jr. and G. Wüstefeld, IEEE Trans on Nuclear Science, Vol. **NS-32**, No. 5 (1985) 2697.

[7] S.A. Martin, E. Zaplatin, P.F. Meads, Jr., G. Wüstefeld and K. Ziegler, Proc. of the 13$^{\text{th}}$ Int. Conf. on Cyclotron and their Applications, Vancouver (1992) 701.

[8] H. Jungwirth, R.L. Kustom, S. Martin, P.F. Meads, Jr., E. Zaplatine and K. Ziegler, Proc. of the 14th Int. Conf. on Cyclotron and their Applications, Cape Town (1995) 625.

[9] M. Aiba, K. Koba, S. Machida, Y. Mori, R. Muramatsu, C. Ohmori, I. Sakai, Y. Sato, A. Takagi, R. Ueno, T. Yokoi, M. Yoshimoto and Y. Yuasa, Proc. of European Particle Accelerator Conference 2000 (EPS-AG, 2000) 581.

[10] T. Adachi, M. Aiba, K. Koba, S. Machida, Y. Mori, A. Mutoh, J. Nakano, C. Ohmori, I. Sakai, Y. Sato, M. Sugaya, A. Takagi, R. Ueno, T. Uesugi, T. Yokoi, M. Yoshii, M. Yoshimoto and Y. Yuasa, Proc. of Particle Accelerator Conference 2001 (2001) 3254.

[11] M. Tanigaki, Y. Mori, M. Inoue, K. Mishima, S. Shiyoya, Y. Ishi, S. Fukumoto, and S. Machida, Proc. of European Particle Accelerator Conference 2006 (2006) 2367.

[12] S. Machida, *et. al.*, Nature Physics, Vol. **8**, No. 3 (2012) 243, DOI: 10.1038/NPHYS2179 (2012).

[13] S. Machida, Phys. Rev. Lett. **119** (2017) 064802.

[14] T. Ohkawa, Bull. Amer. Phys. Soc., **30**, (1955) 20.

[15] J. Teichmann, Sov. J. At. Energ. **12** (1963) 507.

[16] S. Brooks, Phys. Rev. ST Accel and Beams **16** (2013) 084001.

[17] D.W. Kerst, E.A. Day, H.J. Hausman, R.O. Haxby, L.J. Laslett, F.E. Mills, T. Ohkawa, F.L. Peterson, E.M. Rowe, A.M. Sessler, J.N. Synder and W.A. Wallenmeyer, Rev. of Sci. Instrum. **31** (1960) 1076.

[18] A. Letchford, *et. al.*, Proc. of 6$^{\text{th}}$ International Particle Accelerator Conference 2015 (2015) 3959.

3.7 nuSTORM Racetrack Decay Ring

J.-B. Lagrange, STFC/RAL/ISIS, UK.
J. Pasternak, Imperial College London and STFC/RAL/ISIS, UK.
K. Long, Imperial College London, UK.
R.B. Appleby, J.M. Garland, S. Tygier, Cockcroft Institute and Manchester University, UK.
A. Bross, D. Neuffer, FNAL, IL, USA.
A. Liu, Euclid Technologies LLC, NJ, USA.

Abstract

The nuSTORM project addresses essential questions in neutrino physics by providing the means for a precise measurement of neutrino cross sections and opening a way for a search for light sterile neutrinos [1]. This is possible because of the precisely known flavour content and spectrum of a neutrino beam produced from muon decay. In the proposed nuSTORM facility pions would be directly injected into a racetrack storage ring, where a circulating muon beam would be captured. A FODO solution with large aperture quadrupoles, a racetrack FFA (Fixed Field alternating gradient Accelerator) and a hybrid version of the two previous solutions are the options discussed in this paper.

Introduction

The production of a neutrino beam with a defined spectrum and flux composition using muon decay is a well-established idea. The concept was developed in the Neutrino Factory proposal, which was then addressed in several dedicated research and development studies culminating in the International Design Study for the Neutrino Factory (IDS-NF) [2]. The Neutrino Factory consists of a high power proton driver, the output of which is directed towards a pion production target; a decay channel, where the muon beam is formed; the muon front end, where the beam is prepared for acceleration and the muon accelerator to boost the energy to the required value. The muon beam is then injected into the decay ring, with straight sections pointing towards near and far detectors producing neutrino beams for both interaction and oscillation physics. Although it has been shown [2] that such a facility will have superior physics potential for leptonic CP violation searches to a conventional neutrino beam based on pion decay, it requires the construction of new accelerator components and presents many technological challenges. To allow for the start of neutrino physics experiments based on muon decay using conventional accelerator technology, the "neutrinos from STORed Muons" (nuSTORM) project was proposed [3–5]. The main goal of nuSTORM is to precisely study neutrino interactions for electron and muon neutrinos and their antiparticles, but the facility could also contribute to sterile neutrino searches, and serve as proof-of-principle R&D for the Neutrino Factory concept.

In nuSTORM high energy pions produced at the target are first focused with a magnetic horn [6], and directly injected into the ring after passing through a short transfer line equipped with a chicane to select the charge of the beam. Once in the ring, decaying pions will form the muon beam. A fraction of the muon beam with momentum lower than the injected parent pions will be stored in the ring, and a fraction with similar or larger momentum will be extracted with a mirror system at the end of the long straight section to reduce beam loss and avoid activation in the arcs. The extracted beam may also be used for accelerator R&D studies for future muon accelerators, which may serve as another application for nuSTORM. The design and performance of the decay ring is tightly linked to the neutrino physics reach of the experiment, with intrinsic design challenges arising from the large range of beam momenta in the ring.

At the present time there are three options under study for the design of the decay ring. The first option is a FODO solution with large bore, conventional quadrupoles with alternating

gradients [7] in the long straight sections and with a lattice based on separated function magnets in the arcs. This solution provides excellent performance with respect to the transverse acceptance, but it has very limited longitudinal acceptance, resulting directly from the alternating gradient conventional magnet approach. The second solution uses recent developments in FFAs. In these machines, which come in scaling and non-scaling flavours, large aperture, non-linear magnets allow the beam to move through the aperture at varying momenta, with a constant betatron tune in the case of a scaling FFA. The advantage of such a lattice is the large momentum acceptance together with the possibility of a large transverse acceptance, thus increasing the number of stored muons in the ring. The design is realised by keeping the ring zero-chromatic over the whole momentum range, and choosing the tune point far from harmful resonances. Furthermore, to maximise the portion of the ring pointing towards the detector, an FFA racetrack shape is now possible [8], while keeping the ring zero-chromatic for a large momentum range, thanks to the use of straight scaling FFA cells [9]. The third option is a combination of the FODO and FFA solutions, called the hybrid option. It features a production straight section with conventional quadrupoles, as in the FODO solution, and FFA magnets in the rest of the ring, as in the FFA solution.

The constant betatron tune with momentum provides a strong constraint on the fields in a scaling FFA. In the arcs, the vertical magnetic field B_{az} in the median plane produced by the combined-function magnets follows the circular scaling law [10], proportional to a power of the orbit radius. This type of magnet has been successfully built for several machines in the past [11–16]. In the straight sections, the vertical magnetic field B_{sz} in the median plane produced by the combined-function magnets follows the (more complicated) straight scaling law [9]. The beam orbit oscillations through scaling magnets in this type of straight produce a characteristic periodic beam angle oscillation known as a scallop angle, which ultimately limits the achievable neutrino flux. Straight scaling FFA magnets have been successfully demonstrated experimentally [9]. This paper discusses the FFA solution and gives preliminary results for the hybrid option.

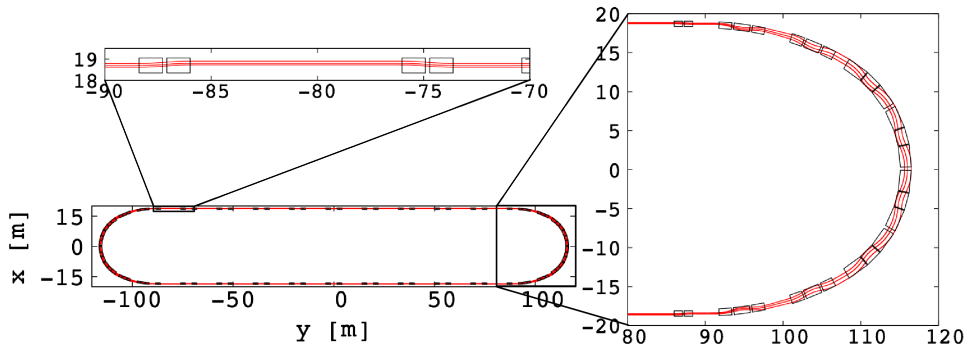

Figure 1: View of the racetrack FFA lattice (bottom left). Enlarged details of the straight section are shown at the top left and of the arc section to the right. Matched, minimum and maximum momenta muon closed orbits are shown in red. Effective field boundaries with collimators are shown in black.

3.7.1 FFA Ring design

The first constraint of the FFA solution is to keep the scallop angle of the reference trajectories in the straight section as small as possible. A large scallop angle, giving the deviation of the beam from a straight line, will alter the spectrum and overall value of the neutrino flux. This goal has been addressed with triplet lattice cells [17]. However a quadruplet cell DFFD gives

an additional long straight between the two F magnets, increasing the efficiency of the neutrino production towards the detector. Furthermore, since the D and F magnets are identical, only one type of magnet needs to be designed and manufactured.

The second constraint is to keep the dispersion small in the muon production straights to give a good muon capture rate. Since the central momentum of the injected pions is different from the central momentum of the circulating beam, the horizontal position of the reference trajectories must be sufficiently close to each other that the muons obtained from pion decay are within the acceptance of the circulating beam. However, the dispersion has to be large where the beam is injected to provide the necessary beam separation, so a dispersion matching section is necessary to accommodate the two constraints. A dispersion suppressor is therefore introduced in the arcs. The concept of a dispersion suppressor in a scaling FFA is to induce a betatron oscillation of the reference trajectories around the periodic trajectory of the matching cell that is different to the arbitrarily chosen, matched trajectory. A π-phase advance in the dispersion suppressor section allows half a complete oscillation and the reference trajectories to be matched. In order to match the horizontal beta-functions, the horizontal phase advance in the arc is an integer multiple of π, and the vertical beta-functions are matched by adjusting the ratio of magnetic fields in the magnets, the so-called F/D ratios. Superconducting magnets are chosen to keep the arc sections compact and ensure a large ratio of the production straight length to the circumference. In the straight sections, to drive down manufacturing costs, room temperature magnets are preferred. However, the use of super-ferric magnets in the straight sections is also being considered owing to their lower power consumption.

A systematic scan of the tune diagram has been conducted to find the optimised parameters of the full FFA solution [18]. The choice of the tune point was based on the dynamic acceptance in both horizontal and vertical planes and the muon capture efficiency in the straight sections. The muon capture efficiency is a function of the dispersion in the straight cells, the distance between the reference orbit of the injected pion beam and the reference orbit of the muon beam, and the maximum stable horizontal amplitude the lattice can accept.

Ring parameters for the chosen lattice are summarised in Table 1. Closed orbits of matching momentum, minimum momentum and maximum momentum are shown in Fig. 1. The dispersion and beta-functions at matching momentum are shown in Fig. 2. The magnetic field for the maximum momentum muon closed orbit is presented in Fig. 3. The stability of the ring tune has been studied over a $\pm 19\%$ momentum range, and the tune shift is presented in Fig. 4. The transverse acceptance in both planes has been explored by tracking over 100 turns a particle displaced from the closed orbit with a small deviation in the other transverse direction (1 mm). This lattice shows a horizontal maximum emittance of about 2 mm.rad, as shown in Fig. 5, a vertical maximum emittance of about 1 mm.rad, as shown in Fig. 6, and a maximum stable horizontal amplitude larger than the distance between the reference orbits of the injected pion beam and and the circulating muon beam.

3.7.2 Hybrid solution

Although estimates promise a higher neutrino flux with the FFA lattice than with the FODO lattice [17], a lattice combining the advantages of the FODO and the FFA solutions would give an improved performance. A production straight made of conventional quadrupoles would remove the problem of the scallop angle, while optimising the muon capture efficiency. The chromaticity of the ring can be greatly reduced if the rest of the ring is made zero-chromatic, as for the FFA solution. Furthermore, a large beta-function is desirable in the production straight to minimise the momentum angle for a given emittance, limiting the phase advance of the section, and thus its natural chromaticity. Such a lattice can keep the tune excursion across a large momentum range confined between half-integer resonances, which allows a large transverse acceptance for

Table 1: Lattice parameters

Parameter	**Value**
Total circumference	502 m
Length of one straight section	180 m
One straight section/circumference ratio	36%
Momentum acceptance	3.7 GeV/c ±19%
Ring tunes (H, V)	(7.18, 4.88)
Number of cells in the ring:	
Straight cells	20
Arc matching cells	8
Regular arc cells	8
m-value in straight cells	$2.2\,\mathrm{m}^{-1}$
Packing factor in straight cells	0.24
Max. scallop angle in straight cells	76 mrad
k-value in regular arc cells	6.056
R_0 in regular arc cells	16.4 m
Packing factor in regular arc cells	0.92
k-value in matching cells	26.0
R_0 in matching cells	36.15 m
Packing factor in matching cells	0.57

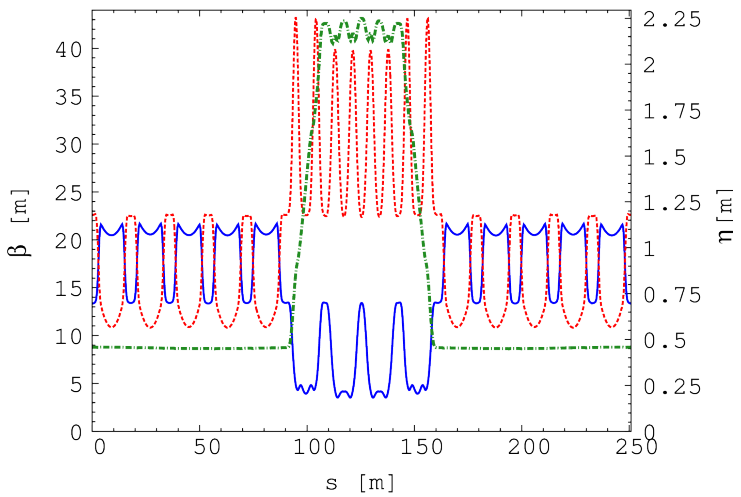

Figure 2: FFA design: Horizontal (plain blue), vertical (dotted red) periodic betatron functions (left scale) and dispersion (mixed green line, right scale) over half the ring for matching momentum. The plot is centred on the arc part.

a large momentum range. Since the dispersion is different in the two straight sections, *i.e.* null in the quadrupole section and constant non-null in the straight FFA section, two different dispersion matching sections have to be designed around the straight sections.

Preliminary design parameters are presented in Table 2. Closed orbits of matching momentum, minimum momentum and maximum momentum are shown in Fig. 7. The dispersion and beta-functions at matching momentum are shown in Fig. 8. The magnetic field for the maximum

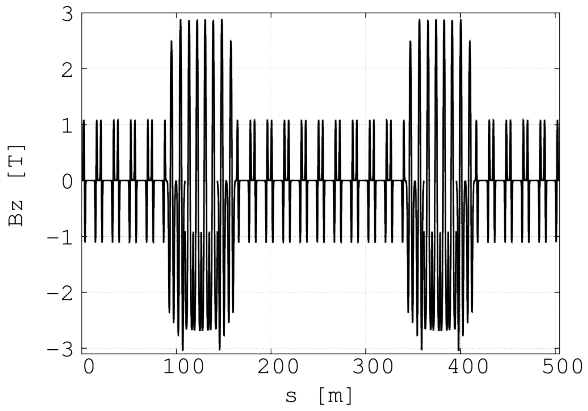

Figure 3: FFA design: Vertical magnetic field on the median plane for the maximum circulating muon momentum over half the ring. The plot is centred on the arc part.

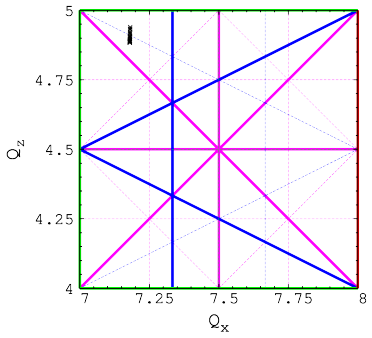

Figure 4: FFA design: Tune diagram for momenta ±19% around 3.7 GeV/c. Integer (red), half-integer (green), third integer (blue) and fourth integer (purple) normal resonances are plotted. Structural resonances are in bold.

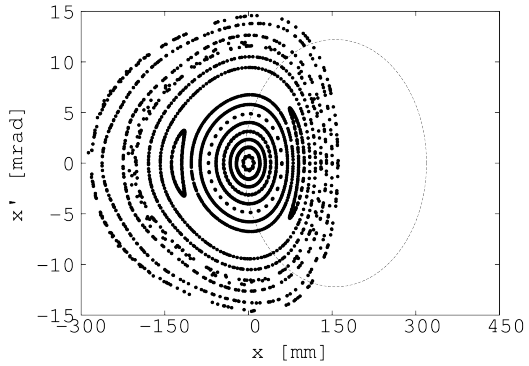

Figure 5: FFA design: Stable motion in the horizontal Poincaré map for maximum initial amplitude over 100 turns for matched momentum. The ellipse shows a 2 mm.rad unnormalized emittance, centred on the closed orbit of the injected central momentum pion.

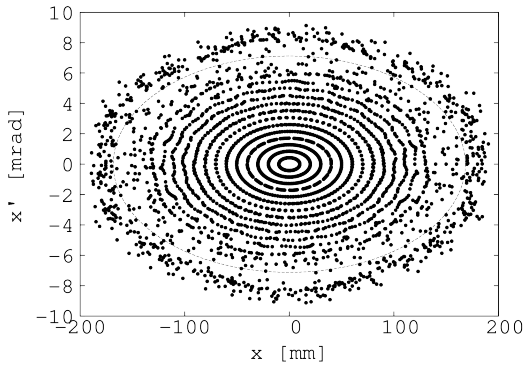

Figure 6: FFA design: Stable motion in the vertical Poincaré map for maximum initial amplitude over 100 turns for matched momentum. The ellipse shows a 1 mm.rad unnormalized emittance.

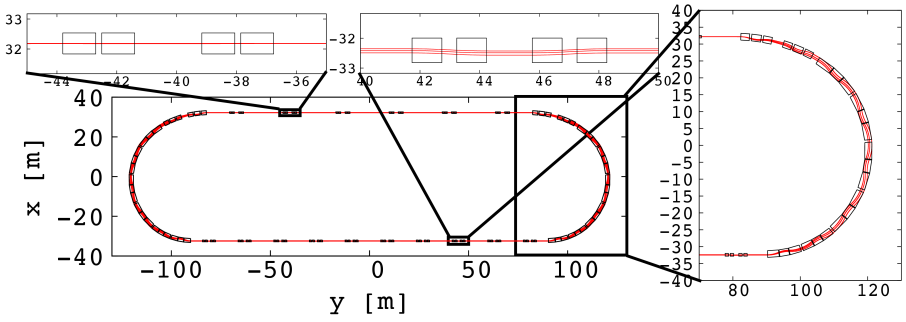

Figure 7: View of the racetrack hybrid lattice (bottom left). The enlargements show the production straight section (top left), the FFA straight (top middle), and the arc section (right). Matched, minimum and maximum momenta muon closed orbits are shown in red. Effective field boundaries with collimators are shown in black.

momentum muon closed orbit is presented in Fig. 9. As for the FFA design, the stability of the ring tune has been studied, in this case over a ±15% momentum range. The tune shift is presented in Fig. 10. The transverse acceptance in both planes has been studied in the same way as in the FFA solution. This lattice gives a maximum emittance of more than 1 mm in both horizontal and vertical planes, as shown in Figs. 11 and 12, respectively.

Table 2: Lattice parameters

Parameter	**Value**
Total circumference	533 m
Length of production straight section	161 m
Production straight section/circumference ratio	30%
Momentum acceptance	5.3 GeV/c ±15%
Ring tune (H, V) at 5.2 GeV/c	(6.20, 3.26)
Number of cells in the ring:	
Quadrupoles straight cells	6
Straight FFA cells	10
Arc first matching FFA cells	4
Arc second matching FFA cells	4
Regular arc cells	8
Field gradient in quadrupoles	-2.34 T/m, 2.31 T/m
Packing factor in quadrupole cells	0.16
m-value in straight FFA cells	2.2 m^{-1}
Packing factor in straight FFA cells	0.24
Max. scallop angle in straight FFA cells	76 mrad
k-value in regular arc FFA cells	7.252
R_0 in regular arc FFA cells	31.2 m
Packing factor in regular arc FFA cells	0.92
k-value in first matching FFA cells	24.969
R_0 in first matching FFA cells	49.08 m
Packing factor in first matching FFA cells	0.62
k-value in second matching FFA cells	13.369
R_0 in second matching FFA cells	30.42 m
Packing factor in second matching FFA cells	0.91

Summary

The nuSTORM project aims to address essential questions in neutrino physics, in particular by offering the best possible way to measure precisely neutrino cross sections and by providing an opportunity to search for light sterile neutrinos. It would also serve as a proof-of-principle experiment for the Neutrino Factory and can contribute to the R&D for future muon accelerators. The FFA solution for the decay ring gives good performance with large transverse and momentum acceptances, but a hybrid solution would give a better result. Work on an optimised version of the hybrid lattice and a full comparison in terms of neutrino flux for the three solutions are still to be carried out.

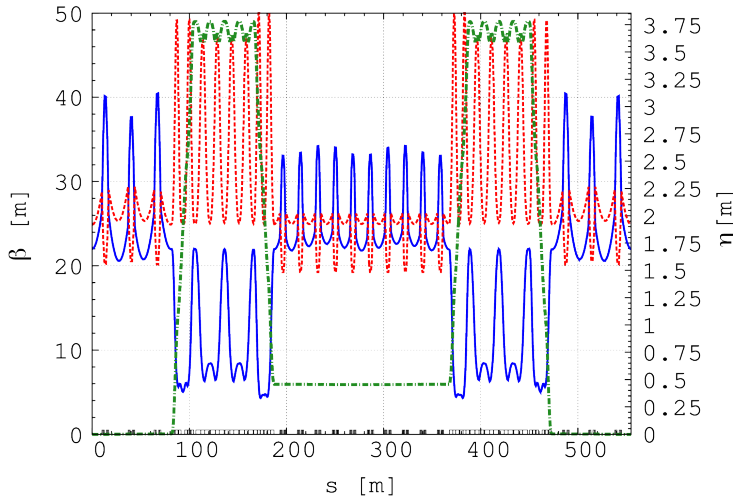

Figure 8: Hybrid design: Horizontal (plain blue), vertical (dotted red) periodic betatron functions (left scale) and dispersion (mixed green line, right scale) in the ring for matching momentum. The plot is centered on the straight FFA section.

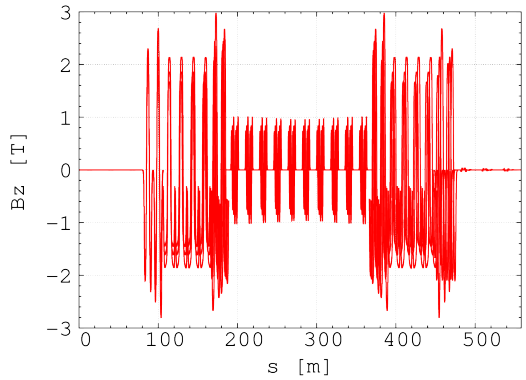

Figure 9: Hybrid design: Vertical magnetic field on the median plane for the maximum circulating muon momentum in the ring (6.1 GeV/c). The plot is centered on the straight FFA part.

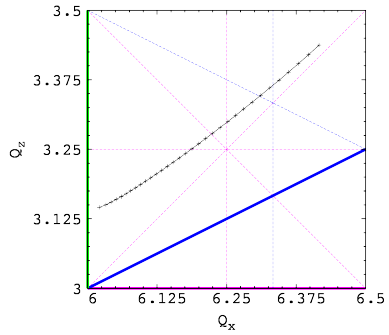

Figure 10: Hybrid design: Tune diagram for momenta ±15% around 5.3 GeV/c. Integer (red), half-integer (green), third integer (blue) and fourth integer (purple) normal resonances are plotted.

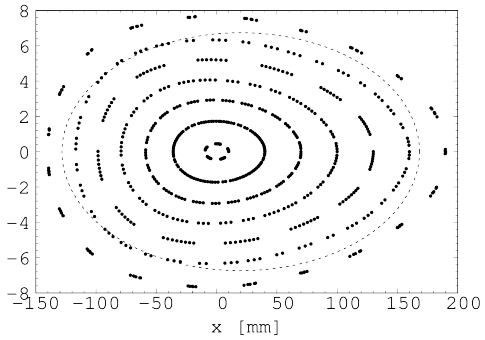

Figure 11: Hybrid design: Stable motion in the horizontal Poincaré map for maximum initial amplitude over 100 turns for matched momentum. The ellipse shows a 1 mm.rad unnormalized emittance.

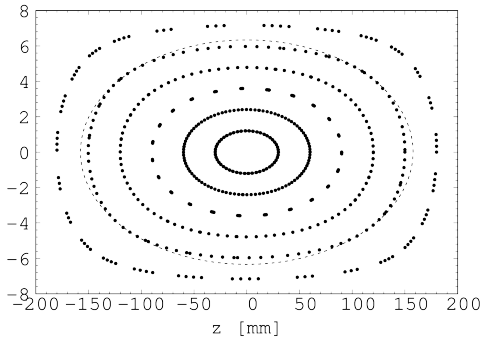

Figure 12: Hybrid design: Stable motion in the vertical Poincaré map for maximum initial amplitude over 100 turns for matched momentum. The ellipse shows a 1 mm.rad unnormalized emittance.

References

[1] J. Jaeckel, M. Lamont and C. Vallee, "Physics Beyond Colliders", 2017, `https://pbc.web.cern.ch`

[2] IDS-NF website: `http://ids-nf.org/`

[3] D. Adey et al., "nuSTORM - Neutrinos from STORed Muons: Proposal to the Fermilab PAC", arXiv:1308.6822 [physics.acc-ph]

[4] K.R. Long, "Neutrinos from Stored Muons", Proceedings, 17$^{\text{th}}$ International Workshop on Neutrino Telescopes (Neutel 2017), Venice, Italy, March, 2017

[5] C.C.Ahdida *et al.* "First discussion of nuSTORM in the context of the Physics Beyond Colliders workshop", 2018, `https://indico.cern.ch/event/765096/contributions/3296001/`

[6] A. Liu et al., "Optimization of the magnetic horn for the nuSTORM non-conventional neutrino beam using the genetic algorithm", Nucl. Instr. Meth. A, vol. 794, pp. 200–205, 2015.

[7] A. Liu, Ph.D. Thesis, "Design and simulation of the nuSTORM facility", FERMILAB-THESIS-2015-04, 2015.

[8] J.M. Garland et al., "Normal-conducting scaling fixed field alternating gradient accelerator for proton therapy", Phys. Rev. Accel. Beams, Vol. 18, 094701, 2015.

[9] J.-B. Lagrange et al, "Straight scaling FFAG beam line", Nucl. Instr. Meth. A, vol. 691, pp. 55–63, 2012.

[10] K.R. Symon, D.W. Kerst, L.W. Jones, L.J. Laslett, K.M. Terwilliger, "Fixed-Field Alternating-Gradient Particle Accelerators", Phys. Rev. 103 (6) (1956) 1837–1859.

[11] F. T. Cole et al., "Electron model fixed field alternating gradient accelerator", Rev. Sci. Instrum. 28 (6), pp. 403–420, 1957.

[12] D. W. Kerst et al., "Electron model of a spiral sector accelerator", Rev. Sci. Instrum. 31 (10), pp. 1076–1106, 1960.

[13] M. Aiba et al., "Development of a FFAG proton synchrotron", Proc. of EPAC 2000 Conf., pp. 581–583, 2000.

[14] S, Machida et al., "Commissioning of 150MeV FFAG synchrotron", Proc. of EPAC 2004 Conf., pp. 2643–2645, 2004.

[15] K. Okabe et al., "An intense neutron source with emittance recovery internal target (nustorm-15) using ionization cooling", Proc. of EPAC?8 Conf., pp. 3512–3514, 2008.

[16] Yasushi Arimoto et al., "Design of PRISM-FFAG Magnet", Nucl. Phys. B 155, pp. 286–287, 2006.

[17] J-B. Lagrange et al., "Racetrack FFAG muon decay ring for nuSTORM with triplet focusing", JINST, 13, 09, P09013, (2018).

[18] J-B. Lagrange et al., "NUSTORM FFAG decay ring", THPMB053, IPAC16 (2016).

3.8 Intense Muon Source with FFA Based Energy Recovery Internal Target (ERIT)[1]

Yoshiharu Mori, Hidefumi Okita, Tomonori Uesugi, Yasutoshi Kuriyama, Akihiro Tanigchi, Yoshihiro Ishi, Masayuki Muto,Yuka Ono,
Research Reactor Institute, Kyoto University, Japan.
Yujiro Yonemura, Hidehiko Arima, Nobuo Ikeda,
Dept. of Engineering, Kyushu University, Japan.
Akira Sato, Dept. of Physics, Osaka University, Japan.
Michikazu Kinsho, Yasuhiro Miyake, Masahiro Yoshimoto, Kota Okabe,
JPARC, JAEA-KEK, Japan.

Introduction

Muons are of interest in various fields such as particle physics, nuclear physics and material science. Important among them is the transmutation of nuclear waste, especially high-level radioactive species such as long-lived fission products (LLFPs) and minor actinides (MAs), for which copious supplies of neutrons are needed. Transmutation can be triggered via muon nuclear transformations. A muonic atom can be formed by trapping a negative muon in the atomic nucleus, and this process has a probability of about 95 per cent success if the atomic number (Z) is more than 30. The muonic atom then transforms to a stable nucleus by beta decay and the emission of neutrons. For transmutation purposes a very high yield of negative muons of the order of $10^{16}\mu^-$/s is necessary [1].

Negative muons from the decay of negative pions are efficiently produced by nucleon-nucleon interactions with a high energy hadron beam colliding with a target nucleus containing neutrons. A hadron beam energy of 300 - 400 MeV/u or more is necessary to produce negative pions effectively [2].

There are difficulties for negative pion production with this energy range. One is energy loss from the projectile proton by ionization in the target. The efficiency of negative pion production drops until the proton energy reaches the threshold energy of pion production at about 250 MeV/u. Another problem is the absorption of negative pions in the solid target. The absorption cross section of negative pions with the target nucleus is so large that a thinner target must be used to eliminate the effect. Thus, a high beam current and a thin target are essential to keep the efficiency large in negative muon production. In order to realize the required negative muon yield of $10^{16}\mu^-$/s, a proton beam current of more than 3 A is necessary if a thin lithium target of 1 cm thickness is used.

Recovery of the beam energy loss by re-acceleration and use of a thinner target, the so called energy recovery internal target (ERIT) scheme [3, 4], is a useful and convenient method for overcoming these difficulties. The ERIT scheme was first proposed for the efficient production of secondary particles such as neutrons and unstable nuclei, and the first ERIT ring was constructed at the research reactor institute of Kyoto University [5]. This paper describes the possibility of applying the ERIT principle for intense negative pion/muon production of more than $10^{16}\mu^-$/s with a wedge type of Li solid target [1] or by creating a target by filling the ring with deuterium gas [6].

[1]This work was partially funded by ImPACT Program of Council for Science, Technology and Innovation (Cabinet Office, Government of Japan).

3.8.1 Principle of ERIT

In the ERIT scheme, projectile particles circulate and pass through a thin target placed in the ring and generate secondary particles such as neutrons, pions, etc. Particles lose energy through ionization interactions (electronic stopping power) and are re-accelerated in rf cavities. Beam emittance growth caused by multiple scattering (Rutherford scattering and straggling) at the target can be counteracted by ionization cooling [7,8]. Re-acceleration imposes only longitudinal momentum transfer, while the energy losses occur in the directioin of particle travel; the overall effect is that both transverse and longitudinal momenta are reduced and the beam emittance does not increase.

Longitudinal cooling occurs if

$$\frac{\partial}{\partial E}\left(\frac{\mathrm{d}E}{\mathrm{d}s}\right) > 0.$$

Here, $\mathrm{d}E/\mathrm{d}s$ is the stopping power. Therefore, if a wedge-shaped target is placed in the ring at a particular position causing orbit dispersion, the longitudinal emittance can be cooled.

The ERIT scheme was demonstrated at the Institute for Integrated Radiation and Nuclear Science of Kyoto University (KURNS) as a low energy neutron source [5]. Figure 1(a) shows a schematic layout and a photograph of the world's first ERIT neutron source with ionization cooling at Kyoto University. The beam optics of the ERIT ring are based on fixed field alternating gradient (FFA) focusing to provide large transverse and longitudinal acceptances. The 11 MeV H^- ion beam is injected from a linear accelerator (linac) into the FFA ring.

The Be(p,n)B reaction is used for neutron production in this scheme. The diameter of the ring at the central orbit is about 4.5 m. A beryllium foil, a few micrometres thick, is placed in the straight section of the ring, where H^- ions from the linac are charge-stripped to protons and merged with the circulating proton beam, and the energy loss at the target is restored by the rf cavity. In this design, neutron production of more than 10^{12} n/s is expected with an average beam current of 100 μA injected from the linac and beam circulation of more than 500 turns in the ring.

We have found that the design configurations and requirements can be well satisfied experimentally. The emittance growth rate in the vertical direction as a function of turn number has been measured with a beam scraper and an electrostatic bunch monitor. The experimental results, shown in Fig. 1(b), indicate that these design configurations and requirements can be satisfied.

3.8.2 Production of negative muons

Scheme 1: MERIT with proton beam and wedge shaped target

In order to produce negative pions/muons with the ERIT scheme, some additional features should be included. In contrast to the original ERIT ring for neutron production where the proton beam energy was very low, the transverse emittance growth caused by multiple scattering is rather modest because the proton beam energy is relatively higher in the case of pion production. The energy spread of the proton beam colliding with the target is mostly enlarged by electron straggling where the emittance growth rate is almost proportional to the proton beam energy at relativistic energies. A wedge-shaped target placed at the dispersive orbit should be used. Moreover, if the injection beam energy is lowered, the load on the injector can be relaxed.

For negative pion/muon production, the ERIT ring provides beam acceleration and storage at the orbit where a wedge shaped target is placed, and seems most appropriate. A new type of ERIT named MERIT (Multiplex Energy Recovery Internal Target) for negative muons has been proposed [1, 9, 10]. A schematic diagram of MERIT is shown in Fig. 2 showing a comparison with the ordinary ERIT.

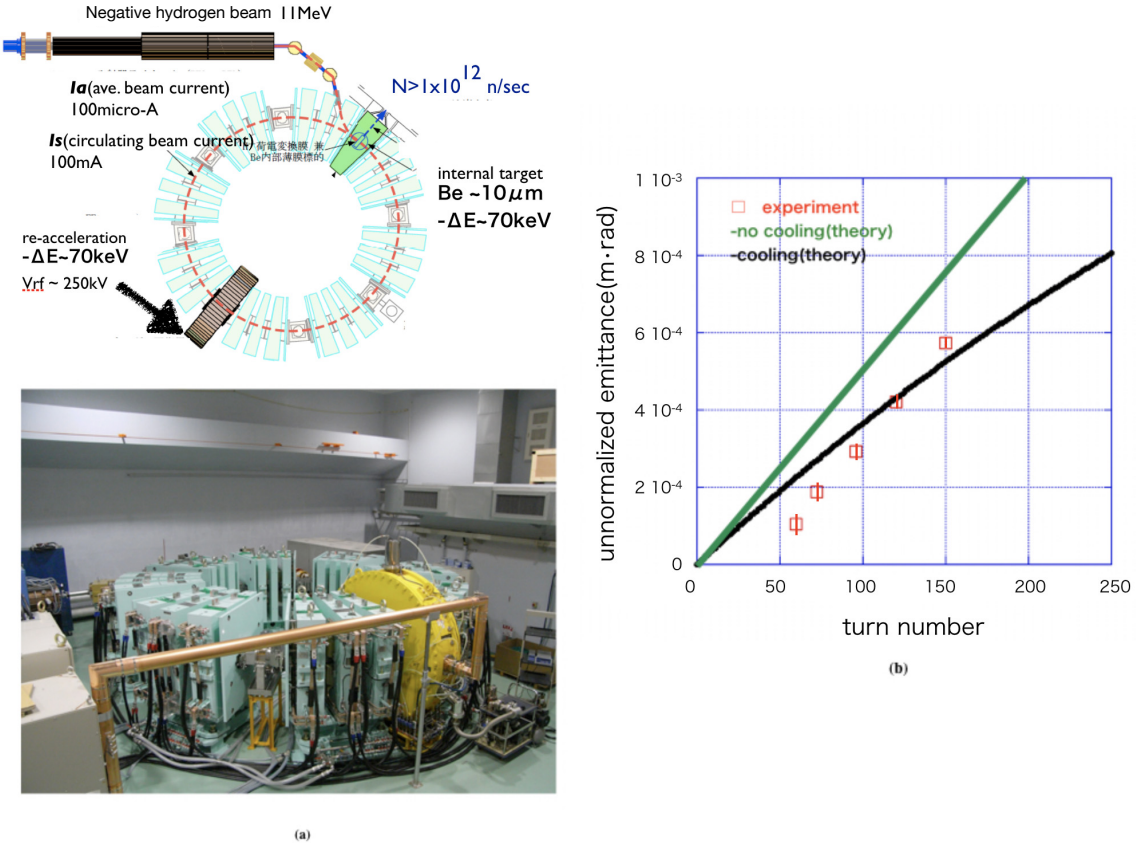

Figure 1: (a) Schematic layout of the ERIT neutron source (upper) and a picture of the apparatus built at KURRI. (b) Beam emittance growth as a function of number of circulating turns in the ERIT neutron ring, measured by the beam scraping method. The error bars in the figure show the systematic errors from the beam scraper positions, which were 0.5 mm in accuracy. The theoretical values estimated from the equations of ionization cooling rate are also shown in the figure.

In this proposal, the projectile particles are protons that are injected at a relatively low energy of 500 MeV and accelerated up to about 800 MeV by an FFA ring accelerator with fixed frequency rf acceleration. To make the use of fixed frequency rf feasible, either serpentine (semi-isochronous) acceleration or a static bucket acceleration scheme is applied.

In serpentine acceleration, the momentum compaction, α, should satisfy the following condition,

$$\alpha \sim \frac{1}{\gamma_s^2}\,.$$

Here, γ_s is the relativistic factor (total energy/rest mass energy) of the beam between its initial and final energies. Momentum compaction in a scaling FFA can be derived from the geometrical magnetic field index, k, through

$$\alpha = \frac{1}{k+1}\,.$$

Figure 3 shows particle paths in longitudinal phase space in a serpentine scenario. Here, the field index $k = 2.43$, $\gamma_s = 1.853$ and the total rf voltage per ring is about 10 MV. The design of the MERIT ring for pion production has been based on these underlying conditions.

The optics of the ring are those of a scaling FFA with an eight-fold symmetry FDF triplet lattice. Table 1 presents the basic parameters of the ring.

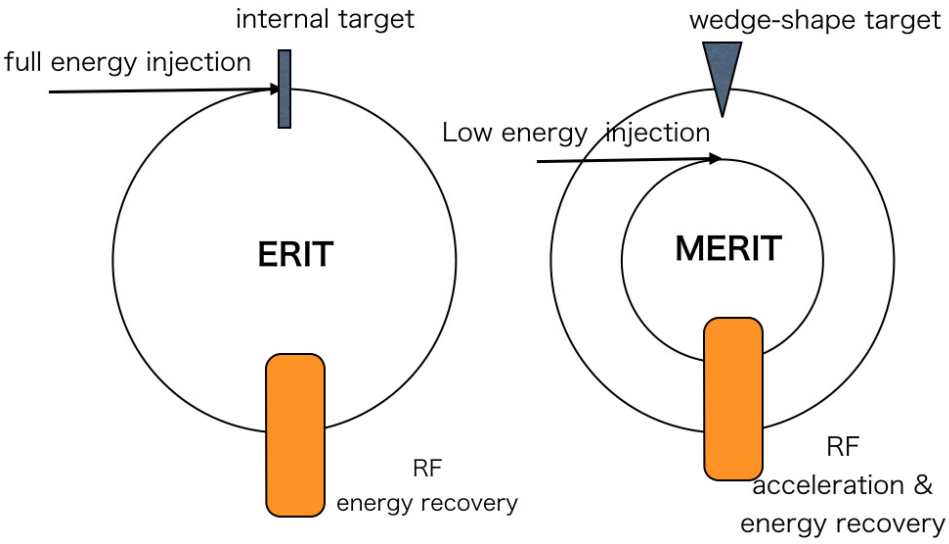

Figure 2: Schematic diagrams of ERIT and MERIT.

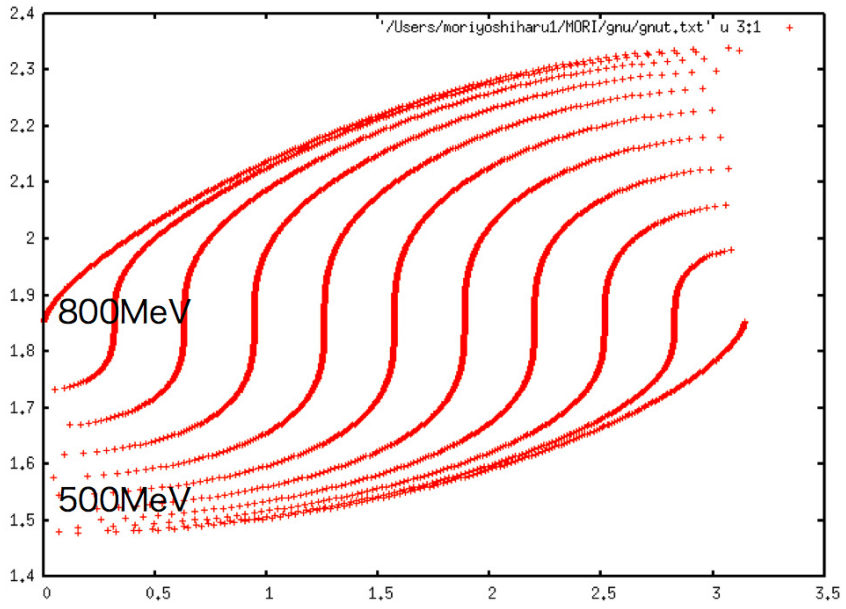

Figure 3: Particle paths in longitudinal phase space under serpentine acceleration.

A schematic layout of the MERIT ring for muon production is shown in Figure 4. A wedge-shaped liquid lithium target whose thickness gradient is $\rho' = 0.27\,\mathrm{g/cm^3}$ is placed at the radial position $R = 5.5\,\mathrm{m}$. The effective thickness of the target is $1.35\,\mathrm{g/cm^2}$ at $R = 5.55\,\mathrm{m}$; therefore the energy loss of protons becomes approximately 2.5 MeV, which can be successfully recovered by rf re-acceleration.

After acceleration to the top energy, the beam is stored with the help of a wedge-shaped, liquid lithium target placed on the maximum energy orbit. If the target becomes thicker towards the outside of the ring, then the beam stays around the maximum energy orbit where beam acceleration and energy loss are well balanced. Also, the ionization beam cooling helps to

Table 1: Basic parameters of MERIT ring for muon production.

Ring configuration	H^- FFA
Energy range (MeV)	500 - 800
Magnetic rigidity (T.m)	3.633 - 4.877
Lattice	FDF
Average radius (m)	5.044 - 5.5
Magnetic field (T): F	1.96 - 2.41
Magnetic field (T): D	1.71 - 2.11
Number of cells	8
Geometrical field index	2.43
Cell tune: H	0.212
Cell tune: V	0.180
Beta function (m) @SS:H	2.5
Beta function (m) @SS:V	2.8
Dispersion function (m)	1.5

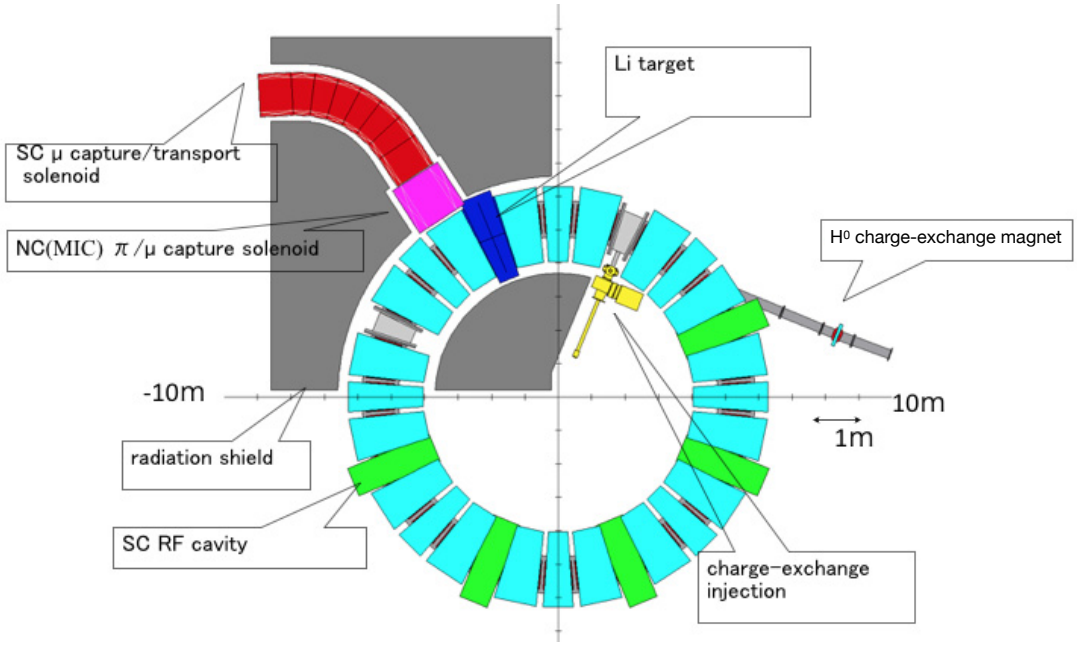

Figure 4: Schematic layout of the MERIT ring for negative muon production.

suppress emittance growth transversely and longitudinally, and the beam circulates for the requisite number of turns needed to generate enough negative pions/muons.

The negative pion yield is estimated from,

$$Y = N_p \, f_0 \, n_t \, l_t \, \sigma_\pi \, .$$

Here, Y is the negative pion yield, σ_π is the negative pion production cross section, N_p is the number of projectile particles (protons) per ring, f_0 revolution frequency, n_t is the target particle

density and l_t is the target thickness. Since the negative pion production cross section for an 800 MeV proton is about 5 mb, a negative muon yield of $10^{16}\,\mu^-/\mathrm{s}$ can be accomplished when $N_p = 1.2 \times 10^{12}$, which is modest compared with the space charge limited beam intensity at the given beam emittance [11]. If the injection proton beam current is 2 mA, the beam needs to be accumulated and stored for at least 600 turns at the circulating, lithium target orbit.

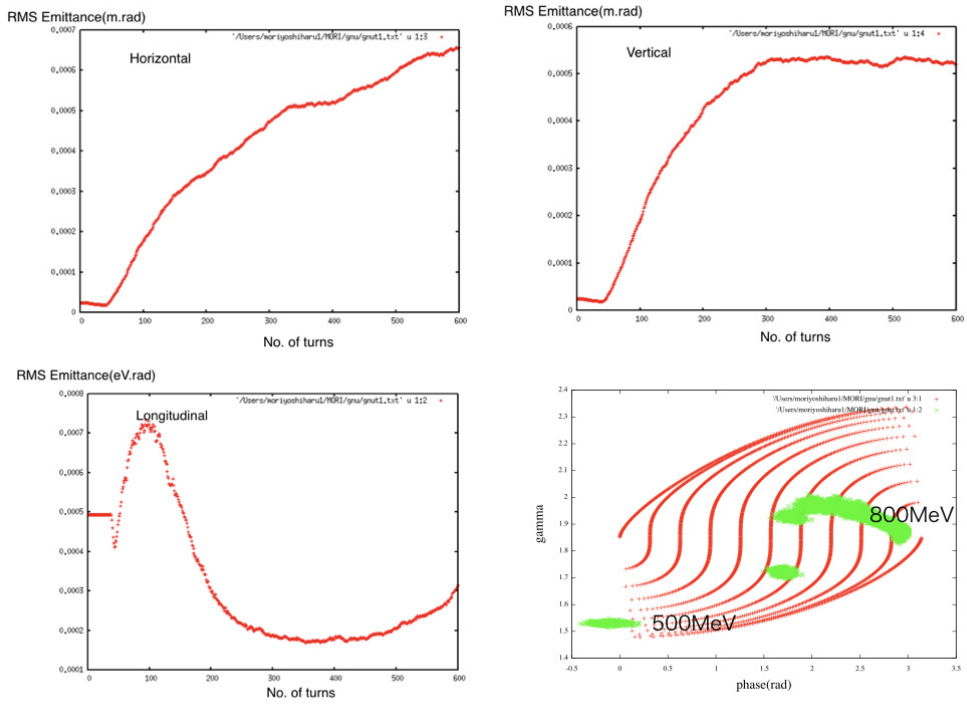

Figure 5: Beam emittance growth in horizontal (upper left), vertical (upper right) and longitudinal (lower left) directions respectively are shown as a function of number of turns. The figure (lower right) shows longitudinal beam behavior in phase space over 500 turns following injection.

The beam is blown up transversely and longitudinally by Rutherford multiple scattering and energy straggling. The beam emittance growth, however, could be cured through the effect of ionization cooling in the energy recovery system. These longitudinal and transverse emittance behaviors can be estimated by simulation codes using particle tracking.

Figure 5 shows the longitudinal and transverse emittance growths as a function of beam turn numbers circulating around the ring, which are simulated by multi-particle beam tracking including the ionization cooling effect. As can be seen from this figure, the beam emittance in the longitudinal direction decreases gradually as a function of turn number. The growths of transverse beam emittance in both horizontal and vertical planes are also suppressed and reach equilibrium values of about 700 mm.mrad (rms) in horizontal and 600 mm.mrad (rms) in vertical directions, respectively. The acceptance of the ring must be large enough to cover these equilibrium emittances during beam acceleration and storage.

In the longitudinal direction, although the phase acceptance is limited to about $\pm\pi/2$, the longitudinal acceptance is large in serpentine beam acceleration, as shown in Figure 3. Since the scaling FFA magnets include non-linear field components, the transverse dynamic apertures for both horizontal and vertical directions must be large enough for the beam emittance. The dynamic apertures have been estimated numerically by particle tracking simulations and the results are shown in Figure 6. The dynamic apertures are about 0.1 m.rad horizontally and 0.07 m.rad vertically, and both are quite large compared with the beam emittance.

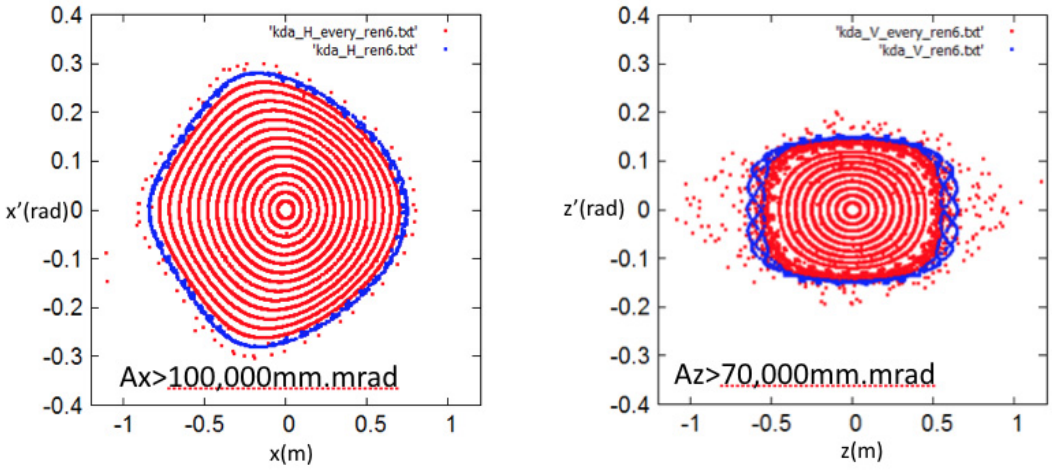

Figure 6: Dynamic apertures (left: horizontal, right: vertical) estimated numerically.

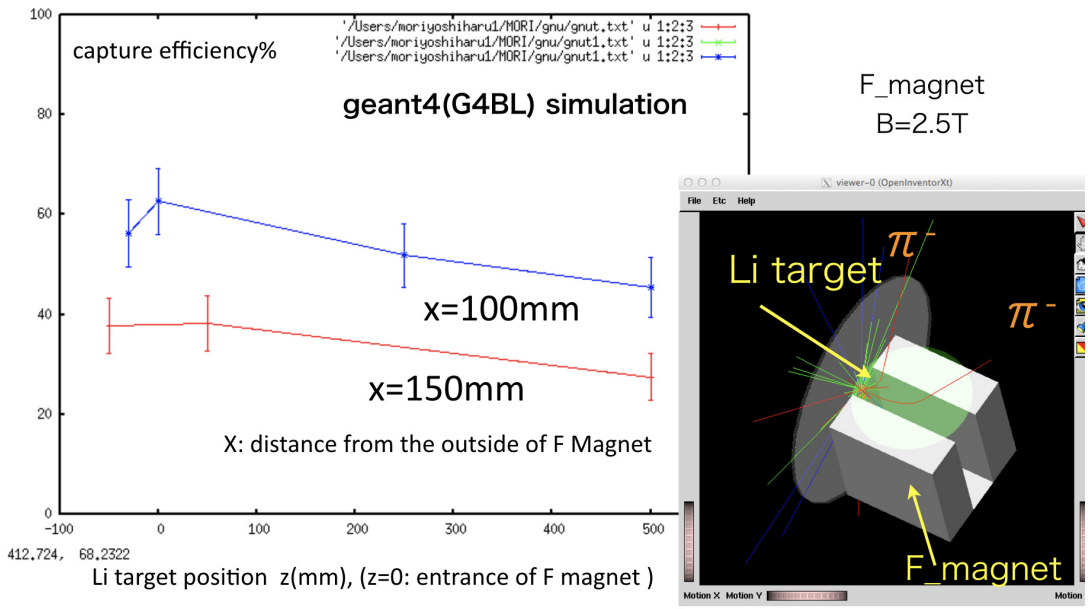

Figure 7: Capture efficiency of π^- for various positions of the lithium target placed in the straight section.

The momentum distribution of negative pions produced at the lithium target was estimated by the Geant4 beam line code, G4BL [12]. Since the dipole magnetic field strength of the F magnet is about 2.4 T and the effective field length is about 1.1 m, almost all the pions could be swept away from the ring. The pions are emitted in various directions and the number of pions within the aperture of the capture solenoid is limited.

Figure 7 shows the π^- capture efficiencies estimated by the G4BL code at the entrance to the 1 m diameter solenoid magnet for various positions of the lithium target in the straight section. The overall π^- capture efficiency is estimated to be about 50 per cent or less. Nevertheless, the production yield of negative muons in this system will still satisfy the production requirements.

Scheme 2: ERIT with gaseous deuterium target

One of the difficulties is how to collect and transport sufficiently many of the negative pions and muons produced at the lithium target to the nuclear waste treatment area. A deuterium gas target filling up the beam pipe of the ERIT ring instead of a liquid lithium thin target may improve the pion/muon capture efficiency and make muon nuclear transformation of long-lived nuclear wastes more manageable. Pions are generated everywhere in the beam pipe around the ring. Negative muons from negative pion decay are swept away to the outside of the beam pipe by the magnetic field and finally trapped as muonic atoms by LLFPs which cover the beam pipe, as shown in Fig. 8. In this scheme, almost all negative muons could be efficiently utilized to mitigate the long-lived fission products. Other energetic particles produced in the deuterium gas target, such as neutrons, protons, positive and neutral pions and gamma rays, could be thermalized by a water cell surrounding the beam pipe.

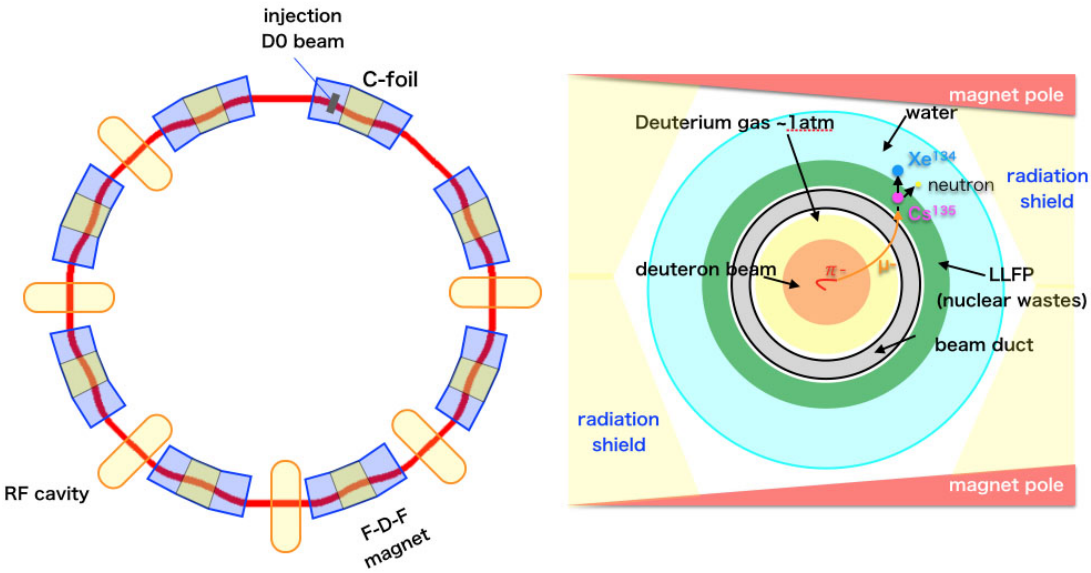

Figure 8: Schematic layout of the ERIT ring for negative muon production (left) and cross sectional view of the ring pipe (right).

In this design, in contrast to Scheme 1, deuterons are chosen as the projectile particles instead of protons. The cross section of negative pion production is almost five times greater than for

protons for a beam energy of about 600 MeV/u, although beam loss caused by the break-up reaction to a proton and neutron is large. The negative pion production cross section for a 600 MeV/u deuteron is about 20 mb [13]. The negative pion yield Y attained with this system is

$$Y = L\sigma_\pi \,,$$

where σ_π is the negative pion production cross section and L is the luminosity expressed as:

$$L = N_d \, v_d \, n_T \,.$$

Here, N_d is the number of projectile particle(deuteron) per ring, v_d (cm/s) is the projectile particle velocity and n_T (cm^{-3}) is the target particle density. A negative muon yield of $1 \times 10^{16}\,\mu^-/\mathrm{s}$ can be achieved when the luminosity is $5 \times 10^{41}\,\mathrm{cm}^{-2}\,\mathrm{s}^{-1}$. When the pressure of deuterium gas target is 1 atm, N_d becomes 7.9×10^{11} deuterons per ring.

The total beam loss cross section, σ_l, including deuteron break-up and pion generation estimated by Geant4:G4BL [12], is approximately 120 mb, which is six times larger than the negative pion production cross section. Thus, a deuteron beam current of about 10 mA should be continuously supplied to the system to attain the negative muon yield of $1 \times 10^{16}\,\mathrm{s}^{-1}$. On the other hand, the mean free path of the projectile particle is about $l_{\mathrm{mfp}} = 1/\sigma_l n_T \sim 3000$ m, which is equivalent to a path length of about 90 turns circumference of the ring whose diameter is about 11 m. Thus, the ring acceptance should be large enough to accept the beam whose emittance has grown by multiple scattering and straggling after 90 turns. The system also involves ionization cooling and through this the beam energy loss by ionization is recovered by rf re-acceleration, and emittance blow up is suppressed. The emittance growth as a function of beam path can be calculated from the ionization cooling rate equations.

Figure 9 shows the transverse beam emittance behavior estimated by the rate equation for the deuteron beam and deuterium target described above as a function of number of turns. Here, a beta function of 4 m averaged over the ring is assumed. As can be seen from the figure, since the normalized rms emittance is about 6×10^{-5} m.rad after 100 turns, a ring acceptance (unnormalized) of more than 5×10^{-4} m.mrad, which is almost ten times the rms emittance, seems to be enough. The stopping power of 600 MeV/u deuterons in deuterium gas is about $3\,\mathrm{MeV/g.cm}^{-2}$ and the energy loss per turn in the ring filled with 1 atm deuterium gas becomes approximately 1 MeV. Therefore, a total rf voltage of more than 10 MV, when the rf harmonic is $h = 1$, seems to be enough for energy loss compensation.

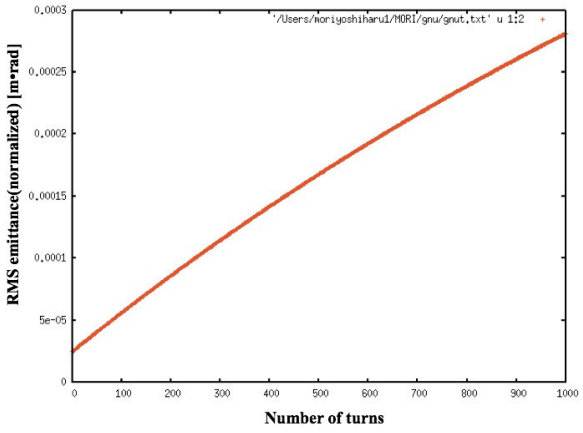

Figure 9: Transverse emittance growth as a function of number of beam circulating turns estimated with the rate equations of ionization cooling.

A preliminary ERIT ring design for negative muon production with a deuteron beam has been carried out. Table 2 is a list of basic parameters of the ring. The ring is composed of an

eight-fold symmetric FDF scaling FFA lattice and superconducting (SC) magnets are assumed to be used for lower electricity consumption and a compact ring size. An average ring radius of 5.5 m is chosen at the central orbit so that the maximum magnetic field strength in the SC magnets can be modest. The betatron tunes per cell are 0.22 and 0.18 in horizontal and vertical

Table 2: Parameters of the ERIT ring for muon production.

Energy	600 MeV/u
Magnetic rigidity	8.126 TM
Lattice	FDF
Average radius	5.5 m
Magnetic field (F)	4.016 T
Magnetic field (D)	3.509
Opening angle (F)	0.2032 rad
Opening angle (D)	0.1432 rad
Geometrical field index	2.4
F/D ratio	1.1
Cell tune: V	0.180
Betatron tune (H)	0.2188/cell
Betatron tune (V)	0.1797/cell
Curvature (F)	2.023 m
Curvature (D)	2.316 m

directions, respectively. The averaged beta functions over the ring are about 3.1 m and 3.8 m in horizontal and vertical directions, respectively. The dynamic aperture of the ring is greater than 2×10^{-2} m.rad for both horizontal and vertical directions, which is large enough for the requirement described above.

The multi rf cavities for recovering the energy lost in the deuterium gas target are placed in each straight section and the total rf voltage should be more than 20 MV when the rf harmonic number is two. The frequency of the rf cavity is 13.8 MHz.

The maximum beam intensity limited by space charge effects can be estimated by the following Laslett tune shift formula [11]:

$$N = -\frac{2\pi\beta^2\gamma^3 B_f \Delta Q}{r_d F}\,.$$

Here, ΔQ is the betatron tune shift caused by the space charge effect, N is the number of particles per ring, ϵ is the beam emittance (m.rad), r_d is the classical deuteron radius (m), F is the form factor and B_f is the bunching factor, β is the relativistic velocity and γ is the Lorentz factor. Assuming ΔQ=-0.25, $\epsilon = 6 \times 10^{-5}$ m.rad, $F = 1$, $B_f = 0.3$, $r_d = 7.7 \times 10^{-19}$ m, $\beta = 0.79$ and $\gamma = 1.64$, then

$$N = 1.0 \times 10^{14}\,.$$

This is well above the beam intensity of 7.9×10^{11} deuterons per ring requested for the production of negative muons, with $1 \times 10^{16}\,\mu^-$/s in this ring.

Beam injection is one of the issues in this scheme. It is favorable to have an injection scheme with continuous beam to avoid sacrificing beam duty factor. Continuous beam injection could be possible with a charge exchange injection scheme using a thin foil. In this case, however, the injected particle should not be a negative deuterium ion but rather a neutral deuterium atom. This is because the ring is fully occupied by a high pressure deuterium gas that would strip the electrons from negative ions. Neutral deuterium atoms can be stripped to deuterons with

relatively higher deuterium gas pressure. However, the beam injection area allocated to the stripping foil should be evacuated to 0.1 atm or less to avoid electron stripping before the foil. An efficient differential gas pumping system at the injection region is essential to prevent the injected neutral deuterium beam from gas stripping and scattering. Obviously, a more detailed design for the beam injection is definitely necessary including new ideas.

Summary

New schemes with energy recovery internal target (ERIT) have been proposed for efficient production of negative muons for various applications including reduction of long lived nuclear waste through muon nuclear transformations.

One of the schemes consists of the MERIT (Multiplex Energy Recovery Internal Target) ring with a hadron beam and wedge-shaped lithium target, which could accelerate and store beam in the ring. In this scheme, it is expected that a muon yield of $10^{16}\,\mu^-$/s can be achieved.

A second scheme is to use an ERIT ring with gas target filling the beam pipe, which could also produce a muon yield of $10^{16}\,\mu^-$/s with a 600 MeV/u and 10 mA deuteron beam with a 1 atm deuterium gas target. Both schemes seem to be feasible using a scaling type of FFA which could provide the large beam acceptance needed in transverse and longitudinal directions.

References

[1] Y. Mori *et al.*, "Intense Negative Muon Facility with MERIT ring for Nuclear Transmutation", JPS Conf. Proc. , 011063 (2018), https://doi.org/10.7566/JPSCP.21.011063.

[2] K. Niita, Y. Nara *et al.*, "Analysis of the Proton-Induced Reactions at 150MeV 24GeV by High Energy Nuclear Reaction Code JAM" (in Japanese), JAERI-Tech, vol.99-065 (1999).

[3] Y. Mori, "Development of FFAG Accelerators and Their Applications for Intense Secondary Particle Production", Nucl. Instr. Meth., PRS, Vol. A562, pp591-595 (2006).

[4] Y. Mori; "Secondary Particle Source with FFAG-ERIT Scheme", Proc. of. International Workshop on FFAG Accelerators (FFAG′05), KURRI, Osaka, p15-20(2005).

[5] Y. Mori *et al.*, "Neutron source with emittance recoevery internal target", Proc. of Particle Accelerator Conference(PAC09),Vancouver, pp.3145-3149 (2009).

[6] Y. Mori *et al.*, "Intense Muon Source with Energy Recovery Internal Target (ERIT) Ring Using Deuterium Gas Target", Memoir of the Faculty of Eng., Kyushu University, Vol.77, No.1, September 2017, http://kenkyo.eng.kyushu-u.ac.jp/memoirs-eng/bulletin.php.

[7] A.N. Skrinsky and V.V. Parkhomechuk; Sov. J. of Nucl. Phys.,vol 12, pp3 (1981).

[8] D. Neuffer, Particle Accelerator vol. 14, pp75 (1983).

[9] Y. Mori, "Muon Nuclear Transmutation Project", International Workshop on FFAG Accelerators (FFAG'16), Imperial College London, UK, Sept.12 (2016).

[10] Y. Mori, "Design and Beam Dynamics Issues of MERIT muon production ring", International Workshop on FFAG Accelerators (FFAG'16), Imperial College London, UK, Sept.12(2016).

[11] L.J. Laslett, "On Intensity Limitations Imposed by Transverse Space Charge Effects in Circular Particle Accelerators", BNL Report, vol.7534 (1963)

[12] T. Roberts, G4beamline User's Guide, ver.2.16 Dec. (2013).

[13] A. Baldini, V. Flaminio, W.G. Moorhead, D.R.O. Morrison, "Total Cross Sections for Reaction of High Energy Particles", Vol. 12a and Vol. 12b, Springer-Verlag Berlin 1988.

3.9 Harmonytron: Vertical FFA with HNJ Acceleration

Yoshiharu Mori, Institute for Integrated Radiation and Nuclear Science, Kyoto University, Japan.
Yujiro Yonemura, Hidehiko Arima and Nobuo Ikeda, Dept. of Engineering, Kyushu University, Japan.

Introduction

The past decade has seen a marked increase in demands for high intensity and high energy hadron accelerators. There is interest in generating intense beams of secondary particles such as pions, muons and neutrons, and several studies have been carried out to design a high intensity machine which is able to accelerate protons or deuterons to an energy of 500 MeV/u - 1 GeV/u and achieve these goals. Both linear and circular accelerators have reached beam powers (beam energy × averaged beam current) of about 1 MW. However, conventional ring accelerators such as cyclotrons and synchrotrons struggle to reach higher levels of 10 MW or more. Here, we propose the new idea of a fixed field, continuous wave (cw) accelerator using a technique known as harmonic number jump (HNJ) acceleration. The machine adopts the concept of a vertical scaling FFA to eliminate transition energy [1].

Fixed magnetic field ring accelerators such as cyclotrons or FFAs [2] have the capability for high intensity beam acceleration. In the cyclotron, however, it has been recognized that the beam bunch shape is deteriorated by space charge forces, and beam extraction becomes difficult, when the beam current exceeds 5 mA. In horizontal FFA accelerators, either scaling or non-scaling, cw operation with a fixed radio frequency (rf) field has difficulties in accelerating non-relativistic heavy particles such as protons. The revolution period is different on each turn for such particles, and synchronization can be maintained only by varying the rf frequency.

The idea behind harmonic number jump (HNJ) acceleration, first proposed by Ruggiero [3], is to, in effect, achieve synchronization for non-relativistic particles and yet have a constant rf frequency. It turns out that such a scheme can also be used for accelerating high energy (relativistic) muons in a scaling FFA [4, 5].

The condition for synchronization in a circular accelerator is

$$f_{\mathrm{rf}} = \frac{h_i}{T(E_i)}\,, \tag{1}$$

where $T(E_i)$ is the revolution period on the i^{th} turn, when the energy is E_i, and f_{rf} is the frequency of the rf field. h_i is an integer number called the harmonic number. Ruggiero [3] showed that it is possible to adhere to this condition in a non-isochronous ring with fixed rf frequency by changing the harmonic number h_i by an integer on each turn.

In general, however, the HNJ acceleration scheme meets some difficulties when accelerating heavy particles such as protons or deuterons over a wide range of medium (non-relativistic) energies. In ordinary strong (AG) focusing circular accelerators, problems can occur at transition energy, leading to beam loss caused by collective beam instabilities such as the negative mass instability. In HNJ acceleration, the sign of the harmonic number increment changes as transition energy is crossed; the harmonic number decreases below transition energy and increases above. However, if the concept of transition energy ceased to become relevant, HNJ acceleration could become an efficient method for accelerating high intensity proton and ion beams.

Transition energy could be inherently eliminated if the momentum compaction were zero. This is true of a linear accelerator but not in a normal circular machine. A vertical scaling FFA accelerator, despite being a ring accelerator, does however have this unique feature; its momentum compaction is zero because it has a constant orbit radius whatever the beam energy.

The idea of the vertical scaling FFA accelerator (vFFA) was originally proposed by Ohkawa in 1955 [6] and recently analyzed in detail by Brooks [7]. It has the unusual feature that the

beam moves vertically and its orbit radius is always constant during acceleration. Constant frequency rf acceleration then becomes possible for relativistic particles, e.g. electrons which may be why Ohkawa named such a machine an "electron cyclotron". Since the orbit radius is always constant, momentum compaction is zero and no transition energy exists. This makes the vFFA a suitable candidate for proton and ion beams using fixed-frequency HNJ acceleration. We have given this new type of machine the name "Harmonytron".

3.9.1 Vertical Scaling FFA for Harmonytron

In a vertical scaling FFA accelerator, the magnetic field strength changes exponentially in the vertical direction to preserve zero-chromatic beam optics with constant orbit radius. The field at $x = 0$ is given by

$$B_y(0) = B_0 \exp(my).$$

Here y is the vertical axis in (x-y) coordinates and the characteristic number, m, is expressed as

$$m = \frac{n}{\rho},$$

where ρ is the orbit curvature and n is the field index, defined by

$$n = \frac{\rho}{B_y} \frac{\mathrm{d}B_y}{\mathrm{d}y}.$$

B_x and B_y, derived from $\mathrm{div}\vec{B} = 0 = \mathrm{curl}\vec{B}$, are

$$B_x = -B_y(0)\sin(mx) \qquad B_y = B_y(0)\cos(mx). \tag{2}$$

The linearized particle motion in the transverse direction, which from eq. (2) is subject to a skew quadrupole magnetic field, can be described by betatron equations in skew coordinates. Since the beam orbit curvature, ρ, is constant whatever the particle momentum, n becomes constant and the betatron tunes stay constant, which complies with zero chromaticity.

The characteristic number m is related to the orbit displacement, y_d, between initial momentum, p_i, and final beam momentum, p_e, through $m = (1/y_d)\ln(p_e/p_i)$. If p_e/p_i equals 3 and y_d is less than 2 m, a value of m greater than $0.55\,\mathrm{m}^{-1}$ should be chosen. Table 1 shows typical machine parameters for a vertical scaling FFA accelerator aimed at accelerating protons from 50 MeV to 500 MeV. The stability of beam optics in the vertical scaling FFA is determined by m and the lattice configuration. Figure 1 shows the stability region in a FD doublet lattice when the number of cells is 16.

3.9.2 HNJ acceleration in vertical scaling FFA

From the synchronization condition of HNJ acceleration given by eq. (1), the required energy gain to jump the harmonic number by $\Delta_i h$ between turns i and $i+1$ can be written as [4]

$$E_{i+1} - E_i = \frac{\Delta_i h}{f_{\mathrm{rf}}\left(\dfrac{\partial T}{\partial E}\right)}. \tag{3}$$

T is the revolution time, piecewise linearized around the particle energy. In ordinary circular accelerators, the relative change in revolution period of a particle with momentum can be expressed via the slippage factor defined as,

$$\eta = \alpha_p - \frac{1}{\gamma^2}. \tag{4}$$

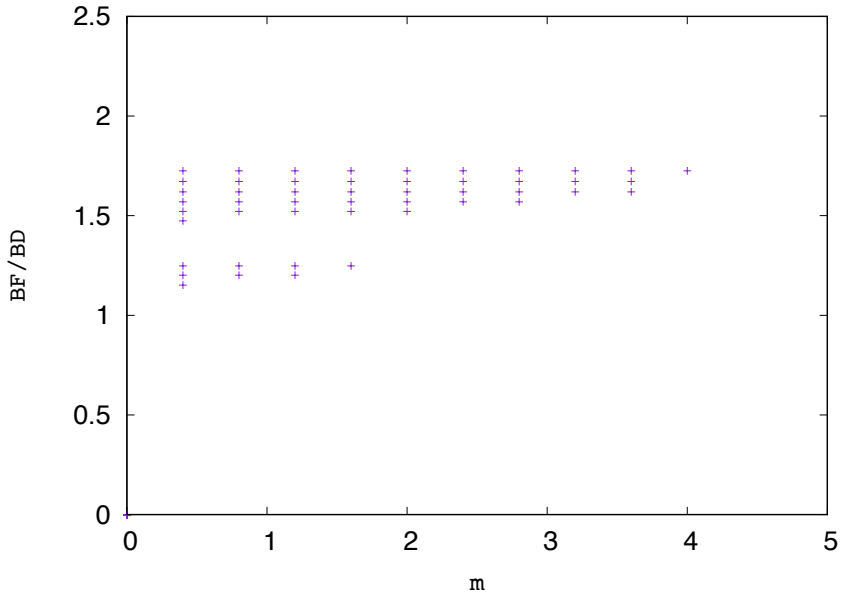

Figure 1: Stability region in FD doublet lattice presented in Table 1 when the number of cell is 16. Horizontal axis shows $m = n/|\rho|$ and vertical axis a ratio of magnetic field strength of F and D magnets, respectively.

α_p is the momentum compaction factor and γ is the Lorentz factor. When η=0 the particle is at transition energy, given by

$$\gamma_t = \frac{1}{\sqrt{\alpha_p}}\,.$$

Below transition energy, $\eta < 0$ and $\dfrac{\partial T}{\partial E} < 0$, so the harmonic number needs to decrease during acceleration. Above transition energy, in contrast, the harmonic number should increase. The rf phase synchronizing the particle's motion is normally less than π below transition energy and greater than π above transition to ensure stable beam acceleration. Therefore, a fast rf phase jump becomes essential when accelerating through γ_t. A horizontal scaling FFA, whose momentum compaction is positive, has difficulty avoiding transition in accelerating protons or ions across a wide energy range. On the other hand, in a vertical scaling FFA accelerator, the momentum compaction is always zero so the transition energy is infinite; effectively transition energy does not exist, the beam is always "below transition" and measures otherwise taken to avoid beam loss at transition crossing are unnecessary.

The term $\partial T/\partial E$ in eq. (3) is related to the slippage factor through

$$\frac{\partial T}{\partial E} = \frac{\eta\,\gamma^2\,C}{M_0 c(\gamma^2-1)^{\frac{3}{2}}},$$

where C is the circumference of the ring, c is the speed of light and M_0 is the rest energy (938.2 MeV for protons). Since the momentum compaction is zero in the Harmonytron FFA, eq. (3) can be expressed as,

$$E_{i+1} - E_i = -\frac{\Delta_i h\, M_0\,(\gamma_i^2-1)^{\frac{3}{2}}}{f_{\rm rf}}\,\frac{c}{C}. \tag{5}$$

As can be seen from this equation, since $f_{\rm rf}$ is constant, the required energy gain per turn is a proportional to $\Delta_i h$, which should be negative for acceleration. Figure 2 shows the energy gain

Table 1: Beam parameters of vertical scaling FFA for proton Harmonytron

Particle type	protons
Number of cells	16
Lattice	FD doublet
Initial harmonic number	80
Change of harmonic number/turn	1
Injection energy (MeV)	50
Extraction energy (MeV)	500
Circumference(m)	64
$m = n/\rho$: field index number (m^{-1})	1
rf frequency (MHz)	117.8
Maximum magnetic field(T):F	2.5
Orbit elevation (m)	1.23
Orbit separation at maximum energy(m)	0.11

per turn given by eq. (5) for the parameters shown in Table 1 and a change of harmonic number per turn $\Delta_i h = -1$. In this case, the harmonic number is 80 at the injection energy of 50 MeV and decreases to 47 at the maximum energy of 509 MeV, as shown in Fig. 3.

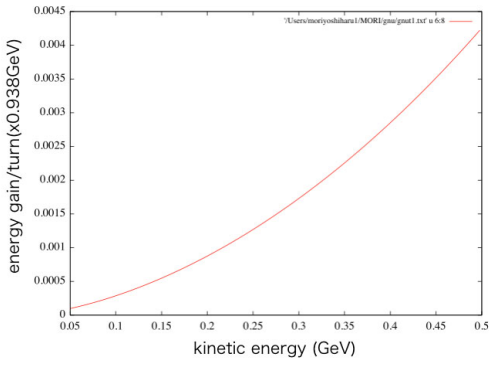

Figure 2: Energy gain per turn as a function of kinetic energy.

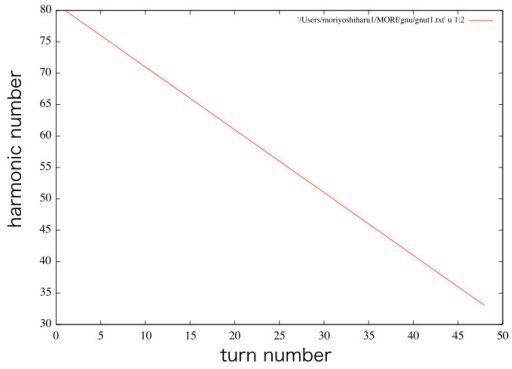

Figure 3: Harmonic number as a function of turn number.

Figure 2 shows that the energy gain required for each turn in HNJ acceleration increases largely according to the beam energy. Figure 3 shows the harmonic number change as a function of turn number. The energy gain per turn is given by the rf voltage V_i and phase Φ_i through

$$E_{i+1} - E_i = QeV_i \sin\Phi_i, \tag{6}$$

where Qe is the electric charge of the particles. Here, either V_i or Φ_i should be varied to give the required energy gain. The energy gain per turn as a function of turn number is shown in Figure 4.

Figure 5 shows the change of required rf voltage, V_i, as a function of the turn number when the stable phase Φ_i is constant at 60°. The change of stable phase, Φ_i, when the rf voltage is constant at $V_i = 50\,\mathrm{MV}$, is shown in Figure 6. The larger increases in energy come towards the end of beam acceleration so that the beam orbit turn separation may become largest on the final turn. This is a good feature for beam ejection, especially in cw operation, since special extraction devices may not be needed. As an example, if $m = 1.0\,\mathrm{m}^{-1}$ as in Table 1, the orbit separation at the final turn is about 11 cm, which should be large enough for beam extraction.

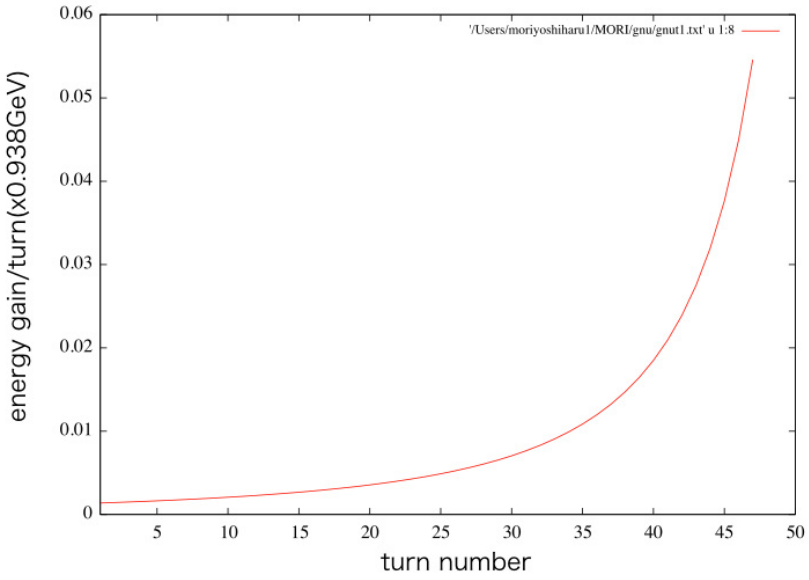

Figure 4: Energy gain per turn as a function of turn number.

As can be seen from Fig. 5 and Fig. 6, with HNJ acceleration, the rf voltage and/or phase have to be changed to satisfy the energy gain per turn shown in eq. (3). Some schemes to change the rf voltage or phase during acceleration were proposed by Ruggiero in his original paper [3]; however, there are practical difficulties in realizing them. Moreover, in HNJ acceleration for medium energy, heavy ions, the energy change per turn (Fig. 4) becomes so large that standard adiabatic conditions in longitudinal focusing (synchrotron oscillations) may not be well-enough satisfied to stay within the large longitudinal beam acceptance.

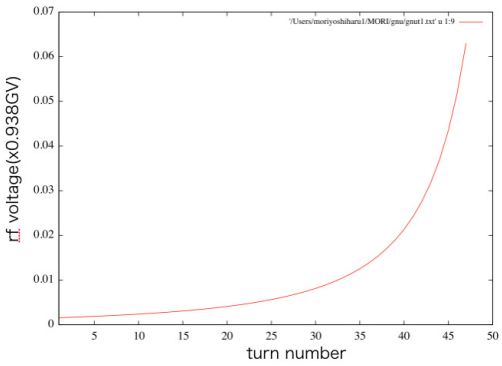

Figure 5: Required rf voltage as a function of turn number when the stable phase is 60°.

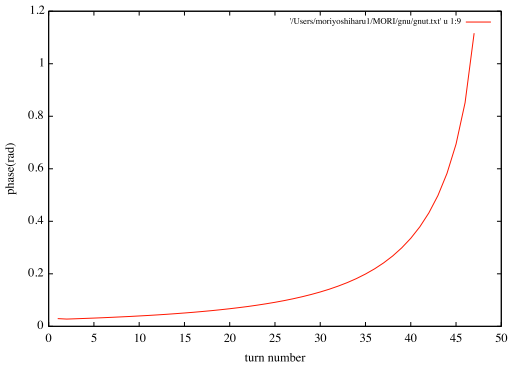

Figure 6: Stable rf phase as a function of turn number when the rf voltage is 50 MV.

Figure 7 shows the distribution of each turn around the ring in longitudinal phase space simulated by multi-particle beam tracking for different initial beam distributions. The beam parameters used in the tracking are also those shown in Table 1, with constant $\Phi_i = 60°$ and a single rf cavity located locally in the ring. The particle distribution in longitudinal phase space at injection is Gaussian in phase with zero energy spread. Examples of initial beam distributions were simulated with phase spreads of 0.02 rad and 0.1 rad. As can be clearly seen from this figure, although the HNJ acceleration works in principle, the beam acceptance longitudinally is very small. All of the particles are accelerated up to the final energy of 500 MeV when $\sigma = 0.02$ rad but a large fraction of particles are lost when $\sigma = 0.1$ rad. Unless these difficulties can be

overcome, HNJ acceleration may not be practical.

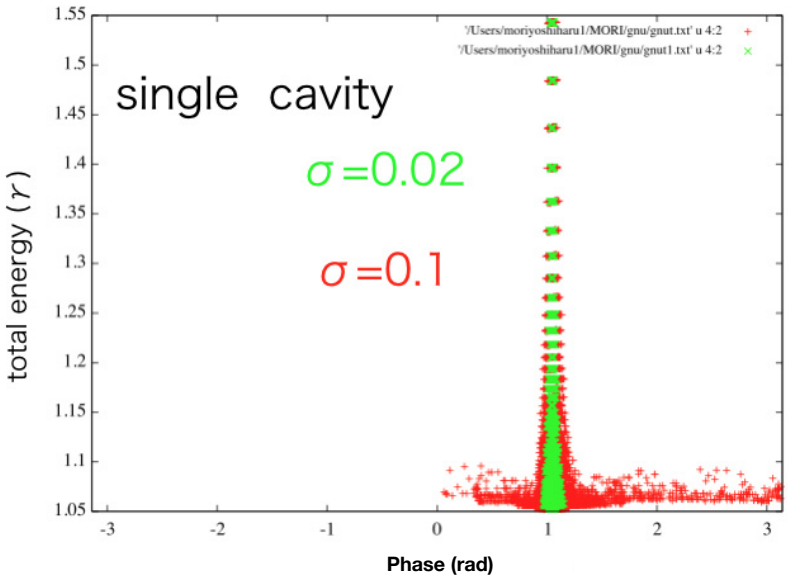

Figure 7: Particle distribution on each turn of the ring in longitudinal phase space simulated by multi-particle beam tracking for different initial beam distributions.

3.9.3 Adiabatic Condition in HNJ acceleration

It was mentioned above that the energy gain per turn in HNJ acceleration changes largely as a function of turn number as shown in Fig. 4. Thus, preserving the adiabatic condition of synchrotron oscillation during acceleration is important to keep a large phase space acceptance. The criterion for adiabaticity during rf acceleration can be expressed as [8, 9],

$$\left|\frac{1}{\Omega_s^2}\frac{\mathrm{d}\Omega_s}{\mathrm{d}t}\right| \ll 1, \qquad \text{or, equivalently} \qquad \Omega_s \gg \frac{1}{A}\left|\frac{\mathrm{d}A}{\mathrm{d}t}\right|, \tag{7}$$

where $\Omega_s/2\pi$ is the synchrotron frequency and A is the bucket area. When this condition is satisfied, the particles are well trapped by the rf bucket and properly accelerated. The condition (7) can be evaluated with the adiabatic parameter η_{ad} given by the following equation when the rf phase is constant ($\Phi_i = \Phi_s$) [9, 10].

$$\eta_{\mathrm{ad}} = \frac{\Omega_s T_{\mathrm{r}}}{1 - \sqrt{V_i/V_i + \Delta V)}}. \tag{8}$$

Here, V_i is the total rf voltage on the i^{th} turn and ΔV is the increment of rf voltage on the rf cavity after that turn, T_{r} is a transit time at the rf cavity gap. The synchrotron frequency is given by,

$$\Omega_s = \omega\sqrt{\frac{h\eta\cos\Phi_s}{2\pi\beta^2\gamma}\frac{eV}{m_0c^2}\frac{Q}{A}},$$

where $\omega/2\pi$ is the revolution frequency, Φ_s is the synchronous phase, m_0 is the rest mass of a particle, V is the rf voltage of a cavity and Q/A is the charge to mass ratio. The parameter n_{ad} is a measure of the adiabaticity of the system, showing how slow is the change in bucket height with respect to the synchrotron frequency. When $n_{ad} \gg 1$, the system can be considered to

be adiabatic. In the present case given by the parameters of Table 1, the adiabatic parameter becomes $n_{\mathrm{ad}} \approx 2$, so that adiabaticity may not be perfectly fulfilled. Thus, the longitudinal acceptance becomes relatively small, as described above.

This problem could be overcome by distributing several rf cavities around the ring and tuning the frequency of each rf cavity [4, 5]. If the rf system consists of N rf-cavities, the adiabatic parameter shown in eq. (8) becomes approximately N times larger than for a single rf cavity. The rf frequency of each rf cavity can be derived from the following equation:

$$f_{i,j} = f_{\mathrm{ref}} \cdot \left[1 + \frac{2j + N + 1}{2N} \frac{\Delta_i h}{h_i}\right]^{-1}.$$

Here i is the turn number, j is the cavity number and f_{ref} is a reference rf frequency. As long as h_i is much larger than its variation $\Delta_i h$, h_0 is also much larger than $\Delta_i h$. The frequency of each cavity is independent of the turn number, and is approximately given by

$$f_{i,j} \approx f_{\mathrm{ref}}\left[1 - \frac{\Delta_i h}{h_0}\left(\frac{2j+1}{2N} + \frac{1}{2}\right)\right].$$

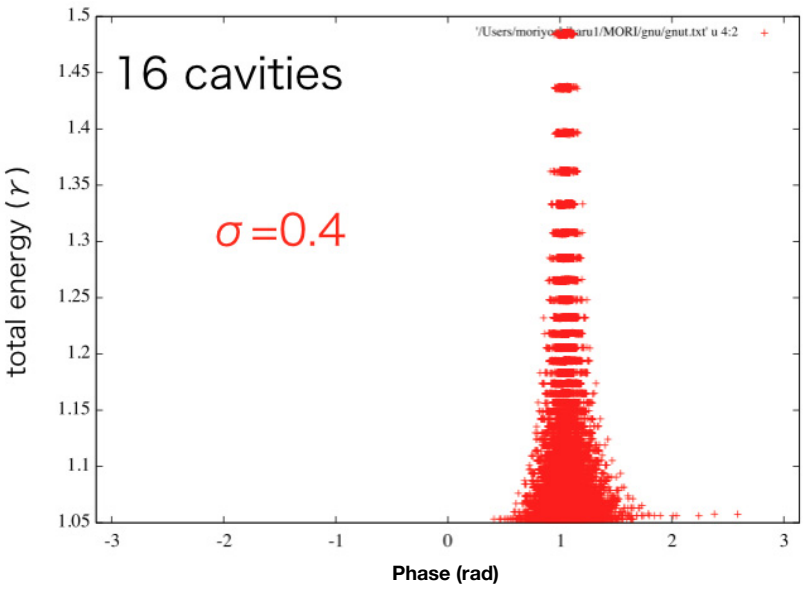

Figure 8: Result of longitudinal beam tracking when 16 rf cavities (instead of a single rf cavity) are distributed homogeneously around the ring, parameters as in Table 1.

From this, the rf frequency of each cavity also increases monotonically as a function of the cavity number when $\Delta_i h$ is negative. Moreover, if $h_0 \gg \Delta_i h$, then $f_i \sim f_{\mathrm{ref}}$.

Figure 8 shows the result of longitudinal beam tracking when $N = 16$ rf cavities are distributed homogeneously around the ring using parameters from Table 1. As can be seen clearly from this figure, all of the particles are captured and accelerated up to the maximum energy even if the rms phase spread of the initial particle distribution is 0.4 rad, which is 20 times larger than is possible when a single rf cavity is placed locally in the ring. Thus, the adiabatic condition on the longitudinal beam motion provides useful guidance on the rf cavity requirements to obtain a large longitudinal acceptance in HNJ acceleration.

Preserving longitudinal adiabaticity introduces another important and valuable feature in HNJ acceleration. The rf voltage and/or phase should vary for each turn in accordance with eq. (3), but practically, it is difficult to change the rf voltage or phase of the rf cavity during beam

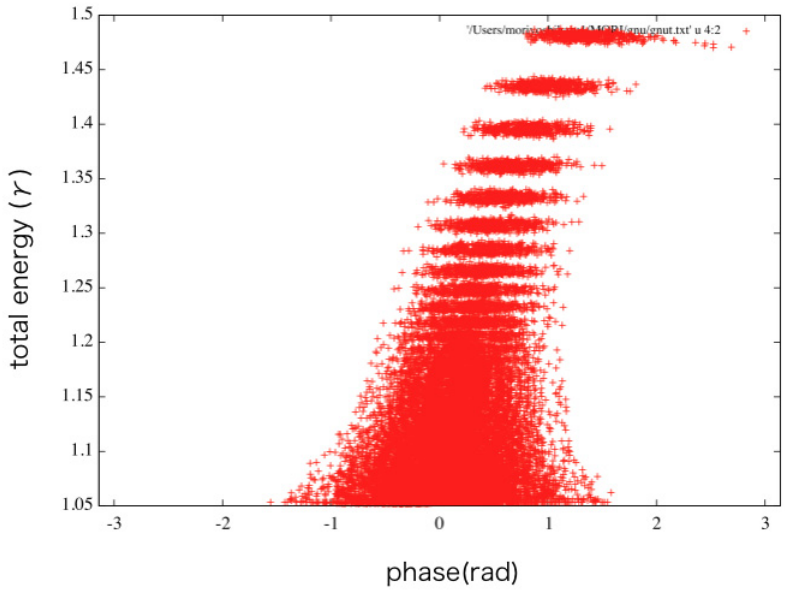

Figure 9: The beam tracking simulation results for longitudinal beam motion with an initial phase spread of $\sigma = 1\,\mathrm{rad}$.

acceleration Normally, the response time for varying voltage or phase in a high-quality factor rf cavity is relatively slow compared with the acceleration ramping time. Even if it is realized with low-quality factor rf cavites, only pulsed, but not cw, beam operation is possible, which sacrifices operational beam duty factor and reduces the average beam current. However, if the longitudinal adiabatic condition of eq. (7) can be satisfied with multiple rf cavities distributed around the ring, this problem could be overcome. When the rf voltage is constant, the rf phase in HNJ acceleration can be varied during beam acceleration. If the longitudinal adiabatic condition is satisfied during acceleration, the particles will be well captured by the rf bucket and accelerated around the stable phase.

Beam tracking simulations showing results for longitudinal beam motion for different initial beam phase spreads are presented in Fig. 9. In this case, the number of rf cavities homogeneously distributed around the ring is 32, each with rf voltage 1.41 MV, held constant during the beam acceleration.

As Fig. 9 shows, the particles are well captured and accelerated up to the maximum energy following the rf stable phase, and the phase acceptance at beam injection is quite large, at more than 70% of 2π. This means that an adiabatic beam capture process can be achieved in an HNJ acceleration scheme using many rf cavities with a small rf voltage, distributed uniformly around the ring. Figure 10 shows beam tracking simulation results for the longitudinal motion ffor the first three turns from an initial phase spread of $\sigma = 2\,\mathrm{rad}$. The particles are captured adiabatically and well accelerated in a bucket using harmonic number jumps.

Summary

In this paper, the vertical scaling FFA accelerator with a harmonic number jump acceleration (HNJ) scheme, named “Harmonytron”, is proposed for medium energy, heavy particle acceleration in cw operation mode.

Harmonytron has several unique features: a wide range of beam energies becomes possible with a monotonic change of harmonic number in HNJ acceleration since no transition energy exists in the ring, and a large longitudinal acceptance with adiabatic beam capture and acceleration can be realized by distributing many rf cavities homogeneously around the ring.

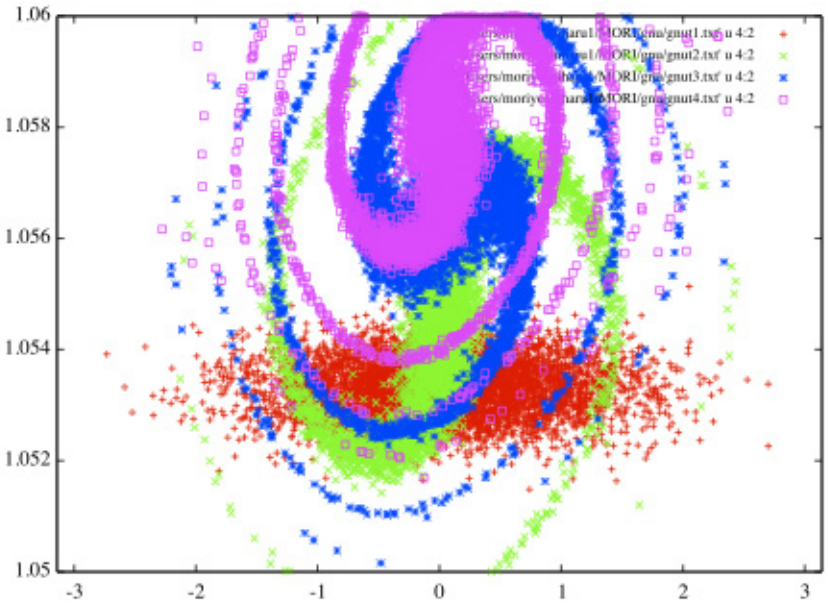

Figure 10: . The beam tracking simulation results for the longitudinal beam motions from 0 to 3 turns. (red: 0^{th} turn, green: 1^{st} turn, blue: 2^{nd} turn, magenta: 3^{rd} turn)

By keeping enough adiabaticity in the longitudinal motion for beam capture and acceleration by distributing many rf cavities around the ring, HNJ acceleration with a constant rf voltage becomes possible, so that cw operation with large longitudinal acceptance can be realized. This is a breakthrough for HNJ acceleration since it had been thought that either rf voltage or phase should be changed to match the energy gain criterion of integer harmonic number jump during acceleration. Moreover, the beam orbit displacement (turn separation) at the maximum energy is fairly large which could make beam extraction easy for cw beam operation.

Harmonytron is a unique accelerator to realize cw operation and potentially high intensity beam acceleration for non-relativistic heavy particles.

References

[1] Y. Mori, Y. Yonemura and H. Arima, "A Proposal of Harmonictron", Memoirs of the Faculty of Engineering, Kyushu University, Vol.77, No.2, December 2017, `http://kenkyo.eng.kyushu-u.ac.jp/memoirs-eng/bulletin.php`.

[2] Y. Mori, "Advancement of the scaling FFAG accelerators for ADSR, pulsed-SNS and muon acceleration", Int. J. Mod. Phys., Vol.A26, pp.1744-1752 (2011).

[3] A.G. Ruggiero, "rf acceleration with harmonic number jump", Phys. Rev. ST Accel. Beams, Vol. 9, 100101 (2006).

[4] T. Planche *et al.*, "Harmonic number jump acceleration of muon beams in zero-chromatic FFAG rings", Nucl. Instr. Meth. Vol.A632, pp.7-17 (2011).

[5] J.S. Berg, "Harmonic number jump in a ring with cavities distributed everywhere", Proc. 2006 International Workshop on FFAG Accelerators, pp.69-76 (2007).

[6] T. Ohkawa, "FFAG electron cyclotron", Phys. Rev., 100, p.1247 (1955).

[7] S. Brooks, "Vertical orbit excursion fixed field alternating gradient accelerators", Phys. Rev. ST Accel. Beams, Vol.16, 084001 (2013).

[8] B.W. Montague, "RF Acceleration", CERN 77-13, pp.63-81 (1977).

[9] K.Y. Ng, "Adiabatic capture and debunching", FNAL Report, FERMILAB-FN-0943-APC (2012).

[10] C.G. Lilliequist and K.R. Symon, "Deviations from adiabatic behavior during capture of particles into an rf bucket", MURA-491 (1959).

3.10 A Single Fixed Field Alternating Linear Gradient Return Line for Multi Pass Energy Recovery Linac for EIC[1]

Dejan Trbojevic, J. Scott Berg, Stephen Brooks, François Méot, Nicholaos Tsoupas
Brookhaven National Laboratory, Upton, NY, USA
William Lou, Cornell University (CLASSE), Ithaca, NY, USA

Abstract

The Fixed Field Alternating Linear Gradient (FFA-LG) concept is implemented as a single return beam line in the Energy Recovery Linac (ERL) for future projects like: PERLE (Powerful Energy Recovery Linac for Experiments), LHeC/FCCeH and eRHIC. The superconducting linacs use the single return beam line for the multiple energy passes of electron beams. This represents an update to the existing Cornell University Brookhaven National Laboratory ERL Test Accelerator-CBETA where the superconducting linac uses a single fixed field magnet beam line with four energy passes during acceleration and four passes during the energy recovery. To match the single fixed field beam line to the linac the CBETA uses the spreaders and combiners on both sides of the linac, while this new concept eliminates them. The arc cells from the single FFA beam line are connected to the linac with adiabatic transition arcs where cells increase in length. The orbits of different energies merge into a single orbit through the interleaved linac within the straight sections as in the CBETA project. The betatron functions from the arcs are matched to the linac. The time of flight of different electron energies is corrected for the central orbits by additional correction magnet controlled induced beam oscillations.

Acknowledgement

Parts of this article first appeared in the Proceedings of ICAP'18 and are reproduced here with the kind permission of JACoW under copyright licence CC-BY 3.0.

Introduction

The ERLs and Recirculating Linacs (RAL) are considered to be a part of the future Electron Ion Colliders in several world programs: LHeC (CERN) [1], FCC eh [2], eRHIC(BNL) [3], ELIC (Jefferson Lab) [4] and EIC@HIAF (China) [5]. A new FFA-LG describes a solution of ERL where the electron beam is brought back to the linac with a single large energy acceptance beam line using a concept of linear fixed field alternating (FFA) gradient. The concept of the FFA beam transport with large momentum acceptance is not a novelty. There are three experimentally confirmed proof-of-principles: EMMA-Electron Model for Many Applications [6], ATF (Accelerator Test Facility) [7] experiment with 12 FFA cells, and Fractional Arc Test of the Cornell University-Brookhaven National Laboratory ERL Test Accelerator-CBETA [8]. A comparison of these three examples are compiled and shown by Stephen Brooks [9] in Fig. 1 and in Table 1.

We present a new concept of the ERLs where the large momentum acceptance linear FFA magnet beam lines bring the electron beam back to the superconducting linac without spreaders and combiners. In multiple passes through the ERLs the acceleration of electrons generated by the linac is too fast to consider any return beam line by using fast cycling magnets. With the large momentum acceptance linear FFA gradient magnets this can be achieved. The first test of the concept will be achieved in 2019 by the ERL CBETA at Cornell University. There

[1]Work performed under Contract Number DE-AC02-98CH10886

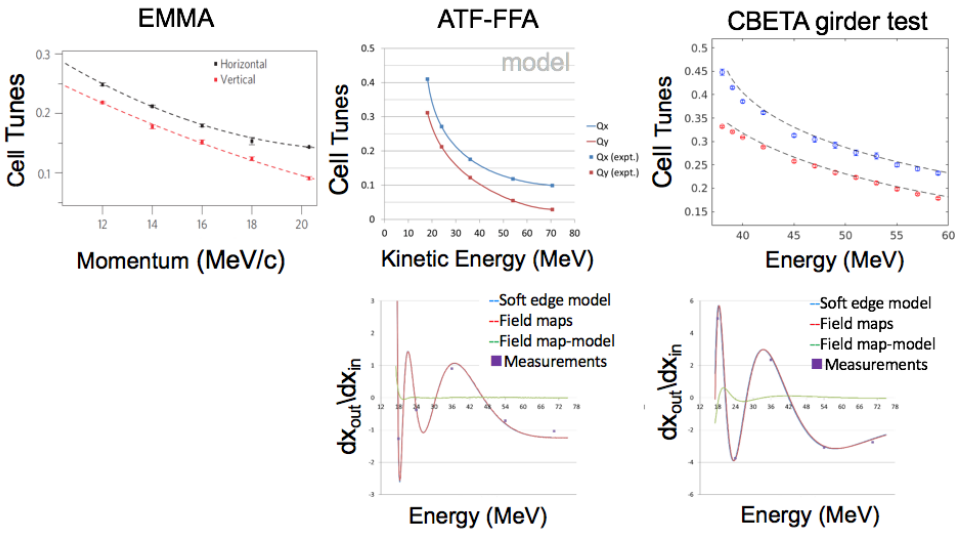

Figure 1: Comparisons on tune dependence on Energy in the three FFA examples.

are many advantages and simplifications: 1) the replacement of multiple returning beam lines with a single beam line reduces the cost and complications; 2) established technology of the Halbach type permanent magnets used at CBETA project will confirm the reduction of cost and simplification of the beam lines; the magnet aperture remains to be very small while transporting multiple energy beams. In the present study the superconducting linac is made of 5-6 cavity cells, each separated with small permanent FFA triplets. The same type of triplet cells continues towards the FFA arc but with an adiabatic reduction of the cell lengths. The betatron and dispersion functions for each energy are adiabatically matched to the corresponding functions of the arc FFA cells.

Recently the National Academy of Sciences released a study entitled "An Assessment of U.S. Based Electron Ion-Collider Science" in which it states:

> ... The principal goals of the study were to evaluate the significance of the science that would be enabled by the construction of an EIC, its benefits to U.S. leadership in nuclear physics, and the benefits to other fields of science of a U.S.-based EIC.

Table 1: EMMA-ATF-CBETA Comparisons

Parameter	**EMMA**	**ATF-FFA**	**CBETA girder**	**CBETA Future**
Energy (MeV)	10–20	18–71	37.5–59	41–150
Mom. ratio	1.953	3.837	1.553	3.572
ρ of curv. (m)	2.637	2.014	5.0879	5.0879
Avrg. dip. (T)	0.026	0.118	0.0983	0.0983
Total angle (°)	360.0	40.0	20.0	280.0
Oper. mode	ring	Tr. line	Tr. Line	ERL
Acceleration?	YES	none	none	linac
Lattice	Doublet	~FODO	Doublet	Doublet
Cell Length (m)	0.395	0.234	0.444	0.444
Cell per turn	42	54	72	107.5
Length (m)	16.57	1.406	1.776	47.73

> ... Several presentations to the committee specifically addressed the challenges and **necessary innovations** in accelerator science needed for constructing an EIC capable of addressing the most important science questions ... To reach the performance goals of the proposed EIC conceptual designs, a number of accelerator advances are required. Several of these advances are common to all EIC designs and include the following: advanced magnet designs, strong hadron beam cooling, **high current multi turn ERL technology**, crab cavity operation with hadron beams, the generation of polarized 3He beams, and development and benchmarking of simulation tools. The successful implementation of an EIC requires the successful validation of these key concepts through high-fidelity simulations and demonstration experiments. The following subsections review these enabling technologies, the present state of the art, and required research and development to meet EIC facility specifications and realize EIC science: **Energy Recovery Linacs**. ... The ERLs required for electron cooling are at scales much larger than supported by present-day experience, so a number of accelerator physics and technology challenges still need to be overcome with focused R&D and great attention to detailed simulations. The challenges center around the following three major areas: 1. Achieving high electron source brightness 2. Maintaining high beam brightness through the accelerator transport-beam dynamics of an unprecedented number of spatially superposed bunches in the SRF linacs; very precise phase and amplitude control 3. Dealing with unprecedented beam currents in SRF linacs (halo mitigation, beam breakup instabilities, higher order mode dissipation). Many of these R&D issues are being investigated vigorously in dedicated test facilities under construction and commissioning in laboratories around the world. Specifically, the 4-pass Fixed Field Alternating Gradient R&D loop for eRHIC, see **CBETA and Fixed Field Alternating Gradient Optics** for Electron Acceleration, could illuminate key issues including multi-turn beam-breakup instability thresholds for proof of possible cavity designs, halo and mitigation, beam-ion effects, and operational challenges such as instrumentation and stability of multi-turn beams.

The suggestions contained in the National Academy of Sciences report emphasize the importance of the CBETA project and further developments towards improvements of the concept.

The study presented here is divided into six sections: the first section describes the arc cell design to allow transport of multiple energy electrons; the second section describes a design of the long straight section to be used for the placement of the linac superconductiong cavities. Acceleration of electrons through the linac requires use of the "normalized betatron functions" as the momentum changes along the length of the linac. To make the matching conditions on both sides of the linac the triplet quadrupoles strength along the linac needs to be adjusted accordingly. The adiabatic transition from the arc FFA cells towards the linac is explained in the next section. Overall solution with orbits, betatron functions, dispersion function is shown in the fourth section. The time of flight adjustment is described in the fifth section while the summary and conclusions are shown in the sixth section.

3.10.1 Linear Fixed Field Alternating (FFA) gradient arcs

The principle of the linear FFA gradient acceleration has been previously described in details [10] and [11]. The main idea of the principle is to keep the value of the dispersion function $\Delta x = D_x \cdot \delta p/p$ as low as possible or to have a control of the *dispersion action* $\mathcal{H} = (D_x/\sqrt{\beta})^2 + (D'_x\sqrt{\beta} + \alpha D_x/\sqrt{\beta})^2$. The accelerator physics program '`Bmad`' [12] is used throughout this study. The main arc FFA cell design is shown in Fig. 2. Figure 3 shows a few arc cells with betatron functions and orbits.

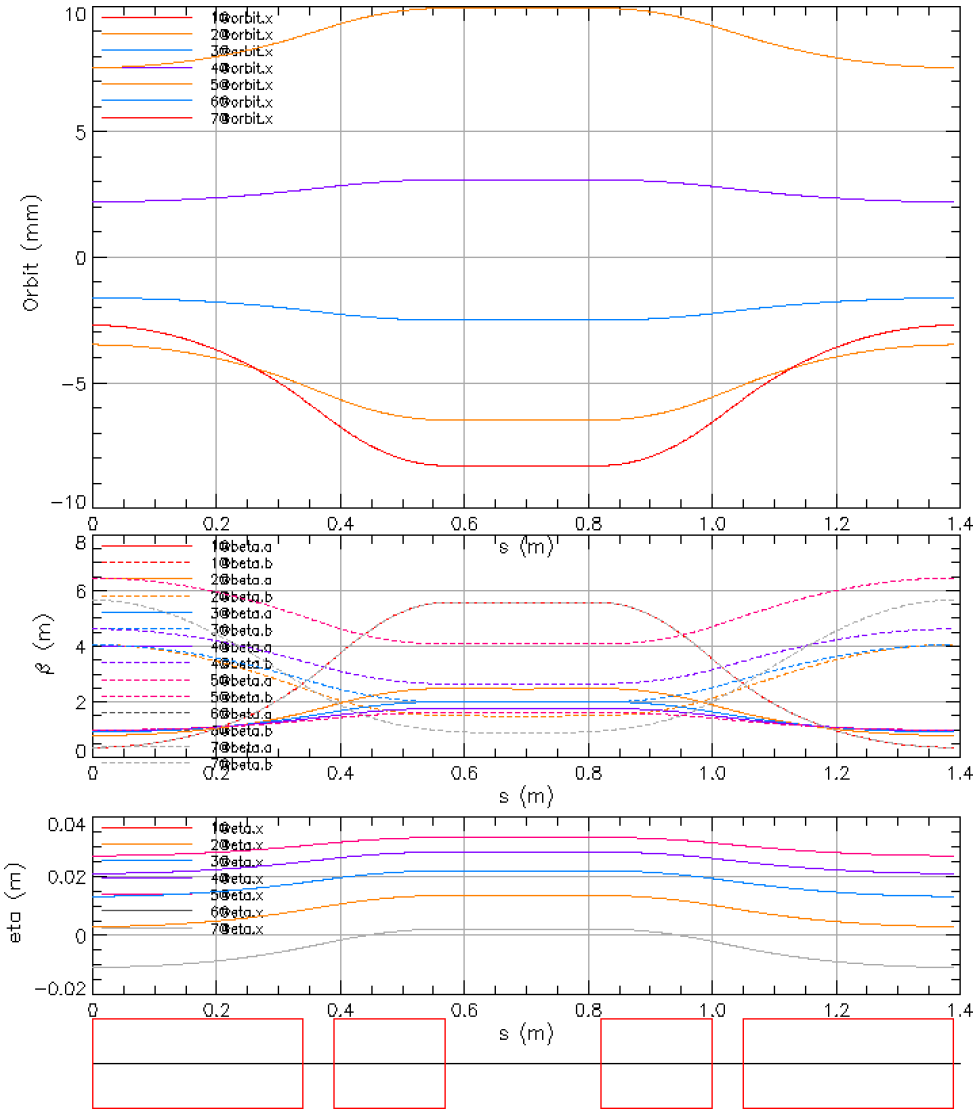

Figure 2: Lattice functions and orbits in the linear FFA arc cell.

3.10.2 Straight section

The linear FFA racetrack design has two straight sections on opposites sides connected to the two arcs with the adiabatic transitions. A problem of the RF straight section is solved in two steps: First, the straight section is designed with 42 cells made of the triplet quadrupoles and drifts without RF cavities matched to the FFA gradient arcs with adiabatic transitions. The second step was done by retuning the 42 triplets with the 1.7 m superconducting 5 cell cavities placed with 3.2-meter long cells, making the total length of each straight section equal to 134.2 m. The accelerator physics code `Bmad` has two ways to present the acceleration through the linac: `lcavity` and `rfcavity` where the `lcavity` represents the accelerating cavity without constant reference energy, while the `rfcavity` is the storage ring cavity with constant reference energy without acceleration. The transverse trajectory in `Bmad` through an `lcavity` is modeled using equations developed by Rosenzweig and Serafini [13] modified to give the correct phase-space area at non ultra-relativistic energies. First step in the the ERL design is to create the straight section with long enough drifts between the triplet quadrupoles to allow placement of the superconducting RF 5 cell modules. The lattice functions of the straight section cell are shown in Fig. 4. The adiabatic transition from the arc FFA cell to the straight section is shown

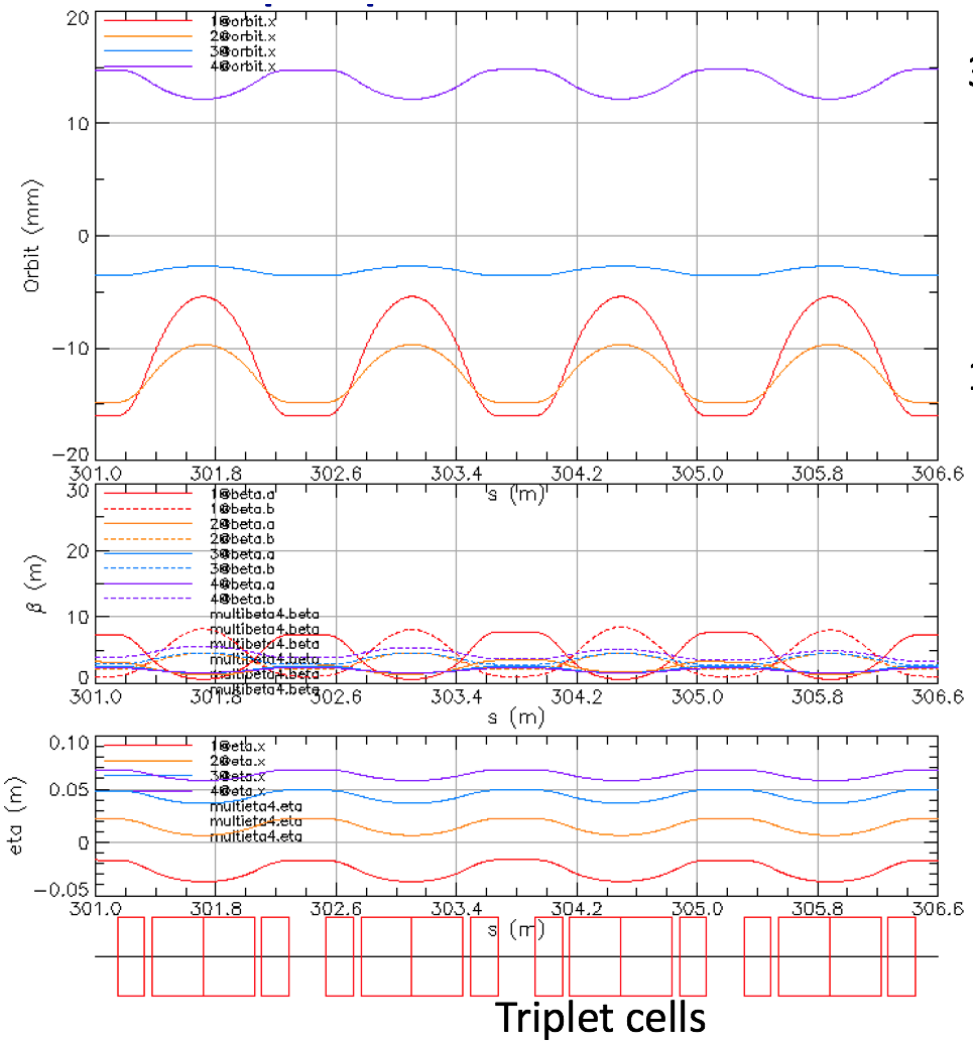

Figure 3: Lattice functions and orbits in a few basic linear FFA arc cells.

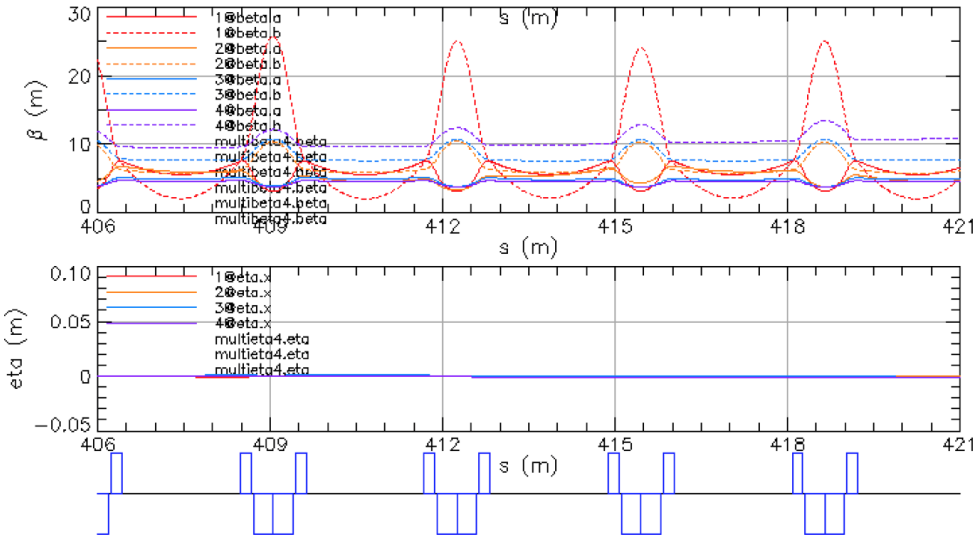

Figure 4: Lattice functions and orbits in the straight section cells.

in details in the next section. The second step in the straight section design is to introduce the 1.7 m long cavity modules of in the available 2.1 m long drift space. The 42 triplet quadrupoles are the variables with constraints related to the six different energies: the first energy is the lowest energy from the injector getting into the straight section. All other betatron function of initial and end values of the linac are already obtained in the results from the step one described above. The triplet quadrupole matching for the six energies, or in the `Bmad` program corresponding six "universes", is possible as there are 12 constraints on both sides of the linac of the $\beta_x, \beta_y, \alpha_x$, and α_y with 42×3 variables of the triplet gradients.

3.10.3 Adiabatic transition

A transition from the linear FFA arc cells to the straight section requires that electron orbits of all energies merge into a single obit without any orbit offsets. In addition the lattice and dispersion functions are matched on both sides. This is accomplished with adiabatic reduction of dipole field down to zero. The combined function magnet properties remain the same but the bending magnetic field is being adiabatically reduced to zero. A problem of merging all arc orbits into a single straight section orbit with the lattice functions was solved previously in the former electron ion collider eRHIC design. The adiabatic function was a polynomial of the third order. The CBETA project follows S. Berg's optimized adiabatic dependence [14] as shown in Eq. (1):

$$f_T(x) = \frac{1}{2} + \left(x - \frac{1}{2}\right) = \sum_{k=0} a_k \binom{2k}{k} x^k (1-x)^k. \tag{1}$$

The adiabatic transition in this design is different as the length of the cells is adiabatiacally increased from the 1.3889 m FFA arc value to the 3.2 m. Details of the adiabatic transition are shown in Fig. 5. The superconducting cavity placement in the straight section is shown in Fig. 6.

3.10.4 Racetrack ERL with linear FFA

The complete layout of the ERL racetrack with the betatron functions in shown in Fig. 7.

The orbit merging in the racetrack from the arc cells through the adiabatic transition cells is shown in Fig. 8.

3.10.5 Time of flight correction

Th most important parameter of the ERL is the electron bunch arrival to the linac as the acceleration is at the top of the sinusoidal RF function. The energy recovery requires a change of the RF phase so the bunches arrive at the bottom of the sinusoidal RF function. This phase flip occurs after the collisions. The electrons are extracted form the adiabatic transition part brought to the collisions with a separate beam line to ions and brought back by the separate beam line with an 0.5 phase difference at the highest energy. The FFA gradient arcs have a parabolic function with respect to the time of flight. The lowest energy has the same value of the time of flight as the highest energy while the medium energies correspond to the minimum of the parabolic function. The orbits in the FFA arc cells oscillate around the middle "central" energy as shown in Fig. 3. The main idea of the time of flight correction is that the central orbit can become longer if additional oscillations are introduced to the mostly circular orbit. This was first tested by using two correction dipoles with opposite kicks. This produced the same time of flight after the first attempt. A more sophisticated method of time of flight correction was developed by Stephen Brooks. The main idea is to use the dependence of FFA arc cell tunes with respect to energy and choose correctors at positions where the betatron phases are equal

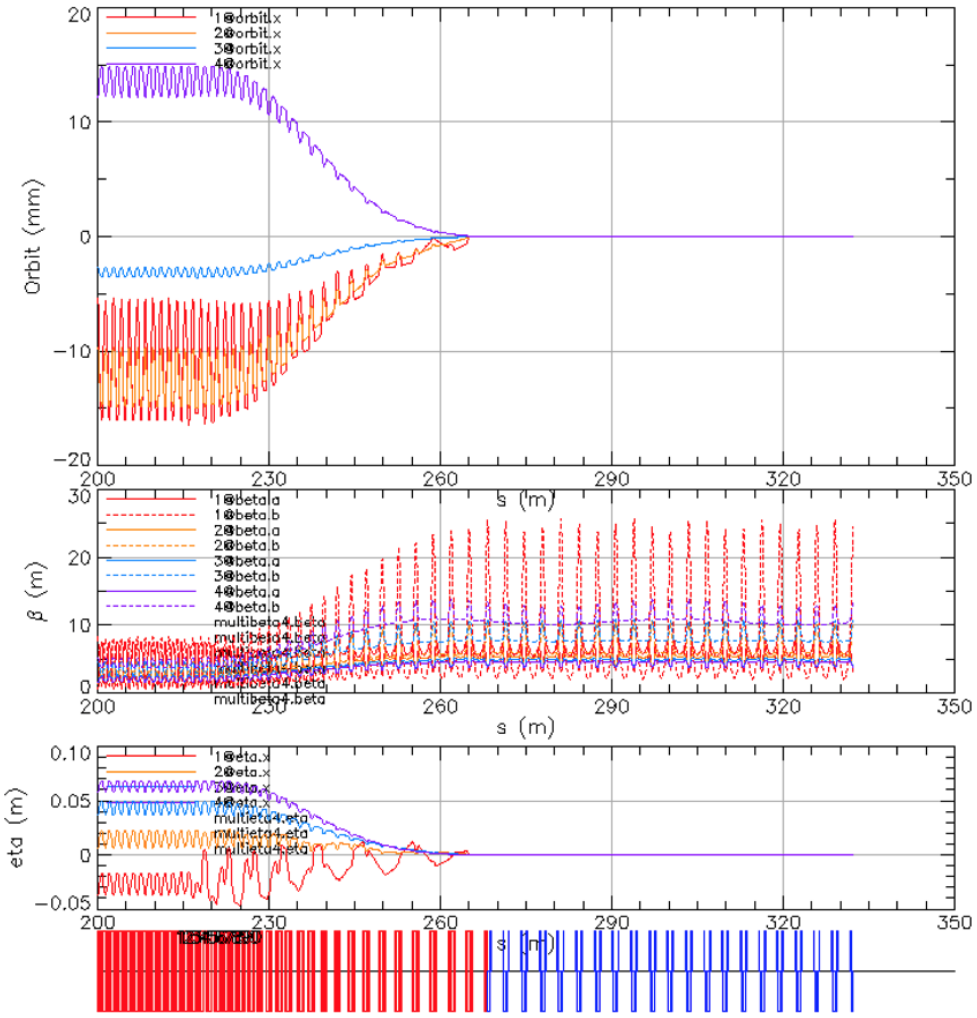

Figure 5: Lattice functions and orbits in the adiabatic transition and straight section cells.

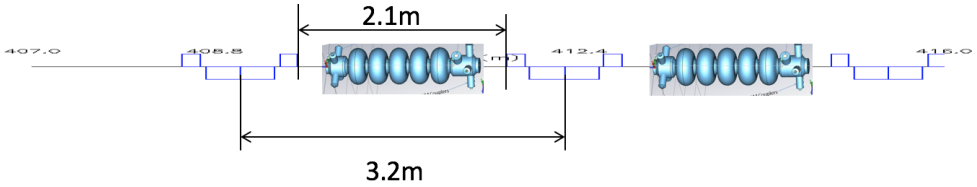

Figure 6: The superconductivity RF modules placement in the straight section.

to zero and make additional oscillation to the orbits. The results of the path length corrections are shown in Fig. 9.

Conclusion

We have shown an example of ERL with the multi-turn single beam line returning the beam to the linac. The arc FFA gradient cells are made of triplet combined function magnets with a 1.3889 m long cells. The arc FFA gradient cells are matched to the straight sections with adiabatic transition cells where the length of the cells is increasing gradually up to 3.2 m, according to the to the function shown in Eq. (1). The matching was done in two steps: the first step is to match the straight section cells made of triplet magnets separated by the drifts. The second step in matching is to introduce in one of the straight sections 1.7 m long superconducting RF

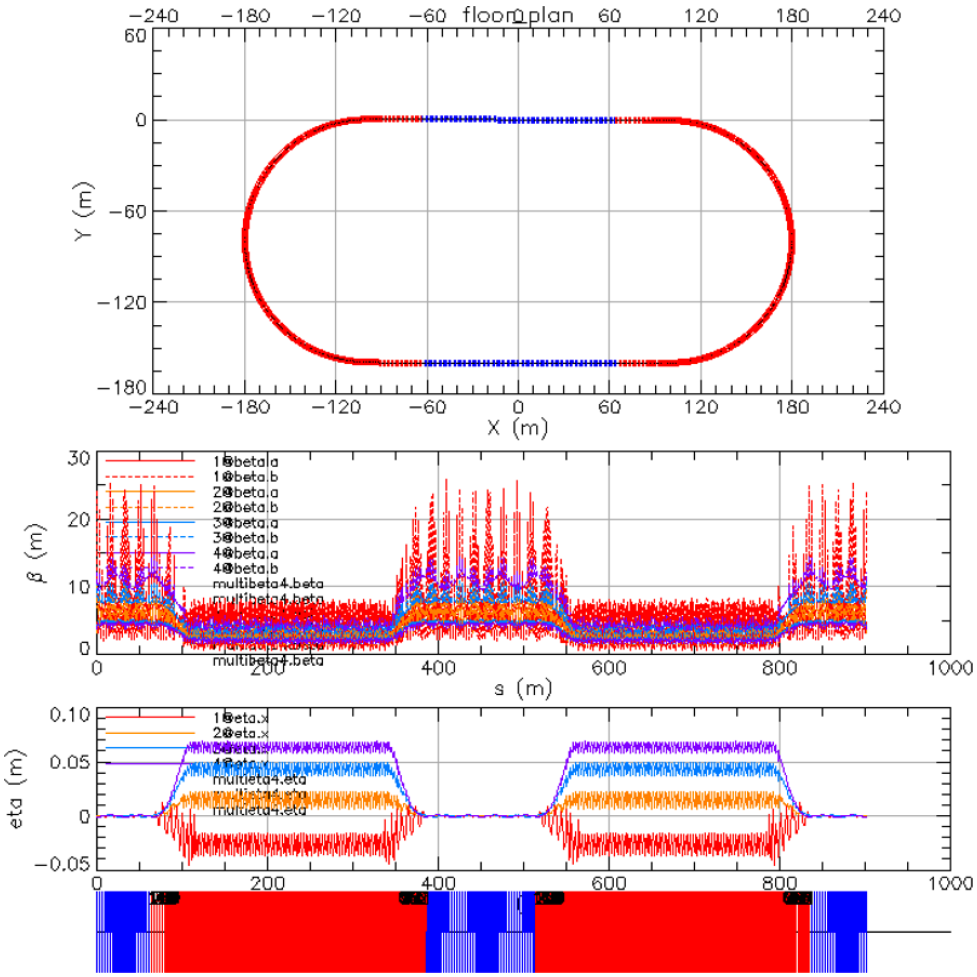

Figure 7: Lattice functions and orbits in the basic straight section cell.

modules and then redo the matching of the betatron functions. The beginning and end of the straight section corresponds to the two values of energy where after each pass energy steps are equal to 1.25 GeV. The initial conditions fou previously correspond to specific energy. There are many advantages of this proposal especially for the future Electron Ion Colliders: the previous splitter and combiner beam lines used to match the linac without any quadrupoles where necessary to to the time of flight correction and betatron function matching. They are eliminated by introduction of the triplet magnets between the RF superconducting modules.

References

[1] LHeC Study Group, J.L. Abelleira Fernandez *et al.* "A Large Hadron Electron Collider at CERN", *Journal of Physics G: Nuclear and Particle Physics*, vol. 39, no. 7, July 2012, pp. 075001. doi:10.1088/0954-3899/39/7/075001

[2] FCC eh: http://lhec.web.cern.ch

[3] eRHIC Design Study, "An Electron Ion Collider at BNL", arXiv:1409.1633, 2014.

[4] ELIC: https://casa.jlab.org/overview.shtml

[5] EIC@HIAF, http://snst-hu.lzu.edu.cn/wiki/index.php/Eic

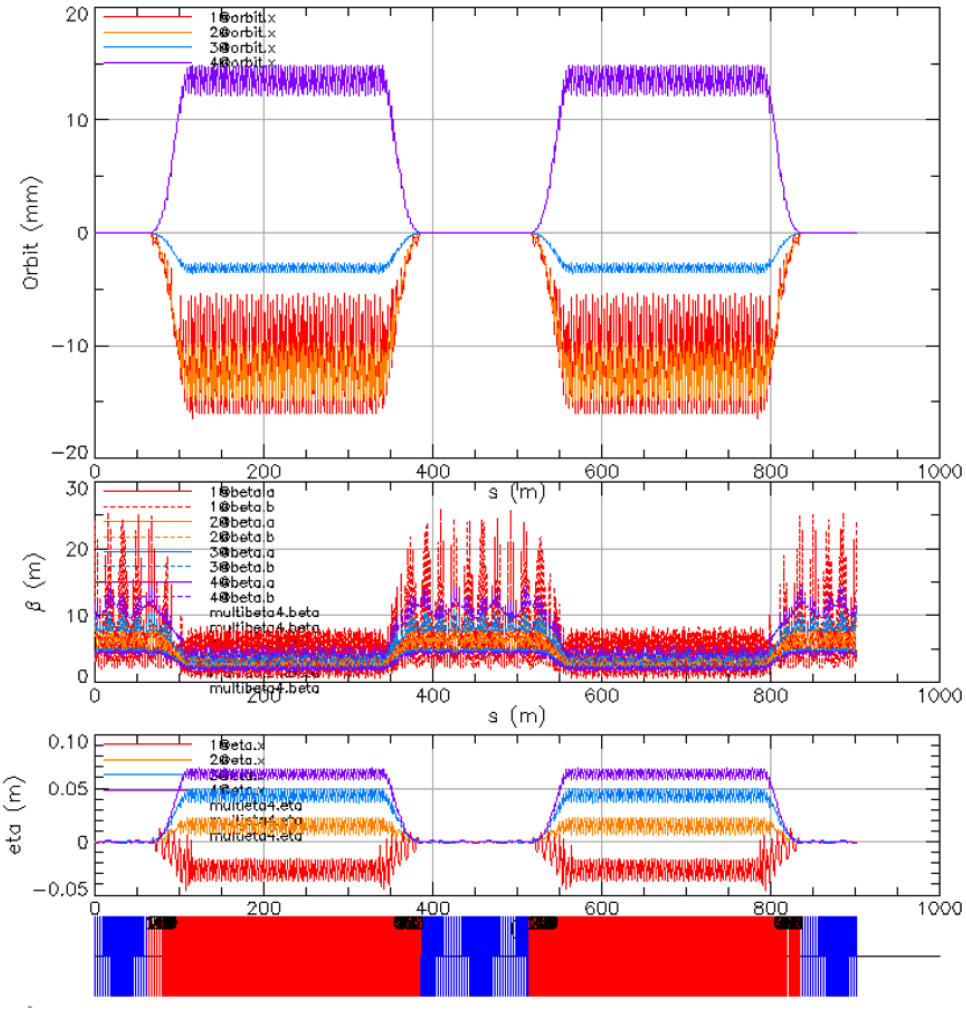

Figure 8: Orbits and dispersion merging from the arc cells to the straight section for different energies in the racetrack.

[6] S. Machida *et al.*, "Acceleration in the linear non-scaling fixed-field alternating-gradient accelerator EMMA", *Nature Physics*, Jan 2012. doi:10.1038/nphys2179

[7] R.C. Johnson (ed.), "Small Accelerator, Big Promise", https://www.eetimes.com/document.asp?doc_id=1332173

[8] CBETA, https://www.classe.cornell.edu/CBETA_PM/

[9] Stephen Brooks, "CBETA Magnet Production", presented at FFA'18 in Kyoto, Japan, Sep 2018. https://indico.rcnp.osaka-u.ac.jp/event/1143/contributions/1213/

[10] D. Trbojevic, E.D. Courant, and A. Garren, HEMC'99 Workshop, Montauk, New York, October 1999.

[11] D. Trbojevic, E.D. Courant, and M. Blaskiewicz, *Phys. Rev. Spec. Topics Accelerators and Beams*, vol. 8, pp. 050101, 2005.

[12] D. Sagan, *Bmad manual*, https://www.classe.cornell.edu/bmad/manual.html

[13] J. Rosenzweig and L. Serafini, "Transverse particle motion in radio-frequency linear accelerators", *Phys Rev* E, vol. 49, p. 1599, 1994. doi:10.1103/PhysRevE.49.1599

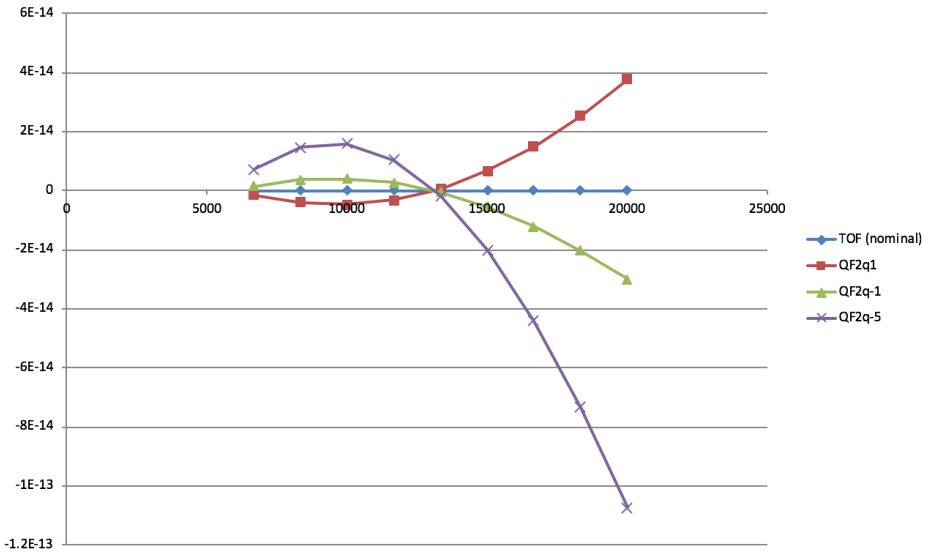

Figure 9: Stephen Brooks' method of time of flight correction.

[14] J.S. Berg, https://indico.bnl.gov/event/2764/contributions/7146/attachments/6425/7812/JSBerg-170909.pdf

3.11 Simulation of an FFA Return Channel ERL in a RHIC-based Electron-Ion Collider

François Méot, Brookhaven National Laboratory C-AD, Upton, NY USA.

Abstract

The linac-ring electron-ion collider designed at BNL is based on a 20 GeV ERL comprised of a 1.3 GeV linac and two 3.8 km FFA lattice return loops placed along the RHIC heavy ion collider. This document introduces the simulation of the FFA ERL in Zgoubi, including a start-to-end 6-D simulation of the acceleration-deceleration cycle of a polarized electron bunch.

Introduction

The design of eRHIC linac-ring EIC ERL [1] is based on a 1.322 GeV linac, and on two FFA loops located alongside RHIC, Fig. 1. The low energy loop recirculates the electron bunches four times on the way up and four times on the way down ($0.012 \overset{up}{\rightarrow} 5.300 \overset{down}{\rightarrow} 0.012$, step 1.322 GeV). The second loop is of concern in this document; it recirculates the electron bunches 12 times up and 11 times down,

$$5.3 \xrightarrow{up} 21.164 \xrightarrow{down} 5.3\,\text{GeV}$$

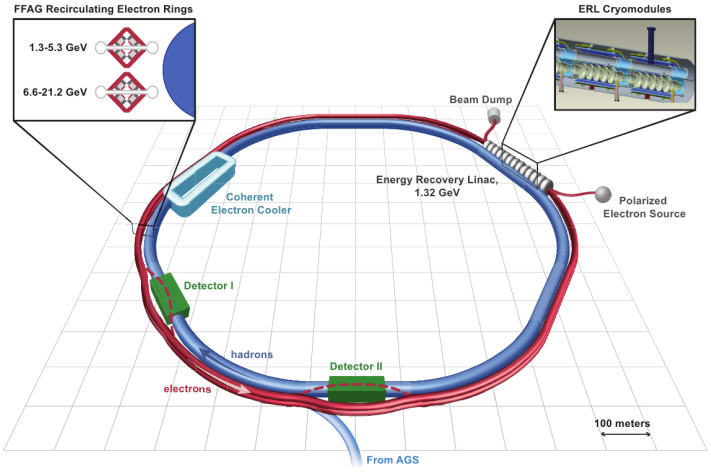

Figure 1: eRHIC ERL with its two recirculation loops alongside RHIC. The top left box shows a cross-section of the low and high energy multiple-beam FFA channels. The 1.322 GeV linac is located in RHIC IR2, it is connected to the FFA loops by a merger section (resp. spreader) at its upstream (resp. downstream) end.

In the following, §3.11.1 discusses the general properties of the 3.8 km FFA loop. The ERL lattice is described in §3.11.2, A 23-pass acceleration-deceleration cycle of a 6D bunch is then simulated. The present document is an excerpt of two BNL internal reports, in which many details of the methods and the results can be found, as well as detailed references [2, 3].

3.11.1 FFA Recirculation Loop, Synchrotron Radiation, Polarization

The structure of the FFA loop is as follows:

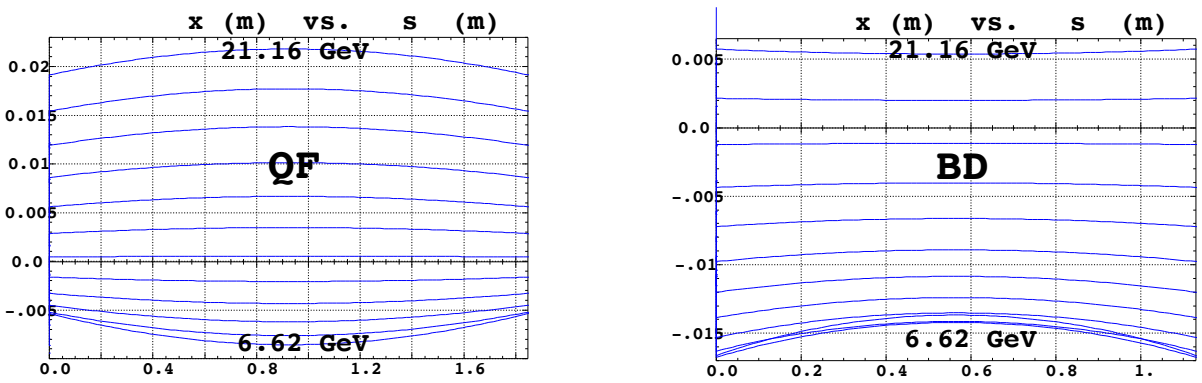

Figure 2: Transverse excursion of the 12 periodic orbits (for 12 different energies) across the FFA cell magnets, shown in the respective magnet frames ($x = 0$ is the quadrupole axis). The optical axes of the quadrupoles in the arc cell are radially shifted by 13.48 mm with respect to one another; this ensures 8.73 mrad orbit bending across the cell.

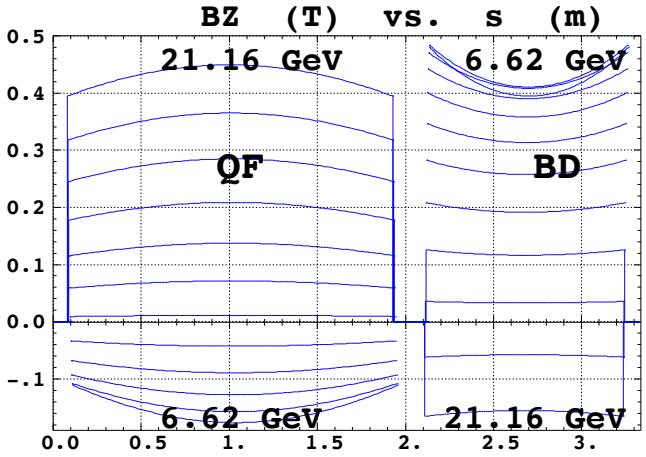

Figure 3: Magnetic field along the 12 orbits in a hard-edge model.

- There are 6 arcs and 6 long straight sections, following RHIC 6-periodicity (Fig. 1).
- An arc is comprised of 102 identical QF-drift-BD-drift cells (Fig. 2) wih QF a pure quadrupole and BD a combined function dipole.
- Five of the six long straight sections (LSS) are identical and each comprises a string of 52 FODO cells with all energies sharing a common optical axis, coinciding with the quadrupole axes.
- Ten dispersion suppression sections (DS) between the arcs and the five LSS are each made up of 18 FFA cells which gradually shift each beam from the LSS axis to its FFA orbit in the arc.
- The remaining LSS (RHIC's IR2 region) is occupied by the 120 m, 42 cavity linac and by the spreader and merger lines at its ends.
- Both start and end points of an arc are at the center of a BD magnet in these simulations, for convenience.
- The 12 spreader lines at their downstream end, as well as the 12 merger lines at their

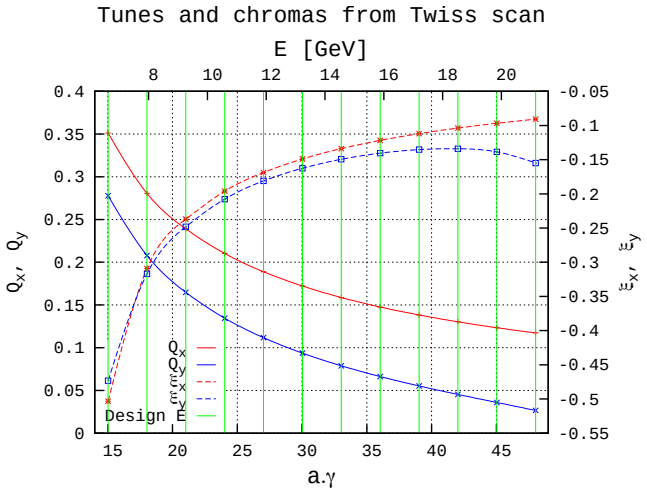

Figure 4: Cell tunes and chromaticities versus energy; the vertical bars correspond to the 12 design energies. Features of the linear FFA cell include tunes decreasing with energy since quadrupole gradients are fixed, and natural chromaticity decreasing with energy.

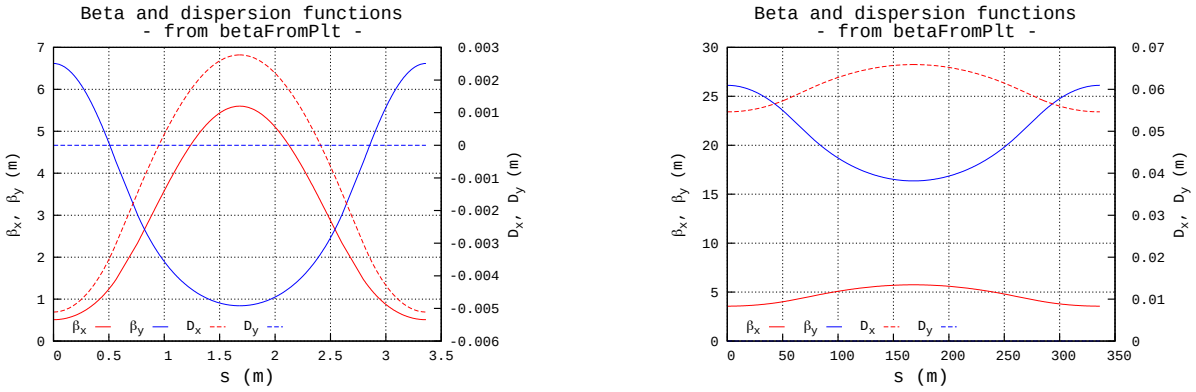

Figure 5: Optical functions at 6.622 GeV (left) and 21.164 GeV (right) from stepwise ray-tracing across the FFA cell.

upstream end, are matched to the 12 sets of FFA orbit optical functions at the center of the arc cell BD magnet.

- The spreader at its upstream end and the merger at its downstream end are matched to the optical functions at linac ends.

- Path length adjustments (since path length is energy dependent in the FFA arcs) are taken care of in the spreader and merger sections.

- In addition, some artefacts are introduced regarding 6D positioning of the bunch at the entrance to the various FFA loop sections. These will be discussed at the appropriate points in the article.

Arc cell

The optical properties of the cell are summarized in four of the figures.

- Figures 2 and 3 show respectively the transverse excursion of, and magnetic field along, periodic orbits across the arc cell for the 12 recirculated energies. It can be seen that the field varies in a substantial fashion along the orbit inside a quadrupole at large excursion.

- Figure 4 shows the energy dependence of tunes and chromaticities (in this figure $a\gamma$ is the spin precession rate, with $a = 1.16 \times 10^{-3}$ the electron anomalous gyromagnetic factor).

- Figure 5 shows the optical functions across the cell at the lower and higher energies.

Synchrotron radiation

Turn-by-turn tracking is performed here, with neither linac nor any spreader and merger sections. The FFA recirculating loop in this first approach is 6-periodic, and perfect fields and perfect optical alignment are assumed.

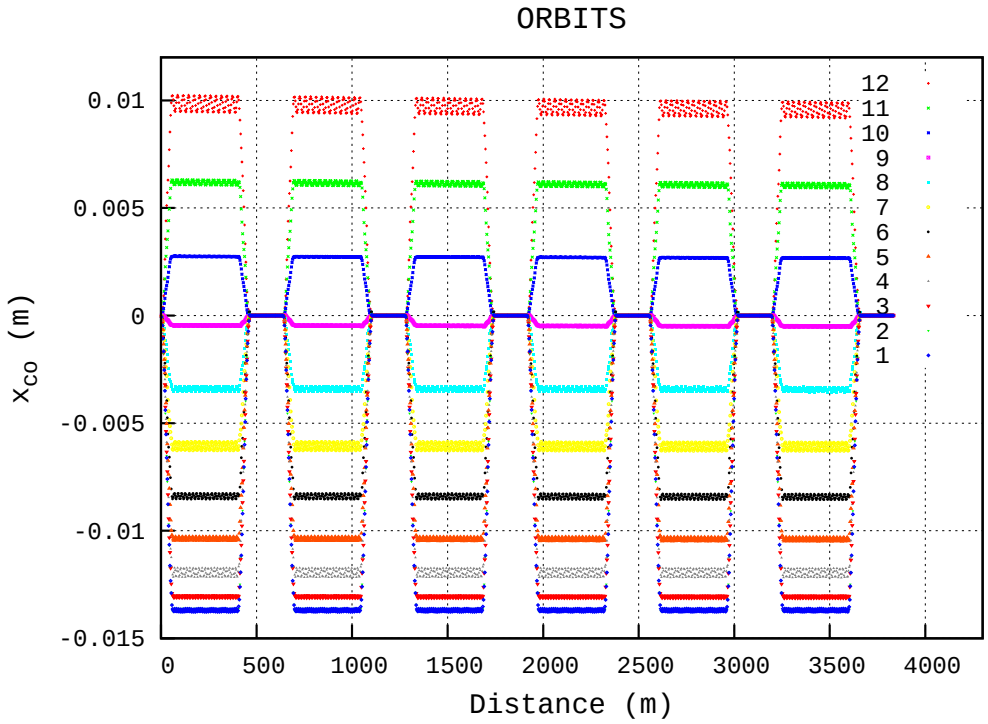

Figure 6: Orbits along the FFA recirculation loop for the 12 energies considered: from bottom to top, E=6.622 to 21.164 GeV in steps of 1.322 GeV. Along the six long straight sections, all energies have a common optical axis ($x = 0$). In the arcs the orbit excursion is recorded in the QF→BD drift. The $\lesssim$mm excursion observed here at all energies (the largest being at higher energy) is due to a residual orbit mismatch at the dispersion suppressors.

Orbit

Figure 6 shows the twelve orbits along the FFA return loop (actually, a plot of the centroid position $\overline{x(s_f)}$ of a 5000-particle bunch), for $E = 6.622$ GeV to $E = 21.164$ GeV in steps of 1.322 GeV. The 12 orbits are all aligned on $x = 0$ along the six long straight sections, whereas in the six arcs they feature an energy dependent excursion (as seen above in Fig. 2).

An orbit oscillation of $\lesssim \pm 1$ mm is visible in the arcs and is also present in the complete ERL simulation (see Fig. 16). This is due to a slight orbit mis-match between LSS and arc across the DS sections. It can be reduced but the main point is what level can be sustained to avoid chromaticity-induced emittance increase [2].

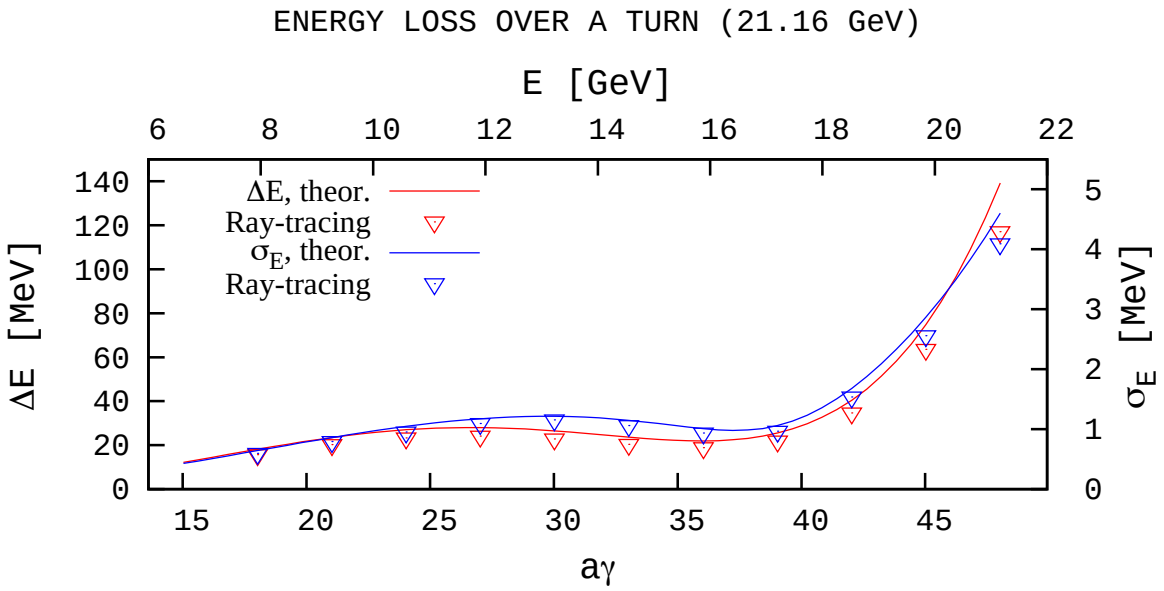

Figure 7: Energy dependence of the single-turn average energy loss (left axis) and energy spread (right axis) in FFA recirculation loop at the 12 recirculated energies (empty triangles). The solid lines (labelled "theor.") are from Eq. (1) for a 6×120 cell ring. The slightly lower SR loss from tracking comes from the smaller number of cells per arc, 102, and lower SR loss in the 18-cell DS sections.

Synchrotron radiation loss

Figure 7 shows the energy dependence of the synchrotron radiation (SR) induced energy loss and spreading over the 6-period, 3.8 km, FFA loop. These quantities are obtained by a one-turn tracking of a 5000-particle bunch with initial null 6D emittance. The theoretical ("theor.") average energy loss and energy spread in the figure are obtained using [2]

$$\overline{\Delta E}\,[MeV] = 0.96 \times 10^{-15}\,\gamma^4 \left(\frac{l_{\rm BD}}{\rho^2_{\rm BD}} + \frac{l_{\rm QF}}{\rho^2_{\rm QF}} \right) \times 6 \text{ arcs} \times 120 \text{ cells/arc} \qquad (1)$$

$$\sigma_E \approx 1.94 \times 10^{-14}\,\gamma^{7/2} \sqrt{ \frac{l_{\rm BD}}{|\rho^3_{\rm BD}|} + \frac{l_{\rm QF}}{|\rho^3_{\rm QF}|} } \times \sqrt{6 \times 120},$$

with 120 the number of cells (as discussed in §3.11.1) necessary to close a circle given the 8.73 mrad single cell deviation (in the FFA loop, the orbit closure is ensured with 102 cells per arc and 18 cells per DS section), and with $l_{\rm QF}$, $l_{\rm BD}$ the magnet lengths and $\rho_{\rm QF}$, $\rho_{\rm BD}$ their average curvature radii as obtained from the stepwise ray-tracing.

Polarization

The spin vector is injected horizontally in the ERL, and precesses around the vertical magnetic field at a rate of $a\gamma\alpha$ (where α is the azimuthal angle) in the course of a recirculation round the FFA loop. The 1.322 GeV energy increment ensures a polarization vector parallel to the longitudinal axis at IP6 and IP8. Due to energy spread, spin precession undergoes spreading ("spin diffusion").

In the following we first assess the effect of SR induced energy spread on spin diffusion, then we assess spin diffusion for a bunch with nominal transverse emittances and momentum spread.

A theoretical approach can be used to check tracking results as follows. The solution of the

diffusion equations in constant magnetic field can be written [4]

$$\begin{pmatrix} \overline{\Delta E^2} \\ \overline{\Delta E \Delta\phi} \\ \overline{\Delta\phi^2} \end{pmatrix} = \begin{pmatrix} 1 & 0 & 0 \\ \alpha s & 1 & 0 \\ \alpha^2 s^2 & 2\alpha s & 1 \end{pmatrix} \begin{pmatrix} \overline{\Delta E^2} \\ \overline{\Delta E \Delta\phi} \\ \overline{\Delta\phi^2} \end{pmatrix}_{s=0} + \omega \times \begin{pmatrix} s \\ \alpha s^2/2 \\ \alpha^2 s^3/3 \end{pmatrix}$$

where s is the distance in the field, $\omega = \dfrac{C}{\rho^3}\lambda\!\!\!^{-}_c r_e \gamma^5 E^2 \approx 1.44 \times 10^{-27}\,\dfrac{\gamma^5}{\rho^3}E^2$, $\alpha = \dfrac{a}{\rho E_0} \approx \dfrac{1}{0.4406\rho}$ (with $\lambda\!\!\!^{-}_c = \hbar/m_e c$ the electron Compton wavelength, $C = 110\sqrt{3}/144$, $E_0 = m_e c^2/e$ the electron rest mass).

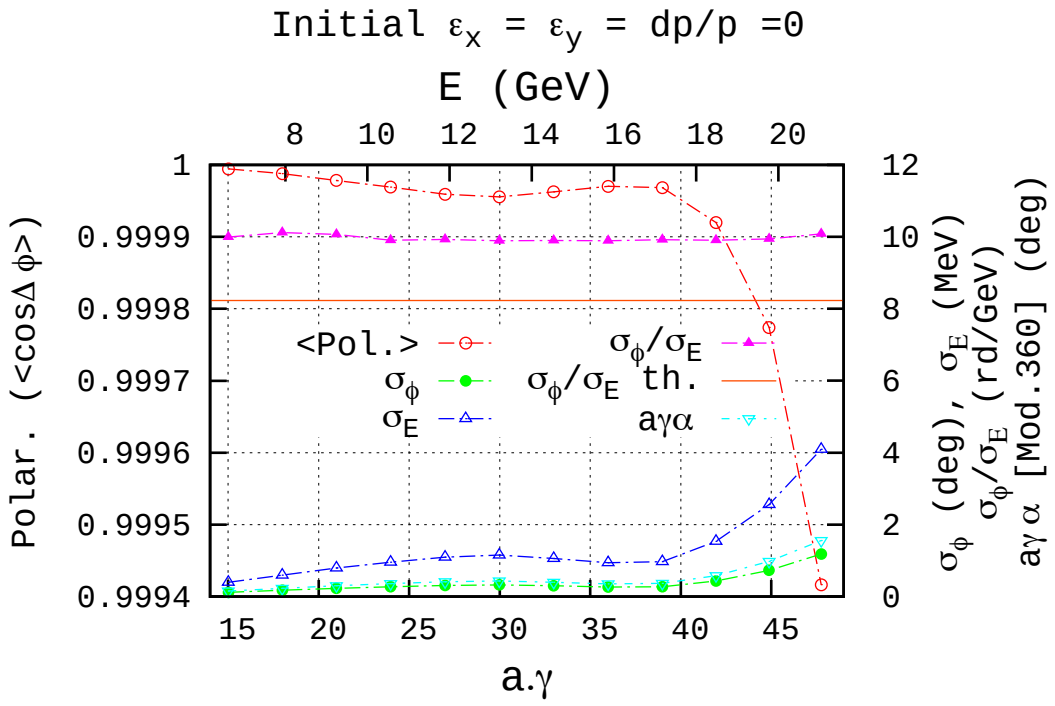

Figure 8: Turn-by-turn in the FFA loop: final polarization $\langle \cos\Delta\phi \rangle$ (left axis) and spin diffusion σ_ϕ (right axis) in a 5000-particle bunch (zero size at start of a turn), for the 12 different energies 6.622 to 21.164 GeV in steps of 1.322 GeV.

Assuming a starting state

$$\begin{pmatrix} \overline{\Delta E^2} \\ \overline{\Delta E \Delta\phi} \\ \overline{\Delta\phi^2} \end{pmatrix}_{s=0} = 0,$$

which is the case for each energy for instance, in the turn-by-turn tracking, yields

$$\sigma_E = \overline{\Delta E^2}^{1/2} = \sqrt{\omega s}$$

(which we note is consistent with the familiar $\sigma_E/E = 3.8\,10^{-14}\dfrac{\gamma^{5/2}}{\rho^{3/2}}\sqrt{s}$), so that

$$\sigma_\phi = \overline{\Delta\phi^2}^{1/2} = \sqrt{\frac{\omega\alpha^2 s^3}{3}} = \frac{\alpha s}{\sqrt{3}}\,\sigma_E \qquad (2)$$

or, given $s = 2\pi\rho$,

$$\frac{\sigma_\phi}{\sigma_E} = 8.23\,[\text{rad/GeV/turn}] \tag{3}$$

Synchrotron radiation effects, turn-by-turn

Spin is tracked turn-by-turn in the 6-period ring as above, namely,

$$6 \times [\text{DS} - \text{LSS} - \text{DS} - \text{ARC}],$$

with neither linac nor spreader and merger sections.

Tracking results are displayed in Figure 8. The "σ_E" curve is that of Fig. 7, for comparison with the spin diffusion angle rms value, σ_ϕ. Their ratio takes a quasi-constant value $\sigma_\phi/\sigma_E \approx 10\,\text{rad/GeV}$ close to the expected 8.23 rad/GeV indicated by Equations (2) and (3)). Note that $a\gamma\alpha$ in this plot appears to differ from an integer multiple of 360 degs (its expected value) by ∼1-2 degs. This stems from the lack of accuracy of SR energy loss compensation at the linac boost, and is of marginal effect here.

An up-down ER cycle, 23 passes, in a six-arc FFA ring

In order to get a sense of orders of magnitude, we conclude this introduction to the FFA loop with an up-down tracking in a model 6-arc ring, comprising 6×120 cells, with, at a single location, a simplified linac simulation using a thin-lens 1.322 GeV boost.

A particle bunch is, in a row, accelerated in 11 linac passes (12 recirculation loops) from 6.622 to 21.164 GeV and decelerated in 11 linac passes (10 recirculation loops) back down to 6.622 GeV. The following features are included in the simulation:

After each turn, prior to tackling the next one,

i) SR loss is compensated at the linac by giving a turn-dependent energy kick $1.322 + \Delta E$ with ΔE computed from Eq. (1);

ii) the bunch is re-centered in position and angle on the theoretical FFA orbit once per turn, next to the boost (according to the orbit dependence on energy).

Two simulations are performed:

i) The first simulation starts with zero 6D emittance (a point object) and produces evolution of the horizontal and longitudinal emittances as displayed in Fig. 9. The vertical emittance remains zero because the photon recoil is not accounted for in the Monte Carlo SR simulation.

   Details of phase space portraits at the various energies are postponed to the complete ERL tracking in §3.11.3, as the present phase space portraits differ only slightly from the full ERL simulation results.

ii) The second simulation is carried out with a nominal starting bunch emittance of $\sim 50\,\pi\mu$m normalized in both transverse planes, a random, uniform momentum spread over $\pm 3\times10^{-4}$, and zero bunch length. The evolution of the horizontal and longitudinal emittances are displayed in Figs. 10 and 11 respectively. In this simulation, different numbers of particles have been tried to test the convergence (1k, 5k and 10k), as well as two different integration step sizes in the two quadrupoles (1 cm and 3 cm). The relative effect is small, the difference is essentially a slight translation of the curves.

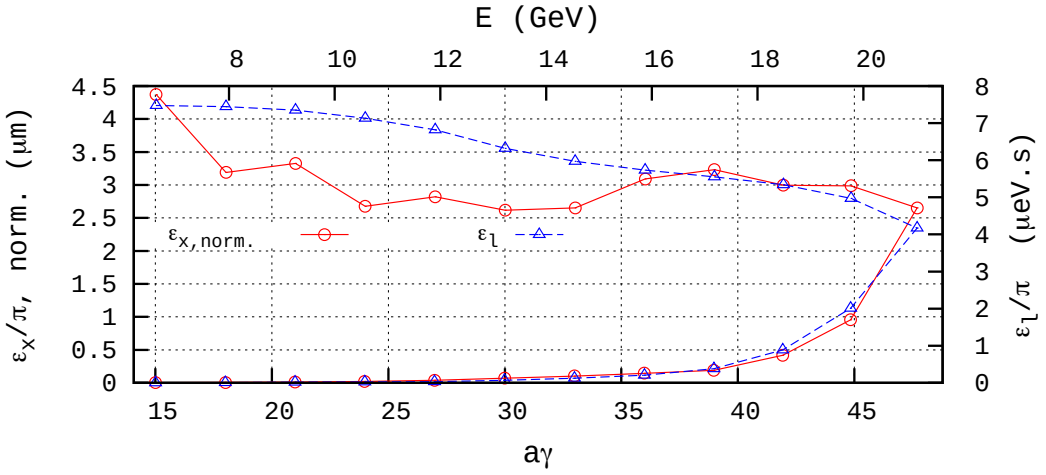

Figure 9: The markers in this figure show the evolution of horizontal (left vertical axis) and longitudinal (right axis) bunch emittances under the effect of SR in the case of an initial point object (zero 6D emittance), over a 23-loop end-to-end up-down cycle in a simplified 6-arc ring (6.622 $\overset{up}{\rightarrow}$ 21.164 $\overset{down}{\rightarrow}$ 6.622 GeV).

We conclude with spin tracking in the previous 6-arc FFA ring, made up of 6×120 cells, with, at a single location, a linac simulation by a thin-lens 1.322 GeV boost. A 5000-particle bunch is taken from 6.622 to 21.164 GeV in 11 linac passes. The results are displayed in Figure 12. The cumulated effect amounts to $\sigma_\phi \approx 15$ degs at the end of the final 21.1 GeV loop (top-left plot). The top-right and bottom plots show that the factor with the dominant influence on the final polarization is the injected bunch energy spread.

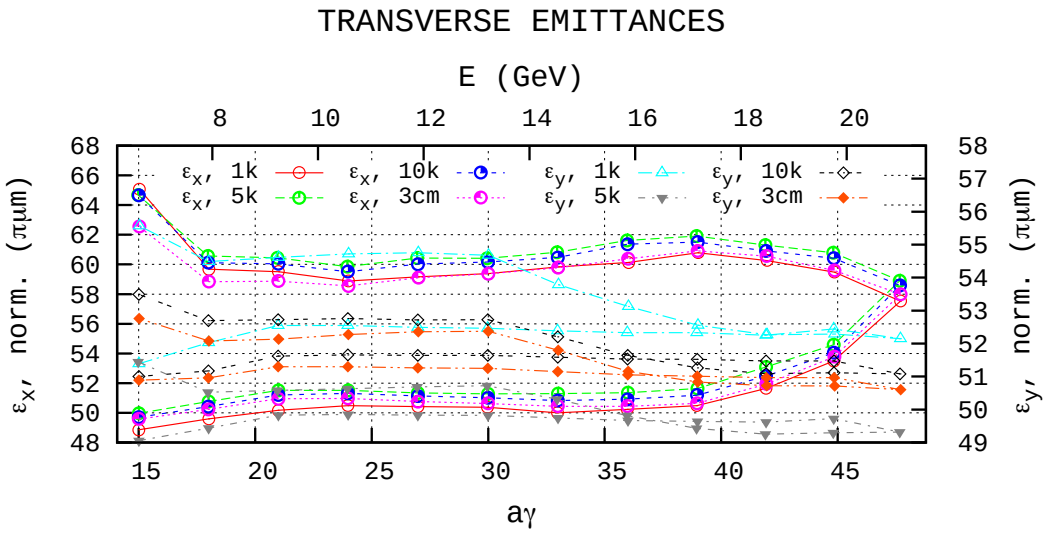

Figure 10: Markers in this figure give the evolution of horizontal (left vertical axis) and vertical (right axis) bunch emittances under the effect of SR for initial conditions $\epsilon_x = \epsilon_y = 50\,\pi\mu$m normalized, $\Delta E/E$ uniform random in $\pm 3\,10^{-4}$ and $\sigma_l = 0$. The bunch is tracked over a 23-loop end-to-end up-down cycle in a simplified 6-arc ring (6.622 $\overset{up}{\rightarrow}$ 21.164 $\overset{down}{\rightarrow}$ 6.622 GeV). The various curves correspond to either a different number of tracked particles (1, 5 or 10 $\times 10^3$), or to different integration step sizes in cell quadrupoles (1 or 3 cm).

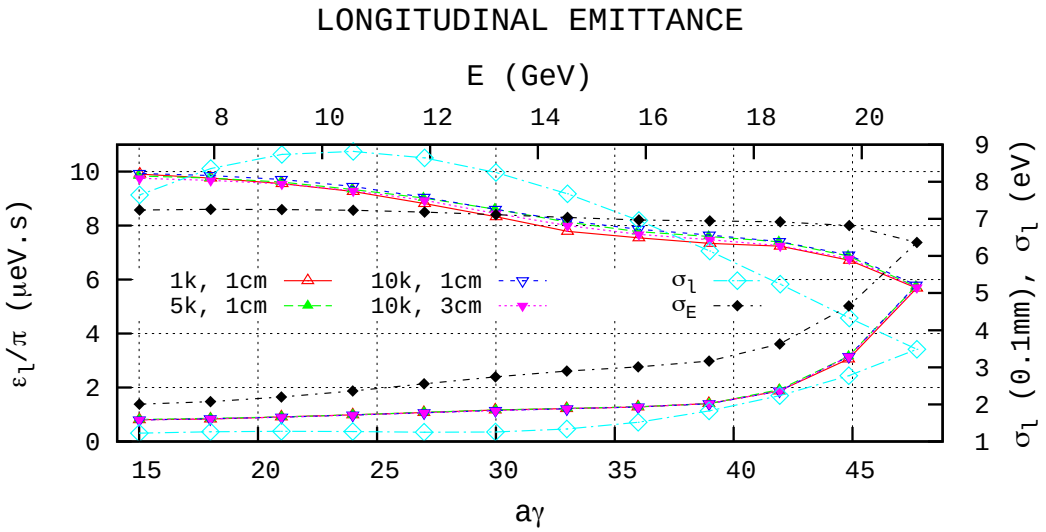

Figure 11: Evolution of longitudinal bunch emittance (left axis, left four markers) and σ_l, σ_E (right axis, right two markers), for initial conditions $\epsilon_x = \epsilon_y = 50\,\pi\mu$m normalized, $\Delta E/E$ uniform random in $\pm 3 \times 10^{-4}$ and $\sigma_l = 0$. The bunch is tracked over a 23-loop end-to-end, up-down cycle in a simplified 6-arc ring (6.622 $\overset{up}{\rightarrow}$ 21.164 $\overset{down}{\rightarrow}$ 6.622 GeV).

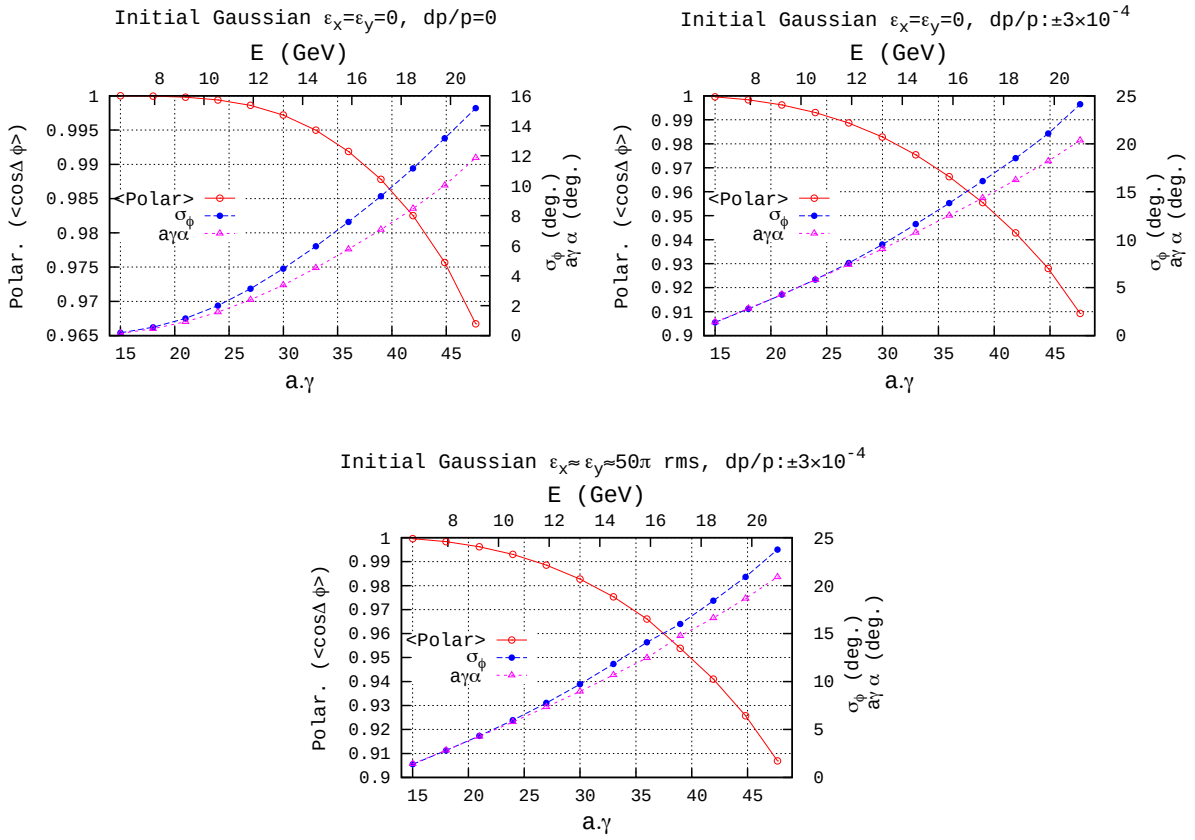

Figure 12: Evolution of cumulated spin diffusion in the case of an 11 linac-pass acceleration cycle (12 complete 6-arc loops), 6.622 → 21.164 GeV, in a simplified 6-arc ring.

3.11.2 ERL optics, complete

This section briefly introduces the handling of the three additional structures needed, namely, the linac, spreader, and merger sections. It concludes with the complete ERL optics, 23 passes.

Linac

Transport through the linac cavities uses "Chambers matrices"; the corresponding source code has been copied from the Saclay code BETA [5] for reliability.

These matrices take the following form:

For both planes (for either x or y):

$$\begin{pmatrix} x \\ x' \end{pmatrix}_{\text{out}} = \begin{pmatrix} \cos u - \sqrt{2}\sin u\cos\phi & vW_{\text{i}}\sin u\cos\phi \\ -\dfrac{\sin u}{vW_{\text{o}}}\left(2\cos\phi + \dfrac{1}{\cos\phi}\right) & \dfrac{1}{W_{\text{o}}W_{\text{i}}}\left(\cos u + \sqrt{2}\sin u\cos\phi\right) \end{pmatrix} \begin{pmatrix} x \\ x' \end{pmatrix}_{\text{in}} \tag{4}$$

with $u = \log(W_{\text{o}}/W_{\text{i}})/(\sqrt{8}\cos\phi)$, $v = \sqrt{8}L_{\text{cav}}/(W_{\text{o}} - W_{\text{i}})$, W_{i}, W_{o} respectively the incoming and outgoing kinetic energies, L_{cav} the cavity length and ϕ the particle phase at the cavity.

If $(W_{\text{o}} - W_{\text{i}})/W_{\text{i}} \ll 1$ the matrix is used in the simplified form

$$\begin{pmatrix} x \\ x' \end{pmatrix}_{\text{out}} = \begin{pmatrix} \sqrt{W_{\text{i}}/W_{\text{o}}} & L_{\text{cav}} \times \sqrt{W_{\text{i}}/W_{\text{o}}} \\ 0 & \sqrt{W_{\text{i}}/W_{\text{o}}} \end{pmatrix} \begin{pmatrix} x \\ x' \end{pmatrix}_{\text{in}} \tag{5}$$

The code works with determinant 1 matrices, obtained by renormalizing the transport coefficients by the square root of the matrix determinant.

Spreader and merger sections

The 12 spreader lines (linac to FFA arc) and 12 merger lines (FFA arc to linac) in the ERL ensure a series of optical functions: orbit positioning, optical matching between linac and FFA loop *i.e.* beta functions and horizontal dispersion, which is non-zero on the FFA side), path length (as it is energy dependent in the FFA loop) and R_{56} adjustments.

In the simulations, for simplicity we use the same design for *all* spreader and merger lines, scaled to the different rigidities. One consequence is that, except for the 21.164 GeV spreader and merger lines, SR effects as well as spin dynamics cannot be evaluated (the bending radii, possible presence of a vertical chicane, and some other aspects, have to be optimized separately (*e.g.* SR has to be minimized) for each spreader/merger line).

ERL optics, readiness

The lattice in the up-down ERL tracking simulations has the following form

$$\text{ERL} = \underbrace{\text{merger} + \overset{\textbf{Observation point}}{\downarrow} \text{linac} + \text{spreader}}_{\text{RHIC IR2 region}} + \text{FFA} \tag{6}$$

with

$$\text{FFA} = \text{ARC} - \text{DS} - \frac{1}{2}\text{LSS} + \underbrace{\left[\frac{1}{2}\text{LSS} - \text{DS} - \text{ARC} - \text{DS} - \frac{1}{2}\text{LSS}\right]}_{\textbf{4 times}} + \frac{1}{2}\text{LSS} - \text{DS} - \text{ARC} \tag{7}$$

and

$$\text{ARC} = 102 \times \left[\frac{1}{2}\text{BD} - \text{drift} - \text{QF} - \text{drift} - \frac{1}{2}\text{BD}\right] \tag{8}$$

Note in particular, compared to the "simplified 6-arc" simulations in §3.11.1 and §3.11.1, the absence of DS sections in IR2 region in this complete ERL layout (actually not fully complete, see below, but close enough that it delivers a qualitative overview of the ERL model to be eventually achieved and the outcomes to be expected).

Some more details regarding the optical structure in this simulation of the complete ERL are as follows:

- An arc is comprised of 102 identical doublet cells (Eq. (8)) with quadrupole optical axes radially shifted by 13.48 mm with respect to one another to ensure 8.73 mrad bending per cell (in keeping with the optical properties described in §3.11.1).

- The five long straight sections (LSS) are made up of a string of 52 such cells with quadrupole axes superimposed instead. These LSS are dispersion free and all energies share a common optical axis (as in Fig. 6), aligned on the quadrupole axes.

- The dispersion suppressors (DS) between the arcs and each of the five LSS are comprised of 18 of these cells and have quadrupole axes shifting gradually from zero at their LSS end to 13.48 mm at their arc end. Six of these DS take the 23 beams (12 recirculations up, 11 down) from their respective FFA optical axes in the arcs onto their common axis in the downstream LSS. The other six DS have the reverse functionality.

- The remaining straight section is occupied by the 120 m, 42 cavity linac and the spreader and merger lines (along RHIC's IR2 region, see Fig. 1). There are no energy loss or energy spread compensation cavities in the present simulations.

- Both start and end points of an arc are at the center of a BD magnet (Eq. (8)), for convenience.

- The spreader at its downstream end and the merger at its upstream end:

  – steer the beam respectively onto and from the (non-zero) FFA orbits,

  – are matched to the optical functions at the center of the arc cell BD magnet.

- The spreader at its upstream end and the merger at its downstream end are matched to the optical functions and dispersion at linac ends.

- The beam transport to the IPs at IR6 and IR8 at top energy (21.164 GeV) is not accounted for; instead the 21.164 GeV recirculation is treated like a regular one, simply taking the bunches back to the deceleration phase for energy recovery.

- Path length adjustments (path length is energy dependent in the FFA arcs) are taken care of in the spreader and merger sections.

Perfect optical alignment and perfect fields are assumed everywhere. Moreover, artificial 6D positioning of the bunch is introduced at various locations: this will be addressed in detail in due course. Note also, in the following simulations the entrance point to the linac is the starting point of the optical sequence in Zgoubi, the "Observation point" in Eq. (6).

The optics properties are summarized in Figures 13-16.

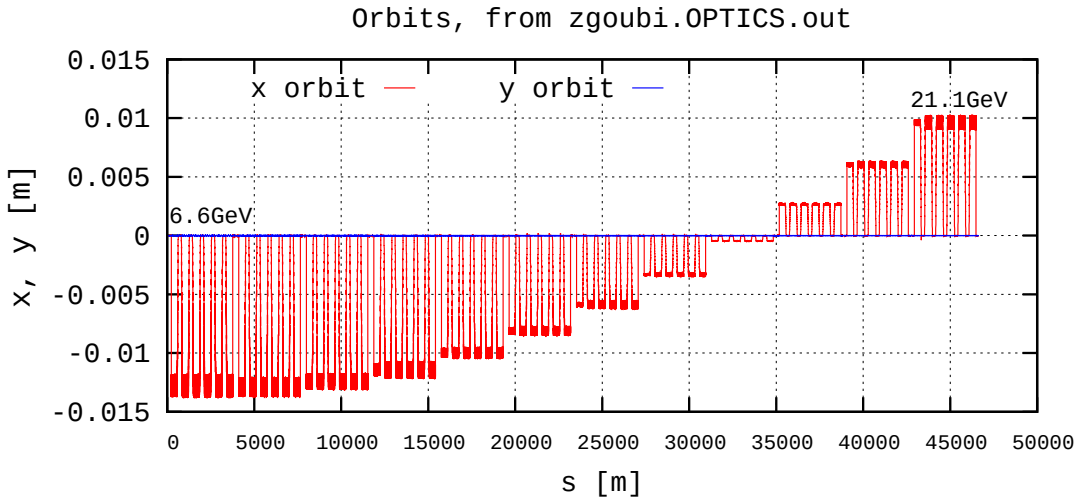

Figure 13: This figure shows the 12 recirculated orbits (obtained by tracking a single particle) from 6.622 to 21.164 GeV, a 12×3.887 km long path. Each of the 12 "steps" in this plot represents a complete ERL turn (Eq. (6)), 3.887 km long. In the arcs the orbit behaves as detailed in Fig. 6, with excursion ranging from ~ -1.35 cm at 6.622 GeV (left hand end) to $\sim +0.9$ cm at 21.164 GeV (right hand end). In the five long straight sections between the arcs and in the linac straight between two "steps", the orbit coincides with the $x = 0$ axis in the figure.

3.11.3 Tracking the ERL

In this concluding section, the full ERL layout is considered, with optical settings as discussed in §3.11.2:

$$\text{ERL} = \underbrace{\text{merger} + \quad \overset{\textbf{Observation point}}{\downarrow} \quad \text{linac} + \text{spreader}}_{\text{RHIC IR2 region}} \quad + \quad \text{FFA}$$

with FFA as in Eq. (7). As pointed out earlier, some artefacts and limitations are imposed on the modeling of the ERL at this stage of its development, as follows.

Artefacts

- Artificial bunch centroid centring is applied along the ERL (using Zgoubi's "AUTOREF" keyword [7]), as follows:
  - on exit of any of the 12 merger lines (*i.e.*, at the entrance to the linac):
    - (i) horizontal (x, x') and vertical (y, y') bunch centring on zero (a substitute to beam steering onto the linac optical axis);
    - (ii) bunch centring on the design momentum (this stands for artificial compensation of the SR loss that occurs in the upstream FFA arc and merger line);
    - (iii) time centring so that at any stage in the acceleration-deceleration cycle bunches will enter the linac centered on the RF crest.
  - on exit of any of the 12 spreader lines there is bunch centring on the current FFA orbit (a substitute for beam steering), centring on the design momentum (this stands for artificial compensation of SR loss in the spreader);
  - at the entrance to each of the five LSS (*i.e.*, going from arc to straight) there is horizontal (x, x') and vertical (y, y') bunch centring on zero (this cancels SR induced orbit in the arcs and induced orbit by the DS section).

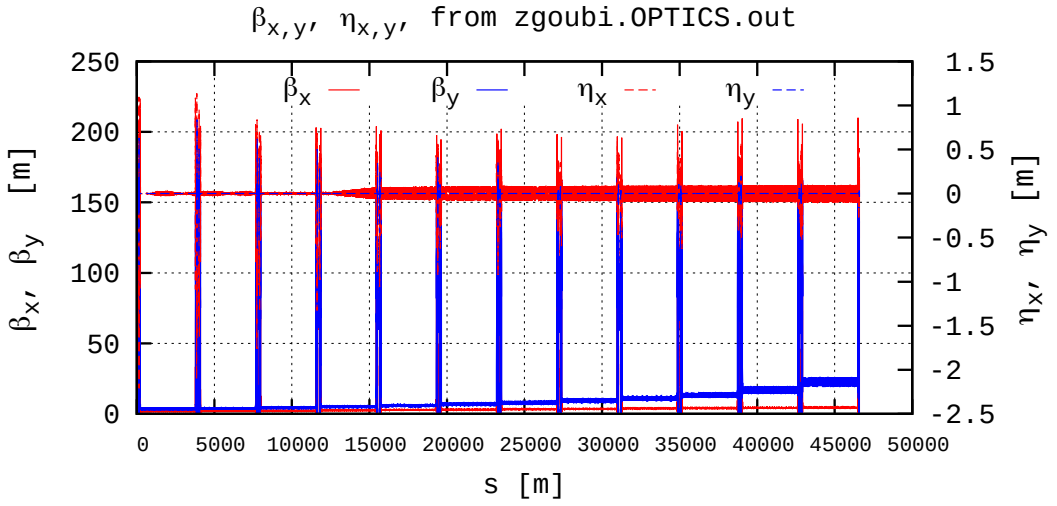

Figure 14: This figure shows the betatron functions from 5.3 to 21.164 GeV (computed from the transport of 11 sample particles).The spreader and merger sections correspond to the ∼200 m spikes. The 120 m long linac section cannot be distinguished, squeezed between spreader and merger lines (see Figs. 15, 16); it has betatron function values $\beta_x = \beta_y = 120$ m at both ends. The 12 regions between the spikes are along the FFA recirculating loop, where betatron functions increase from β_x/β_y =0.51/6.61 m amplitude at 6.622 GeV (leftmost 3.887 km section on the figure) to $\beta_x/\beta_y = 3.57/26.1$ m at 21.164 GeV (rightmost). The right vertical axis is for the dispersion functions; D_y is non-zero along short chicane segments only, in the spreader and merger lines, D_x is in the few centimetres range; the small D_x oscillation from 15 km on is due to a slight mismatch and is a very small effect ($\lesssim$ 10 cm, see Fig. 16).

- Limitations in the model in relation with these artefacts and with other approximations which they entail, include:
  - SR is switched off in all spreader and merger lines (and only there) except in the top energy spreader and merger lines at 21.164 GeV. As a consequence, except for the latter, their contributions to SR induced energy losses and related beam and spin dynamics effects are not accounted for;
  - The same conditions for spin tracking: switched off in all 6.622 to 19.842 GeV spreader and merger lines (and only there).

Way up, 6.622 to 21.164 GeV

Beam ellipses at the linac ends

Correct behaviour of the tracking is first assessed at the linac ends: one hundred particles evenly distributed on the paraxial invariant with $\beta = 120$ m, $\alpha = \pm 1$ (both horizontal and vertical) are launched at the linac entrance with E=5.3 GeV, for a 12 linac-pass tracking up to 21.164 GeV. Betatron damping has been inhibited in this case (Chambers matrices as in Eq. (4) are normalized to have unit determinant).

Tracking shows that beam ellipse parameters remain at $\beta = 120$ m, $\alpha = \pm 1$ at a few % level at both linac ends, in both planes, all the way from 5.3 to 21.164 GeV, see Fig. 17.

5000-particle bunches at linac ends

A 5000-particle bunch is tracked here. We show that transverse and longitudinal bunch emittances, as observed at the linac ends, behave in a reasonable manner. The details still require further investigation.

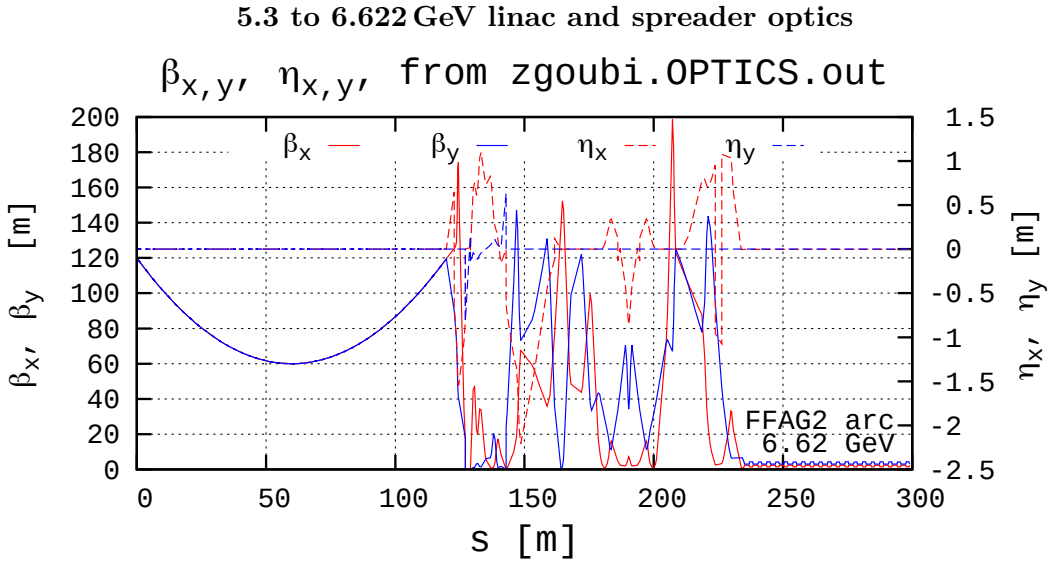

Figure 15: Details of the optical functions (betatron, left axis, and dispersion, right axis), in the case of the 5.3 → 6.622 GeV linac energy step. The β_x, β_y parabolas on the left correspond to the linac (120 m long). The linac is followed by a spreader line which ends up steering the beam on its 6.622 GeV orbit in the FFA loop on the way up. The FFA loop extends into the $s > 230$ m region (to the right), with betatron amplitudes β_x, $\beta_y = 5.6,\ 6.6$ m and dispersion function amplitude -5 to +3 mm (see Fig. 5). The latter features $\sim\pm1.5$ m excursion in the spreader.

Initial bunch emittances at 5.3 GeV are $23\pi\mu$ m transverse, zero longitudinal (both length and $\Delta E/E$ zero). Linac damping is ataken into account as is synchrotron radiation. The results are displayed in Figures 18 and 19.

Up-down cycle in the FFA stage ERL

Linac damping off and SR off

In order to ensure that input data files for the 23 linac passes end-to-end tracking are set up correctly, a preliminary up-down cycle is performed with linac damping off and synchrotron radiation off. A 2000 particle bunch is tracked with initial bunch emittances and longitudinal parameters

$$\epsilon_{x,\,\mathrm{norm}} = \epsilon_{y,\,\mathrm{norm}} = 23\,\pi\,\mu\mathrm{m}, \qquad \sigma_l = 0, \qquad \sigma_E = 0\,.$$

Transverse emittances are expected to be preserved, and longitudinal beam size growth is expected to be commensurate with SR-induced growth observed in the case of the 6-arc model, §3.11.1.

Tracking results are displayed in Figs. 20 and 21. In Fig. 20, a particle is represented by an empty box marker. It can be seen that at each energy the 2000 boxes superimpose perfectly - at that scale. Fig. 21 shows phase space details at the end of the acceleration-deceleration cycle, when the energy has returned to 5.3 GeV. This tracking demonstrates the preservation of the orbits and of the transverse emittances, and small longitudinal emittance growth, over a complete 5.3 $\overset{up}{\rightarrow}$ 21.164 $\overset{down}{\rightarrow}$ 5.3 GeV cycle.

Note that no symplecticity issue is expected: the tracking distance here is very short compared to routinely hundreds of thousands of turns tracked for proton polarization studies in RHIC, using a similar integration step size and non-linear optics.

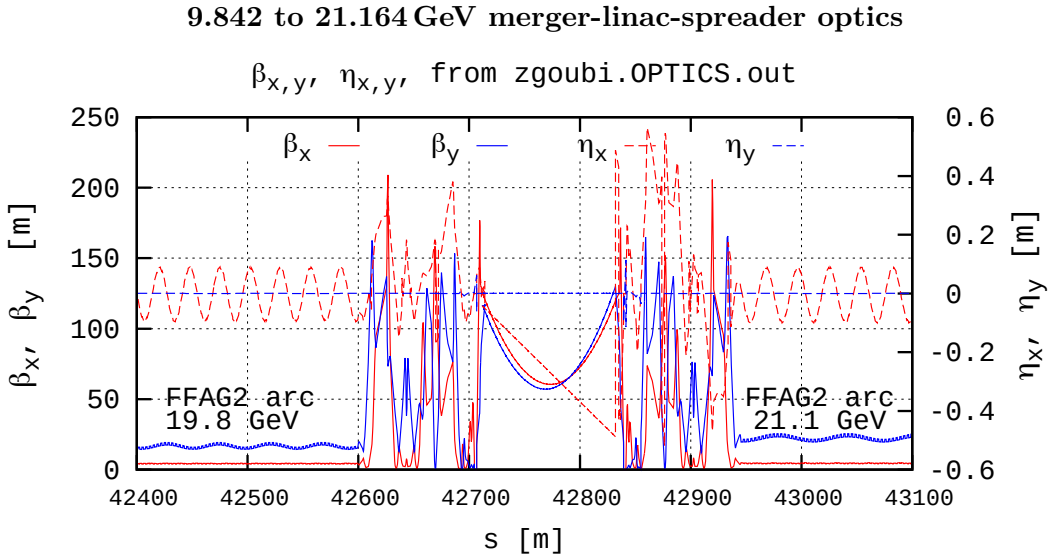

Figure 16: Details of the optical functions (betatron, left axis, and dispersion, right axis), in the 19.842 $\rightarrow$ 21.164 GeV region. The β_x, β_y parabolas in the middle region are in the linac. The linac section is preceded by a merger and followed by a spreader line, with, upstream and downstream of the latter, beam steering from and onto its respective 19.842 and 21.164 GeV orbits in the FFA loop. The FFA loop extends into the $s < 42600$ m and $s > 42950$ m regions, with vertical betatron amplitudes $\beta_y = 20$ m to the left, $\beta_y = 26$ m to the right and, superimposed, an oscillation resulting from cumulated mismatch. The dispersion function has ± 10 cm oscillation in the FFA loop, due to cumulated upstream mismatch.

Linac damping and SR on

An important aspect at this stage is that there has been no optimization regarding bunch transmission. This is beyond the scope of the present work which concerns the setting up of the data and data files for end-to-end simulation studies.

That said, tracking is performed here with synchrotron radiation and with unnormalized Chambers matrices, *i.e.*, betatron damping is accounted for. The results are displayed and commented on in Figs. 22 and 23.

Fig. 22 shows that the bunch undergoes noticeable energy spreading (on the scale of the figure) beyond pass 18 $\sim$ 19 (when the markers no longer superimpose).

Transverse emittance growth observed in Fig. 23 and requires further investigation. A large sine-like distortion of the bunch in longitudinal phase space at the final energy after deceleration (5.3 GeV) can be seen in the bottom plot in Fig. 23. This can be compared with the SR-free case, the bottom plot in Fig. 21.

Fig. 24 shows the evolution of SR energy loss over 23 recirculations from 5.3 to 21.1 GeV and back to 5.3 GeV.

Note that, as mentioned in §3.11.3, bunches always present themselves at the RF crest at the linac entrance.

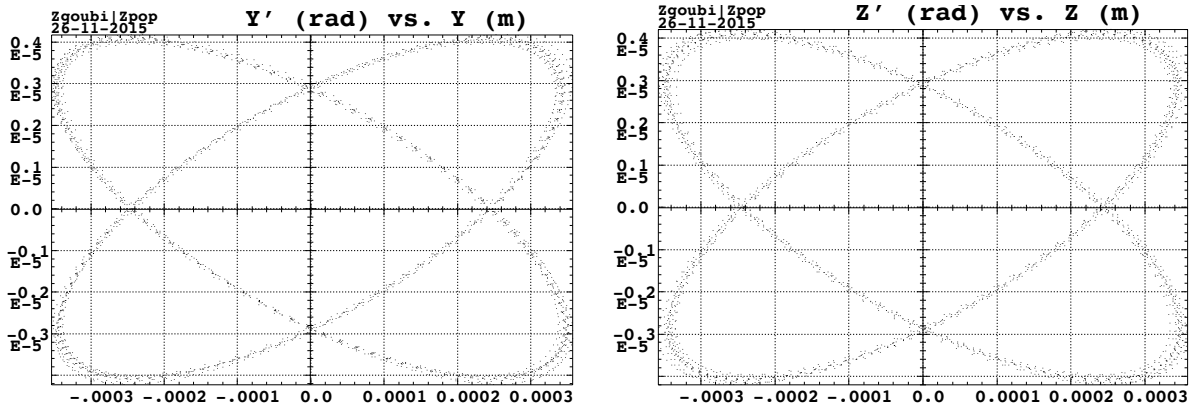

Figure 17: The figure shows a superimposition of 12, 100-particle bunches, at the linac entrance (each 100 particle set is spread on a converging ellipse, all 12 ellipses do superimpose) and the same bunches at the linac exit (each 100-particle set is spread on a diverging ellipse, all 12 ellipses do superimpose).

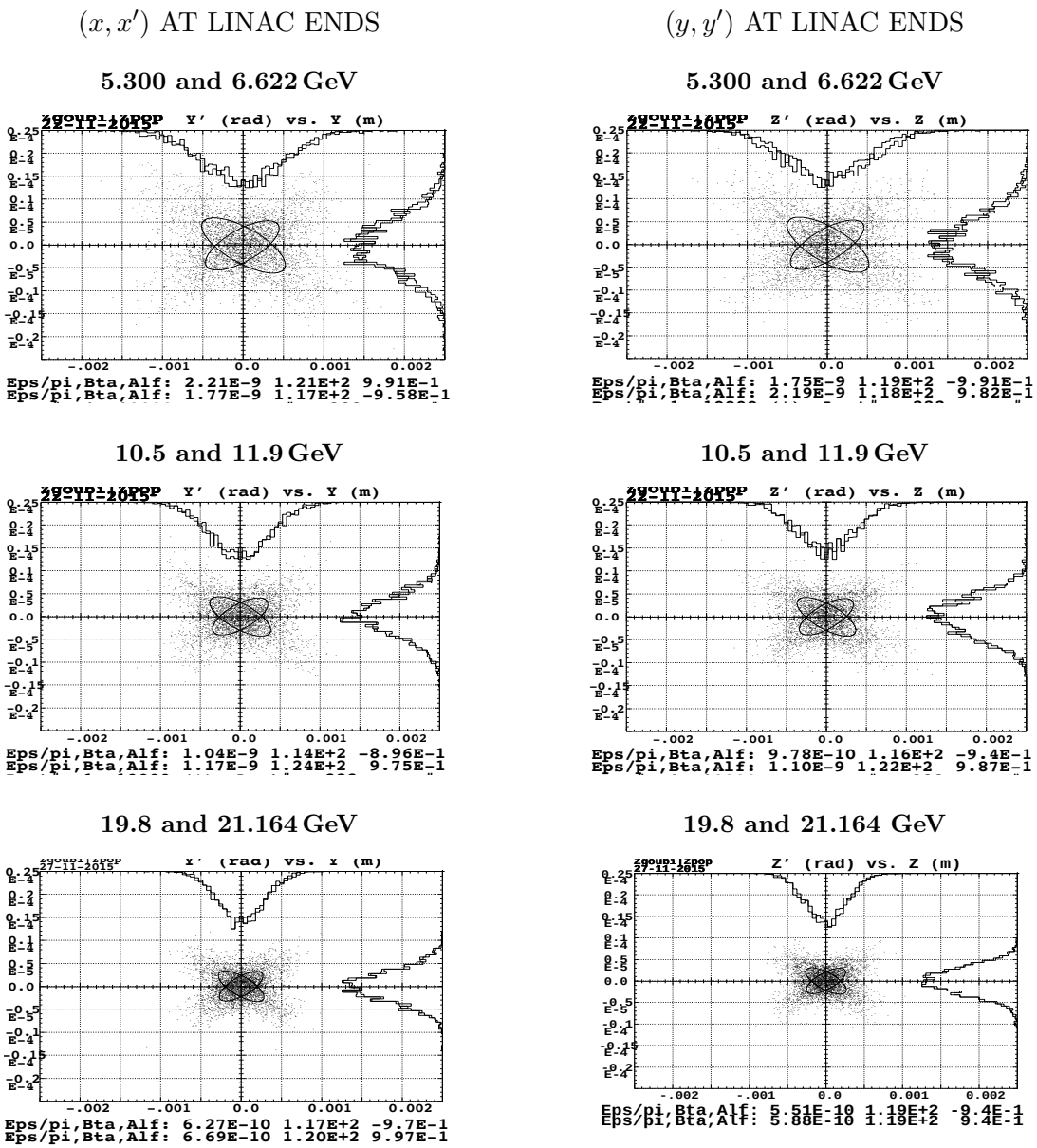

Figure 18: Bunch transverse emittances (non-normalized) and β_x, α_x, β_y, α_y parameters are given below the plots for each energy. These parameters appear to be well preserved, with $\beta\gamma$ betatron damping as expected, *i.e.* the same normalized emittances at the linac entrance and exit.

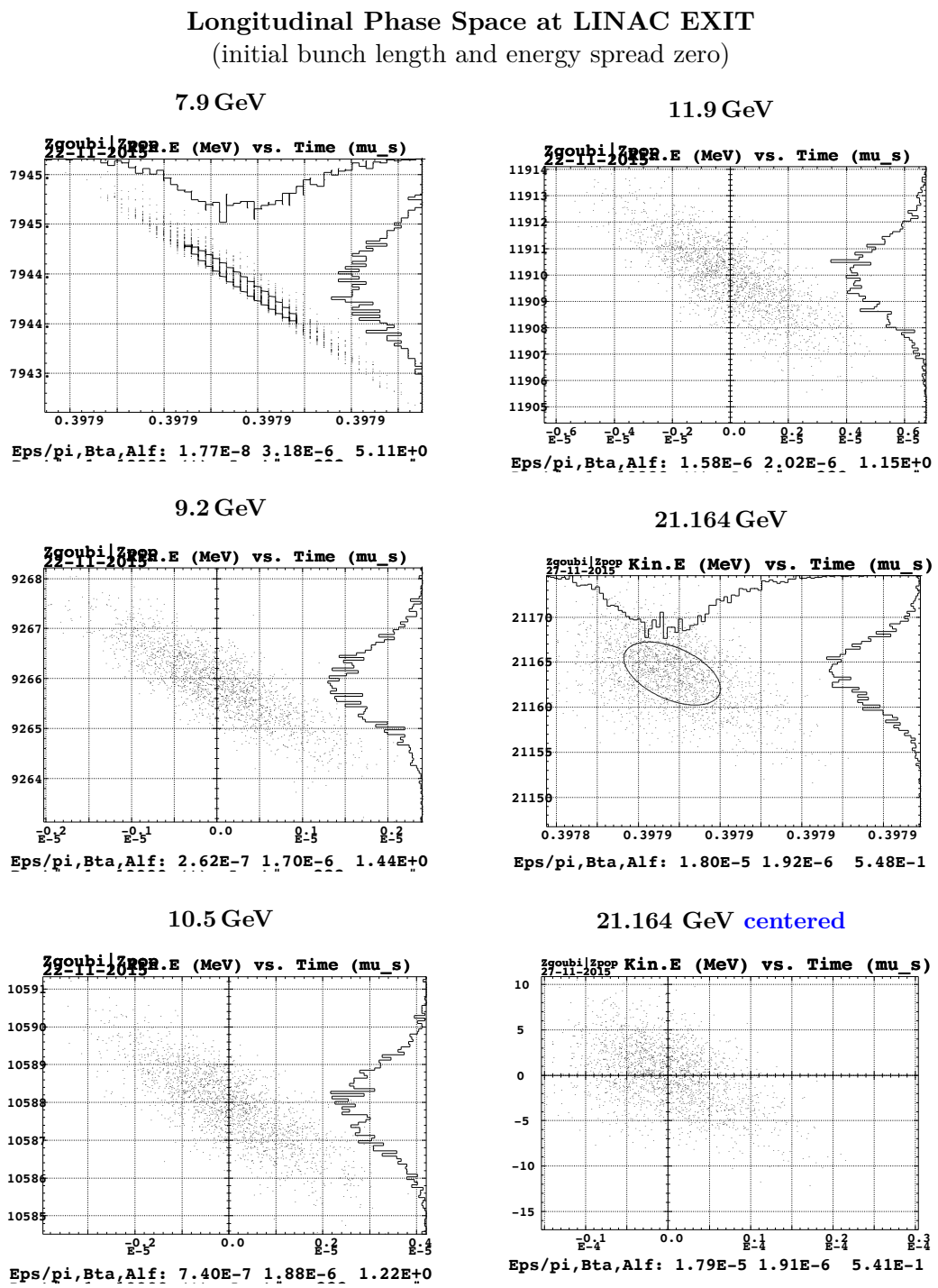

Figure 19: The bunch longitudinal rms emittance (in μeV.s) is given at the bottom of each plot for each energy. It appears to behave reasonably well (simulation-wise) over the full energy range from 5.3 to 21.16 GeV. Initially zero (at 5.3 GeV), ϵ_l remains small at top energy (bottom right plot); growth mechanisms include synchrotron radiation. There remains a need for further investigation.

SR off, DAMPING off

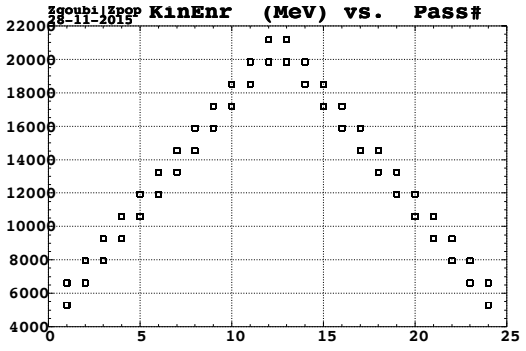

Figure 20: Average kinetic energy of a 2000-particle bunch at entrance and exit of the linac (hence two markers per pass, aligned vertically), as a function of pass number (each particle is represented by an empty box). What appears as one box is actually a superimposition of 2000 boxes, so the bunch is well confined from 5.3 GeV at injection to 21.164 GeV and back down to 5.3 GeV.

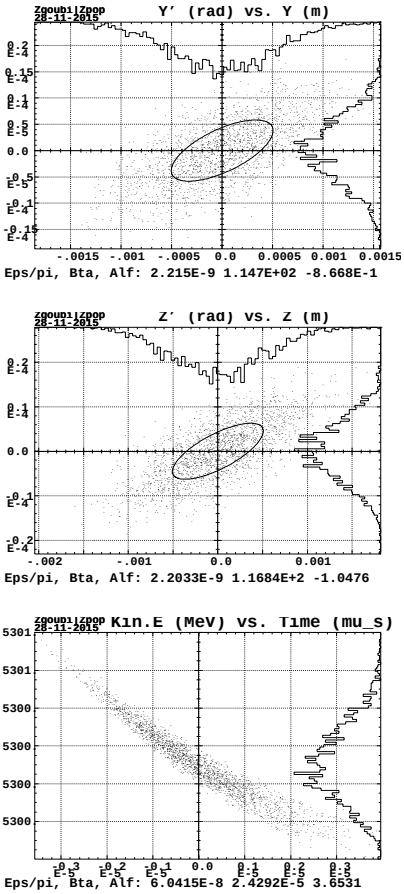

Figure 21: Phase spaces back to 5.3 GeV, horizontal (top), vertical (middle) and longitudinal (bottom). The former two feature a preserved 23 μm normalized emittance, the latter shows a very small final longitudinal emittance.

SR on, DAMPING on

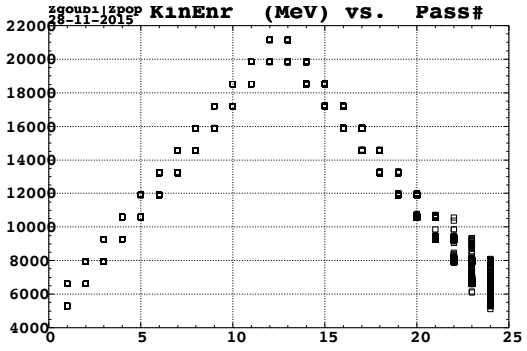

Figure 22: Average kinetic energy of the 2000-particle bunch, at entrance and exit of the linac (hence two markers per pass), as a function of pass number (each particle is represented by an empty box). The bunch appears to undergo serious energy spreading from pass 12 $\sim$ 13 on to final 5.3 GeV.

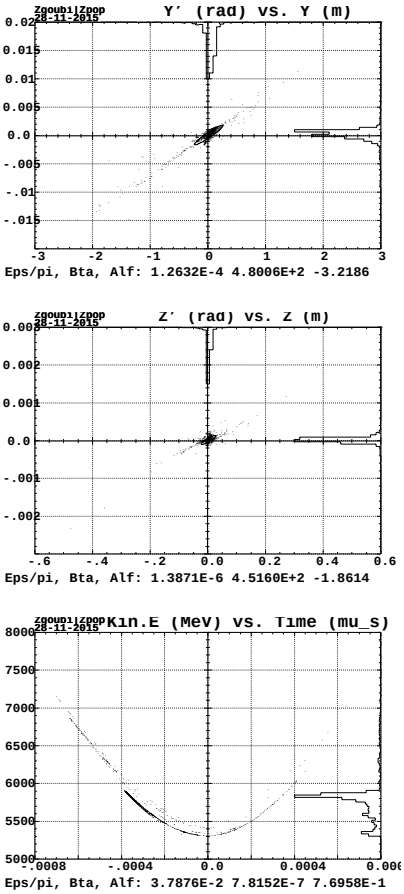

Figure 23: Phase spaces at 5.3 GeV after 23 recirculations, horizontal (top), vertical (middle) and longitudinal (bottom). The effects of SR are substantial.

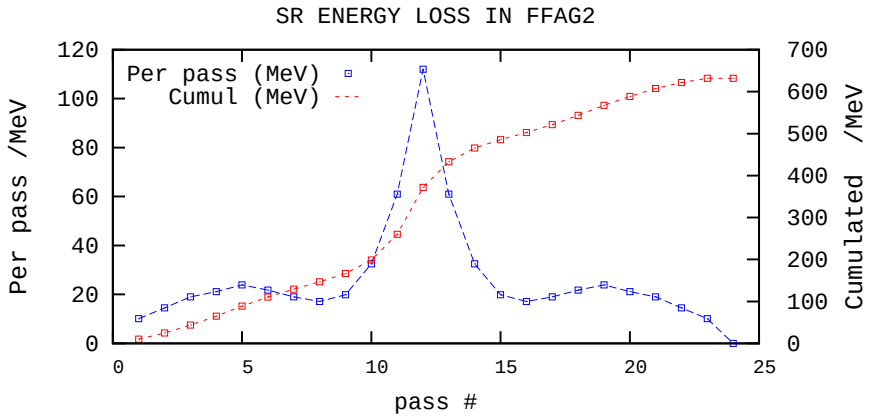

Figure 24: Evolution of SR energy loss over 23 recirculations from 5.3 to 21.1 GeV and back to 5.3 GeV. There are various reasons for the non-symmetry of the "per pass" curve with respect to pass number 12; the dominant cause needs to be investigated.

Polarization

The polarization state out of these simulation, for a 5000 particle bunch at top energy after acceleration from 5.3 to 21.164 GeV, is displayed in Fig. 25, in both SR off and SR on cases.

Bunch polarization at collision energy, 21.164 GeV

SR off:

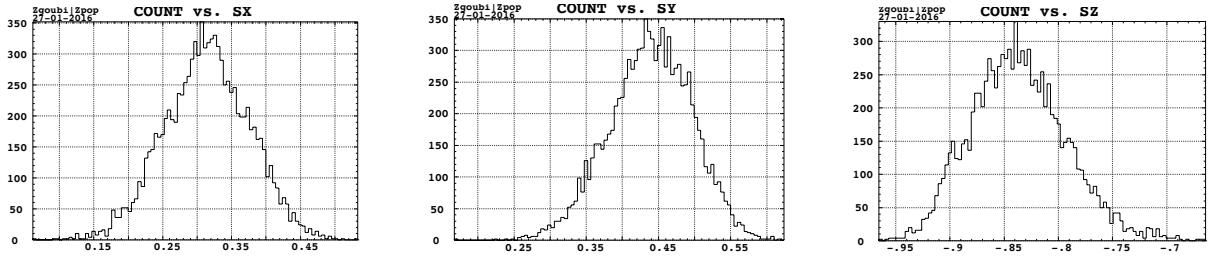

SR on:

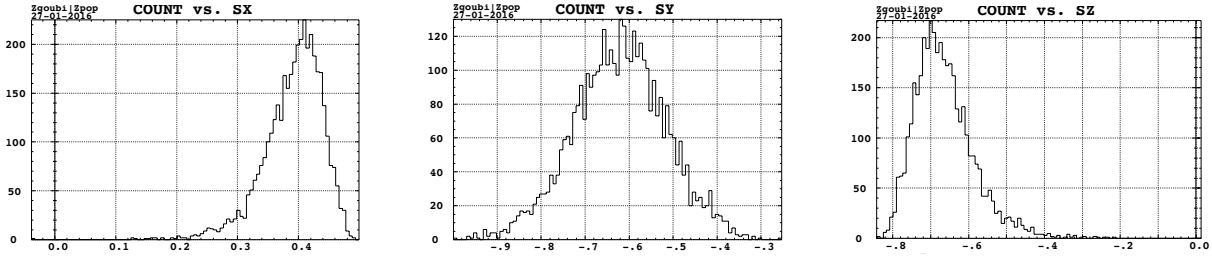

Figure 25: Bunch polarization states (for 5000 particles) at top energy, SR off (top row) and SR on (bottom row).

References

[1] E.C. Aschenauer et al., "eRHIC Design Study, Electron-Ion Collider at BNL", arXiv:1409.1633, Sept. 2014.

[2] F. Méot et al., Tracking studies in eRHIC energy-recovery recirculator, eRHIC Note 45, BNL C-AD (July 2015); `https://www.bnl.gov/isd/documents/89185.pdf`.

[3] F. Méot et al., eRHIC ERL modeling in Zgoubi, eRHIC Note 49, BNL C-AD (2016); `https://technotes.bnl.gov/PDF?publicationId=38865`.

[4] V. Ptitsyn, Electron Polarization Dynamics in eRHIC, EIC 14 workshop, JLab, 17-21/03/2014, `http://appora.fnal.gov/pls/eic14/agenda.full`.

[5] `https://oraweb.cern.ch/pls/hhh/code_website.disp_code?code_name=BETA`

[6] F. Méot, The ray-tracing code Zgoubi - Status, NIM A 767 (2014) 112–125.

[7] F. Méot, Zgoubi users' guide, `http://www.osti.gov/scitech/biblio/1062013`

3.12 Electromagnetic Design and Optical Properties of the CBETA-FFA Cell

Nicholaos Tsoupas, Brookhaven National Laboratory, C-AD, Upton, NY, USA.

Abstract

The CBETA project [1] is an electron accelerator to be commissioned in 2019 at Cornell University. This accelerator is unique, and the first of its type to combine two very important concepts, the Energy Recovery Linac (ERL) concept [2] and the Fixed Field Alternating Gradient (FFA) [3].

The CBETA accelerator consist of:

a) a 1.3 GHz 80 MeV superconducting Energy Recovering Linac (ERL) [2] which will accelerate/decelerate the electron bunches by 36 MeV each time the bunches pass through the Linac,
b) a splitter/combiner consisting of four transport lines placed at the exit/entrance of the ERL, and
c) a single recirculating FFA beam line which transports and recirculates through the ERL the four electron bunches with energies 42, 78, 114, and 150 MeV.

This paper focuses on the electromagnetic design and beam optics of CBETA's FFA cell which consist of a focusing magnet and a combined function magnet both based on the Halbach design [4] and made of permanent magnet material. Each Halbach type of magnet is surrounded by a window frame corrector magnet made of magnetic iron which is included in the electromagnetic calculations of the CBETA cell.

Introduction

The CBETA project [1] is the first electron accelerator which combines both the ERL [2] and the FFA [3] concepts. The project is currently at its initial stage of commissioning, which is scheduled to start this year, 2019. Fig. 1 shows a layout of the CBETA accelerator.

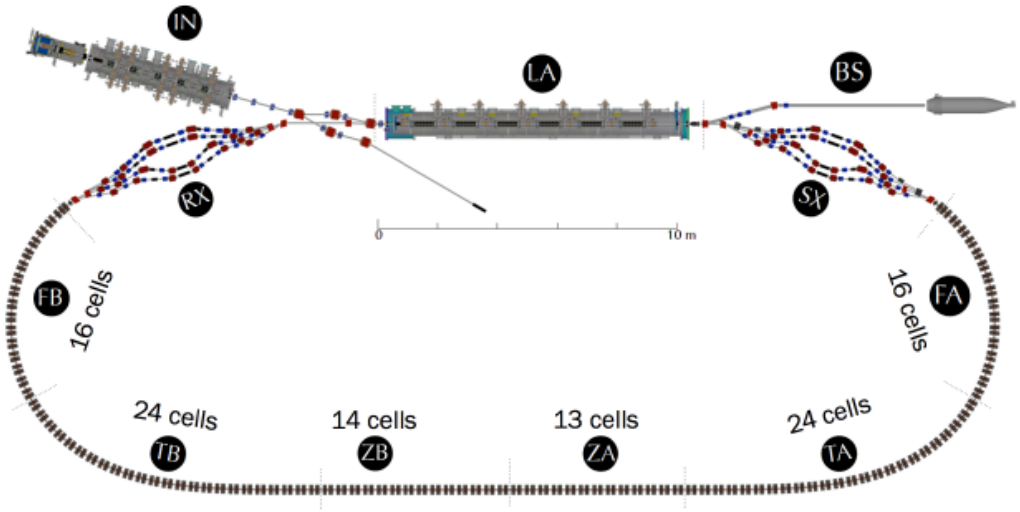

Figure 1: Layout of the CBETA accelerator. The section labeled (IN) is the 6 MeV electron injector into the CBETA accelerator. The section labeled (LA) is the ERL. The sections labeled (FA), (TA), (ZA), (ZB), (TB), and (FB) are the FFA sections which accommodate four recirculating electron bunches in the energy range from 42 MeV to 150 MeV. The sections (SX) and (RX) are the splitter and combiner respectively.

The section labeled (IN) in Fig. 1 is the injector which injects a 6 MeV electron bunch into the ERL (LA) which increases the bunch energy by 36 MeV to 42 MeV. The "40 MeV" beam line of the splitter (SX) transports the bunch to the FFA arc which recirculates the bunch to the entrance of the ERL for the bunch to receive an additional 36 MeV of energy. The bunch attains its final energy of 150 MeV after two more re-circulations in the FFA. Subsequently the energy of the bunch is reduced by 36 MeV each time the bunch passes through the ERL to exit the ERL at 6 MeV after four re-circulations through the ERL. The 6 MeV beam bunch is dumped in the designated electron beam dump (BS) shown in Fig. 1. It is remarkable that the electron bunches with energy range 40 MeV to 150 MeV can be transported by a single FFA transport line which consists of the sections (FA), (TA), (ZA), (ZB), (TB), and (FB) shown in Fig. 1. The straight sections (ZA) and (ZB) of the FFAG transport line consist of 27 cells each comprised of two Halbach type permanent magnets one of a focusing quadrupole and the other defocusing. The arc sections of the FFA (FA), (TA), (TB), and (FB) consist of 80 cells, each cell comprised of a focusing quadrupole (QF) and a combined function magnet (BD) which is the superposition of a dipole and a defocusing quadrupole. Fig. 2 is a perspective view of three (out of 16) consecutive FFA arc-cells of the (FA) and (FB) sections of the CBETA accelerator. Each QF and DB magnets of the FFA cell has a window frame dipole corrector which generates a vertical dipole field for the QF magnet and an horizontal dipole field for the BD magnet.

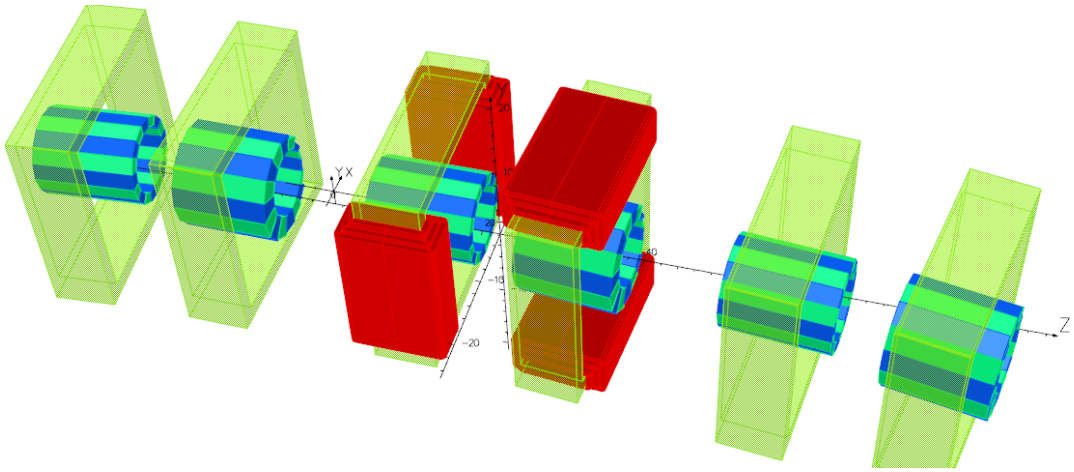

Figure 2: A perspective view of three consecutive cells of the (FA) or (FB) sections of the FFA transfer line shown in Fig. 1. Each cell consists of a focusing pure quadrupole (QF) and a combined function magnet (BD) providing a dipole and defocusing quadrupole. Both magnets QF and BD are Halbach type magnets and each magnet has a dipole corrector window frame magnet which surrounds the magnet. The dipole corrector of the QF magnet generates vertical field and that of the BD generates horizontal field.

The beam optics of each cell and of the whole CBETA accelerator [5] is calculated from 3D field maps which are generated by the OPERA computer code [6]. The cells of the (FA) and (FB) sections are identical but the cells in the sections (TA) and (ZA) vary, and the cells in the straight sections (TB) and (ZB) are mirror images of those in the sections (TA) and (ZA). The subject of this paper is to report on the electromagnetic design of the magnetic elements QF and BD which comprise the cells of the FFA arcs. The study includes the interference between the magnets within each cell and the interference between the magnets of neighboring cells. The iron corrector magnets which surround every magnet of the cell are also included in the interference calculations. This study was initiated at BNL by the author and other researchers at BNL as part of the eRHIC project [7] and subsequently extended to the CBETA project. This paper presents the part of the work done by the CBETA team.

3.12.1 The electromagnetic design of the FFA cell

The initial beam optics [8] of each cell and of the whole accelerator is designed by considering each magnetic element of the accelerator as a lump element represented by a first order transfer matrix (R-matrix). This initial study defines with good approximation the geometry of the magnetic elements (aperture, length) within the cell and the strength of the multipoles (dipole, quadrupole) of each magnet. Following the initial beam optics which define the aperture and strength of the magnetic elements the 2D and 3D electromagnetic design of the cell's Halbach type magnetic elements is performed.

The 2D electromagnetic design

The cross section of the QF and BD magnets of the FFA cell is shown in Fig. 3. Each magnet is made of 16 wedges of permanent magnet material of NdFeB-NEH. The QF magnet has a window frame corrector magnet which generates vertical dipole field and the corrector of the BD magnet generates a horizontal dipole field. The "BH" curve of the NdFeB-NEH material is

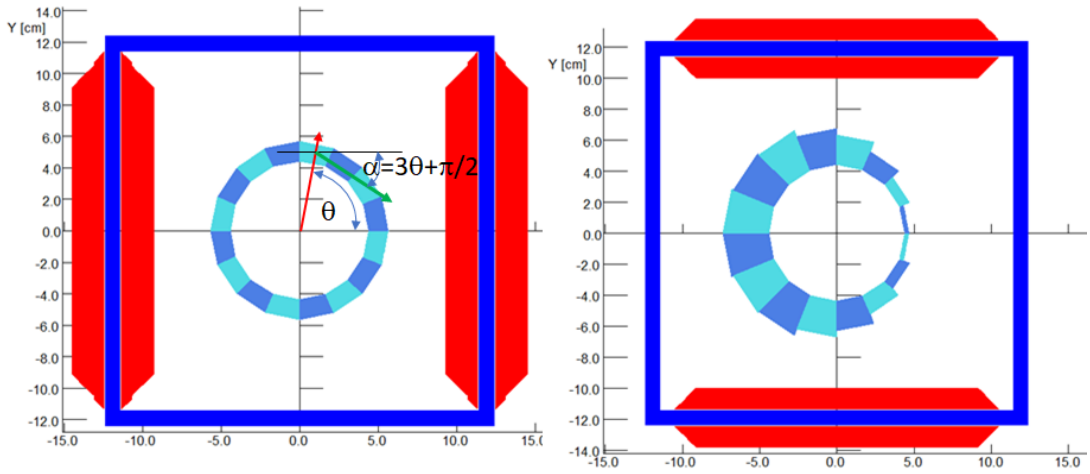

Figure 3: The cross section of the QF (left) and BD (right) Halbach magnets of the FFA arc-cell. Each magnet is made of 16 permanent magnet wedges. The QF magnet has a window frame corrector magnet which generates vertical dipole field and the corrector of the BD magnet generates a horizontal dipole field.

shown in Fig. 4. The value of the remnant field B_r of the NdFeB-NEH material is 1.204 T and the coercive-force H_c=11.9 kOe at a temperature of 20° and the permeability of this material at this temerature is μ=1.012. The size of the permanent magnet wedges of the QF wedges which provide the strength of the magnetic multipoles as calculated by the optics study can be calculated by the formula [9]

$$G(r_i, r_o) = 2B_r \cos^2\left(\frac{\pi}{M}\right) \frac{\sin\frac{2\pi}{M}}{\frac{2\pi}{M}} \left\{\frac{1}{r_i} - \frac{1}{r_o}\right\} \tag{1}$$

In Eq. (1) the symbols G, r_i and r_o are the gradient, inner aperture radius and outer radius of the QF quadrupole Halbach magnet taking into account the BH curve. M is the number of wedges which in this case is 16. Although Eq. (1) defines the gradient and geometry of the QF Halbach magnet quite well, the 2D modeling of the magnet using OPERA provides more accurate values of the r_i and r_o that generate the required gradient of the magnet. The magnetization direction of each wedge which is required in the model for the OPERA calculation and most important

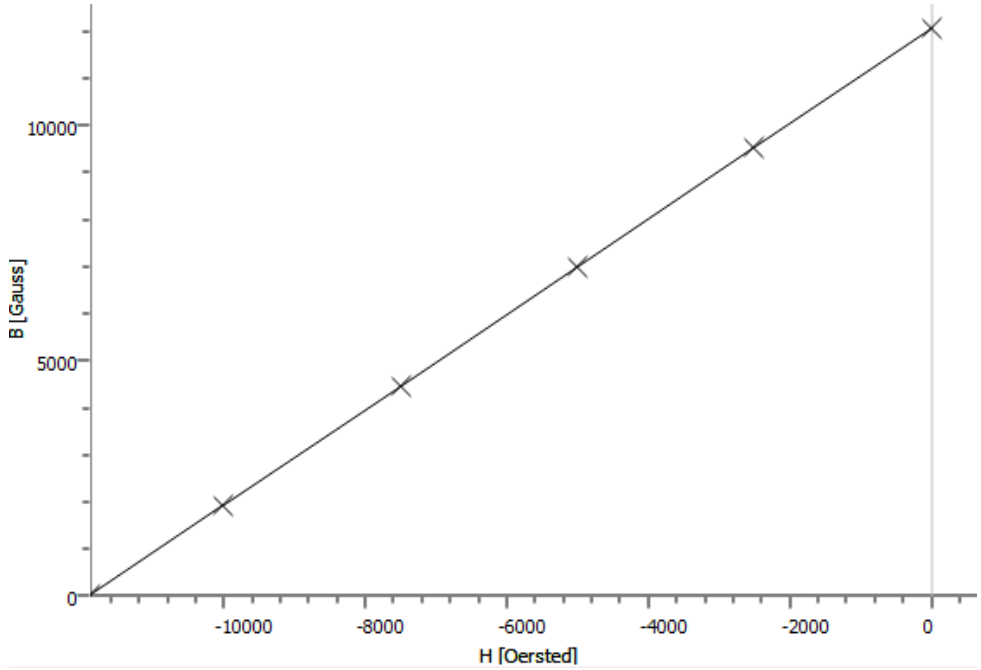

Figure 4: The BH curve of the permanent magnet material NdFeB-NEH. The value of the remnant field B_r is 1.204 T and the coercive-force H_c value is 11.9 kOe. This BH curve corresponds to the 20° temperature. The permeability of the material at this temperature is μ=1.012.

for manufacturing the magnet is given by Eq. (2).

$$\alpha = (n-1)\theta + \pi/2. \tag{2}$$

In Eq. (2) the symbol n is the number of magnetic poles of the multipole generated by the Halbach magnet. In this case $n = 4$ for a quadrupole and the symbols θ and α, which are shown in Fig. 4, are the azimuthal angle of the wedge and the magnetization direction of the wedge with respect to the x-axis. The BD magnet is a combined function magnet to provide a dipole and a quadrupole field. It is a modified type of Halbach magnet which has been made by an optimization process which varies the radial length and the magnetization of each of the wedges [10] to generate the required value of the dipole and quadrupole strength. It is understood that the optimization process satisfies the symmetry properties of the fields. In Fig. 3, the space between the inner region of the window frame magnet and the outer region of the permanent magnets is occupied by an aluminum block. The aluminum block has holes to allow the circulation of constant temperature water to keep the temperature of the permanent magnet stable.

The 3D electromagnetic design

An accurate knowledge of the magnetic field in the regions of the FFA cells, where all four bunches circulate, is needed to ascertain the correct beam optics to keep all four bunches under control. The 3D electromagnetic study of the CBETA magnets provides accurate fields especially in the fringe field regions where the 2D study cannot provide such fields at all. In addition the 3D study will provide the correct fields due to the interference of the QF and BD magnets within the cell as well as the magnets at the neighboring cells including the iron cores of the corrector magnets. In fact two methods were used to calculate the beam optics of the FFA cell. The first method is based on the beam optics which utilizes field maps that include the interference of all the magnets within the cell including the magnets of neighboring cells, and the other method

assumes superposition of the field maps produced by the individual magnets QF and BD of the FFA beam line. It turns out that the beam optics generated by either method almost coincide, both methods providing stable circulating beam [5].

Setting up the 3D model of the FFA cell

As mentioned earlier the initial beam optics calculations of the FFA cell assume that the magnets of the cell generate uniform dipole and quadrupole fields with no fringe fields. This approximation comes under the name Sharp Cut-Off Fringe Field (SCOFF). This initial beam optics study provides with some accuracy the geometry of the cell magnets, their length, aperture, relative position and the strength of the dipole and quadrupole of each magnet. Subsequently a 2D model of each cell magnet provides a more accurate geometry of each magnet by the use of the OPERA computer code. The fringe fields of the magnets are taken into account by the 3D calculations using the "Modeller" module of the OPERA computer code. In addition these 3D calculations take into account all possible interference effects between the magnets within the cell as well as the magnets of neighboring cells. From the results of the OPERA solver a 3D field map on a rectangular grid is generated and is used in the Zgoubi computer code [11] to calculate the beam optics of the FFA cell. A brief description of setting up the 3D model of the cell for magnetic field calculations using the OPERA computer model is given below.

a) The beam optics of the cell generated by the SCOFF approximation model provide the coordinates of the entrance and exit of the cell magnets at the median plane. These coordinates are shown by red dots in Fig. 5 which is a schematic diagram of the cross section at the median plane of three consecutive FFA cells. The highlighted yellow areas in Fig. 5 represent the aperture of the magnets. It is understood that the magnetization vector of the permanent magnet wedges is also rotated when each magnet is rotated about the y-axis which is normal to the (x, z) median plane. Some details on the 3D setup of the cell model appear in APPENDIX I.

b) The cross sections of QF and BD magnets as they appear in the 3D-three-cell OPERA model shown in Fig. 2 have been calculated using the 2D OPERA model discussed earlier, and are shown in Fig. 3.

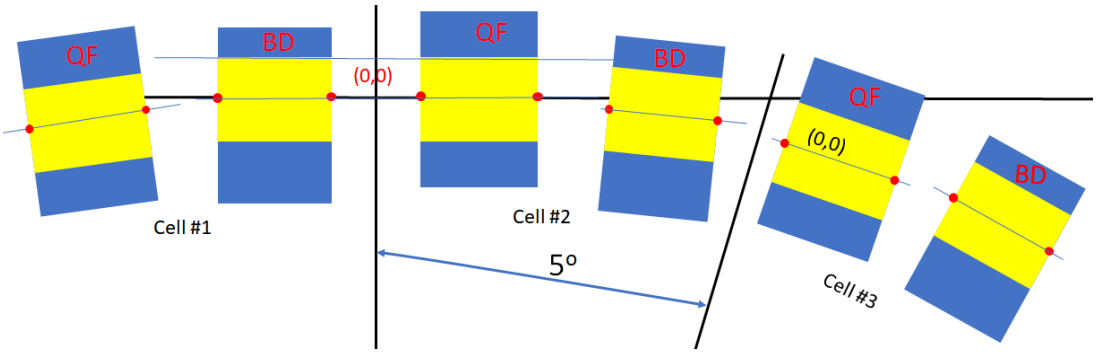

Figure 5: A schematic diagram of the layout of the CBETA Halbach magnets at the median plane of three consecutive FFA arc-cells. The small red circles correspond to the coordinates at the entrance and exit of the magnets. The yellow highlighted areas are the apertures of the magnets at the median plane. The reference trajectories of each of the four bunches with energies 42, 78, 114, and 150 MeV bends by 5° in each cell.

c) Prior to the solution of the 3D-three-cell OPERA model each wedge of the QF and BD magnet is assigned the correct magnetization direction and also assigned the "BH" curve

aa shown in Fig. 4. Some specifications of the QF and BD cell magnets, after the final optimization of the FFA cell, appear in Table 1.

d) Following the solution of the 3D-three-cell OPERA model by the TOSCA module of the OPERA code, a 3D field map is generated on a rectangular three dimensional grid. The field map contains the components of the field at the coordinates of each grid point. This field map of the cell is used by the ray-tracing computer codes Zgoubi [11] or BMAD [12] to calculate the reference trajectories and the beam parameters of the beam bunches circulating in the FFA cells with four different energies.

The final design of the FFA cell's beam optics was obtained after a few iterations. In each iteration a new 3D-three-cell OPERA model was produced and a new field map was generated. In each iteration a change in the aperture, relative location and strength of magnets was introduced to optimize the beam trajectories and the beam parameters in the cell.

Table 1: Some specifications of the QF and DB magnets of the FFA cell.

Magnet	r_{inner} [cm]	r_{outer} [cm]	L [cm]	Dipole [T]	Quad [T/m]
QF	4.405	5.651	12.17	0.0	11.43
BD	4.405	varies	13.33	-0.317	10.87

Field histograms of the FFA cell

This subsection shows a 3D histogram plot of the B_y component of the field at the median plane of one of the FFA arc-cells. Fig. 6 shows the placement of the rectangular patch over which the 3D histogram is plotted and Fig. 7 shows the 3D histogram itself by removing the magnets.

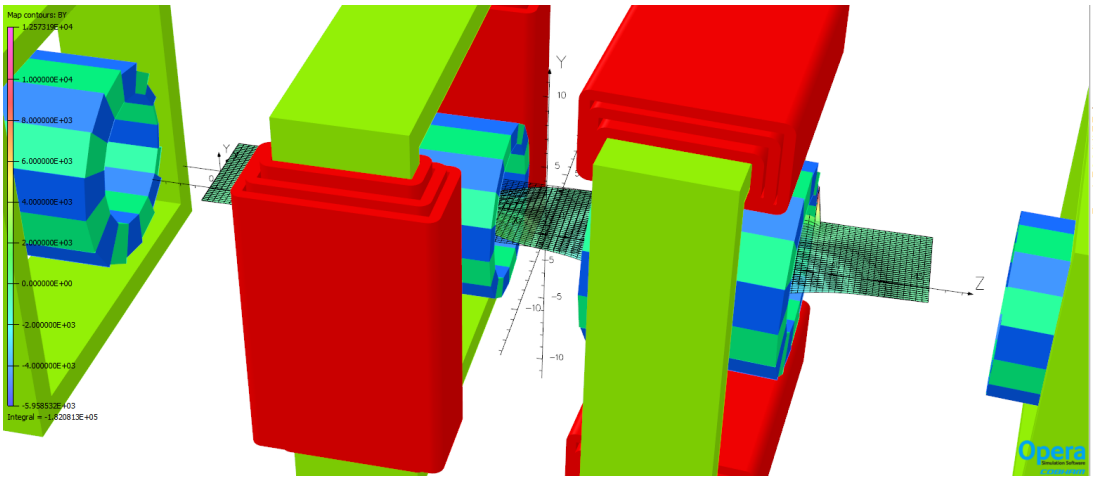

Figure 6: The plot of the B_y component of the field over a rectangular (x, z) batch at the median plane $(y = 0)$ of the FFA cell. A better view of the field is shown in Fig. 7 below.

Measurement and correction of the multipoles of the Halbach magnets

Following the mechanical assembly of each FFA Halbach magnet, the integrated multipoles of the magnet was measured by the rotating coil method [13]. Fig. 8 is a picture of a modified Halbach

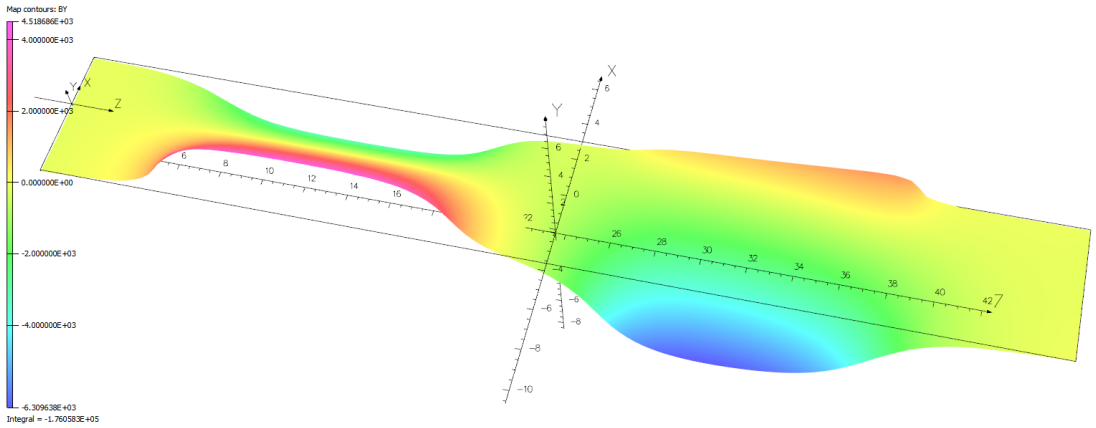

Figure 7: The plot of the B_y field over a rectangular (x, z) batch at the median plane $(y = 0)$ of the FFA cell. The magnets have been removed for a clear view of the B_y components of the field.

quadrupole [14], which avoids the synchrotron radiation emitted by electron bunches, and a rotating coil device which measures the integrated multipoles of the magnet. Any measured

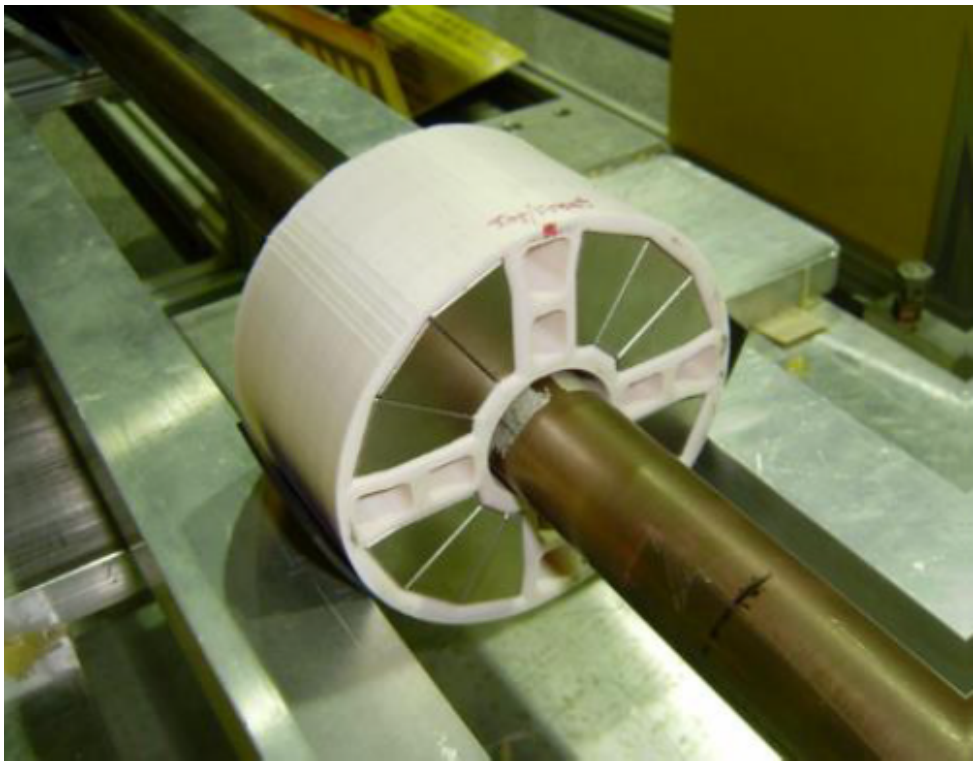

Figure 8: A modified Halbach quadrupole to avoid the synchrotron radiation, and a rotating coil device which measures the integrated multipoles of the magnet. The white material of the magnet is to hold the permanent magnet wedges together for the magnetic measurements only. The actual assembly of the magnet is different.

multipoles with values beyond the acceptable range for a stable circulating beam are corrected by the "wire technique" method which is described in reference [14] with a brief description given here. The left picture in Fig. 9 is a cross section of a modified Halbach quadrupole with holes (blue squares) which can accept wires of soft magnetic material like steel-1006 and of proper thickness. The placement of wires in the appropriate holes reduces the strength of undesired

multipoles which are measured by the rotating coil method. The OPERA computer code without the optimizer module was used initially to calculate the proper placement and wire thickness to minimize a particular multipole at a time. The development of a faster code [15] considerably reduced the time taken for the process of reducing the undesired multipoles. The right-hand picture is the actual modified Halbach quadrupole whose cross section is shown in the picture on the left. The white material in the right picture is to hold the permanent magnet wedges for magnetic measurements only. The engineering of the actual magnet to be used in a beam line will be different.

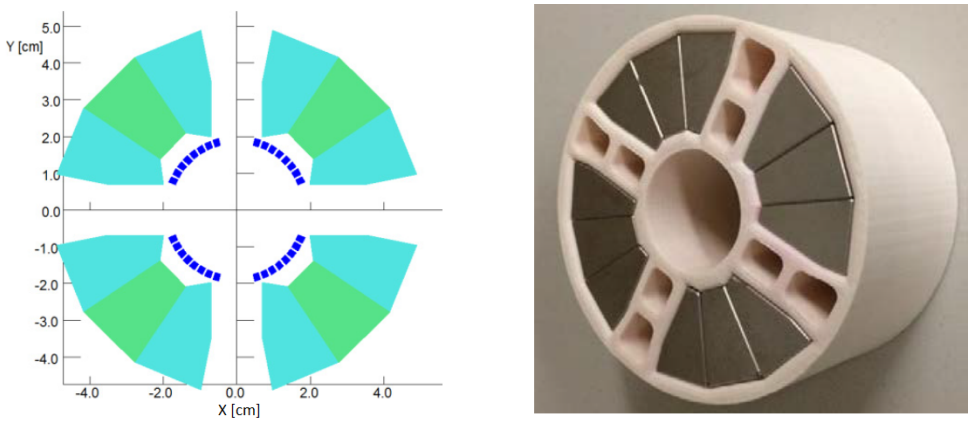

Figure 9: A modified Halbach quadrupole (left) with holes (blue squares) for the placement of magnetic wires to reduce the strength of unwanted multipoles which are measured by a rotating coil. (Right) A picture of a modified Halbach quadrupole magnet whose cross section is shown in the left picture. The white material in the right picture is to hold the permanent magnet wedges for magnetic measurements only. The engineering of the actual magnet to be used in a beam line will have the white material between the wedges removed.

3.12.2 Superposition of corrector fields with the field of the QF and QD magnets

Experimental measurements [16] showed that the excitation of the dipole corrector magnets did not affect significantly the multipoles of the the Halbach type permanent magnets to alter the trajectories of the bunches and the beam optics of the cell to drive out of control the bunches in the FFA line. This experimental observation suggests that the beam optics calculations that are based on the complete 3D OPERA field maps of a the FFA cell as described earlier in the paper, can be simplified by using the individual field maps of the QF and BD magnets including the window frame corrector magnet of each magnet. It is understood that the field maps of the individual magnets will be superimposed properly to represent the location and orientation of the magnets in a cell. Indeed using the Zgoubi computer code [5], it is proven that the beam optics, and the trajectories of the bunches in the FFA arc-cell generated by the field maps derived from the 3D-three-cell OPERA model, are almost identical to the beam optics and trajectories of the reference particles of the bunches when the field maps are generated by the superposition of the individual field maps of the QF and BD magnets.

3.12.3 Example of the beam optics of the FFA cell

This section shows an example of the trajectories and the beta functions generated from the use of the computer code Zgoubi which raytraces using the 3D field maps provided by the OPERA computer code. The left picture in Fig. 10 shows the trajectories of the reference particles for

the four bunches with energies 42, 78, 114 and 150 MeV. The right picture are the $\beta_{x,y}$ and $\eta_{x,y}$ functions in the arc-cell for the energy of 150 MeV.

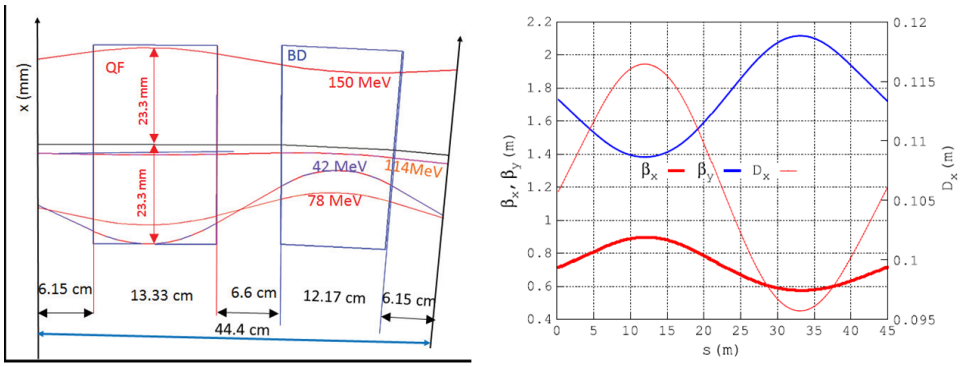

Figure 10: (Left) the trajectories of the reference particles for the four bunches with energies 42, 78, 114 and 150 MeV. (Right) The $\beta_{x,y}$ and $\eta_{x,y}$ functions in the arc-cell for the energy of 150 MeV.

Acknowledgments

Work supported by the United States Department of Energy. The author would like to express his gratitude to all the CBETA collaborators who have brought the CBETA accelerator to the commissioning stage.

3.12.4 APPENDIX I

This section presents some details of the 3D setup of the 3D-three-cell OPERA model. Table 2 shows the coordinates at the entrance and exit of the QF and BD magnets as the magnets are placed to form three consecutive cells as shown in Figs. 2 and 5. These coordinates at the entrance and exit of the magnets in each cell are shown schematically by the red dots in Fig. 5. In the FFA arc-cell it turns out that the BD magnet is rotated about the y-axis by 5° with

Table 2: The entrance and exit coordinates of the QF and BD magnets shown by red dots in Fig. 5.

Cell#1			
QF		*BD*	
x_i z_i	x_o z_o	x_i z_i	x_o z_o
-1.447, -38.191	*-0.288, -24.94*	*0.0, -18.35*	*0.0, -6.15*
Cell#2			
QF		*BD*	
x_i z_i	x_o z_o	x_i z_i	x_o z_o
0.0, 6.15	*0.0, 19.45*	*-0.29, 26.04*	*-1.35, 38.20*
Cell#3			
QF		*BD*	
x_i z_i	x_o z_o	x_i z_i	x_o z_o
-2.42, 50.45	*-3.58, 63.70*	*-4.44, 70.24*	*-6.56, 82.25*

respect to the QF magnet. The QF and BD magnets which comprise the FFA arc-cell form

a periodic structure and as such can be solved by the OPERA computer code by assigning periodic boundary conditions at the entrance and exit of the cell. The solution of such a model having periodic boundary conditions has been obtained; however for reasons that are explained below it was decided to obtain the 3D field map of the cell, not from the cell with the periodic boundary conditions but from the central cell of a three cell-consecutive model as shown in Figs. 2 or 5. In the three-cell model shown in Fig. 5, cell #3 is generated by translating the origin (X, D)=(0.0 cm, 0.0 cm) of the upstream cell #2 by (DX, DZ)=(-7.63 cm, 88.31 cm) and rotating it about this new origin by 5° about the y-axis. The boundary conditions of the three-cell model were set as if the outer surfaces of the air surrounding the three-cell model are at infinity. The solution of the three-cell model is in agreement with the solution obtained from the periodic model when the fields compared are calculated using the "nodal" method but there is disagreement when the fields are calculated using the "integral" method. The "integral" method calculates the fields with better accuracy; therefore we used the 3D field map generated by the 3D-three-cell OPERA model. It is under investigation why the "integral" method of calculating the fields as derived from the solution of the periodic model does not provide the "correct" results.

References

[1] https://arxiv.org/abs/1706.04245

[2] Energy Recovery Linacs - The CERN Accelerator School https://cas.web.cern.ch/sites/cas.web.../2017-09-07-cas17-erl-andreasjankowiak.pdf

[3] https://arxiv.org/abs/1604.05221

[4] K. Halbach, "Application of permanent magnets in accelerators and electron storage rings", J. Appl. Phys., 1985, 57, (8),pp. 3605–3608

[5] F. Méot *et al.*, https://www.bnl.gov/isd/documents/79375.pdf

[6] Vector Fields Inc. http://www.vectorfields.com/.

[7] V. Ptitsyn, "The ERL Based Design of Electron-Hadron Collider eRHIC", J. Appl. Phys., 1985, 57, (8),pp. 3605–3608

[8] W. Lou, *et al.* "THE BEAM OPTICS OF THE FFAG CELL OF THE CBETA ERL ACCELERATOR" IPAC2018, Vancouver, BC, Canada

[9] S.M. Lund and K. Halbach, "Iron free permanent magnet systems for charged particle beam optics", UCRL-JC-121454 (1995)

[10] Private Communication. sbrooks@bnl.gov

[11] F. Méot, "AN ALL-PURPOSE ACCELERATOR CODE, ZGOUBI" Proceedings of Cyclotrons2013, Vancouver, BC, Canada

[12] https://www.classe.cornell.edu/bmad/

[13] https://cds.cern.ch/record/245405/files/p138.pdf

[14] N. Tsoupas *et al.*, "Main Magnets and Correctors for the CBETA and eRHIC Projects, and Hadron Facilities", Physics Procedia, Volume 90, 2017, Pages 143-150

[15] Private Communication. sbrooks@bnl.gov

[16] A. Jain, Private communication, BNL

3.13 A Review of Nonscaling CW FFAs for Proton and Ion Therapy Applications[1]

Carol Johnstone, Fermilab, USA.
Reinhard Schulte, Loma Linda University, USA

Abstract

Significant progress on compact, variable-energy versions of non-scaling fixed field accelerators with alternating strong-focusing gradients (nsFFA) has been made and adapted to proton and ion therapy. Not only has isochronous (CW) capability been demonstrated in a realizable design, an isochronous racetrack format has evolved which supports lengthy, synchrotron-like straight sections. Long straight insertions promote low-loss injection and extraction systems and further facilitate extracting lower-energy orbits using a bipolar bump-magnet system. To efficiently extract variable energy using this method, the accelerator complex requires separated accelerator stages, each stage with limited but therapeutically optimized energy ranges targeting specific cancer types and penetration depths. Different energy stages further support multiple treatment rooms increasing patient throughput and reducing treatment cost. The staged system proposed here also realizes cost savings in gantries by tailoring delivery to different therapeutic energies and beam requirements, promoting the requirement for only one high-energy gantry in the facility. The proposed facility consists of 3 stages, a 30 MeV injector, a 30 - 90 MeV/nucleon FFA for shallow cancers, and 90 - 250/330 MeV/nucleon stage for deep tumors, pelvis for example. The higher energy of the final stage, 330 MeV/nucleon is preferred to support Proton Computed Tomography. Isochronous FFA stages can be designed to accelerate either protons or ions with charge to mass of 1/2.

Introduction

Cancer is the second-largest cause of death in the U.S. with about half of all patients receiving definitive radiation therapy; overall approximately two-thirds of all cancer patients will receive some form of radiation therapy. The majority of radiation treatments are still performed with linacs that generate energetic electron beams directed onto targets producing secondary X-rays for photon therapy. Particle beam therapy using proton and ion beams, however, have better dose specificity and conformal deposition compared with conventional radiotherapy and has rapidly evolved into a frontier in cancer therapy over the last decade. Clinical experience with protons and ions has produced remarkable local tumor control rates in single-institution studies.

However, despite the promise of gross reduction in acute and late effects and overall quality of life after treatment, the expansion of proton and especially ion therapy centers has been limited by initial capital cost, lengthy treatment course, insurance reimbursement schedule issues, and overall economic sustainability of centers, especially in the competitive U.S. environment. This paper addresses limitations of current accelerator systems and single-purpose centers for therapy, and proposes a more economically sustainable, multipurpose center model, in addition to reviewing technical advances in accelerators and beam delivery represented by recent developments in nonscaling FFA technology.

3.13.1 Dual Accelerator Particle Therapy Model

To address non-competitiveness with photon therapy, multiple applications and sources of revenue must be incorporated into the hadron therapy center, optimally at the civil planning stage.

[1]Work supported by Fermi Research Alliance, LLC under contract no. DE-AC02-07CH11359

As discussed in the DOE report "Accelerators for America's Future" [1], the key to further progress in cancer therapy is through research and development. A sustaining facility "would enable biological studies; development of imaging technologies; exploration of scanning and controls for safe, flexible beam delivery; investigation of small-mass dosimetry instrumentation; and, perhaps most important, hosting of clinical research, clinical trials, and advanced patient protocols for newly developed technologies." In 2013 NCI jointly with DOE organized a workshop on ion beam therapy where more than 60 experts from diverse fields related to radiation therapy were asked to define research and technical needs for advancing charged particle therapy, producing a detailed final report [2]. Table 1 summarizes technical accelerator and beam delivery specifications derived from this report. In summary, in addition to progress in technical systems, a sustainable center needs to support research in advanced protocols to reduce overall cost of treatment course (without compromising clinical outcomes), a plan for particle-based imaging and dose verification dosimetry, and have the capability to deliver high intensities ($\geq$20 Gy/min) for radiobiology and hypofractionation research – in addition to including opportunistic commercial revenue streams.

To effectively stage a facility for an economically optimum therapy program, it is critical to first assess therapeutic needs in terms of beam parameters and delivery technology. Table 2 [3] is a model-based treatment using 70 MeV as the lower limit since many nozzles (or energy degraders) only work in the 70 to 250 MeV range. (Lower energies are generally obtained using plastic range shifters placed close to the skin and aperture, for example with breast, pediatric patients, and parotid tumors in the jaw.) The data clearly show a breakdown of cancer by beam energy and argues for a dual energy accelerator system as optimal - where $E \leq 150$ MeV can be used for roughly 50% of the patients. Higher energy is only required for deep tumors such as prostates. Two accelerator stages are therefore optimal for proton therapy. A dual-stage accelerator model has the following applications and advantages.

- Conclusions from patient data
  - 1^{st} Accelerator Stage: $\sim$ 30 to ($\sim$90/150) MeV/nucleon for ions/protons
    Lung, breast, CNS, rectum, pediatric, head & neck : $\sim$50% of patients
  - 2^{nd} Accelerator Stage: ($\sim$90/150) to (250/330) MeV/nucleon for ions/ protons
    Deep tumors, pelvis, and prostate
- Gantry costs
  - Only one high-energy gantry needed
  - Lower-cost, much smaller gantry delivers beam from 1st stage
  - Solves problem of oversubscribed high energy gantry
- Patient Throughput and efficiency
  - Allows simultaneous operation of $\geq$ 2 treatment rooms
  - Multi-room operation will reduce treatment costs

3.13.2 Radioisotope Production in a Therapy Facility

In addition to radiotherapy, an economic opportunity for medical radioisotope production can be implemented exploiting the infrastructure and injector accelerator at incremental additional cost to the overall facility. Radioisotopes can provide substantial income and an ongoing revenue stream to support operational and maintenance overheads for the entire facility, well in excess of any added impact. Production of radioactive isotopes has many applications with the most direct benefits realized in medical diagnosis and therapy - impacting the quality of life for therapy patients [1, 4]. The benefits of expanded availability of key isotopes domestically are considered

Table 1: Ion therapy facility clinical requirements from the NCI/DOE report [2] are summarized.

Multi-ion capability	p, He, Li, B, C (O and Ne also desirable) Fast switching between ion species (≤ 1 sec)
Energy range	60 MeV/nucleon to 430 MeV/nucleon for ions; 250 MeV for protons. Depths up to 30 cm for carbon ions
Field size	At least $20 \times 20\,\mathrm{cm}^2$ (optimally up to $40 \times 40\,\mathrm{cm}^2$)
Real-time imaging (radiography and CT): For tumor position verification and motion control	For patient sizes up to 60 cm in depth. (For protons this is 330 MeV)
Dose delivery rates: Minimum requirement Hypofractionation treatments in under 1 minute, (ideally in one breath-hold for motion control)	 20 Gy/minute up to 5 - 8 Gy/8 sec (breath-hold) for a cubic liter (corresponding to 4×10^{12} p/sec)
Pencil beam scanning: Fast treatment for a large variety of tumor sizes and shapes. Two extremes are considered: 30 cm×30 cm tumor single layer in depth and a cubic volume	Transverse scanning rate of 1-10 cm/msec Energy step time of 10-100 msec (These are present state-of-the-art for NC and SC magnetic components)
Transverse beam size: selectable, with stable, Gaussian profiles.	3 mm to 10 mm FWHM
Energy step size	Protons: 2 MeV (~ 0.25 cm in range) Carbon: 2 MeV/nucleon (~ 0.1 cm in range)
Lateral targeting accuracy at the Bragg peak	Protons: ± 0.5 mm Carbon: ± 0.2 mm
Dose accuracy/fraction	2.5% monitored at ≥ 40 kHz during dose deposition

Table 2: Proton therapy data from Paul Scherrer Institute categorized per cancer (based on discussions with G. Coutrakon, 2009.)

Site	**Percentage**	**Energy Range (MeV)**	
Lung	9%	70 - 170	
Breast	3%	70 - 140	
CNS	15%	70 - 150	(central nervous system)
Pediatric	8%	70 - 150	
Head & Neck	15%	70 - 150	
Prostate	45%	200 - 250	
Other	2%		

substantial and even critical. Such a capability provides added value in that it is aligned closely with the interests of the oncology user community.

One example is Radioimmunotherapy (RIT) with radiolabeled antibodies, a promising, newly emerging cancer treatment modality that has achieved response rates of up to 80 percent in

a limited number of cancers. RIT selectively delivers radionuclides that emit α-particles, β-particles, or Auger electrons to tumors. The isotope group of the Nuclear Science Advisory Committee (NSAC), recognizing the gap between production and demand particularly of α-particle-emitters, advises in their long-range plan that the United States should "invest in new production approaches of ^{211}At emitters with high priority for ^{211}At and ^{225}Ac" [5]; these are produced with an ion and proton beam, respectively.

Specifically, for RIT, production of ^{225}Ac and ^{211}At is considered a top priority for the DOE isotope program. The focus of R&D and one of the main programmatic goals of the DOE Isotope Program therefore is improving and making commercially feasible production of α-emitters ^{225}Ac and ^{211}At in addition to increasing their availability. Both rare isotopes can be produced in an ion injector stage with 30 MeV/nucleon and high currents - hundreds of microamps. A separated sector with high-gradient cavities would support the highest, lowest-loss currents and extraction to a target system. A separated sector would also support internal targets. Features of integrated isotope production are listed below

Integrated Radioisotope Production

- "Dual-function" Injector:
  - Injector to 1st treatment accelerator stage
    ~0.5 - 30 MeV/nucleon (100 microamps)
  - Radioisotope production (outside of treatment hours)
- Internal targets select optimal energy for production
  - Examples:
    H_2^+ ion: PET isotopes, ^{99}Mo (^{99}Tc), FDG
    He^{2+}: PET isotopes
    He^{2+}: alpha emitters (^{211}At, ^{225}Ac for radioimmunotherapy)

3.13.3 Accelerator Options for Therapy

Background

Cyclotrons dominate proton therapy in part due to fixed rather than ramped magnetic fields along with fixed-frequency RF systems, which simplifies machine cost and operation, but mainly due to their ability to deliver variable-intensity, continuous (CW) beam in a compact format. Continuous beam delivery holds a distinct advantage from an operational and treatment standpoint because it not only simplifies accelerator systems, operational overhead, and beam control, it further reduces technical complexity and response times required for accurate dose delivery and real-time verification – impacting critical dosimetry systems and integrated dose control during treatment. CW beam is desirable for pencil beam scanning (PBS) [6], and is a requirement for compatibility with Proton Computed Tomography technology and image reconstruction [7]. Proton Computed Tomography (pCT) has noted advantages in imaging that include lower dose and enhanced tissue identification [8]; current estimates project a factor of 10 less dose to patient for equivalent resolution compared to conventional CT. Reduced dose indicates adaptive therapy could be implemented if pCT were available in proton therapy facilities, with corresponding improved local control over the tumor and more conformal dose distribution. However, pCT requires a maximum energy of 330 MeV protons to fully transit all regions of the human anatomy and current iso-cyclotrons do not presently support this energy; present compact isochronous cyclotrons for proton therapy reach only 250 MeV as required for treatment, but too low for

full pCT capability. Even if a 330 MeV iso-cyclotron were available, degrading the higher fixed-energy output beam to therapy energies is not an attractive solution requiring much higher output primary currents, increased beam emittances, and residual activation. Imaging in general is inherently challenging as variable energy is required combined with precision intensity control (single-proton buckets) – and the degrader complicates both for a cyclotron-based facility.

The ultra-compact synchro-cyclotrons, such as the new S2C2 offered by IBA, are also common therapy machines specifically optimized for PBS (with kHz RF frequency sweep times). However, variable energy still requires a degrader and the single-bucket proton pulse delivered at kHz rates is incompatible with practical imaging systems. The synchrotron can attain the higher energies, but again the low duty cycle does not support useful imaging reconstruction times, nor is the synchrotron slow-spill easily adapted to ultra-low current. Conventional CT scans take 90 seconds and only isochronous accelerators are competitive. Given all the advantages of CW beam in particle therapy and imaging, the next section reviews the challenges of maintaining isochronism in higher-energy proton and ion accelerators while retaining a compact footprint.

Compact isochronous Accelerators

Compact medium to high energy proton and ion accelerators are a challenging, critical technology. Historically, cyclotrons have been the most compact accelerator technology, but only at energies up to a few hundred MeV. As the energy increases, stronger acceleration is required to minimize beam losses and radiation during acceleration and especially during beam extraction. Orbit separation decreases with energy so higher-energy machines require increased acceleration gradients to provide sufficient radial separation between beams that comprise different acceleration turns in order to efficiently extract. A common solution is to separate the magnetic sectors to insert higher-gradient RF structures. However, once space is inserted between the magnetic sectors of the cyclotron, the footprint of the cyclotron grows rapidly. The compromise to retaining compactness in cyclotrons is beam loss and activation during extraction - which can vary from 20% for the 250 MeV Varian cyclotron (used at PSI) and up to 60% for the IBA 230 MeV Cyclone. Losses present operational, maintenance, and personnel exposure issues even at low therapy currents. The vault shielding required is significant and increases rapidly with energy – $15'$ is typical of proton cyclotron vaults and projected to be $\sim 23'$ for ion cyclotron vaults. For a compact AVF iso-cyclotron that provides a 330 MeV beam, degrading to the lowest treatment energies (∼150 MeV and lower) would likely be prohibitively lossy. Even with the present 230/250 MeV output energy, beam transmission and delivery at the lower energies is a fraction of a percent combined with significantly higher associated emittances. The inherent limitations of the cyclotron at higher energies and the possibility of variable energy without a degrader has stimulated interest in the potential of FFAs.

Towards this end, the concept of isochronous orbits coupled to constant machine tune has been explored and developed for the most general type of FFA (termed non-scaling) using powerful new methodologies in fixed-field accelerator design [9–11]. The property of isochronous orbits again enables the simplicity of fixed RF and by inference, CW operation, as in the cyclotron, but with strong focusing. By tailoring a nonlinear radial field profile, the FFA can remain isochronous with stable and strong machine tunes, well into the relativistic regime achieving 330 MeV for protons and 430 MeV/nucleon for ions - maintaining the constant dose characteristic of cyclotrons. Specifically, isochronous compact racetrack designs have been developed for therapy and security applications with the advantage that lower energy beams can be efficiently extracted for patient treatment without changes to the acceleration cycle and ring magnet strengths. The long synchrotron-like opposing straight sections can be exploited for efficient injection and extraction in addition to providing for rapid energy variation, which has

also been explored in other nonscaling FFA designs [12]. The methodology used to design FFA isochronous dynamics is discussed next.

3.13.4 Isochronous Nonscaling FFAs

Isochronous Dynamics in an FFA

The weak-focusing nature of traditional cyclotron fields does not permit long (several meters) straight sections without a significant scaling up of machine radius and size. However, the addition of strong focusing gradients (and corresponding strong beam envelope control) to conventional cyclotron fields – including reversed gradients to capture both transverse planes – does allow insertion of long synchrotron-like straight sections and thus efficient implementation of high-gradient, multiple-cavity RF modules, even SCRF cryomodules. Further, the nonscaling nonlinear FFA designs have evolved into a very compact racetrack shape – essentially a recirculating linear accelerator with FFA arcs. This basics of this new generation of ultra-compact nonscaling FFAs with constant machine tunes are described here. First an overview of the dynamics of FFAs with alternating gradients is reviewed and compared with cyclotrons and synchrotrons, highlighting the potential for isochronous orbits with stable synchrotron-like performance at high energies.

In addition to isochronous central orbits, a key dynamics issue is resonance avoidance nominally through stable, approximately constant machine tunes over the entire acceleration energy range – which can be accomplished in a FFA by applying alternating strong-focusing gradients. Conventional isochronous cyclotron design (both sector and spiral sector) cannot maintain isochronous orbits and stable tunes simultaneously at relativistic energies. Nonscaling FFAs with optimized nonlinear field profiles, however, are capable of both; further they exhibit the strong-focusing machines tunes, tune footprints, and space-charge tune shifts characteristic of synchrotrons. The potential for high-intensity operation and strong-tune tolerance of space charge effects has been reported in published simulations[[13].

There are several important dynamical consequences in relativistic cyclotrons that complicate their design, impact the physical parameters of the machine, and limit their energy reach. These are briefly discussed below without derivation. In cyclotrons the azimuthal B field profile does not change with radius that is, the extent of the "hills and valleys" scale in direct proportion to radius. Due to the fixed azimuthal field profile, $B(\theta)$, the magnitude of the radial B field must increase as $B = \gamma B_0$, to maintain isochronous orbits, withγ the relativistic factor and B_0 the magnetic field at injection ($\gamma \to 1$ at nonrelativistic energies giving the conventional cyclotron).

The increasing peak B field results in a gradient term which changes the machine tune; the tune cannot be held constant in relativistic cyclotrons - it rises radially and decreases vertically. A spiral shape is introduced to increase the vertical edge crossing effect (flutter) with energy to maintain a stable vertical machine tune. Eventually the vertical tune becomes unsustainable. Tune approximations from equation (1) give $\nu_r \approx \gamma$ and $\nu_z^2 \approx 1 - \gamma^2 + F(1 + 2\tan^2\epsilon)$ where F is the flutter and ϵ the spiral angle.

$$F = \left\langle \left(\frac{B(\theta) - B_{\text{av}}}{B_{\text{av}}} \right)^2 \right\rangle \tag{1}$$

where ϵ defines the axis $R = R_0\, \mathrm{e}^{\theta \cot \epsilon}$.

As γ increases, ν_r increases and ν_z decreases. The machine tune changes and crosses betatron resonances with potential for beam blowup and losses. Stable beam properties, dynamics and low-loss operation can in general not be achieved in high-energy cyclotrons unless the acceleration is strong enough to jump across resonances and separate orbits sufficiently for extraction

(alternatively, the machine size can increase significantly decreasing the gradient, hence the large size of the 590-600 MeV cyclotrons at PSI and TRIUMF).

The dynamics of FFAs, both scaling and nonscaling are dominated by synchrotron-like dynamics [14]. In a FFA with alternating gradients all conventional focusing terms are utilized as given in the following thin-lens approximation:

$$\frac{1}{f_{\mathrm{F}}} = k_{\mathrm{F}}\ell + \frac{\theta}{\rho_{\mathrm{F}}} + \frac{\eta}{\rho_{\mathrm{F}}}\,, \tag{2}$$

where f_{F} and ρ_{F} in equation (2) are the focal length in the horizontal plane and bend radius, respectively, ℓ, the horizontally-focussing magnet half length, k_{F} the "local" horizontally focusing gradient for an arbitrary field order, θ the sector bend angle, η the edge crossing angle (the tangent is approximated). In the vertical (non-bending) plane, the sector bend term does not contribute, and the vertical tune depends on only the strong-focusing and the edge-focusing terms. This simple thin-lens expression highlights how the three machines fundamentally operate and determines their ultimate flexibility in format and machine characteristics.

The synchrotron relies on the first strong-focusing gradient term, the cyclotron on the last two terms which are the centripetal (weak focusing, bend plane only) and edge focusing terms, but the FFA utilizes all three terms for beam envelope control and dynamical stability. Further, unlike the scaling version, the non-scaling FFA optimizes the normal and reverse-field gradients and edge angles independently; this is critical for achieving compactness and simultaneous isochronous (CW) dynamics. This last point is very important because individual control over these parameters allows the field, orbit location, and important machine parameters such as tune, footprint, and aperture to be approximately independent and more strongly controlled than in a cyclotron. The reverse gradient is especially critical to a stronger vertical tune than can be achieved in a cyclotron. This increase is not solely due to the addition of strong focusing, but also from the radial increase in edge focusing strength (due to increasing magnetic field). In the non-scaling FFA (only), these different focusing principles can be combined in different and varying relative strengths through the acceleration cycle – this varying composition can be exploited to control the machine tune without applying the field scaling law. The terms can be further inter-played and optimized to achieve stable dynamics in highly flexible and ultra-compact lattice structures.

The design of the non-scaling FFA with its inherent flexibility is even more powerful when a high-order nonlinear field expansion is applied. The nonlinear gradient has the advantage of providing increased focusing in both transverse planes as a function of radius – more than a linear field gradient – thereby providing a strong constant tune in both planes while preserving considerable freedom in physical parameters. When components are designed with independent normal and reverse gradients, the orbital path length can be constrained such that the revolution time at each momentum scales with velocity, and simultaneously the machine tune can be controlled through edge and weak focusing effects independent of this path length – thus impacting tune but not revolution frequency. Expressed in terms of linear dynamics, a focusing "quadrupole-like" gradient is generated locally about each isochronous orbit as a feed-down from the nonlinear radial field profile; by following a nonlinear radial field profile a FODO-like cell tune is controlled and maintained as a function of energy. The terms and field-order in the nonlinear radial magnetic profile must be matched to the isochronous orbit which is dictated by the central field of and trajectory length through the magnet.

Unlike the cyclotron, which relies on a predominately dipole field or fixed B-field scaling with γ, and is therefore limited in adapting path length to velocity as the energy becomes relativistic, the non-scaling FFA can maintain isochronous orbits well into relativistic energy regimes as shown in Figure 1. Only the nonscaling FFA can be CW as there is no flexibility in the scaling law for scaling FFAs. Further, a linear-field nonscaling FFA cannot maintain

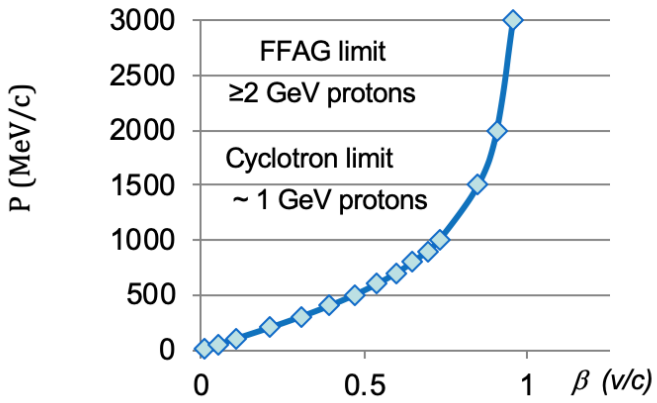

Figure 1: Momentum dependence on velocity. $\langle B_r \rangle \propto p/\beta$ for isochronous orbits that are roughly geometrically-similar.

constant tune, both horizontally and vertically, as a function of energy since relativistic effects are inherently nonlinear. Only a nonlinear gradient can therefore provide increased focusing in both transverse planes stably as a function of energy through the radially-increasing gradient, edge, and centripetal focusing terms. The order of the expansion provides the degrees of freedom necessary to maintain a strong constant tune in both planes, decoupling it from and preserving considerable freedom in physical parameters. Strong tunes, especially needed in the vertical, imply mitigation of space-charge effects and stable acceleration to potentially higher currents than the cyclotron for the same footprint.

Based on optimized nonlinear field profiles, several FFA designs with alternating gradient magnets are presented in this report as follows with emphasis on the racetrack format.

1. 0.2 - 1 GeV proton circular and racetrack variant;
2. 30 - 90 MeV racetrack FFA for therapy;
3. 90 - 250/330 MeV racetrack FFA for deep tumor therapy and pCT.

The 1 GeV proton racetrack is relevant because field strengths and layout for both superconducting and normal conducting versions correspond in physical size and field strengths to a 400 MeV/nucleon ion therapy accelerator. (The applications of 1 GeV protons are irradiation and security applications.)

CW nonscaling FFA Designs

The nonlinear design principles described above have been applied utilizing advanced design algorithms to produce a 200 MeV to 1 GeV quasi-isochronous circular FFA with a small footprint ($dt/t \approx \pm 3.5\%$) [15] and utilizing superferric magnetic fields of 5 T or less. The machine footprint is shown in Figure 2 (left), with four 2 m straights and each cell composed of an FDF triplet. Initially all FFA designs were completely periodic. As the demands for compactness increased and higher energies were requested for protons (1 GeV) and ion therapy (430 MeV/nucleon), eventually all inter-component straight sections became too short for effective extraction or even injection. The number of straights also increased with energy as periodicity was required to increase causing an undesirable increase in footprint. Several of these initial circular FFAs for medical therapy and imaging have been designed and documented [16] but will not be discussed further in this report in preference to the racetrack format. The racetrack configuration optimizes compactness yet provides for RF modules to be inserted in one straight and injection extraction

systems in the opposite straight– an optimal hardware and overall layout configuration. To this end we have designed a racetrack variant that initially eliminated two of the straights in a ring with fourfold symmetry and lengthened the remaining two opposing straights to preserve the total length of straight section as shown in Figure 2 (middle). This preserved both the circumference and the machine tune permitting a dynamical comparison between the circular and racetrack designs. The beam orbits are identical through the common bend or arc structures and are shown in Figure 2 (right) for the range of machine energies. These design orbits were computed with COSY [17].

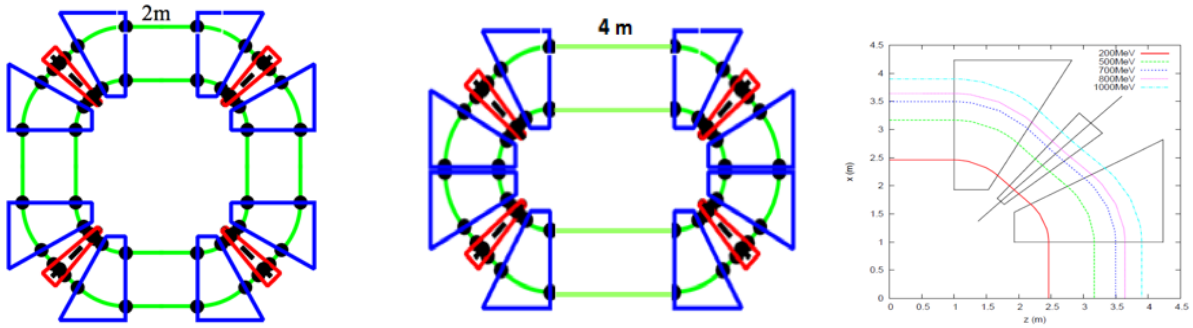

Figure 2: Lattices for 200 MeV to 1000 MeV protons circular and full racetrack FFA layouts. (left, right) shows the normal (blue) and reverse gradient (red) components for a periodic compact FFA and one with two long straight insertions on opposing sides (middle). Particle tracks through the FDF bend structure (right) are identical for both versions since straights are inserted at symmetry points in both lattices.

The ring tunes for the ring and the racetrack lattice versions, as computed from the initial hard-edge design lattice using a fringe field model based on Enge functions and simulated in PyZgoubi [18] are shown in Figure 3. Note the tunes are essentially constant with energy in the horizontal but have some vertical variation that will be addressed in future work. Interestingly, the lattices are almost identical in machine tunes and dynamics if the circumference, focusing strength, and total straight section lengths are preserved. Tracking simulations for both versions are discussed next.

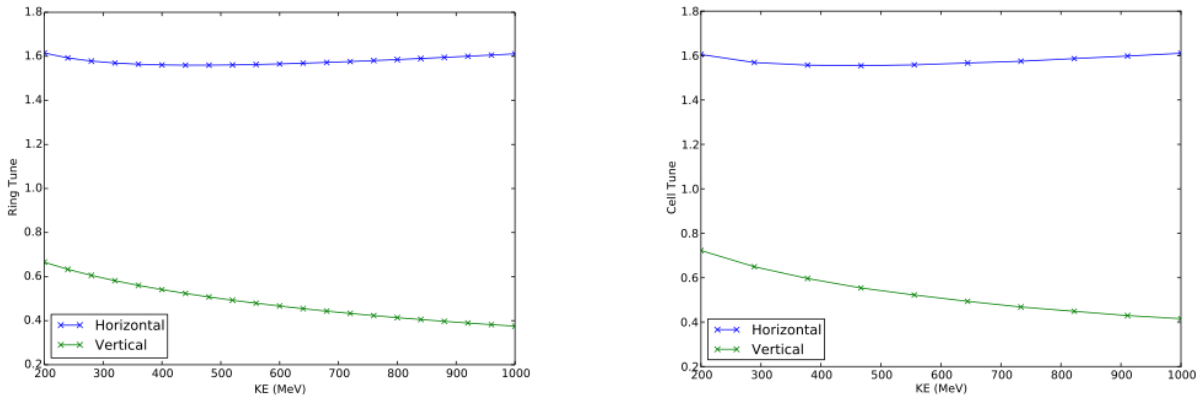

Figure 3: Machine tunes for the 2 m ring (left) and a racetrack nsFFA (right) as a function of beam energy.

Tracking

Given that a nonlinear field profile is required for all compact, fixed magnetic field accelerators to achieve high energies (including synchrocyclotrons), efficient beam transmission is an

overriding concern, so high-order simulation was initiated again using new methodologies in fixed-field accelerator modeling [9–11]. Figure 4 depicts the tracking pictures at high-energy using COSY[17] for singe-particle tracking. In the FFA designs, both circular and racetrack, the geometric emittance was found to be preserved as a function of energy, apparently due to the approximately constant tune and avoidance of resonances. When geometric emittance is preserved, the dynamical acceptance or DA (which is a strong indicator of robust approximately linear dynamics about reference orbits) actually increases and beam transmission appears predicted to be near 100%. The elliptical phase space portraits at the highest nonlinear gradient reference orbit of 1 GeV in Figure 4 support this observation. This is in contrast to the DA predicted for the 8-sector version of an 800 MeV cyclotron [19] which decreases with energy in simulations. Comparison of tracking results indicates about a factor of 4 increase in DA for the raetrack FFA described in this work combined with a factor of 4 decrease in footprint when compared to the published tracking results for this specific cyclotron design [19].

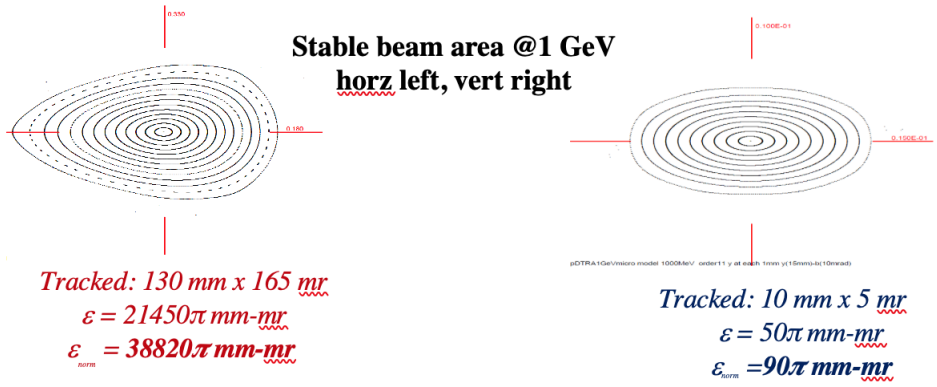

Figure 4: Single-particle tracking in COSY INFINITY showing results for the 1 GeV reference orbit in the racetrack nsFFA. The orbits represent 1 cm steps in the horizontal and 1 mm in the vertical. The aperture limit is reached in the vertical.

Dynamic Aperture

We now consider the dynamic aperture of these FFAs and present an algorithm, implemented in PyZgoubi, for the calculation. The presence of nonlinearities in the accelerator lattice can give rise to unstable motion, and over a very large number of particle turns through the accelerator a particle's motion may become unbounded. The approximate boundary between stable and unstable motion, and the particle amplitude at which this boundary occurs, is termed the dynamic aperture (DA). The period of time over which particles must be followed in simulation to predict the dynamic aperture depends upon the application of that accelerator. For the ultra-compact FFAs discussed here if implemented with SRF, then the protons remain in the accelerator for only around 40 turns, but with NCRF, as in the PSI cyclotron, the number of turns increase by an order of magnitude.

Dynamic aperture is expressed here in terms of the limit in transverse particle amplitudes or, equivalently, the limit in transverse single particle actions $J_{x,y}$. over the number of acceleration turns and is calculated by increasing J_x and J_y until the particle is lost (particle loss defined by the actual physical apertures). We therefore consider increments of J_x and increments of J_y or some combination of both defined the angle in the (J_x, J_y) plane. For the large horizontal and small vertical apertures of fixed-field machines and the midplane symmetry, the DA is best described in terms of these two planes. Single-particle trajectories are generally elliptical at small amplitudes as the dynamics are approximately linear locally about a closed reference

orbit, but become distorted and non-elliptical at larger amplitudes as nonlinear magnetic fields cause increasingly nonlinear motion. Hence we compute the dynamic aperture by combinations of particle coordinates based on the particle action e.g. we increase J_x by increasing the single particle coordinates along the four axes $(+x, 0)$, $(0, +x')$, $(-x, 0)$ and $(0, -x')$ and similarly for J_y. The DA has been computed in the horizontal and vertical using this method over 40 and 200 turns to represent a strong gradient, SC RF version and the impact of a slower acceleration cycle, respectively. To model a more realistic magnet configuration, the DA is simulated using the PyZgoubi framework, with a series of random horizontal misalignments applied to all magnetic elements to study the DA reduction from a perfect lattice. The misalignments are modelled as a Gaussian distribution cut off at 3σ. The DA is shown as the mean over the seeds, with an error bar corresponding to the RMS variation of the seeds. Table 3 shows the DA achieved for the 2 m circular and racetrack versions of the nsFFA in the horizontal and vertical planes computed with PyZgoubi and an Enge function fringe field. Figure 5 shows the fractional decrease of dynamic aperture with respect to the ideal case for the circular 2 m FFA in terms of normalized stored emittance as a function of misalignment width (left). The DA shows a slow decline for misalignment widths up to 600 μm misalignments. The same calculation for the racetrack is shown in Figure 5 (right) and shows a slightly faster decline of DA with misalignment width. However, both machines are surprisingly tolerant to misalignments in the horizontal plane given the nonlinear field profile of these machines.

Table 3: The dynamic aperture in unnormalized emittance units for the circular FFA and the racetrack FFA computed with PyZgoubi.

Dynamic aperture	**Circular FFA Horizontal** π **mm.mrad**	**Circular FFA Vertical** π **mm.mrad**	**Racetrack FFA Horizontal** π **mm.mrad**	**Racetrack FFA Vertical** π **mm.mrad**
200 MeV 40 turns	74700	107	25000	46
200 MeV 200 turns	72600	91	23700	43
800 MeV 40 turns	156300	364	63000	277
800 MeV 200 turns	155100	356	63000	223

To summarize, a 0.2-1 GeV nonscaling FFA design indicates a form factor that is 9 m diameter and a racetrack that is 7 m wide by 11 m long for normal conducting magnets; 6 to 8 combined function magnets and 2 to 4 m long straight sections. Simulations demonstrate that the elongated configuration possesses the same stable beam tunes as the circular FFA configuration. The racetrack accelerators have the potential to approach the low losses of the linac and synchrotron and achieve cleaner separation of beam for extraction given the high gradient acceleration cavities supported. Both designs are fairly insensitive to horizontal misalignments, an important result for achieving a working machine with realistic engineering tolerances. Although this work was for a 1 GeV CW proton accelerator, the field strengths and physical dimensions are similar and can be applied to a 400 MeV/nucleon ion therapy accelerator for a charge to mass ratio of $1/2$ - the nonlinear field radial profile would need to be adapted to different isochronous conditions, as dictated by the relativistic effects and different velocities of the ions traveling similar reference orbits.

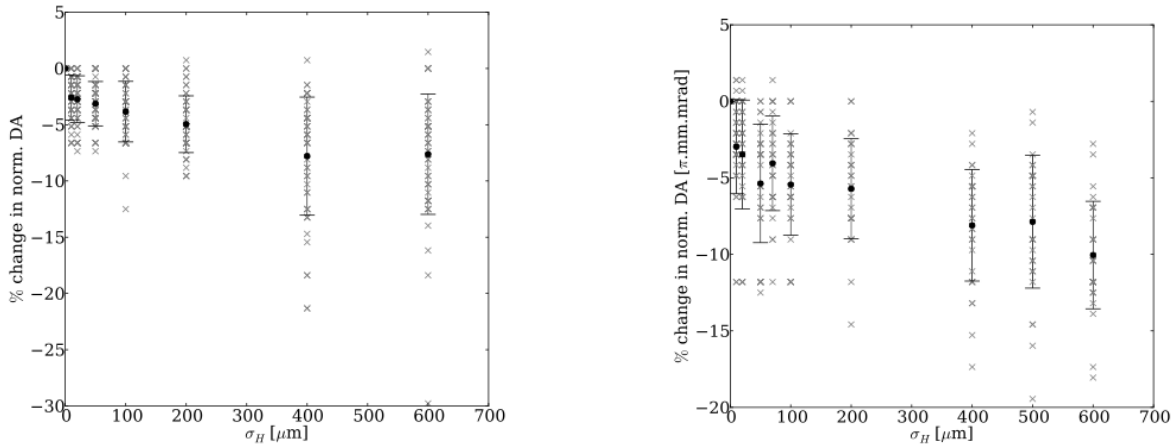

Figure 5: The relative drop in dynamic aperture in percent as a function of misalignment for the circular FFA (left) and racetrack FFA (right) computed with PyZgoubi. Both show stability and similar performance in the presence of large relative 600 μm misalignments of main magnets.

3.13.5 Staging ion Accelerators

The future of particle therapy rests on developing cost-efficient treatment and improved effectiveness; a goal which can for many cancers be accomplished by utilizing higher-RBE ions, and high Linear Energy Transfer (LET) as provided by ion and carbon therapy facilities; in turn the future of versatile light-ion therapy facilities relies critically on the development of compact, operationally manageable accelerator and beam delivery systems that can be implemented economically.

A staged accelerator complex applies to ions as well as protons with a major consideration being variable energy extraction for ions. The use of degraders for changing beam energy becomes even more problematic with ion beams over proton beams given the increased potential for radioisotope production and potential transport of other species during beam delivery [20]. For CW beam a variable energy extraction system requires a system of extraction "bump" magnets and a septum or Lambertson similar to extraction scenarios in synchrotrons. With helium and carbon ions of particular interest, a variable-energy, CW ion accelerator system was designed that reaches an energy of 250/330 MeV/nucleon for acceleration of ions with a charge to mass ratio of 1/2 – a therapeutic energy for H or the higher energy for imaging. He^{2+} is of specific interest and has a 30 cm range for a treatment energy of 250 MeV/nucleon; however treatment with either protons (in the form of H_2^+) and carbon and other light ions is also supported by this accelerator system. Helium has become of significant interest for pediatric cancers given the reduced multiple Coulomb scattering effects on the lateral penumbra and reduced dose to surrounding healthy tissues relative to proton beams. The long straights of the racetrack format again allow insertion of both high-gradient RF modules and an efficient injection and extraction systems in a highly compact footprint. Variable-energy extraction is achieved by varying the strength of fast-sweeping bipolar "bump" extraction magnets. This approach eliminates the high activation and unavoidable radioisotope products from the degrader-based energy control used in a conventional iso-cyclotron.

A dual-stage approach with a lower energy injector (70 - 90 MeV/nucleon) is necessary to facilitate a technically feasible variable-energy extraction system which occupies one of the long straight sections in the higher-energy stage. High-gradient fixed-frequency RF cavities ($\sim$0.3 - 0.5 MeV/turn per cavity) would be installed in the opposing straight section. Peak fields in the arc sections of the racetrack will determine the width or shortest dimension of the higher

energy stage. The injector can be a simpler accelerator, possibly a cyclotron, although rapid switching between ion sources is important. Below are two tables that represent the goals of optimized ion therapy accelerator and beam delivery design. Table 4 lists the clinically-relevant properties for the accelerator system and Table 5 presents realistic design parameters based on normal-conducting guide fields. A comparison of an equivalent circular layout with the compact racetrack form remains important to understand if there are any fundamental performance differences.

Table 4: Clinical specifications for the ion accelerator

Description	**Specification**
Multi-ion Capability	$H^{2+}, D^{+}, He^{2+}, Li, C^{6+}$; Fast switching time between ions (~ 1 sec)
Maximum Energy	330 MeV/μ 60 cm for imaging, protons; [~ 23 m for treatment, carbon; > 30 cm (250 MeV) for treatment, helium]
Injection Energy (preliminary)	79 - 90 MeV/μ
Dose Delivery Rates	5 Gy/min/cubic liter (minimum) Up to 7 Gy/8 sec/cubic liter (hypofractionation)
Energy Step Size	2 MeV
Dose Accuracy per fraction	2.5%

Table 5: Machine specifications for the higher energy stage ion accelerator.

Description	**Specification**
Format	Racetrack: 2-fold periodicity Comparable circular: 4-fold periodicity
Beam structure	CW
Isochronous Level	$\sim 10^{-4}$ - 10^{-5} (initial design 10^{-2} - 10^{-3} only)
Extraction Energy Range	~70-90 MeV - 330 MeV/u
Extraction arc radius	~5 m radius
Maximum B field	< 2.7 T for NC water-cooled magnets
Acceleration Gradient	1 MeV
Dose Accuracy per fraction	2.5%
Nucleon flux	10^{12} u/sec
Machine reliability	>95%
Transverse Emittance (σ)	$\sim 1\,\pi$ mm.mrad (horz and vert, normalized)
Straight section racetrack **Equivalent circular**	≥ 4 m ≥ 2 m

Designing for He^{2+} presents enormous savings in overall facility cost due to the reduced

250 MeV/nucleon (the same optimal energy per nucleon as in proton therapy but at a lower charge to mass ratio) versus the 430 MeV/nucleon required for 30 cm depth carbon therapy as can be seen from Figure 6 [21]. An increase in energy to 330 MeV/nucleon, however, would be required for comprehensive imaging which again requires one particle per RF bucket at a CW rate for practical reconstruction times. Such a machine will accelerate C^{6+} to a penetration depth of 23 cm, making this a viable carbon therapy option for many cancers. Also, protons in the form of H_2^+; i.e. charge to mass of 1/2, can be accelerated in this system as the small differences in nuclear mass are not significant enough to change the isochronous performance.

A dual stage accelerator system is optimal from a beam dynamics perspective as it limits the impact of relativistic effects on orbital revolution time by narrowing the acceleration range. This in turn lowers the order of the field expansion in radial profiles and decreases difficulty in solving for constant machine tunes and adiabatic lattice functions. Dual stage and the racetrack format are required to implement variable energy extraction promoting access to lower energy orbits using technically feasible bump magnets. The low-energy stage further supports an eye line, and treatment of melanoma, mesothelioma, and other skin or shallow tumors. The two stages proposed for proton or ions could comprise the following energy ranges and support listed applications.

- 18 to ∼250-330 MeV H^- or protons
  - Fixed-frequency RF, CW beam
  - Low intensity for pCT
  - Stripping controls extraction energy and intensity for H^-
  - Racetrack is required for variable energy proton beams

Or, for a dual-stage ion accelerator:

1st stage:

- 9 to ∼70/90 MeV charge to mass ratio of 1/2
  - Fixed-frequency RF, DC beam for all ions
  - Variable energy extraction
  - Upstream injector for high-energy ring

2nd stage:

- 70/90 to 250/330 MeV/nucleon
  - Variable energy extraction
  - Adjustable, fast orbit bump magnets/extraction septum in long straight
    - DC extracted beam
    - Variable energy on scale of tens of microseconds
    - Investigating extracted energy range

Note both stages require an injector which could be an off-the-shelf cyclotron.

It is important to understand the relationship between isochronous orbits and aperture which can be approximated in terms of average radius at injection and extraction and approximate main arc magnet apertures using the following equations, where β is the relativistic velocity.

$$\bar{R}_{\text{extraction}} - \bar{R}_{\text{injection}} = \text{Aperture}.$$

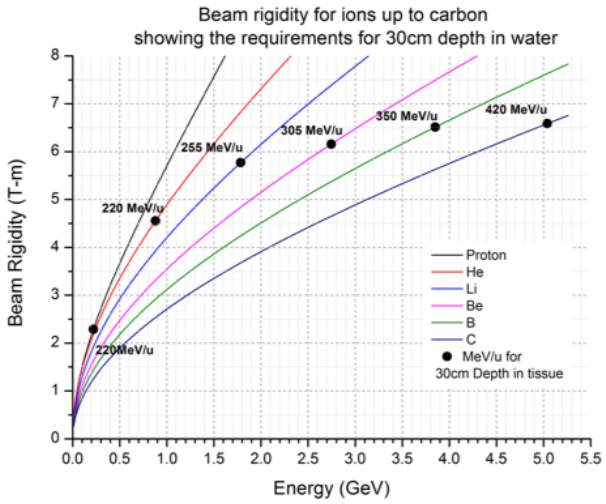

Figure 6: The beam rigidity for fully-stripped, charge to mass of 1/2, light ions as a function of the kinetic energy required to achieve a therapeutic penetration depth of 30 cm in water (human tissue equivalent) computed using SRIM/TRIM [22].

For the isochronous condition, the average extraction radius can be expressed in terms of the average injection radius.

$$\left(\frac{\beta_{\text{extraction}}}{\beta_{\text{injection}}} - 1\right) \bar{R}_{\text{injection}} = \text{Aperture}.$$

Using a normal conducting, extraction-energy radius of ~ 5 m for the arc (2.5 m for superconducting arc version), the long straight section of the racetrack then defines the required magnet aperture as shown in Table 6 for isochronous orbits. A longer straight section increases aperture, but it allows longer extraction magnets to successfully extract the inner, lower energy orbits. Straight sections from 4 to 5.5 m has been successfully incorporated, changing the circular FFA in Figure 7 (top, left) into a racetrack (bottom, left). However stability of the machine tune and overall dynamics were greatly improved by adding a short 1 m straight section as also shown in Figure 7, (bottom, left). This short straight section is extremely useful for diagnostics and potentially additional RF (such as higher harmonic flattop cavities). One additional advantage is only two types of magnet designs are required for the racetrack, eliminating the very large normal-bend magnet at the center of the arc. A comparison of a circular ring design with 2 m straights was also studied for comparison with the reference CW nsFFA. Layouts and radial field profiles are shown in Figure 7.

Optimized radial field profiles were imported into COSY and fields expanded at magnet edges using an Enge function falloff for performance evaluations – the integrated magnetic field is kept constant to maintain the isochronous reference orbits. A field heat map is shown in Figure 8 (left) and the corresponding reference orbits as a function of energy also in Figure 8 (right). Using the COSY field map, machine tunes were then calculated as shown in Figure 9. At injection, near 90 MeV, the fields from the individual magnets merge due to proximity and tunes cannot be calculated. This lack of azimuthal field variation also occurs in an AVF and compact separated-sector cyclotron in the central or injection region, nominally incurring low beam capture efficiency and high loss at injection.

For a cross check, the racetrack was also modeled in the code Cyclops [23], extracting tunes and time of flight (ToF) deviation as a function of energy. These are shown in Figure 10 and are consistent with the COSY calculation. The ToF deviation is $\pm 2\%$, a reasonable level of isochronism for a preliminary lattice design for a CW machine. The isochronism level will

Table 6: Machine horizontal aperture dependence on length of racetrack long straight section for 330 MeV/ nucleon (pCT) and 430 MeV/nucleon (full-depth carbon therapy) ion accelerators.

Energy Range MeV/nucleon	**Straight 0 meters**	**Straight 2 meters**	**Straight 4 meters**
70 - 330	2.28	2.67	2.86
90 - 330	1.96	2.21	2.63
70 - 430	2.2	2.80	3.12
90 - 430	2.5	2.47	2.75

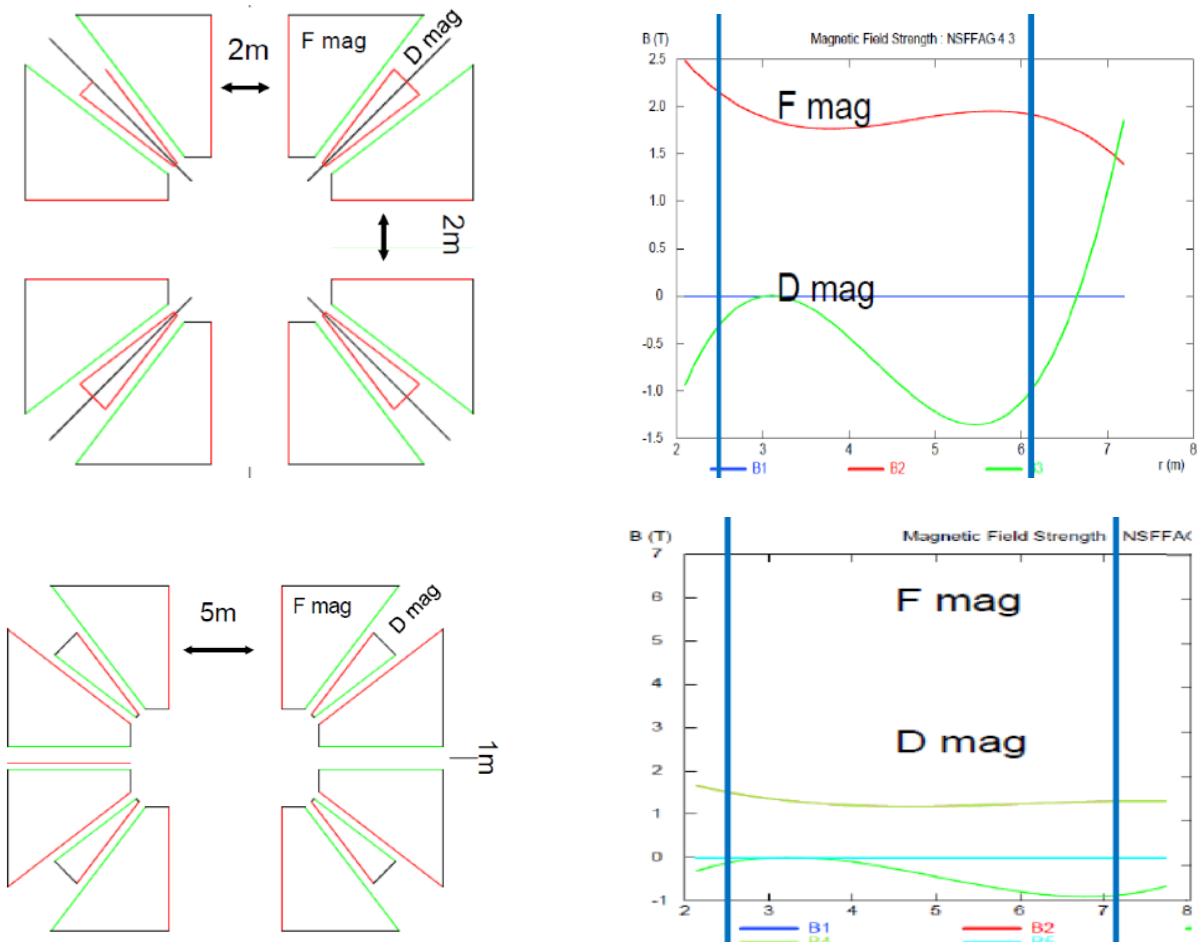

Figure 7: Layout of the circular 90-330 MeV/nucleon with 2 m straight sections (top, left) and a 5 m straight-section racetrack (bottom, left). The associated field profiles are also shown (right) as a function of B(T) versus radius. Note that the extent of the magnet aperture is marked between the blue lines.

need be reduced to 10^{-4} - 10^{-6} depending on the acceleration installed. The final adjustment is nominally done by shimming in the manufactured machine.

An example of a working extraction system layout for a 4 - 5.5 m long straight section is shown in Figure 11. High energy beam (blue trajectory) is extracted for an inward-bending polarity of the bump magnets. As the polarity reverses, inner, low-energy orbits (red trajectory) are swept outward and into the septum extraction magnet.

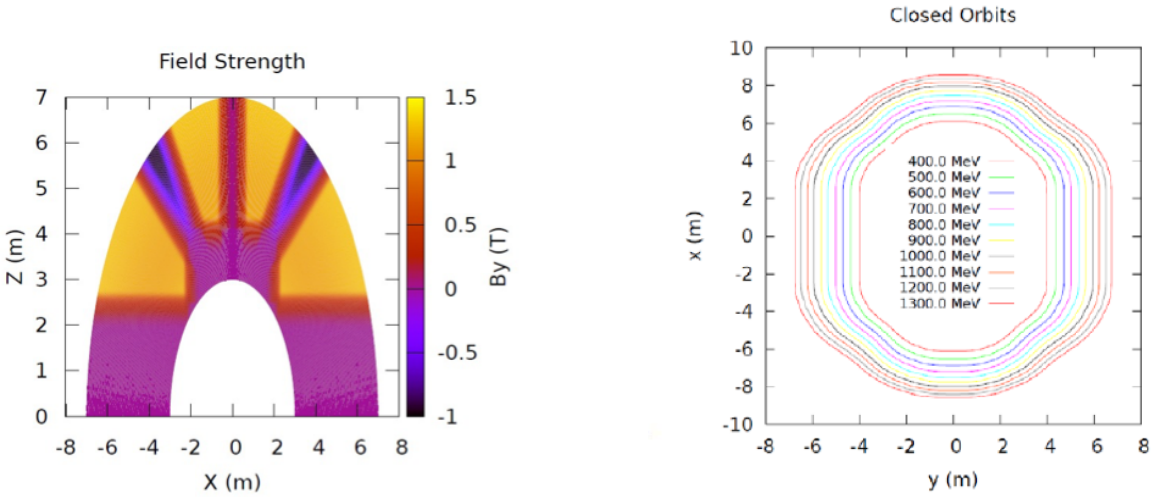

Figure 8: Field gradient strengths for half of the 90 - 330 MeV/nucleon racetrack (left) showing the extended field falloff at the edges and the corresponding closed isochronous reference orbits at different helium kinetic energies (right) for a field map generated by COSY [17].

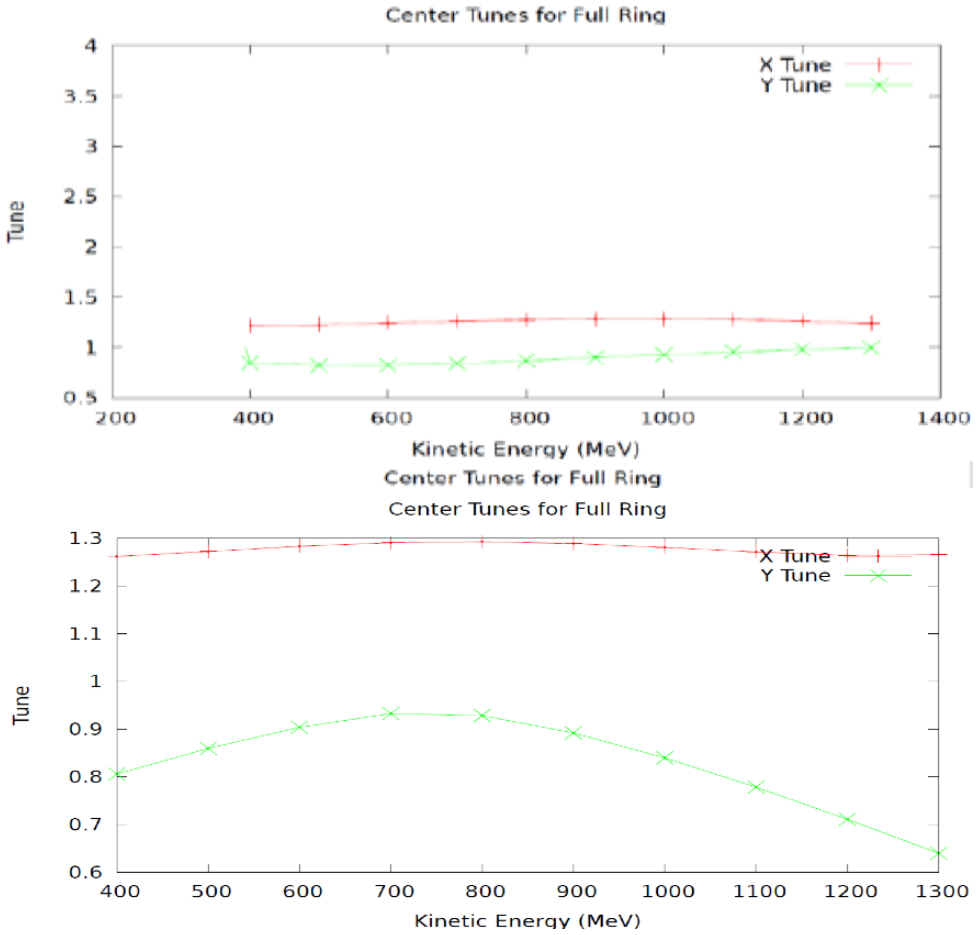

Figure 9: Machine tunes for a 90-330 MeV/ nucleon ion accelerator circular with 2 m straight sections (top) and the racetrack (bottom) with 5 m and 1 m straight sections as shown in the previous Figure 7. The horizontal axis is full kinetic energy for a He^{2+} ion.

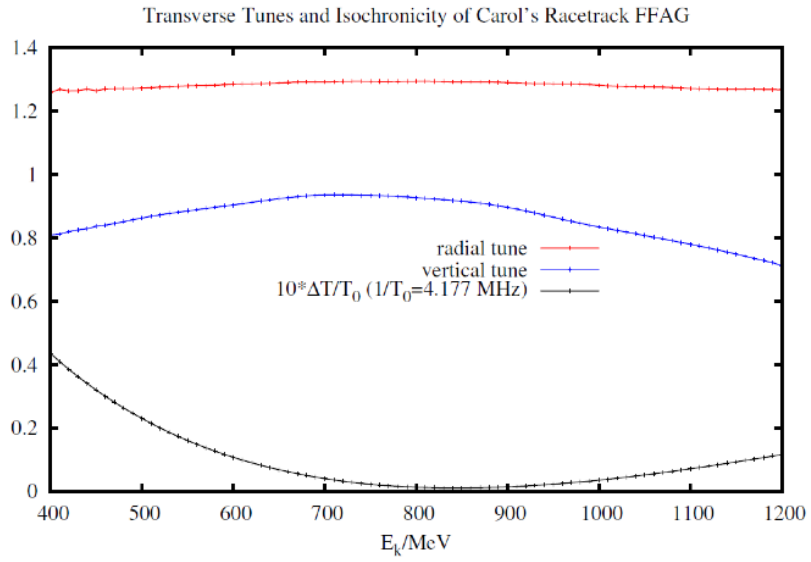

Figure 10: Machine tunes for a 90 - 330 MeV/ nucleon ion accelerator circular with 5 m and 1 m straight sections and corresponding TOF deviation in 10% units relative to the He^{2+} orbit at 800 MeV. Modeling performed in Cyclops [23].

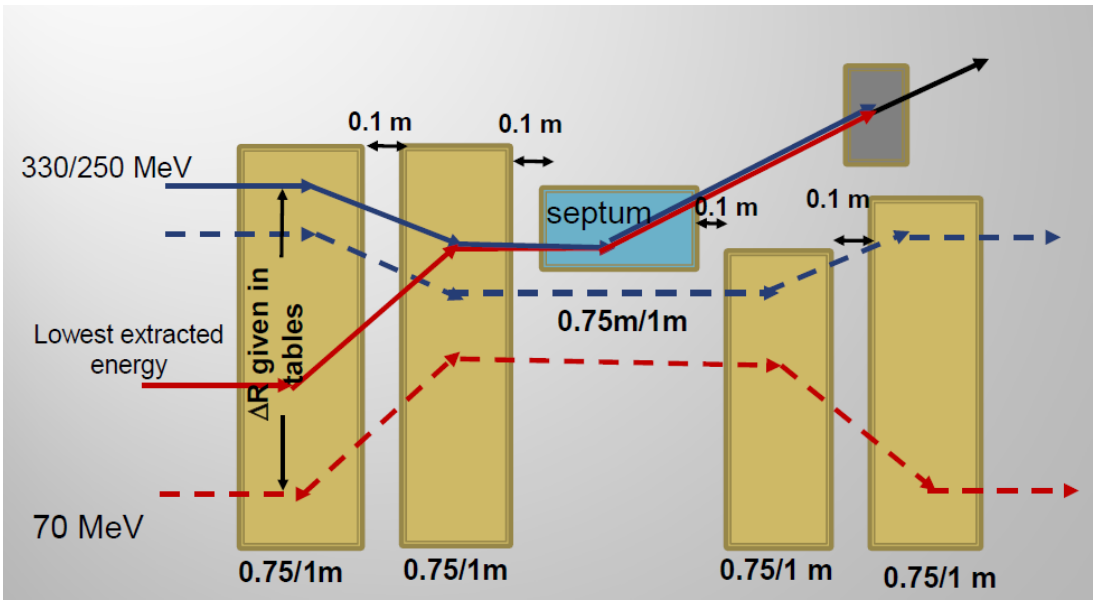

Figure 11: Layout of a 4-bump bipolar extraction system capable of variable energy extraction.

Summary

The FFA with alternating gradients amalgamates the best features of the synchrotron (strong focusing) and the cyclotron (fixed-field magnetic fields) and, for isochronous designs, high-gradient, fixed frequency RF. The high reliability and turnkey operation of fixed-field – and now fixed-frequency RF – accelerators make them ideal for medical and commercial purposes.

With isochronous performance, and strong-focusing optics, these new, advanced non-scaling FFAs have the potential for a low-loss CW machine for combined application in proton and ion therapy and imaging. Significant work has progressed on a stable, CW 30-330 MeV/nucleon isochronous FFA that can support both pCT and proton or ion therapy with minimal or no interruption for imaging diagnostics. This work presents the first CW designs of a relatively compact

accelerator for pCT and proton therapy and one which could potentially replace cyclotrons in many existing facilities. The evolution of the circular CW nsFFA into a racetrack format has significant potential for not only accommodating higher gradient RF modules, including SCRF, but also the potential for variable energy extraction using bipolar orbit-bump magnets in a long, ~ 5 m straight section using an extraction Lambertson or septum, as in synchrotron extraction. The settings of the orbit bump magnets select the internal orbit to extract and therefore the extraction energy. With such long straight sections, variable energy can also now be implemented for ions with a charge to mass of 1/2. For variable-energy without a degrader and, ideally, for therapy optimization, two accelerator stages covering different penetration depths and targeting specific cancers are proposed. Further, an injection energy of 30 MeV was chosen to be compatible with a 30 MeV injector cyclotron, preferably separated-sector, and envisioned for radioisotope production to provide additional revenue capacity to a therapy facility.

In summary nonscaling, nonlinear versions of FFA with alternating gradients provide a new accelerator technology that can deliver continuous beam with high efficiency, but also reliably with "turnkey" operation from the standpoint of fixed magnetic fields and fixed RF frequency. These compact machines support dual energy extraction for therapy and imaging and are envisioned for successful integration into conventional cyclotron facilities for proton therapy; i.e. compatible with existing degrader, beamlines, and treatment rooms (including gantries). The racetrack and dual stage approach further support an ultra-compact variable-energy light-ion facility.

ACKNOWLEDGMENTS

This review paper includes important contributions to the development of nonscaling FFAs from Martin Berz and Kyoko Makino (Michigan State University), Pavel Snopok (Illinois Institute of Technology), Jordan Taylor, David Bruton, and Rob Edgecock (University of Huddersfield), Rob Appleby, Hywel Owen, and Sam Tygier (University of Manchester), and Shane Koscielniak and Thomas Planche (TRIUMF).

References

[1] Accelerators for America's Future. DOE report chaired by W. Henning and C. Shank, 2009. http://www.acceleratorsamerica.org/

[2] U.S. Department of Energy and National Cancer Institute, Workshop on Ion Beam Therapy Summary Report. Bethesda MD, January 2013. http://rrp.cancer.gov/content/docs/Workshop_on_Ion_Beam_Therapy.pdf

[3] G. Coutrakon, private communication, 2009.

[4] V. Sabaiduc, "Best Radioisotope Production Cyclotrons", talk at CAARI, Ft. Worth, TX, Aug 5-10 (2012).

[5] NSCAI, 2015 Report, "Meeting Isotope Needs and Capturing Opportunities for the Future: The 2015 Long Range Plan for the DOE-NP Isotope Program", NSAC Isotopes Subcommittee, July 20, 2015, http://science.energy.gov/$\sim$/media/np/nsac/pdf/docs/2015/2015_NSACI_Report_to_NSAC_Final.pdf

[6] M. Schippers, *et al.* "Fast-scanning Techniques for Cancer Therapy with Hadrons, a Domain of Cyclotrons", invited talk, Proceedings of the 19th International Conference on Cyclotrons and Their Applications, Lanzhou, China, Oct. 6-10, 2010, pp 410-415.

[7] R. Hurley, *et al.*, Med. Phys. 39, 2438 (2012).

[8] G. Coutrakon,"The Proton CT Project", CAARI 22nd Intl. Conference, Fort Worth, TX August 5-10 (2012).

[9] C. Johnstone, *et al.* "Innovations in Fixed-Field Accelerators: Design and Simulation", invited talk, Proceedings of the 19$^{\text{th}}$ International Conference on Cyclotrons and Their Applications, Lanzhou, China, Oct. 6-10, 2010, pp 389-394.

[10] K. Makino, M. Berz, C. Johnstone, "High-Order Out-Of-Plane Expansion for 3D Fields", World Scientific Publishing Company, Int. Journal of Mod. Physics-A, Vol. 26, Nos. 10 & 11, pp. 1807-1821, (2011).

[11] K. Makino, M. Berz, P. Snopok, and C. Johnstone, "High-order Description of the Dynamics in FFAGs and Related Accelerators", Int. Journal of Mod. Physics-A, Vol. 24, No. 5, pp. 908-922 (2009).

[12] K. Peach, *et al.*, "PAMELA Overview and Status", Proc IPAC, 2010.

[13] S. L. Sheey, *et al.*, "The Potential for a High-Power Proton Driver for ADS", `http://inspirehep.net/record/1258459`.

[14] C.R. Prior, Editor, ICFA Beam Dynamics Newsletter Issue 43, August, 2007.

[15] C. Johnstone *et al.*, "A Compact, GeV, High-Intensity (CW) Racetrack FFAG", Proceedings of the 20$^{\text{th}}$ International Conference on Cyclotrons and Their Applications, Vancouver, B.C. Canada, Sept. 16-20,2010, pp 73-75.

[16] C. Johnstone et al, "A CW FFAG for Proton Computed Tomography", Proceedings of the International Particle Accelerator Conference, New Orleans, LA, May 20-25, 2012, pp 4094-4096.

[17] M. Berz and K. Makino. "COSY INFINITY Version 9.1", Beam Physics Manual, Michigan State University, 2011. `http://cosyinfinity.org`. K. Makino, M. Berz, "COSY INFINITY Version 9", NIMA 558 (2005): 346-350.

[18] S. Tygier, see `http://www.hep.manchester.ac.uk/u/samt/` and F. Meot. "The Ray-Tracing Code Zgoubi", Nuclear Instruments and Methods-A. 427 (1999): 353-356. F. Lemuet Physics and F. Meot. "Developments in the Ray-Tracing Code Zgoubi for 6-D Multiturn Tracking in FFAG Rings", Nucl. Instruments and Methods-A. 547 (2005): 638-651.

[19] F. Meot, "MW-class 800 MeV/n H2+ SC-Cyclotron for ADS Application Design Study and Goals", IPAC12, New Orleans, LA, May 2012, THPPR064, p. 412 (2012).

[20] Y. Jongen, "Recent Progress in Cyclotrons for Carbon Therapy at IBA", talk, Workshop on Hadron Beam Therapy of Cancer, Erice, Sicily Apr 24 – May 1, 2009, `http://erice2009.na.infn.it/TalkContributions/Jongen2.pdf`

[21] J. Taylor, "A Fixed Field Alternating Gradient Accelerator for Helium Therapy", Proceedings of IPAC16, Brusan, S. Korea, May 8-16, 2016 pp 1953-1956.

[22] J. F. Ziegler *et al.*, "The Stopping and Range of Ions in Matter", Nuclear Instruments and Methods in Physics Research Section B, 268(11-12), pp. 1818-1823 (2010).

[23] T. Planche, private communication see http://www.triumf.ca/research-program/research-facilities/main-cyclotron-beam-lines and https://cycops.triumf.ca/cycfac.htm

3.14 RACCAM: An Example of Spiral Sector Scaling FFA Technology

François Méot, Brookhaven National Laboratory C-AD, Upton, NY, USA.

Abstract

The RACCAM project prototyped a spiral sector, scaling FFA dipole. It was the first of its kind and a major component in a rapid-cycling compact ring design for a multiple beam proton-therapy installation. A brief description introduces the project and the merits of spiral, scaling FFA technology. The article then focuses on the magnet design, field measurements and their use in beam dynamics simulations carried out to validate the design.

3.14.1 The RACCAM method

The RACCAM project (Recherche en ACCélérateurs et Applications Médicales) covered the period 2006-2009 and was funded by the French Agence Nationale de la Recherche [1]. The RACCAM partnership comprised CEA Saclay and Grenoble CNRS-IN2P3/LPSC laboratories, the SIGMAPHI magnet company, oncologists from Grenoble university hospital, the AIMA cyclotron company at the MEDICYC anti-cancer clinic in Nice, and was later joined by IBA. A number of technical reports were produced in which details of the project and its technical achievements can be found [2, 3]. The project owed much to long term collaborations with Prof. Y. Mori and his team at the Kyoto University Research Reactor Institute (KURRI, since renamed KURNS).

The concept of Fixed Field alternating gradient Accelerators (FFA) was developed in the 1950's and 60's during the early years of the strong focusing and phase stability studies [4]. FFAs benefit nowadays from advancements in 3-D magnet design tools and high gradient RF technologies, and from 6-D beam dynamics simulations. They can call on extensive R&D and experimentation carried out in Japan with electron and proton machines [5].

Drawing on experience at other labs that have looked at spiral FFA design or construction [6, 7], RACCAM prototyped a normal-conducting spiral scaling FFA dipole as a sector of a 10-period ring with the potential for high dose delivery. The ring design was based on fixed-field, synchro-cyclotron style, rapid-cycling techniques, and had the potential for compactness using modern magnet technologies. The magnet design used OPERA for the 3-D field calculations and the Zgoubi ray-tracing code [8] for 6-D beam dynamics validation. The magnet was fabricated and measured at SIGMAPHI. Field measurements were ultimately used to demonstrate constant tunes and large dynamical acceptance and so validate the magnet design and construction.

The different stages of the RACCAM development are addressed in what follows, with the aim of showing the merits and potential of rapid-cycling, spiral sector, scaling FFA technology.

Protontherapy application

A feature of a rapid-cycling FFA machine is that it can deliver a high dose rate, potentially far beyond 5 Gy.litre/minute, in a space-charge free regime. This beam delivery regime is well suited for slice-to-slice energy variation so allowing 3-D conformational irradiation. It allows bunch-to-bunch energy variation and thus 3-D tumor motion tracking. Other potential advantages include the use of non-pulsed power supplies, simple RF systems, simultaneous beam delivery to several treatment rooms and different particle species. In addition, a fixed field accelerator is associated with conservative construction methods and operation, high stability and reliability, low maintenance, and potential for low treatment cost.

With the aim of exploiting FFA potential, the most challenging issues are likely to be: (i) variable energy over a 100 ms time scale; (ii) dose rate of 5 Gy.litre/minute and beyond;

(iii) bunch-to-voxel beam delivery method; (iv) fast bunch-to-bunch energy variation over an energy range, ΔE, of a few 10's of MeV; (v) multiple port simultaneous extraction.

Table 1: Parameters of the proton-therapy accelerator installation.

Energy, variable	MeV	70 to 230
Injection energy, variable	MeV	5.5 to 18
Average intensity	nA	> 100
Extraction efficiency	%	> 95
Extraction mode	single-bunch	
Irradiation mode	bunch-to-voxel	
Repetition Rate	Hz	> 100
Number of beam extraction ports		1 to 5
Repetition rate per port	Hz	20 to 100

The general specifications for the installation are summarized in Table 1[1]. In terms of repetition rate and bunch filling, the parameters and properties on which the RACCAM study was based are the following.

- The reference irradiation volume considered is a $10 \times 10 \times 10\,\mathrm{cm}^3$ cube, comprising $20 \times 20 \times 20$, $0.5 \times 0.5 \times 0.5\,\mathrm{cm}^3$ elementary voxels. The reference irradiation is thus performed by scanning a series of twenty, 5 mm thick slices, 400 voxels each.
- As a consequence, in a single-pass painting mode the repetition rate needs be 8000 voxels per minute, *i.e.* ~ 133 Hz.
- In a 10 cm depth spread-out Bragg peak distribution, the energy deposition is ~ 0.07 J per 10^{11} protons, independent of energy.
- The bunch charge needed is a maximum for the deepest slice, $\sim 20\%$ of the total in the present reference cubic volume. There it reaches $\sim 10^9$ protons per bunch, for 5 Gy/minute in the 1 litre volume considered.
- The time necessary for a change of beam energy from one slice to the next needs to be small, much less than one minute. Referring to the experience at PSI's superconducting medical cyclotron, a conservative 100 millisecond time scale is considered. This suggested the prototype should be constructed with a laminated yoke.

A spiral FFA accelerator system

The principle of the RACCAM multi-beam delivery FFA is sketched in Fig. 1. The ensemble includes a H^- variable extraction energy cyclotron, a short transfer line to the FFA ring and a multiturn injection system. The ring has two RF cavities for $f_{\mathrm{rep}} > 100$ Hz repetition rate, and $N = 2$ to 5 extraction ports that deliver beams simultaneously (at a rate of f_{rep}/N at each port).

Simultaneous beam delivery to several rooms

A detailed layout of a dedicated treatment center, using the multi-port simultaneous extraction system to serve several rooms, has been devised and is shown in Fig. 2. The symmetry of the building is adapted to the configuration of the accelerator and extraction system. Each beam line out of the FFA ring is directed to a treatment room, where beam can be delivered independently of the other rooms at a rate ensuring 2 Gy/minute delivery and beyond.

[1]Parameters of an "optimal medical proton ring" similar to those in Table1 were derived at the FFAG07 Workshop in Kyoto, see Ref. [7],

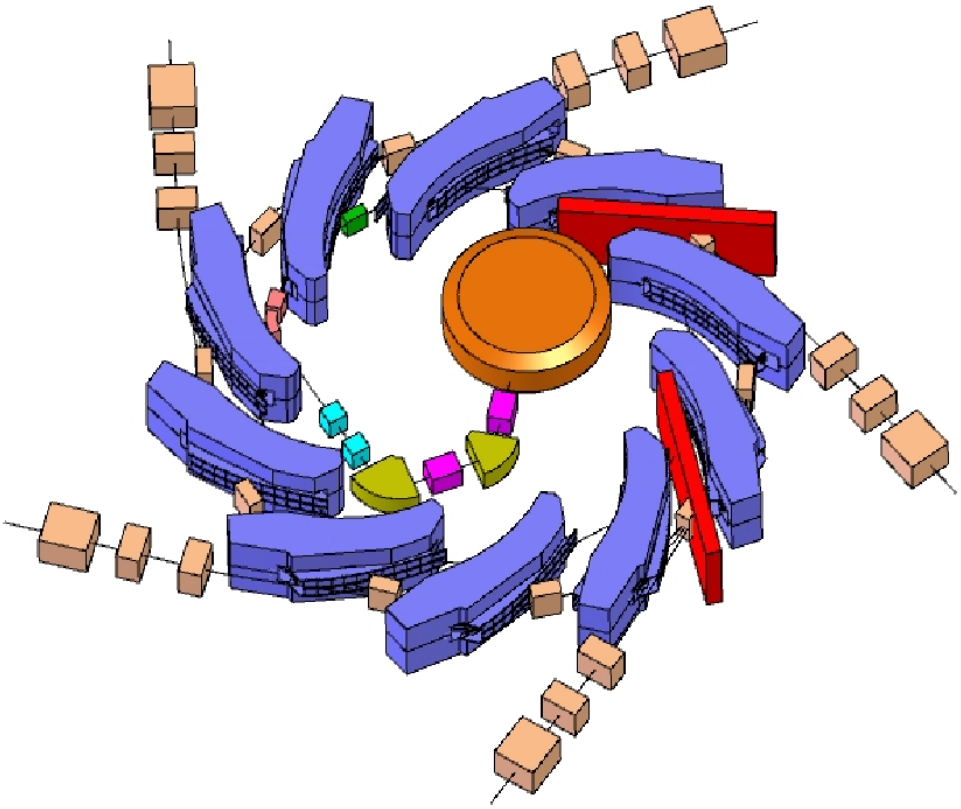

Figure 1: Layout of the RACCAM variable energy FFA ring, with its inner cyclotron injection system, two cavities (red boxes) for high repetition rate and multiple beam extraction systems for simultaneous beam delivery to several treatment rooms.

The FFA ring is located in the basement of the building. The beam lines have vertical bends so as to reach the level of the treatment rooms on the upper floor. Patient preparation rooms and other medical and administrative premises are located in the central area of the building, as well as between the treatment rooms.

The potential advantages of the multi-port polygonal arrangement for beam extraction and delivery, compared to a classical rectangular, single-extraction layout, include:

- potential for a greater number of treatments, Fig. 3;
- potential for more beam time in a single room;
- independent ion species delivery for radiobiology R&D, accelerator and beam developments;
- minimizing building and architectural footprint as well as distances between the various medical zones;
- minimizing the distances to be covered by patients and medical staff;
- reducing the man-power needed to operate the treatment center;
- lowering building construction and operation costs;
- improving architectural aspects such as lighting, radiation shielding, etc.

These considerations meet the objectives of reducing treatment cost, and improve the economic effectiveness of hadron-therapy so that it compares favourably with (X-ray) Intensity Modulated Radio-Therapy (IMRT). It is estimated that the cost of a treatment session is roughly one half of a conventional proton-therapy session, bringing it down to less than twice the cost of an RX session [9].

The hospital and its accelerator installation gain flexibilty, and can, for example, target a specialized type of treatment, meaning a reduced energy range, common to all the rooms. Energy adjustments are thus easier and can even be based on a small scale degrader system. There can be a low energy installation - $\sim 70\,\mathrm{MeV}$ in the case of eye treatment - or a higher, $\sim 180\,\mathrm{MeV}$ installation for head-neck treatment. Such a "specialized energy" hospital may be another advantage of multi-room, simultaneous delivery, and may bring additional reductions in construction and operating costs.

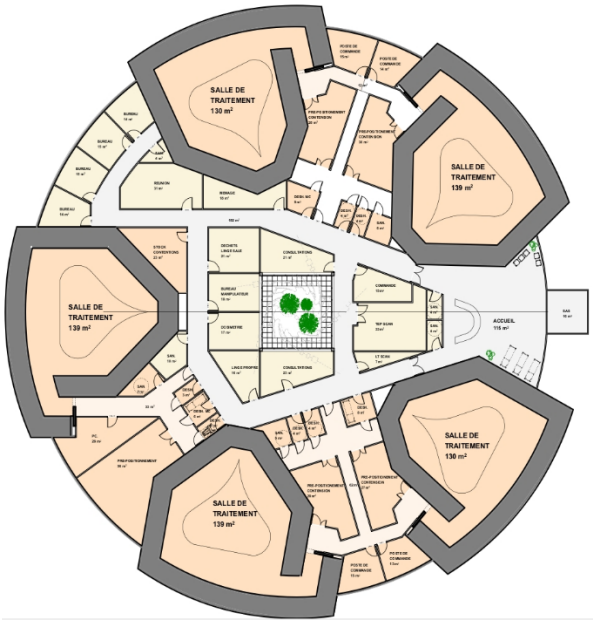

Figure 2: A $2\pi/N$-symmetric proton-therapy center based on a multi-extraction spiral sector FFA ring. The ring is located beneath the treatment floor; its $N = 5$ extraction ports deliver beams to each of the five treatment rooms simultaneously. The building is 58 m in diameter for a 230 MeV installation including gantries (a center specializing in eye tumor treatment for instance would have a smaller accelerator installation, simpler beam lines and less shielding).

3.14.2 RACCAM prototype spiral sector dipole

When spiral sector magnet studies started on RACCAM, various ways were seen to achieve the $B \propto r^K$ scaling law. Coil shaping methods had been studied and implemented in the past [6,10], and would eventually also be studied in the context of this project [11]. However RACCAM opted for an innovative gap-shaping technique for compactness and lower power consumption. This section briefly introduces the theoretical aspects and design principles used.

A spiral sector ring is characterized by a mid-plane field of the form [12]

$$B(r) = B_0 \left(\frac{r}{r_0}\right)^K \mathcal{F}\left(\tan(\zeta) \ln \frac{r}{r_0} - N\theta\right) \tag{1}$$

with θ the azimuthal angle, r the local radius measured from the center of the ring (Fig. 4), K the field index, B_0 the field at an (arbitrary) reference radius r_0, ζ the spiral angle, and N the number of cells. $\mathcal{F}$ is essentially an AVF (Thomas focusing) style of azimuthal periodic form factor, featuring (possibly negative) field valleys between high field hills for a large flutter, as discussed below. A radial dependence of the field of the form $B(r)/B_0 = (r/r_0)^K$ ensures zero chromaticity (horizontal tune independent of energy), a key property of scaling optics (where orbits scale with momentum), and constant vertical tune (ignoring fringe field constraints, addressed below). The

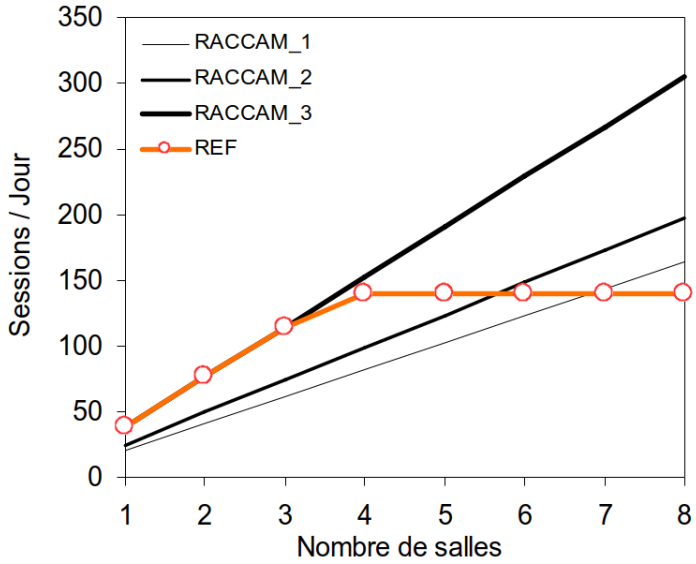

Figure 3: Simultaneous beam delivery to multiple treatment rooms increases beam delivery efficiency (sessions per day) linearly with the number of rooms. The lines labelled RACCAM_1, _2 and _3 differ mostly by the time the patient spends in the treatment room for pre- and post-irradiation procedures, respectively 41, 34 and 22 minutes. By comparison, sequential beam delivery from a single extraction accelerator ("REF", red curve) indicates a maximum of about 150 sessions per day, from 4 or more rooms.

RACCAM dipole acquires the r-dependence of the field from gap shaping, Fig. 5, based on a variable gap size of the form

$$g(r) \approx g_0(r_0/r)^\kappa. \tag{2}$$

The prototype sector dipole has $g_0 = 4\,\mathrm{cm}$ at the maximum orbit excursion $r_0 = 3.46\,\mathrm{m}$ (Table 2) and, from the OPERA optimization, $\kappa = 5.2 \approx K$.

The resulting r-dependent momentum, the momentum compaction and the transition γ can be written, respectively,

$$\frac{p(r)}{p_0} = \left(\frac{r}{r_0}\right)^{K+1}, \qquad \alpha = \frac{\Delta r}{r}\Big/\frac{\Delta p}{p} = \frac{1}{K+1}, \qquad \gamma_{\mathrm{tr}} = \sqrt{1+K}\,.$$

The local radius r and curvature radius ρ (Fig. 4) are related by

$$r\sin(A/2) = \rho\sin(\pi/N) \tag{3}$$

where A is the sector angle of the dipole. A value of $N = 10$ was adopted in the RACCAM prototype approach; however a greater number would allow simultaneous beam delivery from more extraction systems. The logarithmic spiral field boundaries of the magnet (Fig. 6) satisfy $r = r_0\exp(\theta/\tan\zeta)$. The fringe fall-off is characterized by the flutter

$$F = \frac{\overline{B^2}}{\overline{B}^2} - 1 \qquad \text{which tends to} \qquad \frac{r}{\rho} - 1$$

in the case of a hard-edge model. The greater the flutter (closer to hard-edge), the greater the vertical focusing. A rough approximation to the horizontal and vertical tunes given by [12, Eq. 5.2]

$$Q_r \approx \sqrt{1+K}, \qquad Q_y \approx \sqrt{-K + F^2(1+2\tan^2\zeta)} \tag{4}$$

is helpful as a first approach to understanding the respective effects of varying K, ζ or F.

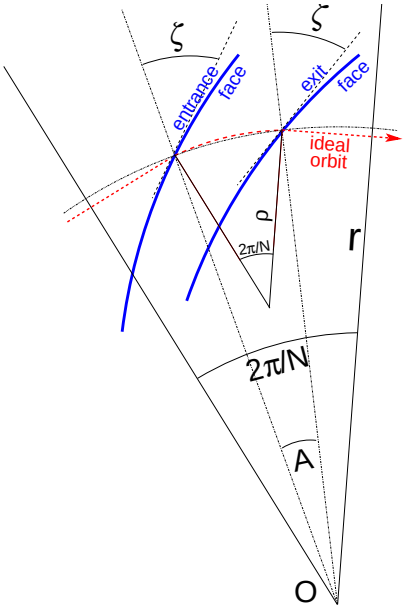

Figure 4: Diagram of a spiral sector FFA cell and its geometrical parameters, nomenclature as in Table 2. The origin of the polar system is at the center of the ring.

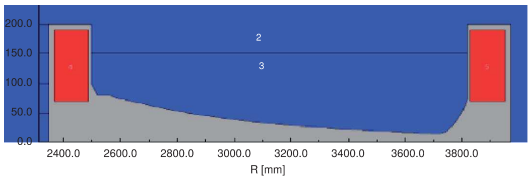

Figure 5: Two-dimensional model of the upper half-yoke, gap and coil in OPERA. This 2-D study gives the proper gap shape to satisfy $B(r)/B_0 = (r/r_0)^K$ for a given K over the useful field region (namely, $2.9 \leq R \leq 3.3\,\mathrm{m}$, in the prototype dipole).

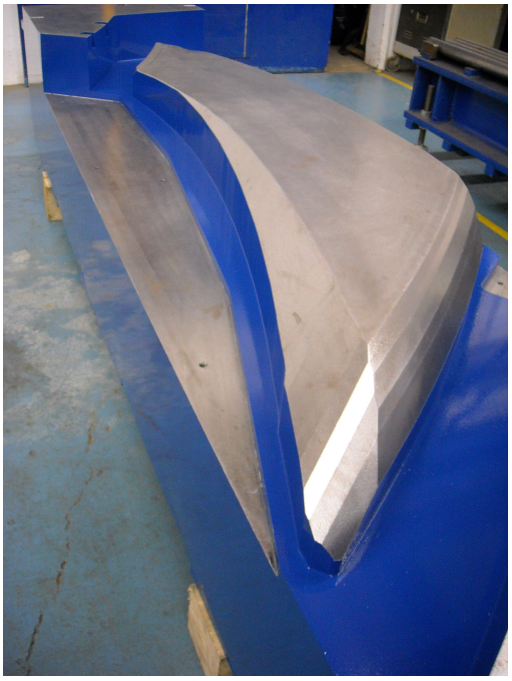

Figure 6: Half-yoke and pole during the magnet construction and assembly at SIGMAPHI, 2008. The wide variation of the chamfer over the radial extent of the pole can be seen on its exit edge (left).

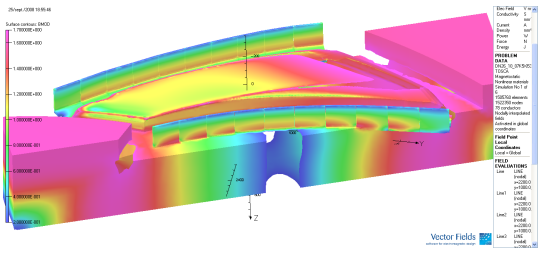

Figure 7: Field densities, from the OPERA 3-D model. The model is complete here: it includes variable chamfers and field clamps, both major ingredients in achieving constant vertical tunes over the 40 cm radial extent of the good field region $2.9 \leq R \leq 3.3\,\mathrm{m}$. The center of the ring is to the left, the gap decreases to the right.

Table 2 summarizes parameter values in the case of the RACCAM dipole. The field index K has been taken large enough to limit the radial beam excursion $r_{\mathrm{xtr}} - r_{\mathrm{inj}}$ from the injection

Table 2: Parameters of the prototype spiral sector (Figs. 6-9), and an FFA ring (Fig. 1).

Prototype gap shaping spiral sector		
Deviation ($2\pi/N$)	deg	36
Reference radius (r_0)	m	3.46
Field index (K)		5.00
Spiral angle (ζ)	deg.	53.7
Sector angle (A)	deg.	12.24
Packing factor (pf)		0.34
Principal FFA ring		
Energy range, high	MeV	70–180
Energy range, low	MeV	6.3–70
Packing factor (pf)		0.34
Maximum field at r_0	T	1.7
Number of cells (N)		10
Q_r		2.76
Q_y for $15 \rightarrow 180$ MeV		$1.55 \rightarrow 1.60$
Transition gamma ($\gamma_{\rm tr}$)		2.45
Orbit excursion	m	$2.794 \leq r \leq 3.460$

In the table "Energy range" indicates what is achievable during operation of the ring, from injection at E_{min} to extraction at E_{max}. This is dependent on the field setting, with 1.7 T at r_0 being the "high" case. "Orbit excursion" stands for the radial span of the orbit, from E_{min} to E_{max}.

to extraction orbits, which follows from

$$r_{\rm xtr} - r_{\rm inj} = r_0 \left(1 - \left(\frac{p_{\rm inj}}{p_{\rm xtr}} \right)^{1/(K+1)} \right) , \tag{5}$$

thus limiting the extent of the magnet. On the other hand, K has been taken small enough that the spiral angle ζ remains below 55 degrees (K and ζ act in opposing ways on the vertical tune, see Eq. (4)). There are three main reasons for this: (i) simplifying the magnet design and construction; (ii) allowing room between magnets in the ring; and (iii) yielding weak non-linear field components to get large enough dynamic aperture (DA). These various constraints and optimizations resulted in $Q_r \approx 2.76$ for all energies, while Q_y varies from 1.55 at injection to 1.60 at extraction.

A note on the vertical tune. The wedge vertical focusing term in the linear approximation can be written $y'/y_0 = \tan(\epsilon - \psi)/\rho$ with ρ the local curvature radius and $\epsilon = 2\pi(1-pf)/N \mp \zeta$, the upstream and downstream wedge angles. pf =magnetic length / orbit length is the packing factor. ψ is a correction term for the fringe field extent and is written

$$\psi = I_1(r)\, \frac{\lambda(r)}{\rho(r)}\, \frac{1+\sin^2\epsilon}{\cos\epsilon} \qquad \text{with} \qquad I_1 = \int \frac{B_y(s)(B_0 - B_y(s))}{B_0^2}\, \frac{ds}{\lambda} .$$

Since the (r-dependent) fringe field extent $\lambda(r)$ is proportional to the gap height $g(r)$ (Eq. (2)), and given that ρ and r are proportional to one another (Eq. (3)), the vertical focusing is r-dependent and thus so is the vertical tune Q_y. The role of the field clamps in the prototype (Figs. 7 and 9), which decrease the fringe extent in the large gap region, and of the variable width chamfer (Fig. 6) that increases the fringe extent in the smaller gap region, is to compensate that effect and substantially reduce the variation of Q_y to $\Delta Q_y \lesssim 0.05$ (Table 2) over the full orbit excursion in the ring ($2.794 \leq r \leq 3.460$).

The electro-mechanical parameters of the fabricated prototype are summarized in Table 3. Note that the "Good field region" does not cover the full orbit excursion in the ring; this is for cost saving purposes.

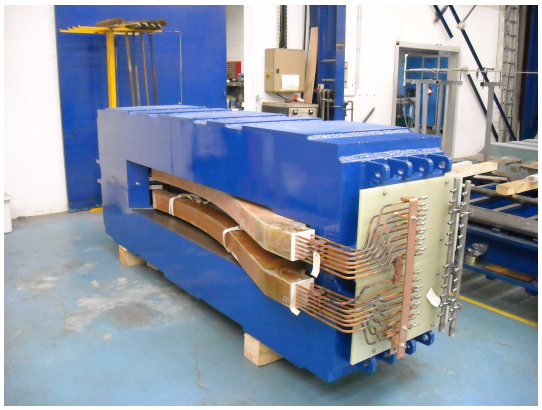

Figure 8: RACCAM spiral dipole during assembly, field clamps not yet mounted.

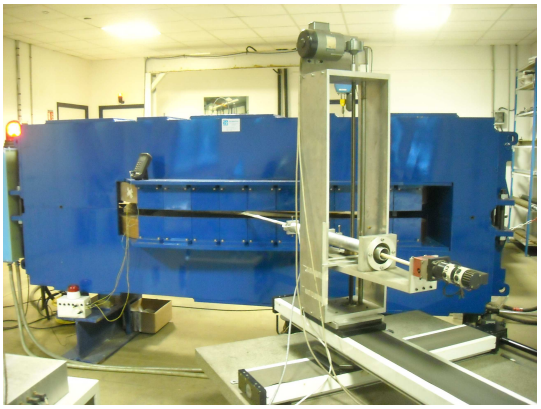

Figure 9: RACCAM dipole during Hall probe measurements using an XYZ table. The field clamps along the coils (hidden) are visible on the right. Their presence helps reduce the fringe field extent in the large gap region.

Table 3: Electro-mechanical parameters of the prototype spiral sector dipole.

Yoke shape		Parallelepiped
Lamination thickness	(mm)	1.5
Gap shape		$\propto 1/r^{\kappa},\ \kappa \approx 5.2$
Gap at 3.46 m	(cm)	4
Gap at 2.794 m	(cm)	11.6
Overall dimension L× W× H	(mm)	2913 × 579 × 1230
Good field region	(m)	$2.9 \leq r \leq 3.3$
Total weight of magnet	(t)	18
PS voltage	(V)	159
PS current (180 MeV operation)	(A)	200
Total water flow	(litres/min)	12.13
Water temperature, in/out	(°C)	24/44

3.14.3 Field measurements

The RACCAM magnet prototype has been designed, constructed and measured to validate the gap shaping method, and the computation and fabrication methods, including thorough comparison of the field derived both. With that in mind, a series of 3D field map Hall probe measurements were performed, using an XYZ table, Fig. 9, over a total period of 600 hours [13, 14].

Mid-plane field measurements have been performed along arcs at constant radius (with center at the origin of the polar frame, Fig. 4) where the field is expected to be constant in the body of the magnet, according to the scaling law, Eq. (1). The azimuthal step of the mesh was 0.2°; the radial values considered were $R_0 \pm 55$ mm in steps of 11 mm (11 arcs) with $R_0 = 2750,\ 2900,\ 3125,\ 3300$ and 3450 mm so ensuring coverage of the good field region of the prototype (2.9 to 3.3 m), Fig. 10.

The measurements were performed at three different intensities:

- $I_{\max} = 225$ A yielding $B(r_0) = 1.933$ T at the extraction radius $r_0 = 3.46$ m, a theoretical extraction energy of 227 MeV, well beyond the 180 MeV RACCAM scope;
- $I80 = 0.8 \times I_{\max} = 180$ A yielding $B(r_0) = 1.606$ T, extraction energy 162 MeV; and

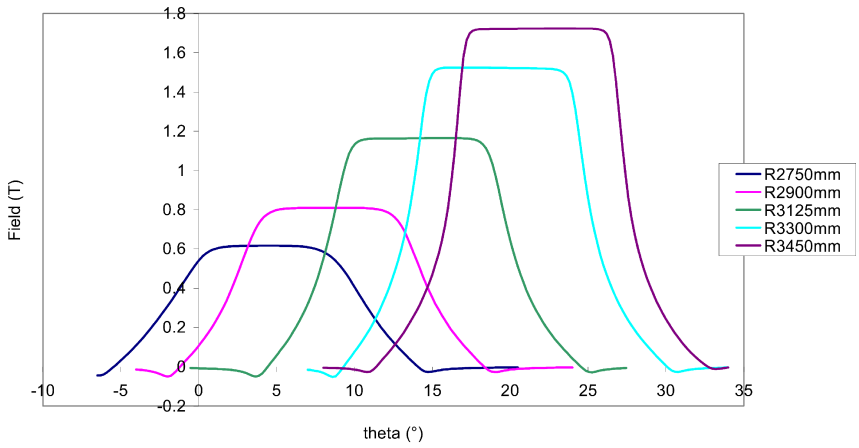

Figure 10: Typical measurements: $B_y(\theta)$ at constant radius, on 5 different radii across the good field region.

- $I60 = 0.6 \times I_{\max} = 135\,\mathrm{A}$ yielding $B(r_0) = 1.227\,\mathrm{T}$, extraction energy 98 MeV.

These detailed measurements allowed a series of cross-checks against values expected from a combination of the OPERA field computations, theoretical modeling of the spiral sector field [2,3, 15], the r-dependence of the field and the integrated field, the field index K and the spiral angle along the entrance and exit field boundaries. The measurements were considered sufficiently comprehensive to be used to validate the magnet design and fabrication; details can be found in Refs. [13, 14].

3.14.4 Validation by beam dynamics

The field measurements validate the design to the extent that fields and parameters derived from the fields are in accord with OPERA design simulations, or, where the agreement is not satisfactory, the reasons can be understood. The latter included effects such as saturation observed at the maximum experimental current, $I = 225\,\mathrm{A}$, which yields 1.933 T at $R = 3.46\,\mathrm{m}$, a value 0.2 T beyond the nominal design value. Nevertheless it was decided that further tests of a beam dynamics nature were necessary for completeness:

- The design is expected to yield constant tunes over the good field region, and at the various operating energies, as a result of the variable chamfer and clamp plate methods. The results are illustrated in Fig. 11,
- From the OPERA design studies, the dynamic aperture of the ring is expected to be of the order of $1\,\pi$mm horizontally and $0.2\,\pi$mm vertically, normalized.(Note that this is well beyond what medical proton beams actually require). This is illustrated in Fig. 12 and in Table 4.

These beam dynamics simulations have been performed using *measured* 2-D mid-plane field maps. They are summarized here, but more detail can be found in Ref. [14].

Table 4 shows that the vertical DA from the measured field maps ($1200 \sim 1500\,\pi\mu$m, vertical) is larger than expected from the OPERA field map ($900 \sim 1000\,\pi\mu$m). This indicates that a greater K could be a considered (which would decrease the vertical DA), so yielding smaller radial excursion over the acceleration range (Eq. (5)) and therefore a smaller magnet.

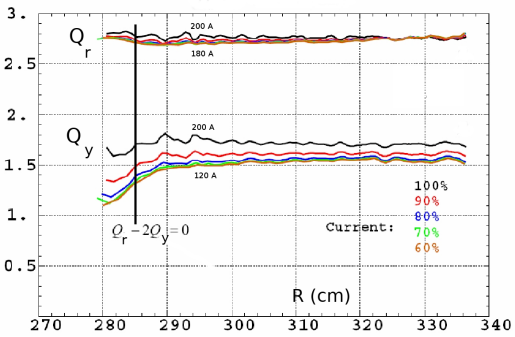

(a) Horizontal tune Q_r derived from OPERA data, with currents in the 120-200 A range. At 200 A the OPERA model field is 1.7 T at R=3.46 m.

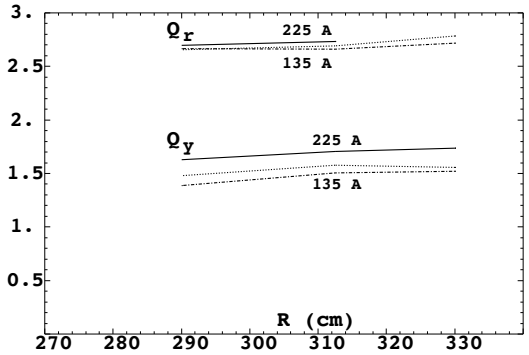

(b) Vertical tune Q_y derived from measured fields at 135, 180 and 225 A. At 225 A the measured field is 1.933 T at R=3.46 m.

Figure 11: Horizontal and vertical tunes from tracking in 2-D field maps. The horizontal motion is found to be unstable at 225 A in the R=330 cm region. This is a consequence of $K \approx 4.6$ (compared to the $K = 5$ design value) due to saturation [13, 14]. However, this happens at a field regime far off the nominal design.

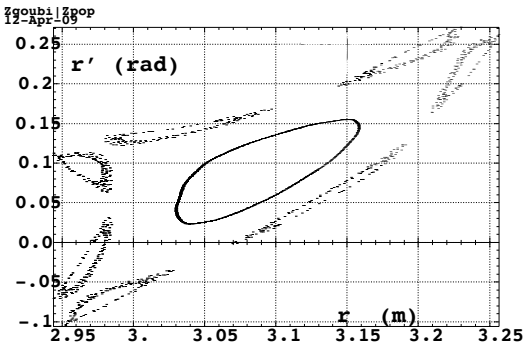

(a) Horizontal

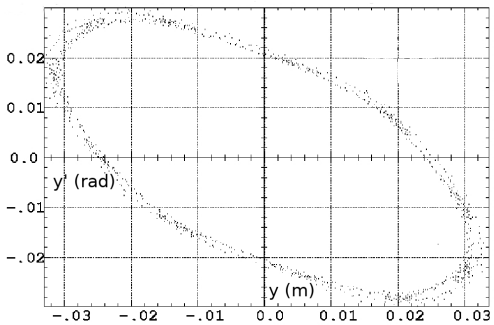

(b) Vertical

Figure 12: Maximum stable motion invariant in the $R = 3125$ mm region. Results from tracking in measured 2-D field maps (a) horizontal, either in the absence of vertical motion, or with small initial vertical motion (inner invariant); (b) corresponding results in the vertical plane.

Table 4: Dynamic apertures (DAx, DAy, horizontal and vertical, respectively) from 1000-turn tracking, using field maps. DAx (respectively DAy) is the area delimited by the largest horizontal (resp. vertical) invariant as shown in Fig. 12a (resp. Fig. 12b).

		From measured field maps		From OPERA 3D field maps	
R region (mm)	E (MeV)	DAx	DAy	DAx	DAy
		($\pi\mu$m)			
Maximal current		*($B_0 = 1.933$ T)*			
2900	38.0	1800	900		
3125	86.5	2600	800		
3300	156	5500	1500		
$80\%I_{max}$		*($B_0 = 1.606$ T)*		*($B_0 = 1.7$ T)*	
2900	15	4000	1500	2500	900
3125	35.9	1500	1200	2900	1000
3300	67.3	1700	1400	3500	950
$60\%I_{max}$		*($B_0 = 1.227$ T)*			
2900	15	1200	900		
3125	35.9	1200	900		
3300	67.3	2200	900		

Conclusions

The RACCAM project opted for a gap shaping method to design a spiral sector, scaling FFA field. The magnet was prototyped and measured. It was the first of its kind and delivered the expected performance.

This technology has the potential for compactness because it allows a high packing factor, which is a consequence of the short drifts, a characteristic of the strong focusing feature of FFA optics. A more compact magnet than the RACCAM prototype, with similar 230 MeV reach, could be achieved based on different technologies (permanent magnets, super-ferric magnets) [16], and possibly with greater field index K for smaller radial beam excursions.

References

[1] S. Antoine et al., "Principal design of a protontherapy, rapid-cycling, variable energy spiral FFAG", NIM A 602 (2009) 293-305.

[2] J. Fourrier, "Les accélérateurs à champ fixe et gradient alterné FFAG et leur application médicale en protonthérapie", PhD Thesis, IN2P3/LPSC and J. Fourier University, Grenoble, Oct. 2008.

[3] T. Planche et al., "Design of a prototype gap shaping spiral dipole for a variable energy protontherapy FFAG", NIM A 604 (2009) 435–442.

[4] F.T. Cole, "A memoir of the MURA years", April, 1994.

[5] FFAG Accelerators, ICFA Beam Dynamic Newsletter, No. 43, Eds. C.R. Prior, W. Chou (2007), pp. 15-156.

[6] A. Osanai et al., "Study of integer betatron resonance crossing in scaling FFAG accelerator", TH6PFP079, Proceedings of PAC09, Vancouver, BC, Canada;
`http://accelconf.web.cern.ch/AccelConf/PAC2009/papers/th6pfp079.pdf`

[7] A link to the FFAG workshops series : `http://www.triumf.ca/ffag2004/links.html`.

[8] F. Méot, "The ray-tracing code Zgoubi - Status", NIM A 767 (2013).

[9] Ch. Mazzara, "Etude medico-economique d'un centre de protonthérapie equipé d'un accélérateur FFAG à extraction multiple", Rapport de stage Master2 de physique médicale, IN2P3/LPSC and J. Fourier University, Grenoble (2010).

[10] See for instance, K.R. Symon et al., "Fixed-Field Alternating Gradient Particle Accelerators", Phys. Rev. 103 6 (Sept. 15, 1956).

[11] D. Neuvéglise and F. Méot, "An Alternative Design for the RACCAM Magnet with Distributed conductors", FR5REP095, Proceedings of PAC09, Vancouver, BC, Canada;
`http://accelconf.web.cern.ch/AccelConf/PAC2009/papers/fr5rep095.pdf`

[12] F.T. Cole, "MARK V expanded equations of motion", MURA/FTC-3, 19 Jan. 1956.

[13] M.-J. Leray et al., "Magnetic measurements of the RACCAM prototype FFAG dipole", Proc. PAC 09 Conf., Vancouver (2009);
`http://accelconf.web.cern.ch/AccelConf/PAC2009/papers/fr5rep110.pdf`

[14] S. Antoine et al., *et al.*, "Tracking periodic parameters in the measured magnetic field maps of a spiral FFAG", Proc. PAC 09 Conf., Vancouver (2009);
`http://accelconf.web.cern.ch/AccelConf/PAC2009/papers/fr5rep094.pdf`

[15] J. Fourrier, F. Martinache, F. Méot, J. Pasternak, "Spiral FFAG lattice design tools, application to 6-D tracking in a proton-therapy class lattice", NIM A 589 (2008) 133-142.

[16] B. Qin, Y. Mori, "Compact superferric FFAG accelerators for medium energy hadron applications", NIM A, Volume 648, Issue 1, 21 August 2011, Pages 28-34.

3.15 Optical Design of a Fixed Field Permanent Magnet Gantry for Hadron Therapy[1]

Dejan Trbojevic, Stephen Brooks, François Méot and Nicholaos Tsoupas,
Brookhaven National Laboratory, Upton, NY, USA.
William Lou, Cornell University, CLASSE, Ithaca, NY, USA.

Introduction

Worldwide, cancer is the second most common cause of death after cardiovascular diseases. There are many types of cancer and many ways of treating the disease, mostly through a combination of methods such as surgery, chemotherapy, immunotherapy, targeted therapy and/or radiation therapy. Conventional radiation therapy relies on X-rays, usually produced from accelerated electrons and focused onto the tumor to destroy the cancerous cells. Techniques such as Intensity Modulated Radiation Therapy (IMRT), 3D-CRT three dimensional conformal radiotherapy, or Image-Guided Radiation Therapy (IGRT) direct the beam from a variety of angles to maximise the effect on the tumor while avoiding surrounding healthy tissues. Success is seldom 100% and the possibility of side effects is a serious risk.

The advantages of hadron therapy - using protons or ions such as carbon instead of X-rays - has been recognised for some time. A beam of protons can penetrate tissue with very little diffusion. The particles deposit their maximum energy almost immediately before stopping. This property (the "Bragg peak") allows precise location of the specific region that needs to be irradiated and damage to the surrounding healthy tissue can be minimised. This is especially critical in the case of children. Because of the success of the treatment, the number of hadron therapy centers has been growing strongly in recent years, and a total of about 200,000 patients have treated to date.

The importance of hadron therapy has been recognized by Governments worldwide. A recent workshop on Ion Beam Therapy [1] concluded by emphasizing the need for new technological developments particularly with a view to reducing the costs involved in further hadron therapy expansion. A major concern is the gantries used for the beam delivery systems which are huge and exceedingly heavy. They need to be far less massive and more compact. Ideally a technology is needed that can provide for rapid scanning (one or two seconds) of the beam over the tumor volume in three dimensions.

This is where the FFA linear gradient magnet comes into its own. The momentum acceptance of such a magnet can be very large, of the order $\Delta p/p = \pm 33\%$, which gives a momentum range corresponding to the proton kinetic energy range, 65-250 MeV, required for patient proton radiation therapy. The large momentum acceptance allows fast energy change without any magnetic field variation. The patient treatment time can be made shorter, and the operation is simplified because there is no need to change the magnetic fields. There are corresponding advantages in lower power consumption (operating costs), and the simplified design has a considerable effect in reducing the gantry cost. The reduction in the weight and size of the magnets allows lighter, rotating structures.

3.15.1 A proton therapy gantry based on FFA linear gradient magnets

For maximum effectiveness in focusing on the tumor while avoiding sensitive organs like the spine or the cardiovascular system, the proton gantry needs to be isocentric and able to rotate around the patient, allowing all possible angles of incidence. The design presented here assumes that at the entrance to the gantry protons within the required energy range (65-250 MeV) enter

[1]Work performed under Contract Number DE-AC02-98CH10886.

with zero offsets. Since the patient will usually be lying flat, the structure is such that the beam is bent to one side (left or right) or above the patient before being focused in onto the treatment area. Transverse spot scanning requires control over transverse distances of at least ±10 cm. Previous studies [2] showed how to merge multiple energy orbits from an FFA structure into a single orbit. This single orbit can be obtained by introducing a triplet of combined function magnets in front of the merging point, as shown in Fig. 1.

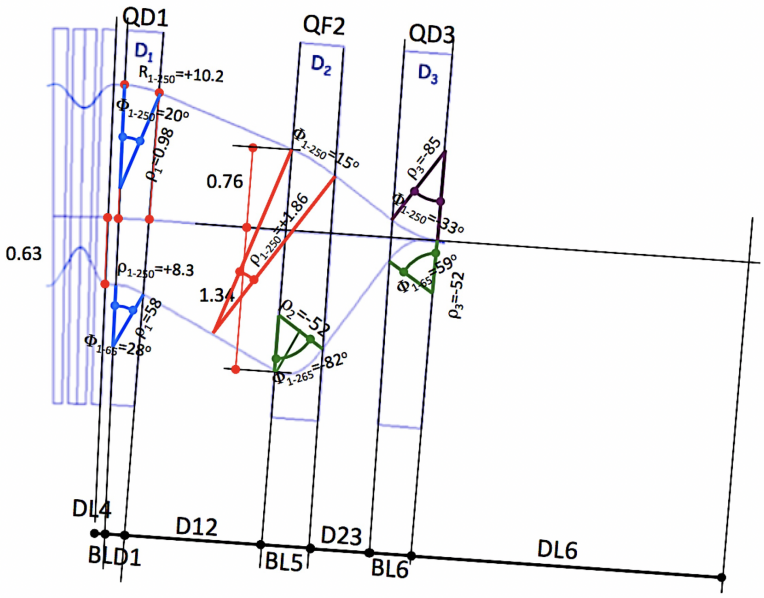

Figure 1: Merging orbits from the FFA gradient structure into a single orbit by using three combined function magnets.

The gantry itself is shown in Fig. 2 and comprises several modules. It rotates about the horizontal (X) axis. The beam enters from the left and exits at the vertical section at $X \sim 9.6$ m. The first module, M1, the section to the left as far as coordinates $X = 4.2, Y = -2.4$, accepts all proton energies and is achromatic. Each of the different energy orbits reaches its maximum offset at the middle of the module, where the slopes of the optical betratron and dispersion functions are zero. This module is mirror symmetric about its mid-point, so all orbits are merged into a single orbit on exit with the same betatron and dispersion values as at the beginning.

The magnets bend in the opposite direction in the second module, M2, with the first half being the reverse of the second half of M1. This is followed by a matched FFA gradient arc, M3, which bends the beam into a perpendicular direction onto the patient, with the same repetitive structure of the FFA cells. The final section of the gantry, M4, merges the different energy orbits onto the same final path to the patient. The distance of the last magnet from the patient is 1.435 m, where the horizontal and vertical betatron functions have values as close as possible to ∼1 m. A patent [3] covers the design of the transverse scanning system, which uses two magnets, the first following the triplet magnets and the second above the patient, separated by a distance of about 1 m.

Figure 3 shows the layout of the magnets, the orbits (upper part) and the betatron and dispersion optical functions (middle and lower parts). The curves are for protons with energies from 65 MeV to 250 MeV in steps corresponding to momentum variations with respect to the central energy $E = 160$ MeV of $\Delta p/p$= -0.38, -0.2, -0.1, 0.0, 0.1, 0.2 and 0.28. Similar details of the optical properties for the whole gantry are shown in Fig. 4.

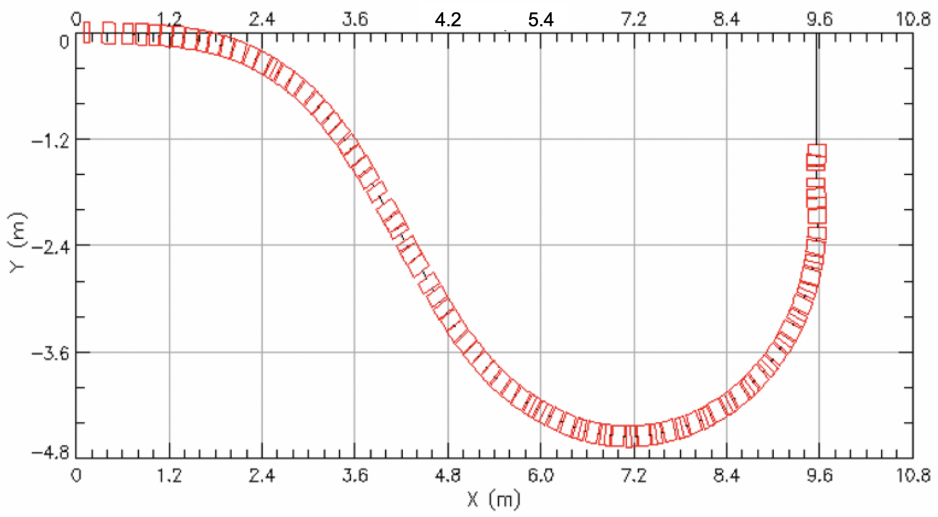

Figure 2: Layout of the whole gantry showing the relative magnet positioning. The first module, M1, is the section from $(X, Y) = (0, 0)$ to $(X, Y) = (-2.4, 4, 2)$. The X-axis is the axis of rotation.

3.15.2 Permanent Halbach-type magnet technology

The gantry magnets are Halbach type [4] built by the KYMA Italian-Slovenian company [5]. Combined function magnets are chosen with most of the bending coming from the defocusing magnet (shown in Fig. 5a). The focusing magnet is effectively a regular focusing quadrupole as it has very small bending angle. The technological development benefits from experience of building permanent magnets for the FFA gradient test at BNL's Accelerator Test Facility (ATF). Here electrons at four different energies were succesfully transported through an FFA gradient structure [6]. BNL subsequently built 220 combined function magnets for the Cornell University and Brookhaven National Laboratory Electron Test Accelerator, CBETA [7].

Special assembly devices, shown in Fig. 5b, were built by KYMA to construct the gantry magnets. The magnets are very similar to the BNL Halbach permanent magnets but with the aluminium wedges replaced by 16 separate NdFeBr wedges.

Summary and Conclusions

In summary, there are significant advantages in using protons and ions in cancer therapy because of the confinement and consequent safety aspects afforded by the "Bragg peak". However, for hadron therapy centers to be more widespread requires cheaper facilities, achieved principally through a reduction in the size, weight and therefore cost of the gantries. In this respect, the use of FFA-type linear gradient magnets offers several advantages:

(i) The magnetic field is fixed throughout the whole gantry, and the only variable aspect comes from the scanning dipoles at the end of the gantry. Transverse scanning is significantly slower as longitudinal energy scanning occurs automatically for each radial position.
(ii) The magnets are made of permanent magnet material (NdFeBr) and are small and light.
(iii) The large momentum acceptance of FFA's means that the energy range needed for proton therapy of 65-250 MeV, can readily be met.
(iv) A rapid energy change can be carried out without need for magnetic field variation.
(v) The patient treatment time is shorter as there is no need to change settings of the gantry magnets.
(vi) There is a significant reduction in the electricity power bill as the magnets are made of permanent magnet material.

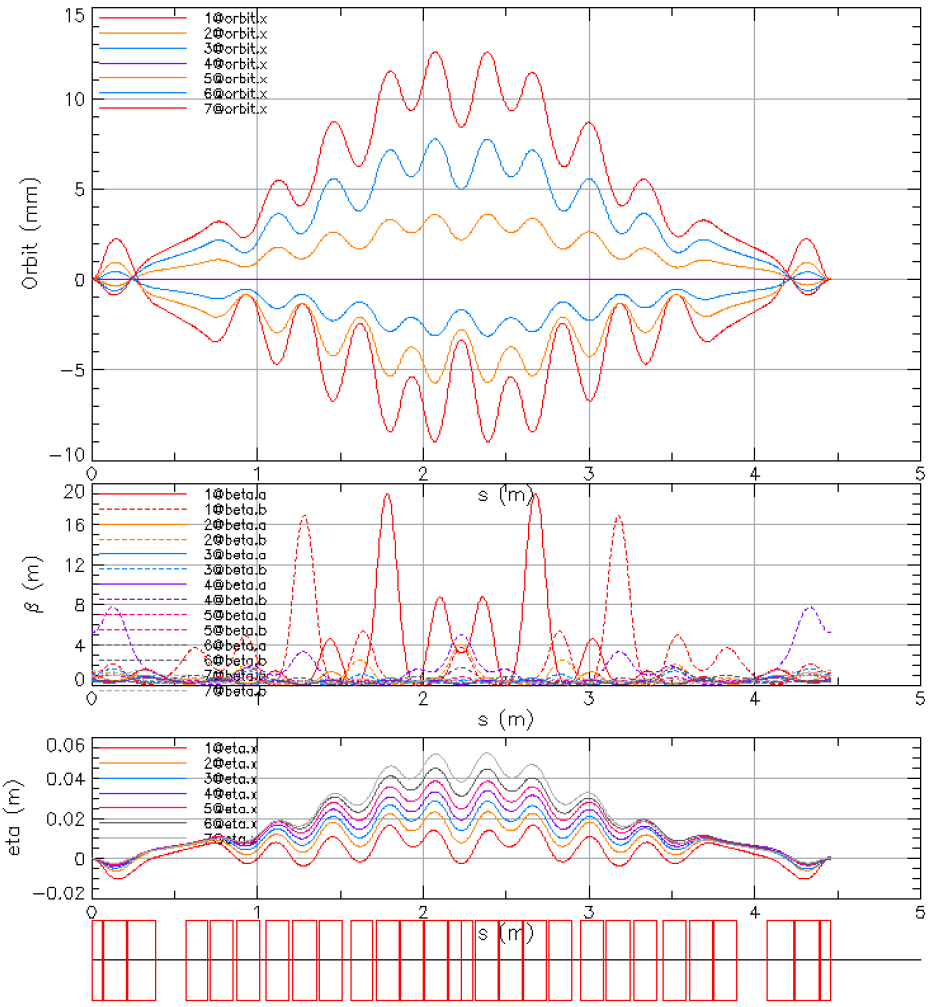

Figure 3: Beam dynamics in the first achromatic module of the proton gantry. Orbit offsets are shown at the top, betatron functions in the middle, while the dispersion functions are show at the bottom.

(vii) The overall cost is much reduced and the overall weight of the gantry is notably smaller.

(viii) As the rotating structure is so much lighter, it is easier to construct with consequent cost reduction.

(ix) The design allows very easy operation and no tuning is necessary.

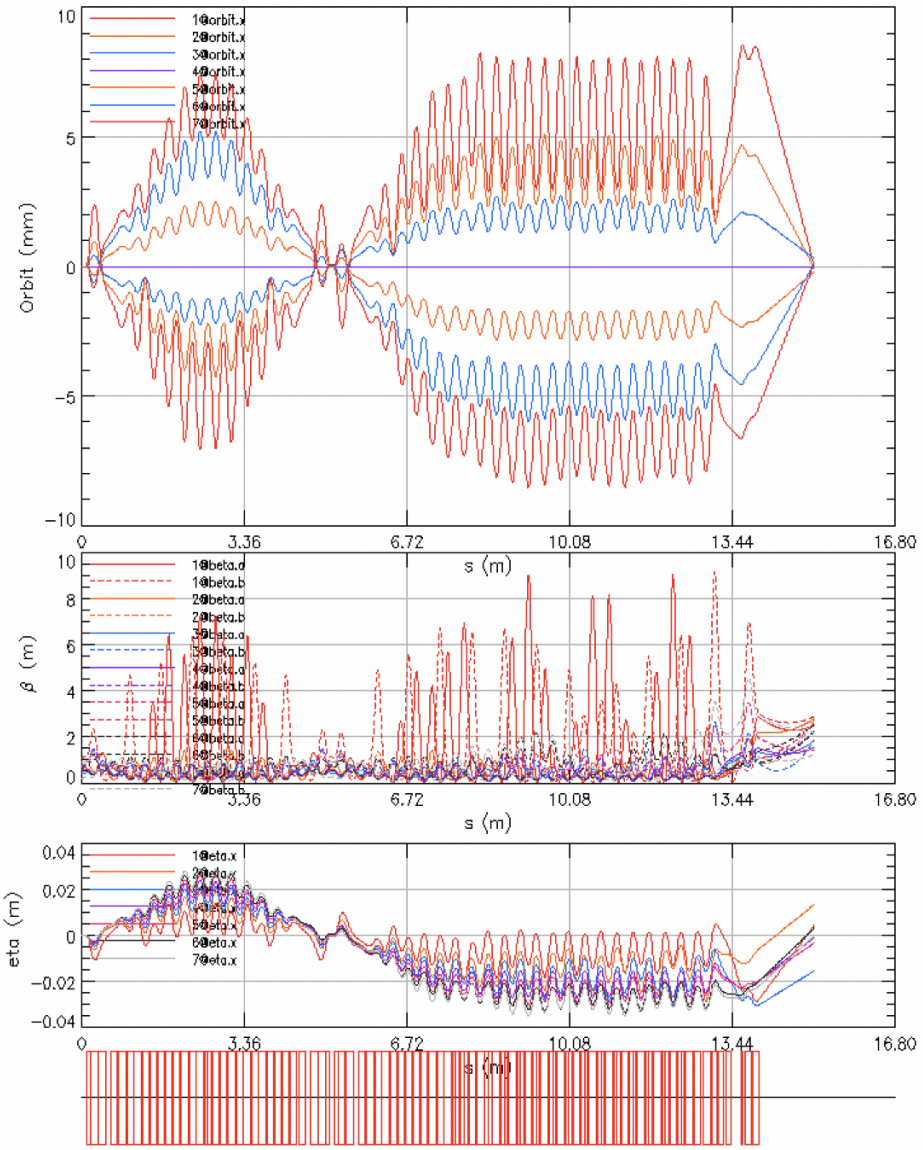

Figure 4: Orbits of the proton beams with energies within 65-250 MeV (upper part), the betatron functions (middle), and the dispersion functions (lower) for the complete gantry

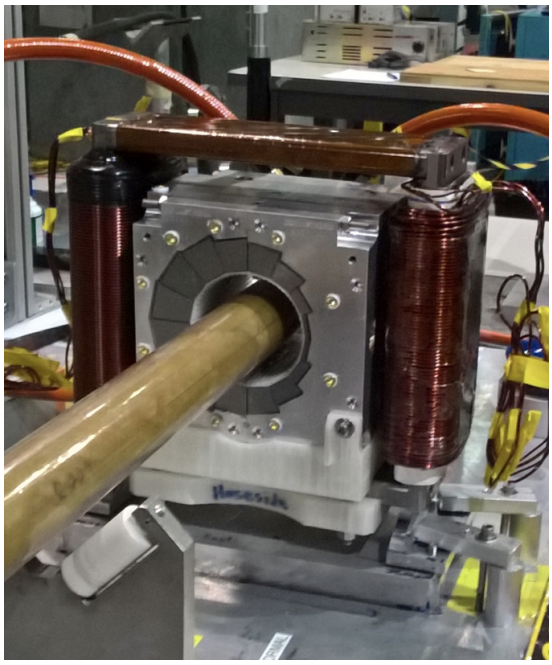

(a) Defocusing magnet together with the frame dipole corrector surrounding the magnet.

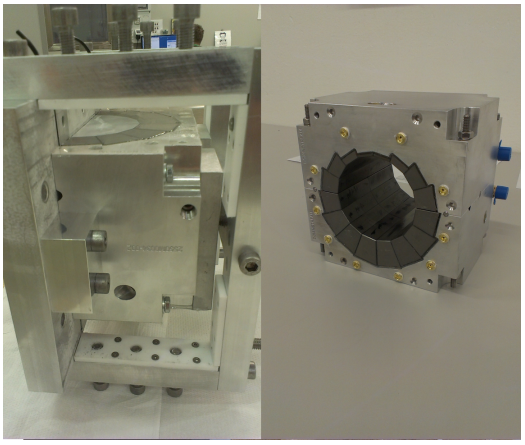

(b) Assembly structure and defocusing magnet.

Figure 5: Details of the KYMA-built magnets at BNL

Acknowledgments

We acknowlege the contribution of the KYMA company in producing combined function magnets of superb quality.

References

[1] Summary report on: Workshop on Ion Beam Therapy, Bethesda, Maryland, USA, January 9-11, 2013.
https://rrp.cancer.gov/content/docs/ParticleTherapyWorkshopProccedings.pdf

[2] D. Trbojevic, "Proton Therapy Gantry," presented at the International Fixed Field Alternating gradient Workhop (FFA'18) in Kyoto, Kyoto University, 10-14 September 2018, https://indico.rcnp.osaka-u.ac.jp/event/1143/contributions/1219/

[3] D. Trbojevic, "Scanning System for particle cancer therapy," United States Patent US 9,095,705 B2, August 4, 2016.
https://patentimages.storage.googleapis.com/3b/e5/e5/63cc90ecb034c8/US9095705.pdf

[4] K. Halbach, "Application of permanent magnets in accelerators and electron storage rings", J. Appl. Phys., 1985, 57,(8), pp. 3605–3608

[5] "KYMA - High Quality insertion devices for light sources", http://kyma.elettra.eu/

[6] Stephen Brooks, "Successful Test of Small-Scale Accelerator with Big Potential Impacts for Science and Medicine," https://phys.org/news/2017-08-fixed-field-multiple-particle-wide-range.html

[7] CBETA Design Report, Cornell-BNL Test Accelerator: https://arxiv.org/abs/1706.04245

3.16 Application of Tabletop Ion-Trap Systems to FFA Studies

Hiromi Okamoto, Kiyokazu Ito,
Graduate School of Advanced Sciences of Matter, Hiroshima University, Japan.
Lucy Martin, Suzanne Sheehy, University of Oxford, United Kingdom.
David Kelliher, Shinji Machida, Christopher Prior,
STFC Rutherford Appleton Laboratory, United Kingdom.

Introduction

The Fixed Field Alternating-gradient (FFA) accelerator was first invented in the 1950's and 1960's as an alternative to synchrotrons and cyclotrons. The machine achieves focusing using the alternating-gradient (strong) focusing principle, but the magnetic fields vary with radius rather than in time. The orbits are geometrically similar (i.e. photographic enlargements at higher energies) and the focal length scales with the orbit radius, resulting in a constant field index, k. This allows for DC magnets with low power consumption, fast acceleration limited only by the RF system and an energy reach which exceeds that available with cyclotrons. However, the scaling FFA also has a larger aperture vacuum chamber than a synchrotron and the magnet designs can be considerably more complex, with detailed pole shaping required to achieve the highly nonlinear fields.

In the 1990s a new type of FFA was invented, called a non-scaling FFA, where the magnetic guide fields consist only of dipole and quadrupole fields (i.e. linear fields). This concept was tested and demonstrated using the EMMA non-scaling FFA at Daresbury Laboratory, UK, commissioned between 2010 and 2012 [1]. While the machine is conceptually simpler in terms of guide field, the beam dynamics are more complex than in the scaling case.

In the non-scaling type, the horizontal and vertical bare betatron tunes (ν_{0x}, ν_{0y}) per unit focusing cell decrease during beam acceleration. The operating point of the machine then crosses resonance stop bands inevitably, which may seriously deteriorate the beam quality. This unique nature of non-scaling FFAs can be studied systematically with a novel tabletop system, such as a Paul ion trap, instead of relying on a large-scale machine.

A Linear Paul Trap (LPT) traps ions using an electric quadrupole field, rather than the magnetic quadrupole used to confine particles in a conventional accelerator. As briefly explained in the next section, a one-component nonneutral plasma in a linear Paul trap obeys the equations of motion physically equivalent to those governing a charged-particle beam in an alternating-gradient (AG) focusing channel [2, 3].

There are currently two LPTs dedicated to accelerator physics, the Simulator of Particle Orbit Dynamics (S-POD) [4,5], at Hiroshima University, Japan, and the Intense Beam Experiment (IBEX) [6], at the Rutherford Appleton Laboratory, Oxfordshire.

The LPT consists basically of four electrode rods placed symmetrically around the trap axis, which generate a radio-frequency (rf) quadrupole field for transverse ion confinement [7]. These rods are axially divided into several electrically isolated pieces, so that we can apply different bias voltages to form an axial potential well. Figure 1 is a picture of the LPT currently used for the S-POD system at Hiroshima University. The nominal operating rf frequency is 1 MHz. Both S-POD and IBEX systems have been optimized to confine $^{40}Ar^{+}$ ions, but the species of confined ions is of no essential importance in FFA studies.

In this paper, we first introduce the LPT concept, then work chronologically through beam studies relevant to FFAs, including crossing low-order space charge driven resonances and integer resonances (at low intensity) relevant to linear non-scaling FFAs. We then introduce the concept of a nonlinear Paul trap for control of higher order field components, which would be necessary to study dynamics of scaling FFAs.

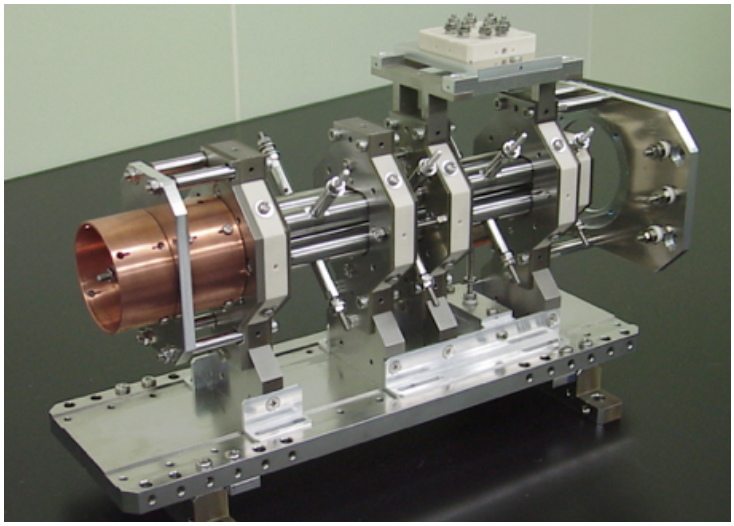

Figure 1: Typical linear Paul ion trap employed for beam dynamics experiment. A large number of ions are confined transversely within the space surrounded by four quadrupole rods. The aperture size is 1 cm in diameter. Axial ion confinement is usually achieved by DC voltages applied to separate quadrupole sections at both ends. The overall length is shorter than 30 cm.

3.16.1 Transverse Dynamics in Linear Paul Traps

All studies using Paul traps so far have kept the axial potential well static to concentrate on transverse dynamics. The equations of transverse ion motion in a regular LPT can be derived from the Hamiltonian

$$H = \frac{p_x^2 + p_y^2}{2} + \frac{1}{2}K(\tau)\left(x^2 - y^2\right) + I_p\,\phi, \tag{1}$$

where the independent variable has been scaled from time t to the length $\tau = ct$ with c being the speed of light, $K(\tau)$ is proportional to the rf voltages on the quadrupole rods, I_p is a constant parameter depending on the particle species, and ϕ is the collective Coulomb potential that satisfies the Poisson equation. Equation (1) has the same form as the well-known Hamiltonian of an AG beam transport channel. Since the particle distribution function in phase space obeys the Vlasov equation in both dynamical systems, they are physically equivalent; namely, what happens in a beam transport channel also happens in an LPT, which allows us to employ the compact LPT for beam dynamics studies [2, 3]. Of practical importance is the fact that the focusing function $K(\tau)$ is highly flexible. Unlike in a real accelerator, the waveform of $K(\tau)$ can readily be controlled over a very wide range simply by modifying the time structure of the rf voltages. It is thus straightforward to replicate various AG lattices and even move the operating point over an arbitrary range at arbitrary speed. We note that in future it may also be possible to excite an equivalent of synchrotron motion, if necessary, by introducing a periodic modulation to the bias voltages for axial ion confinement. However, this will not be considered further in this paper.

In the following, the sinusoidal focusing is employed because it has no essential difference from the most standard FODO focusing [8]. We also assume for the sake of simplicity that the bare tunes per AG cell (a single sinusoidal period) are always equal; namely, $\nu_{0x} = \nu_{0y}\big(\equiv \nu_0\big)$.

3.16.2 Resonance Crossing Experiment

Crossing of low-order space-charge-induced resonances

No single-particle resonance is expected in the range $\nu_0 < 0.5$ under the strictly linear focusing field. In any real machines, however, lattice imperfections are unavoidable, which gives rise to additional stop bands. Even in an ideal machine without imperfections, we still have a possibility of space-charge-induced resonances when the beam density is high. The latter collective effect is inherent in high-intensity FFAs. Lee *et al.* have argued that the fourth-order and sixth-order space-charge resonances at the cell tunes $\nu_0 \approx 1/4$ and $1/6$ will impose a fundamental limitation on the non-scaling FFA performance [9,10]. These stop bands can be identified in Fig. 2 obtained through systematic ion-loss measurements with S-POD at many different fixed tune values. The severe instability at $\nu_0 \approx 1/3$ is caused by the third-order error field due mainly to electrode misalignments. The other two regions of ion losses slightly above the cell tunes of $1/4$ and $1/6$ almost completely vanish in the low-density regime, which strongly suggests that the space-charge potential is responsible for these instabilities. It is worth noting that the instability at $\nu_0 \approx 1/4$ is particularly severe. It turns out to be more serious than the third-order resonance at $\nu_0 \approx 1/3$ in the high-density regime. This observation can be explained by the coherent resonance condition [11]

$$m\,(\nu_0 - C_m \Delta\bar{\nu}) = \frac{n}{2}, \tag{2}$$

where m represents the resonance order, C_m is a constant depending on the order number, $\Delta\bar{\nu}$ is the root-mean-squared tune shift induced by space charge repulsion, and n is an integer. The growth rate of the coherent parametric resonance under the above condition is proportional to the beam perveance. This type of collective instability is more enhanced as the beam density becomes higher. Conversely, it disappears at the low-density limit. According to Eq. (2), the instability at $\nu_0 \approx 1/4$ should be interpreted as the linear ($m = 2$) resonance rather than the fourth-order ($m = 4$) [12]. The former is two orders lower than the latter and, therefore, much stronger at high density, which is consistent with the experimental observation in Fig. 2. Similarly, the intensity-dependent resonance at $\nu_0 \approx 1/6$ should be understood as the third order ($m = 3$) instead of the sixth order ($m = 6$).

We employed S-POD to see what happens when the operating tune traverses these major stop bands. The number of ions surviving after single resonance crossing is plotted in Fig. 3 as a function of the crossing speed u. u is defined as the ratio of δ (the width of cell-tune variation during acceleration) to $n_{\rm rf}$ (the number of AG periods for the cell tune to go across the width δ). A vertical broken line in each panel indicates the crossing speed corresponding to the 20-turn extraction from EMMA. In the left panel, the cell tune has been changed from 0.4 down to 0.32, so that the operating point traverses the third-order stop band at $\nu_0 \approx 1/3$ in Fig. 3(a). Since the primary source of this resonance is the external error field, the ion-loss behaviour is relatively insensitive to the initial ion number. Severe ion losses have occurred even at low density. In contrast, the possible linear coherent resonance at $\nu_0 \approx 1/4$ has caused considerable ion losses in Fig. 3(b) only when the initial plasma density is high. As for the weak space-charge-driven resonance at $\nu_0 \approx 1/6$, we detected no noticeable ion losses, at least, within the same range of the crossing speed u [12].

Crossing of error-induced integer resonances

A dipole perturbation can be produced easily in the LPT to investigate the effect of integer resonance crossing in FFAs. By applying pulse voltages of opposite signs to the horizontal (or vertical) pair of quadrupole rods, we can add a new driving term to the Hamiltonian H in Eq. (1) [13]:

$$\tilde{H} = H + D(\tau)x, \tag{3}$$

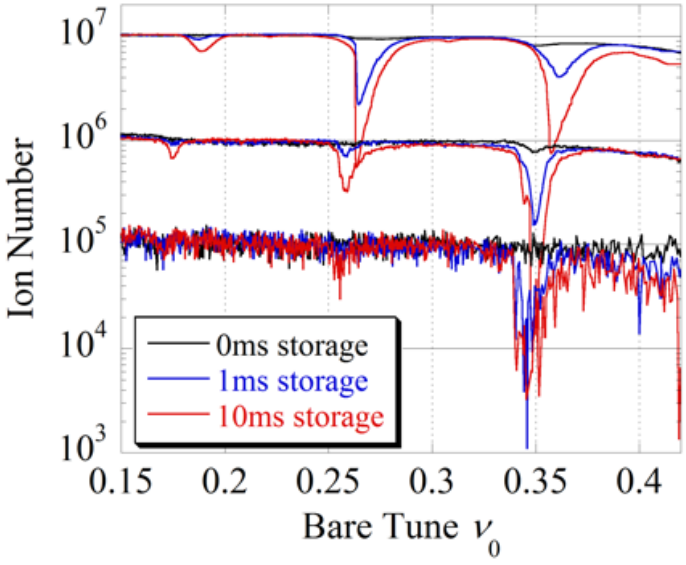

Figure 2: Major resonance stop bands observed in S-POD at different initial plasma densities. The ordinate represents the number of ions extracted from the LPT after three different storage durations; namely, 0 ms (no storage, immediate extraction from the LPT), 1 ms (10^3 AG periods), and 10 ms (10^4 AG periods).

where $D(\tau)$ is proportional to the strength of the dipole perturbing field. Figure 4 shows the stop-band distribution measured in S-POD with and without the dipole perturbation. As an example, we have assumed a circular machine with 42-fold lattice symmetry ($N_{\rm sp} = 42$), keeping the EMMA structure in mind. The sharp drop of the ion number observed at $N_{\rm sp}\nu_0 \approx 42/3$ in the absence of the dipole field (left panel) is attributed to the error-driven third-order resonance. Many additional stop bands have appeared with the dipole perturbation on (right panel). As expected, all of them are located at integer tunes.

In reference to the previous section, we note that the lowest-order ($m = 1$), thus strongest coherent resonance takes place at *half-integer* tunes as predicted by Eq. (2), which corresponds to the instability of the dipole oscillation mode [14]. The so-called "integer resonance" is none other than this type of instability enhanced by external dipole error fields.

The rate of surviving ions after crossing a single integer stop band at $\nu_0 = 8$ was measured in S-POD over a wide range of crossing speed u. The results in Fig. 5 indicate that higher u is naturally required under stronger perturbation to keep ion losses to a negligible level. The measurement data are in excellent agreement with multi-particle simulations.

3.16.3 Control of Nonlinear Driving Forces

The controllability of low-order nonlinear fields within the LPT aperture is of crucial importance because the scaling type of FFA has a high level of inherent nonlinearities. In the conventional four-rod configuration, however, nonlinear fields come from mechanical errors, which means that we cannot control their strengths and time structure independently of the main quadrupole focusing field. All kinds of fields are excited simultaneously while rf voltages are applied to the quadrupole rods. A modified LPT was, therefore, designed and constructed for future studies of nonlinear beam dynamics. As can be seen in Fig. 6, the new trap has four extra electrodes inserted in-between the quadrupole rods [15]. The use of these extra electrodes enables us to activate the sextupole and octupole fields at arbitrary timing. The performance test is now in progress at Hiroshima University.

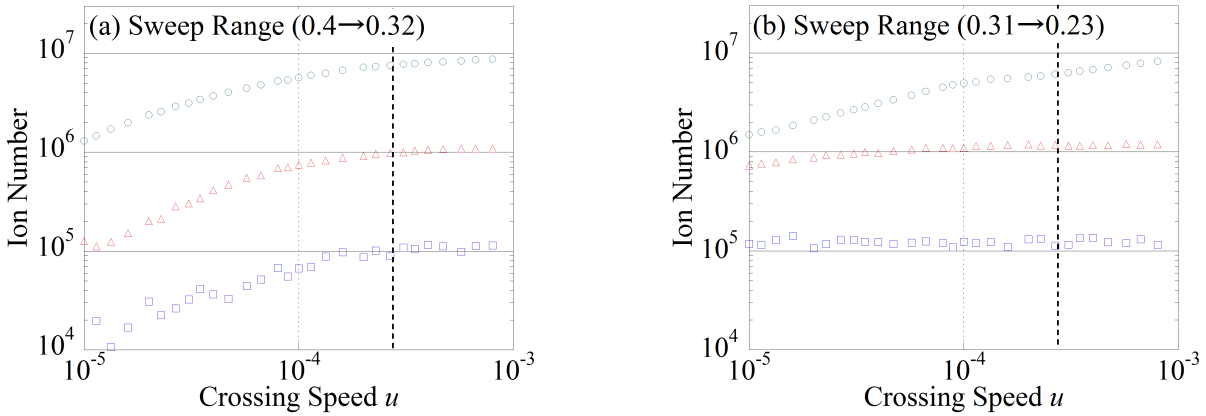

Figure 3: Number of remaining ions after crossing a resonance band at various speeds (note that a faster speed corresponds to a larger value of u). The sweep range of the cell tune ν_0 is (a) $0.4 \rightarrow 0.32$ and (b) $0.31 \rightarrow 0.23$.

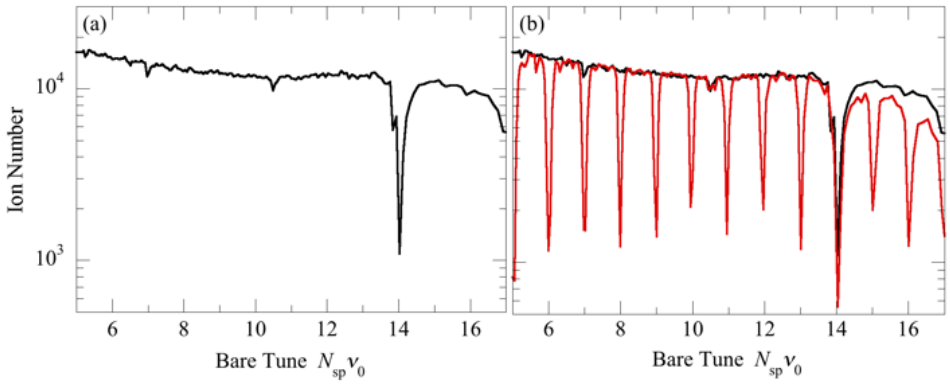

Figure 4: Measured stop-band distribution assuming a circular machine composed of 42 identical AG cells. The abscissa is not the cell tune but the one-turn tune ($N_{\rm sp}\cdot\nu_0$) around the ring. (a) With no strong imperfection. The lattice holds exact 42-fold symmetry ($N_{\rm sp} = 42$). Since the plasma density is kept low, the space-charge-driven resonance bands of the second and third orders, located at $N_{\rm sp}\nu_0 \approx 42/2m$ with $m = 2$ and 3, have not manifested themselves clearly. (b) With a dipole field excited in the LPT. A single dipole kick is applied to the confined plasma every 42 AG periods. Before extraction, ions have been stored in the LPT for 10 ms corresponding to 10^4 AG periods.

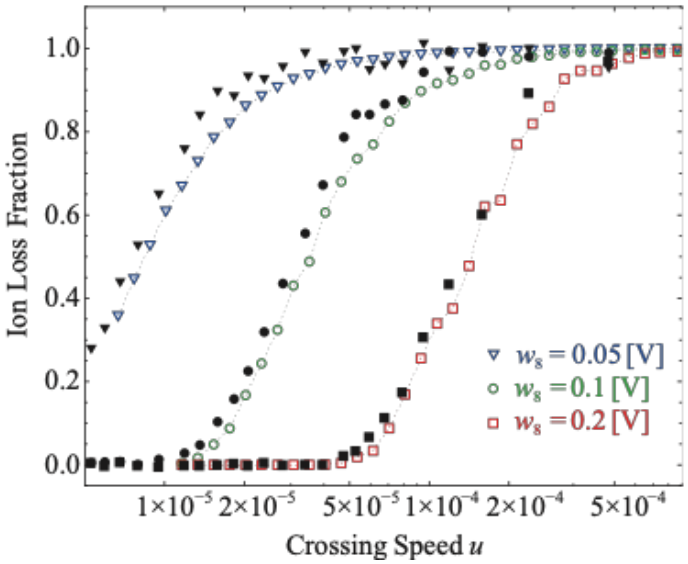

Figure 5: Fraction of measured ion losses *vs.* resonance crossing speed. A single dipole resonance is crossed at different speed. The parameter w_8 in the picture corresponds to the strength of the dipole kick to excite the integer resonance at $\nu_0 = 8$ [13]. Filled and open symbols represent the results of S-POD measurements and multi-particle simulations, respectively.

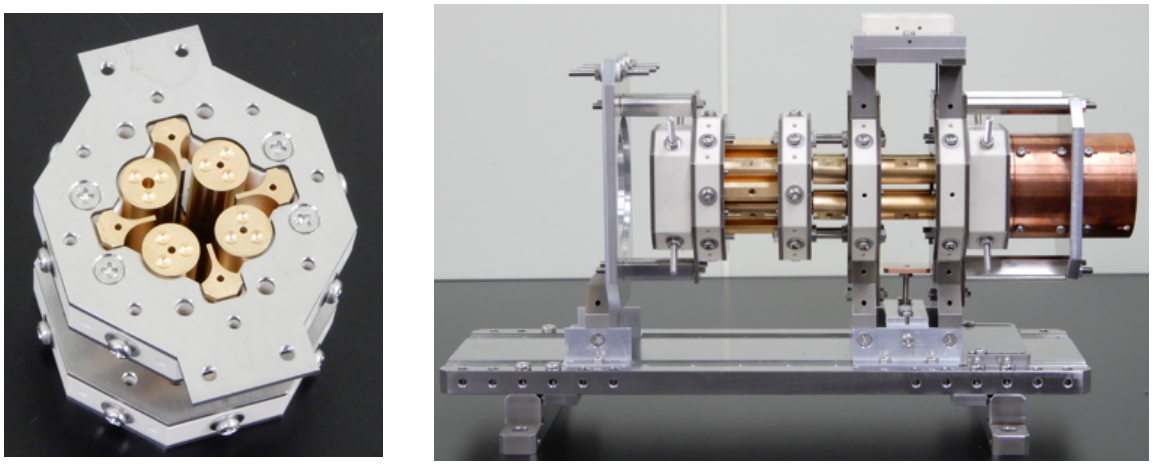

Figure 6: A new type of Paul ion trap with extra electrodes to control the sextupole and octupole rf fields in the aperture. (Left): the cross section of the ion confinement region. (Right): the overall view of the new trap recently introduced to S-POD III at Hiroshima University.

Conclusions

Linear Paul traps such as S-POD and IBEX have already been used effectively to study a wide range of high intensity physics as the transverse Hamiltonian of a LPT is equivalent to that of an alternating gradient beam transport channel. S-POD has been used to simulate integer resonance crossing in linear non-scaling FFAs, emulating the machine EMMA. However, in a linear trap higher order fields cannot be controlled. A new trap, built at Hiroshima University and currently undergoing testing, has 4 further electrodes, allowing sextuple and octupole fields to be carefully excited. This will allow experiments relevant to resonance crossing in scaling FFAs to be conducted, as such machines are inherently nonlinear.

References

[1] S. Machida, *et al.*, Nature Physics 8, 243 (2012).

[2] H. Okamoto and H. Tanaka, Nucl. Instrum. Meth. A 437, 178 (1999).

[3] H. Okamoto, Y. Wada, and R. Takai, Nucl. Instrum. Meth. A 485, 244 (2002).

[4] R. Takai *et al.*, Jpn. J. Appl. Phys. 45, 5332 (2006).

[5] H. Okamoto *et al.*, Nucl. Instrum. Meth. A 733, 119 (2014).

[6] S.L. Sheehy *et al.*, Jour. Phys.: Conf. Series 874, 012067 (2017).

[7] P.K. Ghosh, Ion Traps (Oxford Science, Oxford, 1995).

[8] K. Ito *et al.*, Phys. Rev. Accel. Beams 20, 064201 (2017).

[9] S.Y. Lee *et al.*, New J. Phys. 8, 291 (2006).

[10] S.Y. Lee, Phys. Rev. Lett. 97, 104801 (2006).

[11] H. Okamoto and K. Yokoya, Nucl. Instrum. Meth. A 482, 51 (2002).

[12] H. Takeuchi *et al.*, Phys. Rev. ST Accel. Beams 15, 074201 (2012).

[13] K. Moriya *et al.*, Phys. Rev. ST Accel. Beams 18, 034001 (2015).

[14] K. Moriya *et al.*, Phys. Rev. Accel. Beams 19, 114201 (2016).

[15] K. Fukushima and H. Okamoto, Plasma and Fusion Res. 10, 1401081 (2015).

3.17 OPAL Simulation Code

Chris Rogers, ISIS, Rutherford Appleton Laboratory, United Kingdom.
Andreas Adelmann, PSI, Villigen, Switzerland.

OPAL (Object Oriented Parallel Accelerator Library) [1] is a parallel open source tool for charged-particle optics in linear accelerators and rings, including 3D space charge. Using the MAD language with extensions, OPAL can run on a laptop as well as on the largest high performance computing systems. OPAL is built from the ground up as a parallel application exemplifying the fact that high performance computing is the third leg of science, complementing theory and experiment. The OPAL framework makes it easy to add new features in the form of new C++ classes. OPAL comes in two flavours:

- OPAL-cycl: tracks particles with 3D space charge including neighbouring turns in cyclotrons and FFAs with time as the independent variable.
- OPAL-t: models beam lines, linacs, rf-photo injectors and complete XFELs excluding the undulator.

The code is managed through the git distributed version control system. A suite of unit tests have been developed for various parts of OPAL, validating each part of the code independently. Unit tests use the google testing framework. System tests validate the overall integration of different elements. Documentation is written in asciidoc. Tools are available to readily convert asciidoc into formats such as pdf and html for display.

The OPAL code supports simulation of FFAs using analytical scaling field maps, 3D sector field maps and variable frequency RF cavities characteristic of many FFA designs. The FFA routines complement the existing cyclotron models and full three-dimensional space charge solvers including boundary conditions.

User configurable modules provide different tracking routines and field map routines. Fields are placed in a three-dimensional world and macro-particles are tracked through the field maps.

3.17.1 Field models

Several field map routines are provided that support implementation of scaling and non-scaling FFAs, both in the design and operation phase of the accelerator.

Scaling FFA Magnet Model

For a perfectly scaling sector field, fields off the midplane are calculated to arbitrary order using a recursive power series. Considering a coordinate system (r, ϕ, z), the field can be written as

$$
\begin{aligned}
B_z &= \sum_{n=0} f_{2n}(\psi) h(r) \left(\frac{z}{r}\right)^{2n} \\
B_\phi &= \sum_{n=0} f_{2n+1}(\psi) h(r) \left(\frac{z}{r}\right)^{2n+1} \\
B_r &= \sum_{n=0} \left[\frac{k-2n}{2n+1} f_{2n}(\psi) - \tan(\delta) f_{2n+1}(\psi)\right] h(r) \left(\frac{z}{r}\right)^{2n+1}
\end{aligned}
$$

with ψ representing the azimuthal angle in spiral coordinates

$$\psi = \phi - \tan(\delta) \ln(r/r_0),$$

and $h(r)$ the field dependence on radius

$$h(r) = B_0 \left(\frac{r}{r_0}\right)^k.$$

The fringe field on the midplane is modelled using

$$f_0(\psi) = \frac{1}{2}\left[\tanh\left(\frac{\psi+\psi_0}{\lambda}\right) - \tanh\left(\frac{\psi-\psi_0}{\lambda}\right)\right]$$

so that ψ_0 represents the length of the flat-top and λ represents the length of the field fall-off. Away from the midplane, the coefficients f_n are calculated by requiring that Maxwell's equations are observed, yielding a recursion relation in terms of the derivatives of f_0

$$f_n = \sum_{i=0} a_{i,n} \partial_\psi^i f_0$$

with even and odd terms related by

$$\begin{aligned} a_{i,2n+1} =& \frac{a_{i-1,2n}}{2n+1} \\ a_{i,2n+2} =& \frac{1}{2n+2}\big(a_{i,2n+1} 2(k-2n)\tan(\delta) \\ & - \frac{(k-2n)^2}{2n+1} a_{i,2n} - (1+\tan^2(\delta)) a_{i-1,2n+1}\big). \end{aligned}$$

$f_0(\psi)$ is implemented using C++ inheritance making alternate fringe field models, for example Enge function, simple to implement so long as the function and its derivatives are continuous. The coefficients of f_n are calculated during the lattice construction to minimise overhead during stepping.

Multipole Model

Multipole models are provided to enable modelling of non-scaling FFAs. Because OPAL enables arbitrary placement of potentially overlapping fields, such multipoles can be used to represent field errors in FFA main magnets.

Rectangular and sector multipoles are enabled with soft edged fringe fields. Sector multipoles can be configured with fixed radius of curvature or in the case of dipoles and combined function magnets, a radius of curvature programmed to follow a reference trajectory.

Pillbox RF Cavity

Rectangular pillbox-style RF cavities can be tracked with hard- or soft-edged fields. In the hard-edged model, time variation of the field is given by

$$E_s = V(t)\sin(\Omega(t)t + \Phi(t)).$$

where Ω, Φ and V are parameters of the RF cycle whose time dependence can be programmed by the user according to a polynomial. All other components of the field are zero.

Soft-edged cavities are described in Cartesian coordinates (x, z, s, t) by a series expansion off the midplane,

$$\begin{aligned}
E_x &= 0 \\
E_z &= V(t) \sum_n z^n g_n \sin(\Omega t + \Phi) \\
E_s &= V(t) \sum_n z^n f_n \sin(\Omega t + \Phi) \\
B_x &= V(t) \sum_n y^n h_n \cos(\Omega t + \Phi) \\
B_y &= 0 \\
B_z &= 0.
\end{aligned}$$

It is assumed that variations in Ω, Φ and V occur on a timescale much longer than the RF frequency Ω so that they do not contribute significantly to the magnetic field. Recursion relations can be derived assuming Maxwell's laws,

$$\begin{aligned}
g_{n+1} &= -\frac{1}{n+1} \partial_z f_n \\
h_{n+1} &= -\frac{\omega}{c^2(n+1)} f_n \\
f_{n+2} &= -\frac{\omega^2 f_n + c^2 \partial_z^2 f_n}{c^2(n+1)(n+2)}.
\end{aligned}$$

Odd terms of f_n and even terms of g_n and h_n are 0.

3D Field Map

OPAL can read in a 3D magnetic field map placed on a regular grid in cylindrical polar coordinates. The field at an arbitrary point is inferred by tri-linear interpolation.

Field Map Output

Output of the field map is an essential part of the validation of a given lattice. OPAL provides methods to write out the electromagnetic field map as a four-dimensional grid in Cartesian or cylindrical polar coordinates and time. Field maps can be written over an arbitrary region in space-time.

3.17.2 Examples

To demonstrate the simulation in OPAL, a radial sector magnet with DF geometry is considered. In this lattice, protons are simulated between 3 and 30 MeV. The lattice has 8 cells and a 3 m inner diameter with a field index 3. The doublet structure in each cell can be seen by examination of the field maps. The orbit excursion is approximately 1 m. The similarity of the orbits and the radial dependence on energy can be observed in fig. 1. The orbits at different azimuthal angles are identical bar an increase in radius and a concomitant increase in beam energy, as expected from the scaling condition.

In a scaling FFA both the closed orbit and the linear order transverse optics must scale with momentum. The constancy of tune with energy is shown in fig. 2. At each energy a particle has been tracked on the closed orbit and another particle has been tracked with the same energy but initially deviating from the closed orbit by 2 mm and 1 mm in horizontal and vertical space respectively. The phase advance of each particle is calculated on a cell-by-cell basis and this is converted to the fractional part of the cell tune. The tune is seen to be constant as expected.

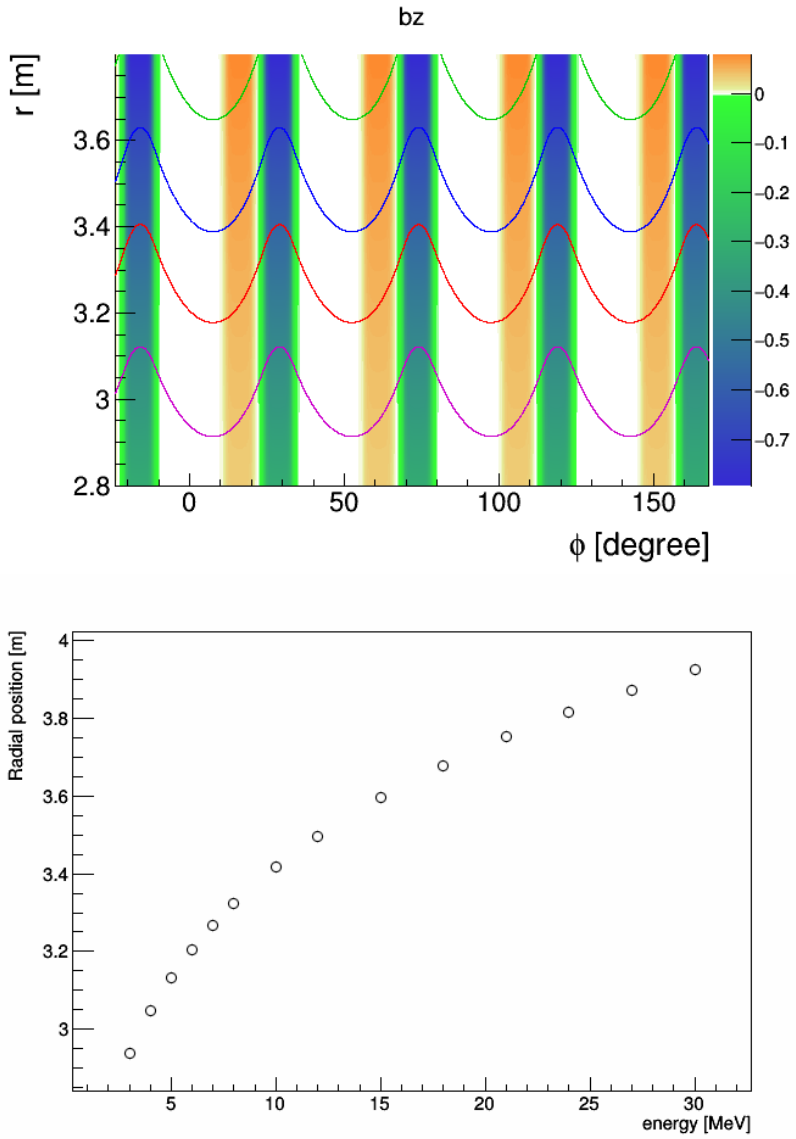

Figure 1: Simulated closed orbits for a number of orbits at different energies (top) and dependence of the closed orbit radius on kinetic energy (bottom). The closed orbit demonstrates radial scaling with momentum.

Injection Simulation

More complicated arrangements can also be simulated to support injection, extraction and acceleration studies. Consider the lattice shown in fig. 3. In this example, spiral FFA magnets have been modelled with a field index of 7.1, and a spiral angle of 41°. Injection dipoles have been added in order to simulate a closed orbit bump onto a foil that might be used for injection. The dipole fields were chosen to return the circulating proton beam to the closed orbit following the beam bump. Several different injection dipole fields were simulated, and all of the closed orbits have been superimposed onto the same figure to demonstrate simulation of painting at injection. Very wide dipoles have been simulated in order to support optimisation of the lattice; where the bump dipoles overlap the FFA main magnets OPAL superposes the two fields. Following optimisation, the radial extent of the dipoles can be curtailed as desired by the user.

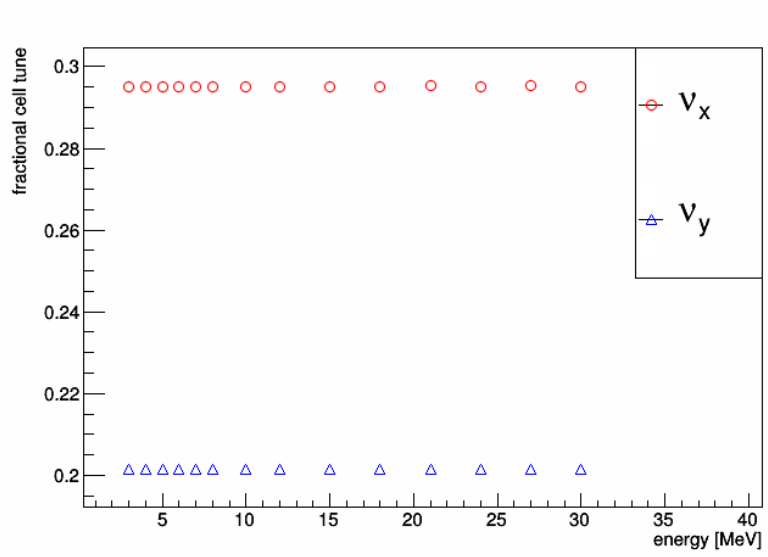

Figure 2: Simulated cell tune for a number of different kinetic energies. The tune is constant with energy indicating the field scales correctly.

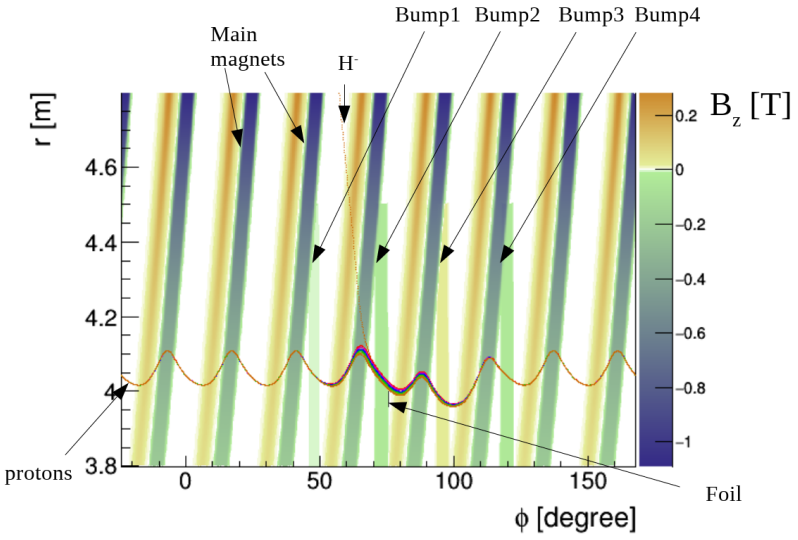

Figure 3: Simulation including bump magnets for injection.

Acceleration Simulation

An example of an acceleration cycle for the spiral FFA lattice described above is shown in fig. 4. Here a few particles have been simulated accelerating over a 0.5 ms acceleration cycle from 3 MeV to 30 MeV. Particle were simulated initially at the reference phase, but with kinetic energy deviations of up 0.5 MeV from the reference particle. The frequency was varied during the acceleration cycle to keep the synchronous phase constant despite the change in time-of-flight around the ring with energy. In this example the RF voltage was held constant during the acceleration cycle. The simulated particles were successfully accelerated except for the particle with initially 2.5 MeV energy, which was lost from the RF system.

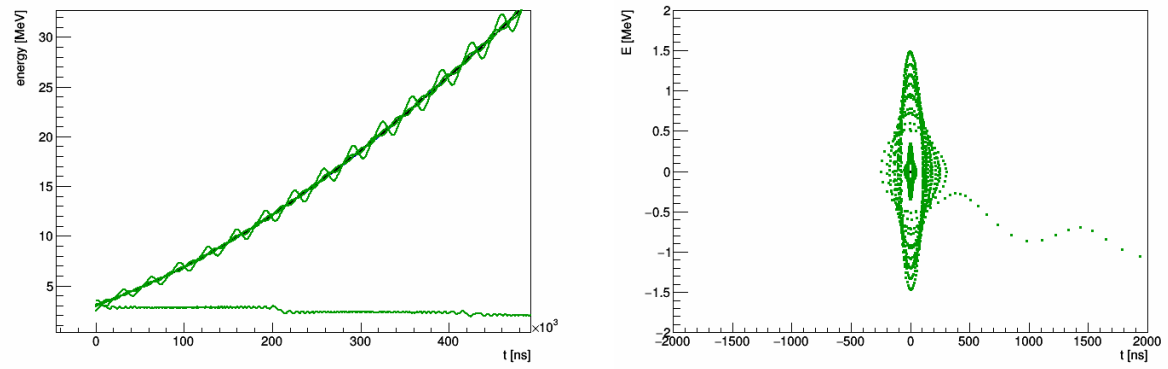

Figure 4: Simulation of the acceleration cycle (left) particle time and energy over the full cycle and (right) particle time and energy relative to the reference particle over the full cycle.

Conclusions

OPAL can be used to simulate FFAs in a number of different circumstances. A number of field models are available in OPAL to support both analytical and numerical calculation of FFAs, together with injection, acceleration and extraction systems. The extensions to OPAL for FFA simulation complement the existing cyclotron models and full three-dimensional space charge solvers.

References

[1] https://gitlab.psi.ch/OPAL/src/wikis/

3.18 The Ray-tracing Code Zgoubi - Latest Developments

François Méot, Brookhaven National Laboratory C-AD, Upton, NY, USA.

Introduction

The reader is referred to the ICFA-BD-NL No.43 [1], and to a more recent status article in NIM A [2], regarding the technical details of the Zgoubi tracking engine and its accuracy, which make it "near-symplectic" - sufficiently so to model millions of turns in large hadron colliders, - and its potential for pushing particles in complex accelerator structures and accelerator optical elements or their field maps.

Extended documentation can be found in the regular FFA workshops [3] as well as in the SourceForge code development site where in particular many examples of beam lines, FFAs and other ring simulations are maintained [4]. There is also a comprehensive user's guide [5]. Further documentation, including an attempt to demonstrate 6D simulation in all possible types of particle accelerators, can be found in the "Computer Laboratory" Stony Brook University "PHY689" semester series [6].

A recent activity and source of documentation is the project led by D. Abell and the Radiasoft Company, "New Algorithms in Zgoubi" [7], including web interfacing [8], as part of a US DOE computing tools development program in relating to the electron-ion collider R&D [9].

Finally, the download tool on Zgoubi SourceForge site seems to indicate a steady increase in popularity, with over 3500 downloads from the site, covering about 60 countries, since the code was installed on the web in 2007 [10]. This may be a good indication of its efficiency in solving, at least some classes of, charged particle optics and accelerator design problems.

The latest developments in Zgoubi have found their motivation, as usual, in the requirements for new applications. This will be the focus of the present very brief state-of-the-art review, which starts in § 3.18.1 with a simulation of the 4-pass 150 MeV CBETA ERL at Cornell, of which the return loop is based on a single FFA channel that accepts four different energies [11]. This simulation of CBETA has benefited from earlier developments in the code when simulating a 7 GeV energy-recovery experiment at the CEBAF recirculating linac [12]; thus a few words will be said on that, § 3.18.2. As mentioned above, an important topic these days is the EIC R&D. This provides an opportunity to benchmark simulation of spin diffusion in a 21 GeV FFA ERL [13] and to develop an ergodic approach to the polarization lifetime in an electron storage ring [14]. This is addressed in § 3.18.3. Finally, a space charge model has been installed in the code for the purpose of studying the effect of inter-particles forces on beam optics in a scaling FFA. The interested reader is referred to related publications [15]. These diverse accelerator design activities have fostered the development of a series of new functions in Zgoubi ("`keywords`") and these are described in § 3.18.4.

Note, finally, that the Zgoubi development program now includes contributions from several others, including the aforementioned [7], whose work can be found for instance by using the OSTI [16] or the JACoW accelerator conference [17] search tools. Developments include interfacing, such as the earlier web-based SIREPO, and other python based tools [18, 19]. However this article will essentially focus on developments by the code's author and originator.

3.18.1 CBETA

The design of the Halbach technology FFA cell [20] for the Cornell-BNL CBETA ERL used, and was validated using Zgoubi [21]. In the framework of CBETA commissioning, which commences in 2019, Zgoubi is one of the commissioning tools, simulating the ERL components using their field maps [22] for accurate ray-tracing regarding an accelerator system which amounts to a time-of-flight spectrometer [23] and as such requires accuracy on path length computation.

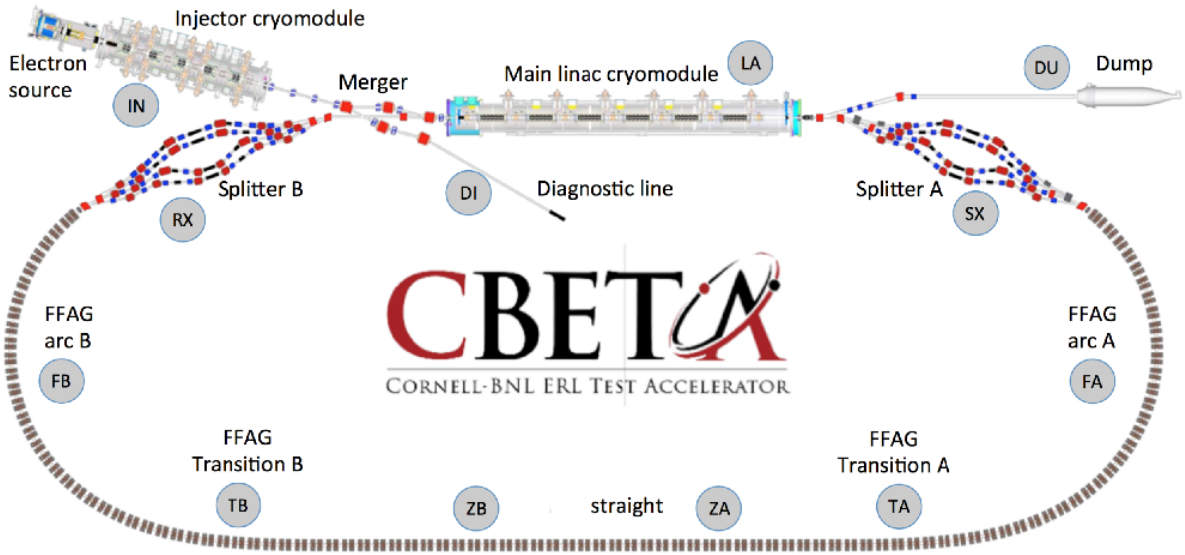

Figure 1: CBETA 150 MeV ERL. The linac (LA) is 36 MeV, and four different energies circulate concurrently in the single-channel return loopc(FA-TA-ZA-ZB-TB-FB): 42, 78, 114 and 150 MeV. Four spreader (SX) and recombiner lines (RX), at the linac downstream and upstream ends, respectively, ensure proper orbits and optical functions into and out of the return loop.

CBETA is a four-pass, 150 MeV, 40 mA energy recovery linac, Fig. 1. It uses a single channel loop to recirculate four energies, 42, 78, 114 and 150 MeV, four-passes up, four-passes down. The loop comprises 107 quadrupole-doublet cells, built using Halbach permanent magnet technology, Fig. 2. The arcs (FA-TA and TB-FB sections) use fixed-field alternating gradient (FFA) optics; the straight section (ZA-ZB) is a FoDO channel with all 4 energies on the common quadrupole axis. Spreader (SX) and combiner (RX) sections (4 independent beam lines, S1 to S4 and R1 to R4, respectively) connect the 36 MeV linac to the FFA arcs; they use conventional electromagnets.

Figure 3 gives an insight in the subtleties of the predictions of ray-tracing, depending on the method used to model the magnetic fields: three different models of the same magnet give three different sets of transport coefficients (only one of the models has proper field simulation, using field maps) which, cumulated over meters of beam line, result in noticeable differences in zero-th and first order optics. On top of this would be high order transport for halo simulations for instance, where accuracy on fields far off-axis is needed. Using field maps allows accurate computation of transverse motion across the Halbach cells, Fig. 4.

Figure 4 is a glimpse at the 4-pass up/4-pass down start-to-end orbit and optics simulations undertaken using Zgoubi, as part of the commissioning of CBETA.

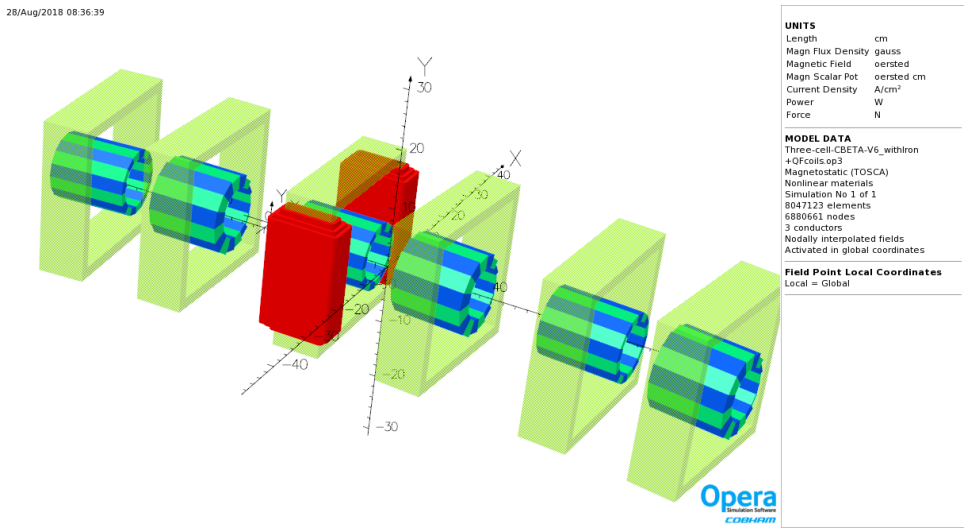

Figure 2: OPERA simulation of three CBETA Halbach magnet FoDO cells. The cell includes horizontal and vertical orbit corrector dipoles (iron yoke electromagnets) on top of, respectively, the focusing and defocusing Halbach magnet (the sole QF corrector is highlighted in red here).

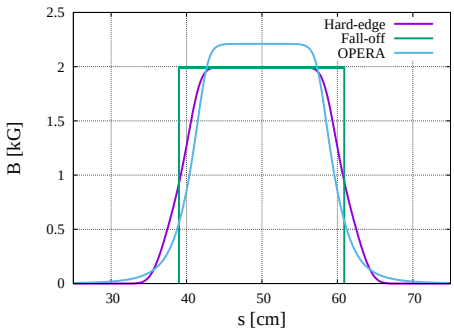

Figure 3: Field along the reference orbit across one typical dipole of the SX or RX beam lines. Three different field models are stepwise ray-traced: (i) hard edge; (ii) pure dipole field with field fall-offs; (iii) OPERA field map of the dipole. The field integral ($\int B(s)\,\mathrm{d}s = 0.044\,\mathrm{T\,m}$ in this particular dipole) is the same in all three models.

$[R_{\mathrm{i=1-4,5;j=1-4,6}}]$ transport matrix from (i) hard-edge model for reference; (ii) pure dipole field with fringe fields; (iii) OPERA model:

```
(i) Hard-edge.  Arc length: 22.0606 cm
 1          0.216997     0            0          -3.436E-02
 0           1           0            0          -0.316659
 0           0           0.950276     0.220605    0
 0           0          -0.439585     0.950276    0
-0.31666    -0.034357    0            0           3.6085E-03

(ii) Fringe field.  Arc length: 22.0511 cm
 0.98493     0.216780    0            0          -3.433E-02
-0.13788     0.984953    0            0          -0.314304
 0           0           0.97108      0.220804   -0
 0           0          -0.258899     0.970985    0
-0.31430    -0.034326    0            0           3.7942E-03

(iii) OPERA map.  Arc length: 21.9227 cm
 0.983444    0.215709    0            0          -3.4153E-02
-0.151999    0.983583    0            0          -0.314091
 0           0           0.969607     0.218802    0
 0           0          -0.273559     0.969615    0
-0.314079   -0.0341572   0            0           3.60475E-
03
```

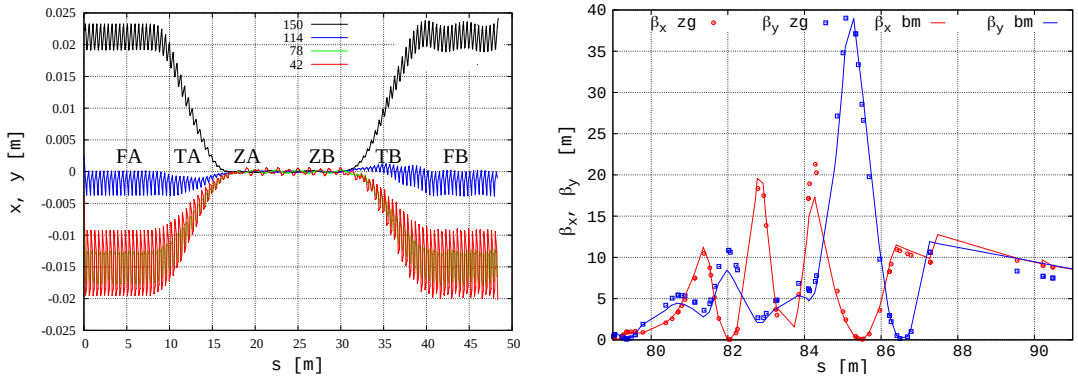

Figure 4: Left: 42, 78, 114 and 150 MeV orbits along the return loop, freely propagating through the field map string, without any correction, from their initial theoretical value at the start of the FA arc. Right: 42 MeV betatron functions along R1 after propagating freely from S1 to R1, with merely their initial values imposed at the exit of the linac; differences appear compared to when theoretical initial values (those at FB end) are imposed at start of R1: minor re-tuning however is sufficient to take care of that and get properly matched values at the linac entrance. Markers: records from field map simulations. Thin lines: from Cornell's BMAD [24] model for comparison.

3.18.2 ER@CEBAF

In 2015, as part of the electron-ion collider accelerator R&D at BNL [13], a proposal was made to test high-energy, 5-pass (10 linac passes) energy recovery (ER) at CEBAF [12], Fig. 5. This new experiment extends the 2003, 1-pass, 1 GeV CEBAF-ER demonstration [25], and will study ER and recirculating beam dynamics in the presence of synchrotron radiation, provide an opportunity to develop and test multiple-beam diagnostic instrumentation, and can also probe BBU limitations.

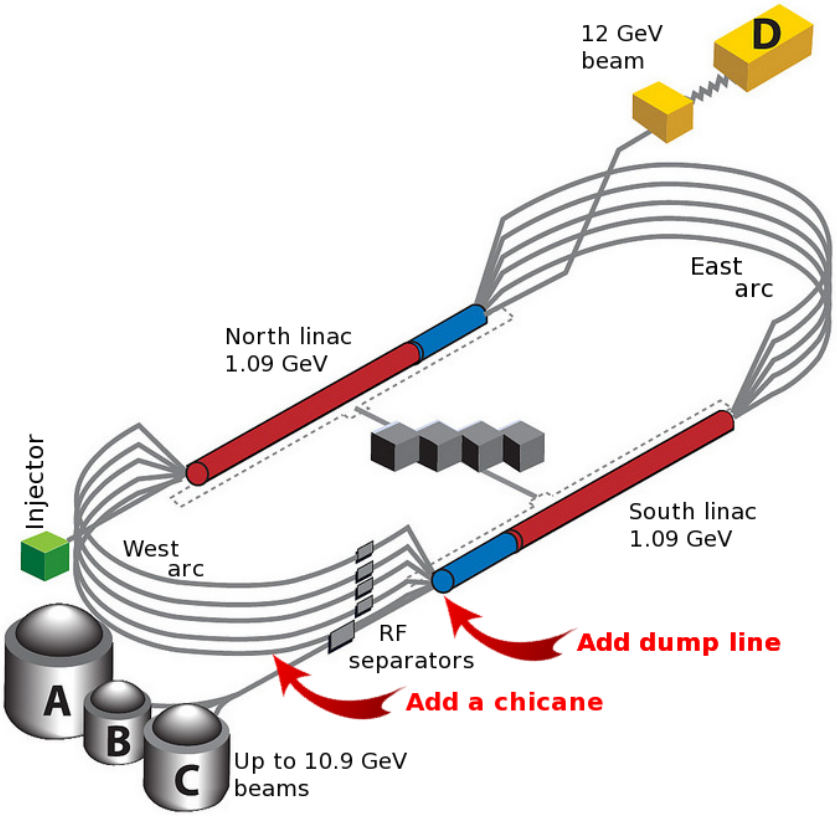

Figure 5: 12 GeV CEBAF recirculator and systems to be added for a 5-pass up/5-pass down 7 GeV ER experiment (in addition to multiple-beam diagnostics).

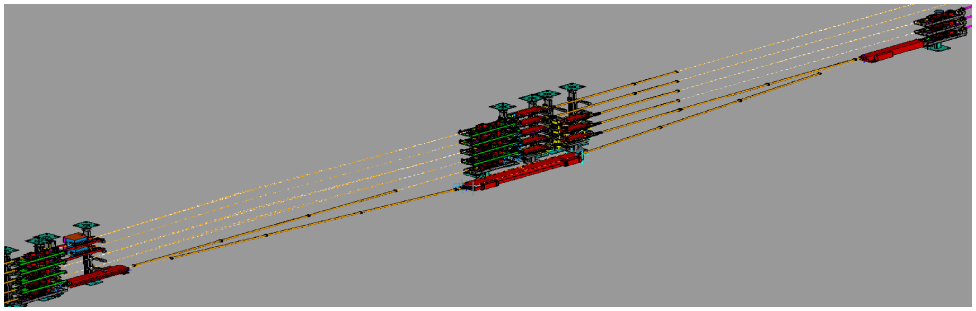

Figure 6: The 3-bend phase chicane to be installed along Arc A. It will use main bends recuperated from Cornell's CESR brightness upgrade.

Dipole magnets recuperated from the CESR upgrade at Cornell in 2018 have been moved to JLab. They will be used for the phase-shift chicane, Fig. 6.

As part of the preparations for the ER@CEBAF experiment, simulations including the ef-

fect of synchrotron radiation at high energy (which limits the maximum energy feasible in ER configuration to about 7 GeV) have been undertaken using Zgoubi [26]. A sample of the findings is given in Fig. 7, a 1-pass simulation (2 linac passes, from 78.5 MeV to 1.4 GeV), which would be the starting step. Complete ER@CEBAF modeling, 5-pass up/5-pass down, is on-going.

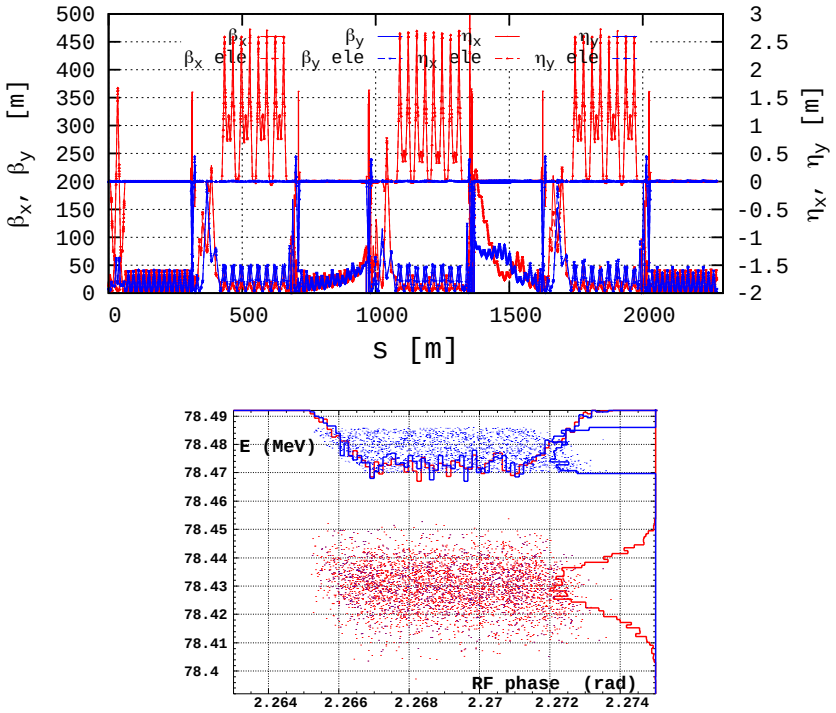

Figure 7: Top: Optical functions in the 1.4 GeV 1-pass up, 1-pass down ER configuration, from both Elegant [27] and Zgoubi, superimposed. Bottom: longitudinal phase-space portraits of the ER'ed bunch, observed at exit of south linac, in the presence of SR (78.43 MeV region), and without SR (78.48 MeV region).

3.18.3 Spin diffusion

Zgoubi has been able to treat spin polarization since the late 1980s [29]. Synchrotron radiation (SR) was included inthe early 1990s [30], and radiation in beam lines and damping in rings was thoroughly benchmarked in the late 1990s-2010 [31,32]. However it is only in the context of the EIC R&D that the opportunity presented itself to assess the combined effect of spin diffusion.

The first combined use of spin and SR came in the eRHIC 21 GeV FFA ERL design [13], where dedicated benchmarking showed that the numerical computation is in very good accord with theory. This is illustrated in Fig. 8 [33, Fig. 24].

A second combined use of spin and SR concerns a more recent study of spin diffusion in the 18 GeV electron storage ring of the eRHIC electron-ion collider. This prompted development of an ergodic approach to the computation of polarization lifetime [28], which can be summarized as follows.

The evolution of spin polarization with time, from an initial P_0 to an equilibrium P_{eq} (an asymptotic quantity with time constant τ_{eq} to be determined from the simulations), satisfies

$$P(t) = P_{eq}(1 - e^{-t/\tau_{eq}}) + P_0\, e^{-t/\tau_{eq}} \quad (1)$$

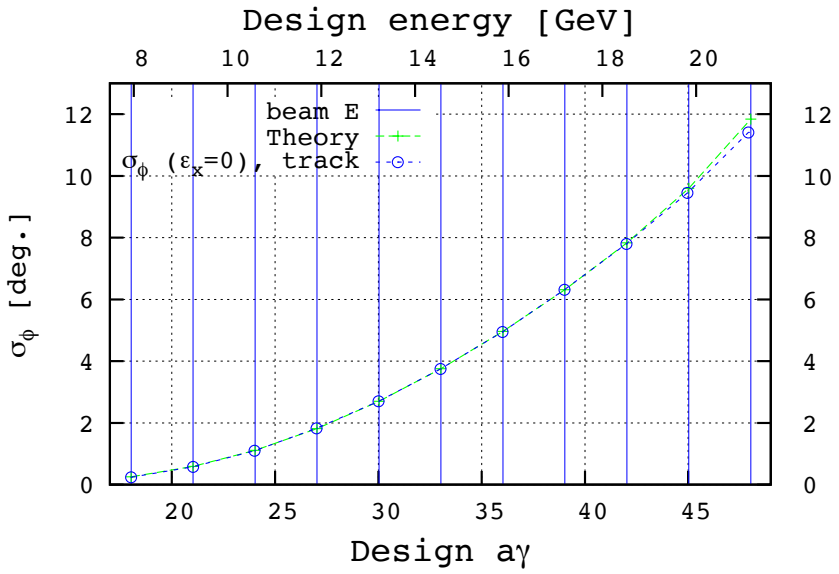

Figure 8: Polarization loss by spin diffusion in eRHIC FFA ERL under the effect of SR induced energy spread [13], including theoretical expectation [33, § 5]. σ_ϕ is the spin angle spreading with distance in the ERL, from theory ("theor.") and from tracking ("track"). Horizontal axis: $a\gamma$ is the number of spin precessions per turn, with $a = 0.00116$, the electron anomalous magnetic moment, and γ the Lorentz relativistic factor.

This results from (i) synchrotron-radiation self-polarization (index SP) with time constant $\tau_{\mathrm{SP[sec.]}} \approx 99\rho^2_{\mathrm{[m]}}\mathrm{R}_{\mathrm{[m]}}/\mathrm{E}^5_{\mathrm{[GeV]}}$ (equating to about 30 min at eRHIC at 18 GeV), asymptotic value P_{SP} (92.4% in a defect-free flat ring), and (ii) polarization loss by diffusion (index D), with time constant τ_{D}, such that

$$1/\tau_{\mathrm{eq}} = 1/\tau_{\mathrm{SP}} + 1/\tau_{\mathrm{D}} \tag{2}$$

One has in particular

$$\mathrm{P}_{\mathrm{eq}} = \mathrm{P}_{\mathrm{SP}} \times \tau_{\mathrm{eq}}/\tau_{\mathrm{SP}} \tag{3}$$

The goal in tracking spin motion is (i) to derive polarization lifetime in order to (ii) validate a ring design, including preservation of polarization under the effect of defects, corrections, spin rotators, etc., and (iii) to determine an optimal ring operating point $a\gamma_{\mathrm{ref}}$ that maximizes P_{eq}. It follows that this entails maximizing the diffusion time constant τ_{D}.

Usually the polarization lifetime is obtained by tracking a bunch of a few hundred particles over a few thousand turns at store, for each energy bin (one energy bin represents one ring set for a particular beam rigidity - or equivalently, $a\gamma_{\mathrm{ref}}$). The ergodic method instead tracks a single electron per energy bin, so resulting in a substantial saving in memory and CPU time. A typical outcome is displayed in Fig. 9 [28, Fig. 9]. Note the clear region of minimal spin diffusion in the graph, indicating where the storage ring rigidity setting should be chosen.

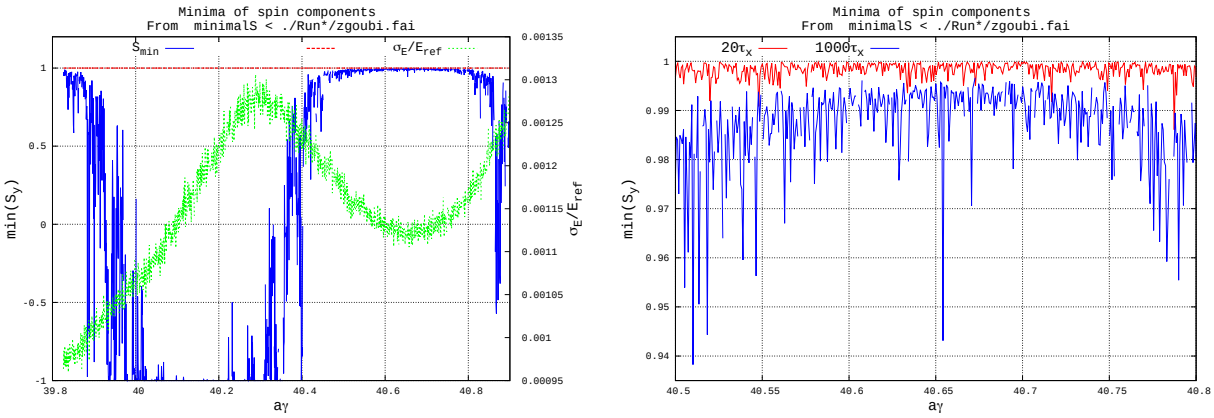

Figure 9: An ergodic approach to polarization lifetime in the 18 GeV eRHIC electron storage ring. Left, blue curve: depolarization landscape $S_{y,\min}(a\gamma_{\rm ref})|_{t\in[0,T]}$ (the smallest value reached by the vertical spin component over the tracking interval $[0, T]$) over $39.8 < a\gamma_{\rm ref} < 40.9$ (200 bins of $\Delta E = 0.44$ MeV, a single particle per bin), after T ≈several thousand turns tracking. The right vertical scale (green curve) is the *rms* width of the energy interval explored by a particle during the tracking. Right: a zoom in on a reduced $40.5 < a\gamma_{\rm ref} < 40.8$ interval, showing $S_{y,\min}(a\gamma_{\rm ref})|_{t\in[0,T]}$ at (red) 9500 turns and (blue) 450,000 turns (6 s storage).

3.18.4 New keywords

The diverse accelerator design activities using Zgoubi fostered the development of a series of new functions ("`keywords`"): for instance `GOTO`, a tool for beam switching, `INCLUDE` (a similar effect to the Fortran or LaTeX"include" statement) to concatenate s eparate optical sequence segments, `SVDOC` to doctor perturbed orbits, `SPACECHARGE` for simulation of the eponymous effect. All keywords are documented in Zgoubi User's Guide [5].

Three are introduced here, as an illustration in relation with the previous sections.

`INCLUDE` and `GOTO`

`INCLUDE` behaves in a similar way to the Fortran or LaTeXinclude: it uploads (into the data sequence from which it is called, say a parent file "A") a part of an external file (say file "B"). This may be convenient for repetitive structures. However the main goal is, rather, to allow the code access to B, or a part of it, properly set, for instance with optimal fields or element positioning as resulting from a prior fitting procedure.

The interest is that B can be worked on independently for optimal setting: when A is then Zgoubi'ed, it will always grab B as optimized.

`GOTO` can be used to signify a switch in an optical structure. It can for instance be a switch from an injection line into the main ring where multiturn can then occur, followed by a second switch into an extraction beam line, all that in a single Zgoubi run. An example of such a structure: injection+multiturn+extraction, was developed for a start-to-end simulation of the EMMA FFA [34] (however `GOTO` was not available at that time). Another obvious use is in recirculating linacs, where `GOTO` is used to switch the beam between linac, splitters and return arc(s).

The example of CBETA is given below, featuring 4 passes up and 4 passes down, all in a single input data file, using both `INCLUDE` and `GOTO`.

In this example, the linac, return FFA loop, spreader and combiner sequences are given in separate files, uploaded by the parent file using `INCLUDE`s. Doing so has a series of merits :

- it shortens the parent input data file, so making the optical structure more apparent,

- it allows the linac, optical spreader, combiner and return loop sequences to be picked from files that may actually be Zgoubi'ed independently, for instance, to compute their optical parameters proper.

Labels (such as "S1_#S", "S1_#E" below) are used for this targeted picking : they define the ends of the sequence to be `INCLUDE`'d, ignoring the remaining upstream and downstream parts in the file subjected to that `INCLUDE` (these ends may be specific, for instance, to `MATRIX` [5] computations).

`GOTO` for its part allows throwing the beam to (and getting it back from) the linac, spreader lines, combiner lines, and recirculating loop.

```
!! OBJECT DEFINITION
'MCOBJET'                 ! MONTE CARLO GENERAOTR
0.14008655052543029e3     ! 42 MeV REFERENCE RIGIDITY
3
10000                     ! 10,000 PARTICLES IN THIS RUN.
2 2 2 2 1 1                          ! 6-
D GAUSSIAN DISTRIBUTION
1.69E-04  -2.36E-2 0. 0. 0. 2.7144593 ! CENTER OF DISTRIBUTION
-1.01 0.58  1e-3   3       ! BEAM ALPHA_x, bETA_x
 1.80 1.09  1e-3   3       ! BEAM ALPHA_y, bETA_y
 0. 1. 0. 1                ! BEAM ALPHA_l, bETA_l
  123456 234567 456789
 'PARTICUL'
ELECTRON

!! ALLOW RANDOMFIELD ERRORS
 'ERRORS'
0 1 123466                   dB(kG)
MULTIPOL{}  1  BP A U 0.d0   0.0  9999

!! RACETRACK SEQUENCE STARTS HERE, AT LINAC ENTRANCE
! Linac
'INCLUDE'
1
./LA/LA_obj5.inc[LA.MAR.BEG\1:LA.MAR.END\1]

!! GOTO SPREADER LINE, DEPENDING ON PASS NUMBER
 'GOTO'
PASS#
S1 S2 S3 S4 S3 S2 S1 DUMP
 'MARKER' RT_SX

!! GOTO FFAG RETURN LOOP.
 'GOTO'
PASS#
FFA FFA FFA FFA FFA FFA FFA FFA
 'MARKER' RT_FFA

!! GOTO COMBINER LINE, DEPENDING ON PASS NUMBER
 'GOTO'
PASS#
R1 R2 R3 R4 R3 R2 R1
 'MARKER' RT_RX

 'MARKER'
 'REBELOTE'  ! DO NEXT PASS: SEND ZGOUBI POINTER BACK TO
7  0.1  99   ! THE TOP (i.e., LINAC ENTRANCE), 7 TIMES.

! DUMP LINE FOLLOWS
'MARKER'  DUMP
....

 'STOP'
!////////////////////////////
!// job done, job ends here //
!////////////////////////////
```

```
! 4 SPREADER LINES, S1-S4
'MARKER'  S1
'INCLUDE'
1
./SX/S1.inc[S1_#S:S1_#E]
 'GOTO'
GOBACK
..... ETC
'MARKER'  S4
'INCLUDE'
1
./SX/S4.inc[S4_#S:S4_#E]
 'GOTO'
GOBACK

'MARKER'  FFA - FFAG RETURN LOOP, TAKES THE 4 ENERGIES
'INCLUDE'
1
./FFA/FFA.inc[FFA#S:FFA#E]
 'GOTO'
GOBACK

! 4 COMBINER LINES, R1-R4
'MARKER'  R1
'INCLUDE'
1
./RX/R1.inc[R1_#S:R1_#E]
 'GOTO'
GOBACK

........ ETC.

'END'
```

• What the S1.inc spreader line `INCLUDE` file may look like:

```
'OBJET'   PARTICLE DEFINITION FOR BEAM MATRIX COMPUTATION
1000.
5.01
.001 .01  .001 .01  .001 .0001
0.  0.  0.  0.  0. 1.
-0.975 13.64 -
0.975 13.64 0. 1. 0. 0. 0. 0. ! OPTICAL FUNCTIONS AT LINAC

'MARKER' S1_#S       ! INCLUDE GRABS FROM HERE
'INCLUDE'
1
S1_sEQUENCE[LA.MATCH1:S1.MAR.END]
'MARKER' S1_#E       ! INCLUDE GRAB ENDS HER

'FIT'
 ... A set of variables and constraints
 ... which match S1 to FFA loop entrance beta functions.
'MATRIX'  ! DELIVERS TRANSPORT AND BEAM MATRICES, FOR CHECKS.
1 0
'END'
```

SVDOC

Orbit defects and correction, for the vertical orbit in particular, are paramount in the study of polarization transport and lifetime. Accounting for that requires a random generator (Zgoubi's "`ERRORS`" available for that generates all sorts of random field and positioning errors [5]) and a correction algorithm. This is the role of the new "`SVDOC`".

Figure 10 shows an application in the case of the 3.8 km long RHIC polarized proton collider [35]. `SVDOC` offers also the possibility of generating, in a single run, an arbitrary number of corrected random orbits, in as many Zgoubi input files ready to run, this is for the purpose of possible statistics.

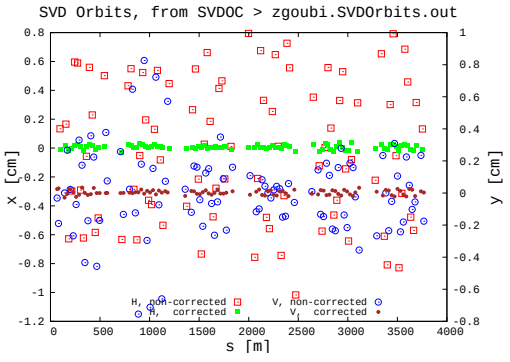

Figure 10: Orbit correction in the RHIC lattice, using `SVDOC`. Empty markers represent the initial random H (squares) and V (circles) orbits, measured at RHIC pickups; the solid markers represent the corrected H and V orbits.

• What `SVDOC` looks like in a Zgoubi input data sequence [5]. Note that it is preceded by a "`FIT`" of which the task, as part of the algorithm, is to find the closed orbit coordinates.

```
'ERRORS'                ! GENERATE RANDOM ERRORS. "MULTOPOL"s ARE CONCERNED.
0  2 123456             ! RANDOM SEED.
MULTIPOL{QF} 1 BP A U 0. 2e-2 3  ! FIELD IN ALL "QF" (PARAMETER "12" IN SVDOC).
MULTIPOL{QD} 1 BP A U 0. 2e-2 3  ! FIELD IN ALL "QD" (PARAMETER "22" IN SVDOC).

 'FAISCEAU'
 'FIT'            ! CLOSED ORBIT FINDING.
 4                ! VARIABLES: VARY INITIAL H AND V COORDINATES
Vary Y0; Vary T0; Vary Z0; Vary P0
 4                ! CONSTARINTS: INITIAL AND FINAL COORDINATES IDENTICAL
Yfinal = Y0; Tfinal = T0; Zfinal = Z0; Pfinal = P0

'SVDOC'           ! ALGORITHM THAT COMPUTES THE SVD MATRIX AND APPLIES IT
1  0              ! ON 50 (SEE BELOW) RANDOM DEFECT ORBITS.
PUH{HMON} PUV{VMON}  ! NAMES OF H-, V-, HV-PICKUP FAMILIES, AND
CRH{HKIC} CRV{VKIC}  ! NAMES OF H- & V-
CORR FAMILIES, TO GENERATE SVD MATRIX.
1.e-3      1.e-3     ! KICK VALUES FOR COMPUTATION OF SVD MATRIX.
1  2  50   ! "1" TRIGER "ERRORS" KEYWORD; 2 CHANGES PRIOR TO THAT; 50 ORBITS.
ERRORS  12 ! "12": VALUE OF HKIC IN "ERRORS" (it will deteemine the H orbit),
ERRORS  22 ! "22": VALUE OF VKICK IN "ERRORS" (will determine the V orbit).

'SYSTEM'          ! SYSTEM CALL WHICH DELIVERS THE FIGURE ON THE LEFT,
1                 ! PRIOR TO TERMINATING ZGOUBI EXECUTION.
gnuplot <./gnuplot_SVDOrbits.cmd &
'END'
```

References

[1] F. Méot, *6-D beam dynamics simulations in FFAs using Zgoubi*, ICFA Beam Dynamic Newsletter, No. 43, Eds. C.R. Prior, W. Chou (2007), pp. 15-156.

[2] F. Méot, The ray-tracing code Zgoubi - Status, Nuclear Inst. and Methods in Physics Research, A 767 (2013).

[3] A link to the FFA workshop series : `https://www.bnl.gov/ffag17/pastWorkshops.php`

[4] Zgoubi examples on SourceForge `https://sourceforge.net/p/zgoubi/code/HEAD/tree/trunk/exemples/`.

[5] Zgoubi user's guide, `https://sourceforge.net/p/zgoubi/code/HEAD/tree/trunk/guide/Zgoubi.pdf`.

[6] `http://case.physics.stonybrook.edu/index.php/PHY689_spring_2019`

[7] D. Abell, F. Méot, New Algorithms in Zgoubi, Proc IPAC18 Conf., Vancouver (2018); `http://accelconf.web.cern.ch/AccelConf/ipac2018/papers/thpak079.pdf`

[8] SIREPO, `https://beta.sirepo.com/#/accel`.

[9] The Electron-Ion Collider User Group Home Page, `http://www.eicug.org/`

[10] Zgoubi download status on SourceForge, `https://sourceforge.net/projects/zgoubi/files/stats/map?dates=2007-09-17%20to%202019-03-23`.

[11] CBETA Cornell-BNL ERL Test Accelerator, `https://www.classe.cornell.edu/Research/ERL/CBETA.html`.

[12] F. Méot et al., A high-energy, multiple-pass energy recovery experiment at CEBAF, Proc. IPAC16 Conf., Busan, Korea (2016); `http://accelconf.web.cern.ch/AccelConf/ipac2016/talks/tuoba02_talk.pdf`.

[13] F. Méot, Simulation of eRHIC 12-pass 21 GeV FFA ERL, this ICFA-BD-NL publication.

[14] F. Méot et al., Polarization lifetime in an electron storage ring, an ergodic approach in eRHIC EIC, MOPAF03.PDF, Proc. ICAP'18 13th International Computational Accelerator Physics Conference, Key West (Oct. 2018);

[15] M. Haj Tahar, F. Méot, Space charge effects in FFA, 57th ICFA Advanced Beam Dynamics Workshop on High-Intensity and High-Brightness Hadron Beams (HB2016); https://www.bnl.gov/isd/documents/93368.pdf.

[16] OSTI publication repository, https://www.osti.gov/search/semantic:zgoubi

[17] JACoW accelerator conference site, https://www.JACoW.org/Main/Proceedings

[18] pyZgoubi, https://sourceforge.net/projects/pyzgoubi/.

[19] zgoubidoo, https://github.com/chernals/zgoubidoo.

[20] N. Tsoupas et al., The Beam Optics of the FFA Cell of the CBETA ERL Accelerator, MOPIK122, Proceedings of IPAC2017, Copenhagen, Denmark; http://accelconf.web.cern.ch/AccelConf/ipac2017/papers/mopik122.pdf.

[21] F. Méot et al., Beam dynamics validation of the Halbach technology FFA cell for Cornell-BNL energy recovery linac, Nuclear Inst. and Methods in Physics Research, A 896 (2018) 60–67.

[22] F. Méot et al., Simulation of the CBETA 4-pass FFA ERL using field-maps - exclusively, Proc. ICAP'18 13th International Computational Accelerator Physics Conference, Key West (Oct. 2018); under publication in the Int. J. Mod. Phys. A (2019).

[23] Citing D. Douglas, JLab, regarding CEBAF or CBETA style of RLAs.

[24] Cornell's BMAD is the CBETA on-line model engine; https://www.classe.cornell.edu/bmad/.

[25] A. Bogacz, A. Hutton et al., CEBAF-ER Experiment Proposal, Jefferson Lab, Newport News (June 2002).

[26] F. Méot and Y. Roblin, ER@CEBAF: Modeling code developments, eRHIC/52, BNL-112107-2016-IR (2016); https://www.bnl.gov/isd/documents/93028.pdf.

[27] Elegant; https://ops.aps.anl.gov/manuals/elegant_latest/elegant.html.

[28] F. Méot, An ergodic approach to polarization in eRHIC electron storage ring, eRHIC/52, BNL-209351-2018-TECH (2018); https://www.osti.gov/servlets/purl/1480979.

[29] F. Méot, A numerical method for combined spin tracking and ray tracing of charged particles, Nuclear Inst. and Methods in Physics Research, A 313 (1991) 492-500.

[30] F. Méot, Synchrotron radiation interferences at the LEP mini-wiggler, CERN-SL/94-22 (1994).

[31] F. Méot and J. Payet, *Numerical tools for the simulation of synchrotron radiation loss and induced dynamical effects in high energy transport lines*, Report DSM/DAPNIA/SEA-00-01, CEA Saclay (2000).

[32] F. Méot, *Simulation of radiation damping in rings, using stepwise ray-tracing methods*, 2015 JINST 10 T06006.

[33] F. Méot, et al., Tracking studies in eRHIC energy-recovery recirculator, eRHIC/45, BNL-108286-2015-IR; `https://www.bnl.gov/isd/documents/89185.pdf`.

[34] F. Méot et al., End-to-end 6-D tracking using EMMA on-line model, MOPPT018, Proceedings of Cyclotrons2013, Vancouver, BC, Canada;
`http://accelconf.web.cern.ch/AccelConf/CYCLOTRONS2013/papers/moppt018.pdf`.

[35] `https://www.bnl.gov/rhic/`.

4. FROM OUR REGULAR CORRESPONDENTS

4.1 Accelerator-related Activities in Australia

Suzie Sheehy, University of Melbourne, Australia

It is a pleasure to write as a new correspondent for the ICFA Beam Dynamics Newsletter, representing the Australia/New Zealand accelerator physics community. With lots of activity happening here – including IPAC'19 in Melbourne in May 2019 - I look forward to bringing news as our accelerator community grows.

There is an incredibly strong history in the field of accelerators in Australia and NZ, from Marc Oliphant (Australia) who invented the concept of the synchrotron, Ernest Rutherford (New Zealand) who famously created the desire for us to build accelerators in the first place to the Braggs famed for X-ray crystallography. The largest accelerator in Australia at present is a synchrotron light source, the Australian Synchrotron, operating since 2007. This major facility has 10 user beamlines including a dedicated medical research beamline, X-ray absorption spectroscopy through to the far infrared beamline and benefits around 5000 users annually.

In recent years, Australia has been moving ever closer to building their first large scale hadron accelerator, not of hadron collider proportions of course, but for proton therapy. The federal government have now committed funds for this and through a series of national symposia and working groups the clinical, medical physics and technical communities are working hard to bring this to fruition. What of the beam dynamics community? From March 2019, I'm pleased to say a new group has started in Accelerator Physics focusing on medical applications at the University of Melbourne. Plans are afoot for a Masters level accelerator physics course, helping to strengthen the accelerator physics community in the region.

We are very much looking forward to hosting our colleagues from around the globe for the upcoming 10^{th} International Particle Accelerator Conference, IPAC'19, to be held in Melbourne, Australia in May 2019. I hope to catch up with as many of you as possible and that you'll enjoy Melbourne's vibrant food, coffee and culture as much as I do.

4.2 The International Day of Light

Sameen Ahmed Khan, Dept. Mathematics & Sciences, Salalah, Sultanate of Oman.

Logo of the International Day of Light (Courtesy IDL Steering Committee)

On 14 November 2017, the UNESCO (United Nations Educational, Scientific and Cultural Organization) proclaimed 16 May as the International Day of Light (IDL), during the 39th Session of the UNESCO General Conference. The inaugural day was celebrated in 2018. The IDL was endorsed by the Executive Board of the UNESCO in October 2016. The press release at that milestone stated 'The purpose of an International Day of Light is to provide an annual focal point for the continued appreciation of the central role that light plays in the lives of the citizens in the world in areas of science, culture and art, education, sustainable development, and in fields as diverse as medicine, communications and energy' [1–3].

The International Day of Light is a direct and enduring legacy of the International Year of Light and Light-based Technologies (IYL2015). We recall the relevant details regarding IYL2015. The IYL2015 was proclaimed by the United Nations General Assembly 68^{th} Session on 20 October 2013. The resolution for the IYL2015 was presented to the United Nations General Assembly by UNESCO in 2013 [4–7]. IYL2015 recorded 93 National Nodes [4]. IYL2015 led to 13,168 events in 147 countries with about 23,000 mentions in the media of 120 countries. The estimated audience is believed to be over a hundred million. To mark the year, thirty countries issued commemorative postage stamps and currency coins [1, 8, 9]. Undoubtedly, IYL2015 has been one of the most successful International Years of the UNESCO. Moreover, it is one of the few science related years, which were also endorsed by the United Nations.

The first laser was demonstrated on 16 May 1960 by engineer and physicist Theodore Harold Maiman using a synthetic-ruby crystal [10]. At that time Maiman (1927-2007) was at the Hughes Research Laboratories, a Division of Hughes Aircraft Company, Malibu, California, USA. Maiman's demonstration made use of a solid-state flash-lamp-pumped synthetic-ruby crystal and produced a red laser light at 6943Å(694.3 nanometres). The three-level pumping design scheme limited Maiman's laser to pulsed operation. Historically, this demonstration turned out to be ahead of several other teams including that of Charles Hard Townes (who received the 1964 Nobel Prize in Physics with Nicolay Gennadiyevich Basov and Aleksandr Mikhailovich Prokhorov), Arthur Leonard Schawlow (who received the 1981 Nobel Prize in Physics with Nicolaas Bloembergen and Kai Siegbahn) and Gordon Gould [11]. It is to be noted that Maiman's single author report in Ref. [10] acknowledges the joint article by Schawlow and Townes [12]. Laser science has evolved over the decades and has found applications in numerous disciplines including healthcare and telecommunications. Many discoveries in recent decades have made use of lasers and over twenty of the Nobel Laureates are related to lasers and arising from its diverse applications [1]. We shall consider an example from physics and chemistry each. In 1965, Charles Kuen Kao achieved the transmission of light in fibers for optical communication [13]. Ahmed Hassan Zewail (1999 Chemistry Nobel Laureate) pioneered the use of lasers to probe chemical reactions [14].

The International Day of Light was introduced to UNESCO by sponsors Ghana, Mexico, New Zealand and the Russian Federation, and supported at the UNESCO Executive Board and the General Conference by 27 countries: Argentina, Colombia, Czech Republic, Democratic

Republic of Congo, Dominican Republic, Ecuador, Egypt, Finland, Iran, Ivory Coast, Kenya, Lebanon, Madagascar, Malaysia, Morocco, Nicaragua, Serbia, South Africa, Sudan, Sweden, Nigeria, Paraguay, Qatar, Togo, Vietnam, Uganda and Zimbabwe. The International Day of Light is administered from UNESCO's International Basic Science Programme by a Steering Committee that also includes representatives from: the American Institute of Physics (AIP), the American Physical Society (APS), Bosca beverages, the European Centres for Outreach in Photonics (ECOP), the European Physical Society (EPS), the International Association of Lighting Designers (IALD), the Abdus Salam International Centre for Theoretical Physics (ICTP), the IEEE Photonics Society (IPS), the International Commission on Illumination (CIE), lightsources.org - the international network of accelerator based light sources, Light: Science and Applications, the Optical Society (OSA), Philips Lighting, the International Society for Optics and Photonics (SPIE), the Synchrotron-Light for Experimental Science and Applications in the Middle East (SESAME) and Thorlabs (optical instruments company, New Jersey, USA) [3].

As the light sciences play an important role in the various facets of human endeavours, the logo of the International Day of Light has incorporated the logo of the Sustainable Development Goals (SDGs). It is to be recalled that the SDG's emerged from the 2015 United Nations Summit for its 2030 Agenda for Sustainable Development. The SDG's are a successor of the Millennium Development Goals. There are 17 Global Goals, which are measured by progress against 169 specific targets [15, 16]. The goals are: 1. No Poverty, 2. Zero Hunger, 3. Good Health and Well-Being, 4. Quality Education, 5. Gender Equality, 6. Clean Water and Sanitation, 7. Affordable and Clean Energy, 8. Decent Work and Economic Growth, 9. Industry, Innovation and Infrastructure, 10. Reduced Inequalities, 11. Sustainable Cities and Communities, 12. Responsible Consumption and Production, 13. Climate change, 14. Life Below Water, 15. Life on Land, 16. Peace, Justice and Strong Institutions, and 17. Partnerships for the Goals.

The inaugural International Day of Light was marked in a grand ceremony at the UNESCO Headquarters in Paris, France on 16 May 2018. The Illuminating Education Conference is the Flagship Celebration of the International Day of Light 2019, scheduled to be held at the Abdus Salam International Centre for Theoretical Physics, Trieste, Italy on 16 May 2019. The expected worldwide annual events will provide a platform to highlight the role of light sciences in fields as diverse as medicine, communication. John Michael Dudley (working at the CNRS-University of Franche-Comté joint research institute in Besançon, France) had served as the Chairman of the IYL2015 International Steering Committee [4, 8, 9]. Now, he is serving as the IDL Steering Committee Chair [3]. There are 67 National Nodes (including India) recorded at the IDL website and this figure is sure to increase [3].

The IDL is aimed at stimulating worldwide interest, especially among young people in light and related sciences & technologies. It will highlight to the citizens of the world the importance of light and optical technologies in their lives, for their futures, and for the development of society. A variety of events and activities will be organized world-wide. In view of the strong relationship between the world of accelerators and light sciences, IDL will be an excellent platform to conduct accelerator related outreach programmes. Cornerstone projects such as a Synchrotron Day or Synchrotron Week (or an Accelerator Day or Accelerator Week) can be organized, when synchrotron radiation facilities (and other accelerator facilities) around the world will open their doors to public visitors. This will enable to highlight the role of accelerators in human endeavours, ranging from basic particle physics research to diverse applications in medicine and industry [17].

References

[1] Editorial, Light is in the air. Nature Photonics, 2017, 11 (8), 453; doi: 10.1038/nphoton.2017.138.

[2] Proposal for the Proclamation of an International Day of Light, UNESCO Executive Board 200th Session, 200 EX/27, (19 September 2016); http://unesdoc.unesco.org/images/0024/002460/246046e.pdf.

[3] International Day of Light (IDL), https://www.lightday.org/.

[4] International Year of Light and Light-based Technologies (IYL2015), http://www.light2015.org/.

[5] Khan, S. A., 2015 declared the International Year of Light and Light-based Technologies. Current Science, 2014, 106 (4), 501.

[6] Khan, S. A., International Year of Light and Light-based Technologies, LAP LAMBERT Academic Publishing, Germany (2015). http://isbn.nu/9783659764820/.

[7] Khan, S. A., Reflecting on the International Year of Light and Light-based Technologies. Current Science, 2016, 111 (04), 627-631; doi: 10.18520/cs/v111/i4/627-631.

[8] González, J. R. and Dudley, J., Inspired by light: close of the International Year of Light, Europhysics. News, 2016, 47(2), 6-7. https://www.europhysicsnews.org/.

[9] Dudley, J., González J. R., Niemela, J. and Plenkovich, K., The International Year of Light and Light-based Technologies 2015, A Successful Community Partnership for Global Outreach Final Report. 2016, Document code: SC/2016/IYL; Catalog Number: 246088; http://unesdoc.unesco.org/images/0024/002460/246088e.pdf and http://www.light2015.org/Home/About/IYL-Final-Report.html.

[10] Maiman, T. H., Stimulated Optical Radiation in Ruby. Nature, 1960, 187, 493-494; doi: 10.1038/187493a0.

[11] Hecht, J., Beam: The Race to Make the Laser, Oxford University Press, (2005). http://isbn.nu/9780199738717/.

[12] Schawlow, A. L. and Townes, C. H., Infrared and Optical Masers. Physical Review, 1958, 112 (6), 1940-1949; doi:10.1103/PhysRev.112.1940.

[13] Bose, D. N., Technology breakthroughs win 2009 Physics Nobel. Current Science, 2010, 98 (3), 299-301.

[14] Khan, S. A., Ahmed Hassan Zewail (1946-2016). Current Science, 2016, 111 (5), 936-937.

[15] Kamepalli, L. B. and Pattanayak, S. K., From Millennium to Sustainable Development Goals and need for institutional restructuring. Current Science, 2015, 108 (6), 1043-1044.

[16] Swaminathan, M. S. and Kesavan P. C., Guest Editorial: Achieving the sustainable development goals. Current Science, 2016, 110 (2), 127-128.

[17] Sameen Ahmed Khan, Particle Accelerators and the International Year of Light, ICFA Beam Dynamics Newsletter, 2014, 63, 9-15.

4.3 SESAME: the First Solar-Powered Accelerator Complex

Sameen Ahmed Khan, Dept. Mathematics & Sciences, Salalah, Sultanate of Oman.

On Tuesday the 26 February 2019, a ceremony was held to mark the official inauguration of the solar power plant of SESAME: Synchrotron-light for Experimental Science and Applications in the Middle East [1]. This makes SESAME the very first large accelerator complex to be fully powered by solar energy. The SESAME synchrotron located in Jordan also has the distinction for being the first synchrotron in the region of the Middle East. In this note we recall the significance of the solar energy in the accelerator context along with the origins and of the SESAME synchrotron facility [2, 3].

Like all other accelerator facilities, SESAME also consumes a huge amount of electricity. In Jordan, the electricity costs are rather high and the annual electricity bill of SESAME was about two million US$. The recent inauguration of SESAME's 6.48-megawatt photovoltaic plant will now save this huge annual expenditure. The current capacity of the solar power plant will suffice the projected needs for the next several years. The power plant using monocrystalline solar panels was built locally at a site 30 km away from the SESAME facility. The power is transmitted through an on-grid photovoltaic system. The required funding for the solar power plant became available in late 2016 when the Government of Jordan through the Ministry of Energy, generously agreed to allocate about seven million US$, from funds provided by the European Union to support the deployment of clean energy sources in Jordan [1]. The example set by SESAME is a source of encouragement for other accelerator facilities around the world.

Let us briefly recall the origins of the SESAME. In the 1990s, the BESSY-I synchrotron was to be replaced by a more facility BESSY-2 in Berlin. Instead of dismantling, Herman Winick of the Stanford Linear Accelerator Center (SLAC) in California and Gustav-Adolf Voss, a former director of the Deutsches Elektronen-Synchrotron (DESY) in Hamburg, Germany suggested to donate the BESSY-I to the region of Middle East. After an international bid, Jordan became the host to the relocated synchrotron under the auspices of UNESCO. The 800 MeV BESSY-I was upgraded to a 2.5 GeV SESAME. On 6 January 2003, His Majesty King Abdullah II of Jordan laid the cornerstone for the then upcoming International Center. The ceremony was attended by, the UNESCO Director General Koichiro Matsuura. On 16 May 2017, the SESAME light source was officially opened by His Majesty King Abdullah II of Jordan. The ceremony included ambassadors, ministers, former and current directors of CERN along with Irina Bokova, the then director-general of UNESCO [1].

Since the opening of SESAME in July 2018, twenty-three user groups have utilized its facilities. A call for beam time in September 2018, resulted in a record number of 103 applications to utilize the XAFS/XRF (X-ray Absorption Fine Structure/X-Ray Fluorescence) spectroscopy and IR (Infrared) spectromicroscopy beam lines. The Facility is now working on construction of four more beamlines. These are the MS (Materials Science), MX (Macromolecular Crystallography), and BEATS (BEAmline for Tomography at SESAME) beamlines, as well as a soft X-ray beamline. The current Members of SESAME are Cyprus, Egypt, Iran, Israel, Jordan, Pakistan, Palestine, and Turkey. The Current Observers are Brazil, Canada, China (People's Republic of), the European Organization for Nuclear Research (CERN), the European Union (EU), France, Germany, Greece, Italy, Japan, Kuwait, Portugal, Russian Federation, Spain, Sweden, Switzerland, the United Kingdom, and the United States of America [1].

An international synchrotron facility is also needed in the populous continent of Africa [4, 5]. There was a special session on SESAME during the World Science Forum (Dead Sea, Jordan, 7-11 November 2017). The idea of the African Synchrotron was also mentioned during this and other sessions. Since, it takes decades to plan and start such facilities, an early start is essential [6].

References

[1] SESAME: Synchrotron-light for Experimental Science and Applications in the Middle East. http://www.sesame.org.jo/.

[2] Sameen Ahmed Khan, Jordan to host Middle East Synchrotron, ICFA Beam Dynamics Newsletter, 22, 6-7 (August 2000).

[3] Sameen Ahmed Khan, The Middle East Synchrotron Laboratory and India, Current Science, 80 (2), 130-132 (25 January 2001). (Fortnightly Publication of the Indian Academy of Sciences).

[4] Sameen Ahmed Khan, Ground Breaking for the Middle East Synchrotron; Armenian Synchrotron; Time to Launch the African Synchrotron Research Programme, ICFA Beam Dynamics Newsletter, 30, 88-89, (April 2003).

[5] Sameen Ahmed Khan, Need to Create Regional Synchrotron Radiation Facilities (RSRF), IRPS Bulletin, 17 (2), 7-13 (July 2003). (IRPS: International Radiation Physics Society). http://www.canberra.edu.au/irps/bulletin/1996-2005/docs/17-2.pdf.

[6] Sekazi K. Mtingwa and Herman Winick, SESAME and beyond, Science, 356 (6340), 785 (2017). doi:10.1126/science.aan6880.

5. RECENT DOCTORAL THESES

5.1 Coupling Impedance and Single Beam Collective Effects for the Future Circular Collider (Lepton Option)

CANDIDATE: Eleonora Belli, La Sapienza, Rome
SUPERVISOR: Mauro Migliorati (La Sapienza), Giovanni Rumolo (CERN)
GRADUATION: October 2018

The PhD activity of Eleonora Belli concerned the study of collective effects for the electron-positron accelerator FCC-ee. In particular for the machine at the lowest energy, a very high current of 1390 mA is foreseen. Because of such high beam current, collective effects are of particular relevance. The electromagnetic interaction of the beam with the vacuum chamber and electron cloud effects, generated by the interaction of the beam with the photoelectrons produced by photoemission due to synchrotron radiation, have been studied in detail, together with predictions of their effects on beam dynamics and potential solutions for their mitigation.

During her PhD, in 2017, Eleonora Belli won the FCC Innovation Award for her contribution to the FCC collaboration.

5.2 Simulations of RF Beam Manipulations Including Intensity Effects for CERN PSB and SPS Upgrades

CANDIDATE: Danilo Quartullo, La Sapienza, Rome
SUPERVISOR: Mauro Migliorati (La Sapienza), Giovanni Rumolo (CERN)
GRADUATION: October 2018

The PhD activity of Danilo Quartullo concerned the study of the longitudinal beam manipulations of high intensity bunches in the framework of the LHC Injector Upgrade program. In particular his work can be divided into two main parts. The first part is related to analysis of the CERN PS Booster operation after the LIU upgrades. The second is devoted to studies of momentum slip stacking of HL-LHC ion beam in the SPS. He analysed beam stability for future cycles and intensities, finding some important machine limitations.

During the last year of his PhD Danilo Quartullo won the Premio Minerva of La Sapienza (2nd edition) for his important contribution to the advancement in his subject area (sciences and technology). The prize was awarded in March 2019.

5.3 Investigation of a Compact Accelerator for Radioisotope Production

CANDIDATE: David Bruton, University of Huddersfield, U.K.
SUPERVISOR: Prof. R. Barlow
GRADUATION: February 2019

This thesis covers the design and performance of a non-linear non-scaling Fixed Field Alternating Gradient (FFA) accelerator. The imagined application of the design is for radioisotope

production and in particular the production of ^{99m}Tc and ^{211}At. The performance of the design in combination with an internal target and recycled beam is also investigated as a potential way to increase isotope yields.

The basic design consists of four separate radial sector magnets and two RF cavities. The design differs from a conventional cyclotron in that the edge angles have been optimised with the field gradient to produce a lattice that is isochronous to ±0.15% and has stabilised tunes.

Simulations conducted using the OPAL code showed that the dynamic apertures are large, peaking at 150 and 41.4 π m.mrad in the horizontal and vertical planes respectively. Acceleration with protons is possible at up to the 5$^{\text{th}}$ harmonic with an accelerating gradient of 100 kV/turn and at the 1$^{\text{st}}$ harmonic for alpha particles.

Space charge simulations suggest strong performance under high current conditions. A proton beam of 20 mA was simulated with 2.3% losses, dropping to 0% losses at 4 mA. Alpha particle beams were simulated with beam currents of up to 800μA with minimal losses. The best harmonic to operate at for handling high currents was found to be either the 2$^{\text{nd}}$ or 3$^{\text{rd}}$.

Simulations of the internal target demonstrated that ionisation cooling has an effect even with high Z materials. Two aspects were identified as key to increasing beam survival; the vertical aperture and cooling the beam longitudinally. It was found that increasing the vertical aperture by ±1 cm could double the beam survival time. Additionally by using a combination of a wedge shaped target and RF stabilisation to cool the beam longitudinally, a 140% increase in beam survival time was achieved.

Finally several iterations of the design were created investigating possible improvements including tune adjustment by introducing a magnet shift, a dual proton alpha particle design and a compact 35 MeV design.

5.4 Development of high-resolution cavity beam position monitors for use in low-latency feedback systems

CANDIDATE: Talitha Bromwich, University of Huddersfield, U.K.
SUPERVISOR: Prof. P. Burrows
GRADUATION: June 2018

The thesis work was carried out with the Feedback On Nanosecond Timescales (FONT) group at the John Adams Institute for Accelerator Science at the University of Oxford. The FONT intra-train feedback system is designed to provide beam position stabilisation in single-pass accelerators. The studies focused on a feedback system utilising beam position information from three high-resolution cavity beam position monitors (BPMs) at the interaction point (IP) of the Accelerator Test Facility 2 (ATF2) at KEK, Japan, with the goal of stabilising the low-emittance electron beam to the nanometre level. The operation, optimisation and resolution performance of this IP system formed the subject of the thesis.

The work achieved an improvement in the cavity BPM resolution estimate from 50 nm to 20 nm using waveform integration in analysis of the BPM signals. A multi-parameter fit was used to address inaccuracies in calibration methods and unwanted charge-dependencies to achieve more consistent resolution performance and produce a best-ever resolution estimate for the BPMs of 17.5±0.4 nm. A novel mode of IP beam position stabilisation using two BPMs as input to the feedback was also successfully demonstrated. The beam position was stabilised to 57±4 nm, as measured at an independent BPM. The analysis suggested correction capability could be enhanced by feedback firmware waveform integration to achieve a measurable beam stabilisation of the order of 40 nm in the future. This work will be continued by the FONT group and collaborators at the ATF2.

Any future accelerators, including linear colliders like the ILC and CLIC, and X-ray free

electron lasers, will require BPMs for diagnostic purposes and orbit feedback to enable very precise beam handling. High-resolution beam position measurements and low-latency feedback systems capable of nanometre-level position stabilisation will be vital to realise this precise beam handling. The PhD work is expected to contribute towards the advancement of these future endeavours.

5.5 Numerical simulation of electromagnetic fields in complex multi-cavity superconducting radio frequency resonators

CANDIDATE: Johann Heller, Rostock University, Germany
SUPERVISOR: Prof. Dr. Ursula van Rienen
GRADUATION: December 2018

This thesis deals with the computation of electromagnetic fields in complex, superconducting resonators. For the operation and design of such resonators, an efficient and accurate computation of these fields is necessary, which is hardly possible on conventional hardware in many cases. Due to this limitation, there are generally two different approaches in practice: on the one hand, the parallelization of the problem on costly hardware with high power consumption and, on the other hand, the simplification of the structure. In this thesis a method is investigated and automated to close this gap, which can solve the considered problems without extensively simplifying the structure on workstation computers. The used method, State-Space Concatenation (SSC) employs a combination of model order reduction and domain decomposition to significantly reduce the computational effort needed. For an efficient use of SSC, in this thesis an automation, ready to handle almost arbitrary high-frequency resonators is implemented and tested. Another problem is the efficient calculation of the losses of such resonances by the couplers and beampipes. Hence, this work is using a perturbation approach based on SSC. The resulting nonlinear eigenvalue problem is solved by using the Newton method, which allows for the comparatively fast computation of such losses. The exploited method is tested for physical consistency and partly compared to measurement results. In summary, all the methods discussed and implemented in this work are tested for three state of the art problems from accelerator physics. In the process current research questions for the Third Harmonic Module of the FLASH accelerator, the bERLinPro linear accelerator (linac) and the BESSYVSR cavity-design will be answered.

5.6 Dielectrically Lined Rectangular Waveguides as Wakefield Based Dechirper Structures

CANDIDATE: Franziska Reimann, Rostock University. Germany
SUPERVISOR: Prof. Dr. Ursula van Rienen
GRADUATION: December 2018

In the physics of particle accelerators, light sources and compact accelerators are gaining more and more importance for various fields of science, medicine and industry. This is coupled to increasing demands on the beam quality, like, e.g., the need for ever higher charge densities and pulses in the range of sub-picoseconds.

Another requirement for particle beams, especially in a linear accelerator (linac) or linac-based X-ray Free Electron Laser (FEL), is a small energy width. In fact, large energy spreads have been present in accelerator science for a long time. In the last years, however, a new concept has been proposed as a counter measure to this problem: the so-called ‘dechirper’ or ‘silencer’, a passive, geometrically simple structure based on the use of the interaction between

the particle beam and its own wakefield.

The aim of this thesis is to provide a comprehensive study of the general properties of a specific type of dechirper: a rectangular waveguide coated with dielectrics. For this purpose, a semi-analytical model is developed which calculates the wake function inside the dechirper using an eigenmode expansion. As a second step, this model is implemented in the programming language Python and benchmarked against simulations with CST Particle Studio® (CST PS). These studies show that the geometrical simplicity of the chosen dechirper type makes an analytical treatment of the wakefield possible, even though the final computation of the wake function has to be performed numerically. This method has the advantage of delivering the wakefield of a point charge, the so called wake function, as a result. The wake function can be considered a Green's function and enables the calculation of wake potentials of arbitrary bunches by a simple convolution. The programme, named Wakefield Calculation In Rectangular Waveguides Lined with Dielectrics (WIzaRD), is then used to perform parameter studies to provide an overview over the influence of variations of the geometrical and dielectric properties on the magnitude of the wakefield. Here it is shown that the most powerful parameters to adjust the magnitude of the wakefield are the length of the dechirper, the total charge of the particle beam that generates the wakefield, and the distance between the upper and lower dielectric in the dechirper, the gap width. Especially the latter enables a tuning of the wakefield after the construction of the dechirper and during experiments, which also makes it possible to turn off the dechirper without removing it from the beamline.

The underlying project work of this thesis has been performed in collaboration with the Helmholtz-Zentrum Dresden-Rossendorf (HZDR). The ultimate goal of the simulation phase has been providing simulations for the later test of a dechirper prototype at the Electron Linac for beams with high Brilliance and low Emittance (ELBE) facility at the HZDR. Consequently, the geometry of a prototype dechirper is introduced in this thesis. Following this, the results of experiments carried out with this prototype are presented here and compared to simulations performed with the aforementioned semi-analytical programme algorithm. The experiments underline the tuning possibilities of the wakefield that the gap width provides. Comparisons with semi-analytic results show a qualitative agreement between theory and experiments.

5.7 Characterisation of Mechanical and Thermal Properties of Tungsten for High Power Spallation Target Applications

CANDIDATE: Jemila Habainy, Lund University, Sweden
SUPERVISOR: Prof. Srinivasan Iyengar
GRADUATION: October 2018

The European Spallation Source (ESS), which is currently under construction in Lund, will use pure tungsten as the spallation neutron target. The tungsten will be irradiated by a 2 GeV proton beam, pulsed at a repetition rate of 14 Hz. Each pulse will deposit 357 kJ in the tungsten causing an instantaneous temperature rise of approximately 100° C, during the 2.86 ms pulse duration. The target is wheel-shaped, 2.6 m in diameter, and will be rotating at 0.39 Hz to distribute the proton beam loads. The tungsten target consists of nearly 7000 bricks with dimensions $80 \times 30 \times 10\,\mathrm{mm}^3$. The bricks are separated by 2 mm wide cooling channels in which helium gas flows at a rate of 2.85 kg/s. The proton beam will be more powerful than the beam used at any other existing neutron spallation facility. Thanks to the high beam power and innovative moderator design, ESS will become the brightest neutron source in the world.

However, designing the target is challenging, as its structure should withstand loads from the high beam power. The high intensity proton beam will not only cause cyclic thermo-mechanical loading of the tungsten, but also irradiation damage in the form of displacements of atoms

in the microstructure, and production of a wide range of radioactive isotopes such as gaseous transmutation elements, and a significant fraction of solid transmutation elements, which will alter the thermal and mechanical properties of tungsten. Using such a powerful beam requires an optimal design of the target and a good understanding of the complex physical, mechanical, and thermal changes occurring in irradiated tungsten. It is also important to identify and mitigate potential issues and accidental scenarios during operation of the ESS target.

The present work aims to characterise thermal and mechanical properties of high-energy proton and spallation neutron irradiated pure tungsten, for the use as a spallation target material. The work includes studies on fatigue properties of unirradiated tungsten from various processing routes, to determine which type of tungsten is the most durable under cyclic loads. The fatigue study served as a basis for setting the maximum acceptable stress of 100 MPa in the tungsten bricks during operation, as well as choosing rolling as the most suitable manufacturing method. The tungsten volume will be contained in a stainless-steel target vessel, which confines the helium gas target-coolant. Tungsten is known to be readily oxidised even at moderate temperatures, which makes even impurity levels of oxygen and water vapour in the helium a potential issue. Therefore, oxidation behaviour of tungsten in mildly oxidising atmospheres and temperatures relevant to ESS operation, was characterised. The results were used to set the upper temperature limit in the tungsten target during normal operation, as well as the maximum allowable temperature during off-normal incidents. However, both temperature and thermo-mechanical stress in the tungsten will alter as the properties of the material change due irradiation.

The available data on proton irradiated tungsten is very limited. Therefore, in the present work, large efforts have been made for studying tungsten irradiated under similar conditions as the future ESS target material. Specifically, irradiation induced changes in thermal diffusivity, hardness, ductility, and ultimate tensile strength of tungsten irradiated by a high power proton beam at Paul Scherrer Institute (PSI), were studied. The results point towards a severe embrittlement of irradiated tungsten. Virtually zero plasticity was found in specimens tested up to 500° C, and the hardness increased by more than 50%. Thermal diffusivity decreased by 28-51%, depending on the test temperature (25-500° C). All tested irradiated specimens had lower irradiation damages than the ESS tungsten is expected to accumulate during the 5-year life time of the target.

Finally, a concluding study is presented in which new calculations of temperature and the maximum stress in the bricks were made, based on the obtained experimental data on the thermal and mechanical properties of irradiated tungsten.

5.8 Design and Analysis of the Medium-β Elliptical Cavities for the European Spallation Source Accelerator

CANDIDATE: Gabriele Costanza, Lund University, Sweden
SUPERVISOR: Prof. Anders Karlsson
GRADUATION: January 2017

This thesis is dedicated to the design and analysis of superconducting elliptical cavities. Elliptical cavities play a central role in modern particle accelerators due to their high efficiency. After an introduction to the European Spallation Source project, the thesis goes through the design of the medium-β cavity. The RF design of the inner cell and end cell are presented in sequence in paper I. The design is completed by the chapter on the mechanical performances of the cavity (paper II). Papers III, IV and V are instead dedicated to the analysis of the cavity. The necessary mathematical tools for the analysis are presented in paper III which, after stating fundamental results on hollow cavities, presents a spectral decomposition used in the following papers. In

paper IV, a time-domain model for the power dissipation induced by the excited higher-order-modes is presented. Such modes are excited by the particle beam that passes through the cavity and are detrimental to the performances of the accelerator. Paper V presents a time-domain model of the cavity coupled to an externa circuit to a coupler. The model is functional to the design of the cavity control system.

5.9 The Characterization of Metal Photo-cathode for High Brightness Electron Beam Photo-injectors

CANDIDATE: Jessica Scifo, La Sapienza, Rome
SUPERVISOR: Prof. Massimo Ferrario
GRADUATION: September 2018

A high peak current and low emittance electron beam is required by several applications in the accelerator physics field, e.g., Free Electron Laser (FEL) radiation sources, Plasma Wake Field Acceleration (PWFA) experiments, generation of THz radiation and Inverse Compton Scattering sources. The performance of the photo-cathode is essential to increase the brightness of the electron beam, and so it is therefore of primary importance to analyze and optimize the quantum efficiency (QE) of the photo-cathode and the intrinsic emittance of the emitted electrons. For this reason, in several facilities, many experimental and computational studies are in progress to produce more efficient photo-cathodes. This approach looks at the photo-cathode like a "variable" and sensitive object in terms of surface modifications and contaminants due to laser radiation, RF fields breakdown and vacuum variation of its environment. A R&D activity on photo-cathodes is under development also at the SPARC_LAB test facility in order to fully know and characterize each stage of the photo-cathode "life" and improve their performances in terms of quantum efficiency and electron beam intrinsic emittance. In the present work, two distinct aspects of emittance study are presented: the theoretical study of solenoid optics and the surface preparation and analysis. Since the Cu QE is rather low (≥ 105) and since several applications demand high QE electron sources, there is a growing interest in the international community to investigate the behavior of novel photo-cathode materials. In this regards I have performed also preliminary characterization measurements on a Yttrium thin film grown by pulsed laser ablation technique on Cu photo-cathode.

5.10 Beam Loading Assisted Matching Working Point for PWFA Beam Driven Experiment at SPARC_LAB

CANDIDATE: Stefano Romeo, La Sapienza, Rome
SUPERVISOR: Prof. Massimo Ferrario
GRADUATION: September 2017

We propose and numerically design a working point for beam driven plasma wakefield acceleration that allows to preserve the witness quality. This working point belongs to a new kind of scheme where a low density driver generates a wakefield in linear regime and the witness transverse evolution is dominated by the beam loading effect. We derived optimized conditions to prevent the phase space degradation by means of transverse envelope equation and a simplified model to describe the effect of the plasma wakefield on the longitudinal phase space.

5.11 Experiment and Machine Protection from Fast Losses caused by Crab Cavities in the High Luminosity LHC

CANDIDATE: Andrea Santamaria Garcia, Ecole Polytechnique, Lausanne
SUPERVISOR: Helmut Burkhardt (CERN), Leonid Rivkin
GRADUATION: May 2018

The High Luminosity Large Hadron Collider (HL-LHC) upgrade aims for a tenfold increase in integrated luminosity compared to the nominal Large Hadron Collider (LHC), and for operation at a leveled luminosity five times higher than the nominal LHC peak luminosity. In order to compensate the geometric luminosity loss due to the increased crossing angle, crab cavities will be used to transversely rotate the beam bunches, allowing quasi head-on collisions at the experiments. Crab cavity failures can be very fast, having time constants similar to the reaction time of the machine protection system. In such a scenario the beams cannot be immediately extracted, making the protection of the accelerator fully rely on passive protection devices such as the collimation system. At the same time the energy stored in the HL-LHC beams will be doubled with respect to the LHC to more than 700 MJ, which increases the risk of damaging the accelerator and the experiments in case of failure. Crab cavity failures have the potential to displace the beam core and create considerable particle losses around the accelerator, posing a machine protection challenge. Any increase in failure rates will be difficult to compensate, affecting the performance of the HL-LHC and therefore the integrated luminosity goal. This is why it is important to correctly interlock the accelerator and make sure that certain types of failure never happen. In order to do this advanced simulations are needed well before the crab cavity prototypes can be tested in real operating conditions. This thesis analyzes different failure scenarios for crab cavities installed around the ATLAS and CMS experiments. The selected failure scenarios are later simulated with the tracking code SixTrack thanks to a newly developed functionality. The distribution of the particle losses in space and time are analyzed for the different failure cases and a quantitative estimate of the impact in the collimation system is given. The results are analyzed from a machine protection point of view, where the time for the beam abort trigger is calculated for each failure case and mitigation techniques are proposed. These results allow identifying corner cases corresponding to the most dangerous crab cavity failure scenarios, serving as input for the design of the future interlocking system.

6. FORTHCOMING BEAM DYNAMICS EVENTS

6.1 Slow Extraction Workshop 2019

CONTACT: Vladimir Nagaslaev (chair), FNAL

The third in the successful series of Slow Extraction Workshops will be held at Fermilab from July 22$^{\text{nd}}$ to 24$^{\text{th}}$, 2019.

The objectives of the meeting are to:

- Review the state of the art in present Slow Extraction performance in terms of beam loss and spill quality.
- Gauge the present state and future potential of SX performance with theoretical limitations.
- Review the design performance parameters in view of the experimental requirements.
- Propose and discuss new methods, technology improvements and ideas for Slow Extraction.
- Identify new future challenges for further increasing the beam power with SX, and the key research directions needed to mitigate them.
- Review collaboration progress and identify new research interests where the focused effort of multiple institutions would gain a significant progress. Build a way for new collaborations between the labs.
- Discuss issues and effective techniques of machine protection.
- Promote education and institutional knowledge retention in SX techniques.

Further details can be found on the workshop website `https://indico.fnal.gov/event/20260/overview`

6.2 Fixed Field Alternating Gradient Workshop, FFA2019

CONTACT: Andreas Adelmann, Chair of FFA2019

The latest in the series of annual workshops devoted to the study of FFAs will be hosted by the Paul Scherrer Institute in Switzerland from November 19$^{\text{th}}$ to 22$^{\text{nd}}$ 2019. The workshop will provide an opportunity to hear about operational discoveries on the existing FFA machines in Japan, progress in construction and commissioning of the FFA sections of the new CBETA project in the U.S.A. and the latest in theoretical studies being carried out in laboratories and universities around the world. As many aspects as possible of FFAs will be addressed over the period of the workshop, from applications and modelling codes through to magnets, rf and proposals for future FFA projects. Depending on the program and time available, we hope to include a session on the two main codes used to model FFAs - Zgoubi and OPAL - as well as a tour of the accelerator facilities at PSI.

Further details will be available on the workshop website `https://indico.psi.ch/event/7313/`.

6.3 Workshop devoted to the Accelerator Tracking Code Zgoubi

CONTACT: Dan T. Abell, dabell@radiasoft.net

A workshop devoted to the particle accelerator code Zgoubi will take place in Boulder, Colorado, USA from 26$^{\text{th}}$-30$^{\text{th}}$ August 2019.

The particle tracking code Zgoubi evolved from a tool for modeling spectrometers in 1972 to what it is today: one of the most complete single-particle dynamics codes. Used by labs worldwide for a wide range of particle accelerator modeling tasks, Zgoubi is especially valued for studies of polarization in electron-ion colliders, as well as for studies of the complex dynamics in fixed-field accelerators (FFAs) and medical synchrotrons.

The goal of the Zgoubi Workshop is to promote an exchange of knowledge about the Zgoubi code. Presentations on important scientific applications will motivate the associated practical tutorials. Bringing together both developers and scientist users will facilitate coordinated development that will leverage expertise from both groups and result in new tools and interfaces having consistent approaches.

* Please visit the conference website: `https://zgoubi-workshop.com/`
* If you are interested in giving a talk or tutorial, please contact us: `zgoubi-workshop@radiasoft.net`
* If you are unable to attend, but are interested in being on the mailing list, please let us know: zgoubi-workshop@radiasoft.net

6.4 63$^{\text{rd}}$ ICFA Advanced Beam Dynamics Workshop on Energy Recovery Linacs, ERL2019

CONTACT: Atoosa Meseck (workshop chair)

The 63rd ICFA Advanced Beam Dynamics Workshop on Energy Recovery Linacs (ERL2019), organized by Helmholtz-Zentrum Berlin, will take place from Sunday, September 15$^{\text{th}}$, to Friday, September 20$^{\text{th}}$, 2019 on the Science & Technology Campus, Berlin-Adlershof, Germany.

ERL'19 is the eighth in the series of biennial international workshops covering the accelerator physics and technology of Energy Recovery Linacs. The workshop will serve as a forum for scientists and engineers from around the world to review and discuss the latest developments in ERL physics, technology and applications. Among the issues to be addressed are: ERL facilities, beam dynamics and instrumentation, electron sources and injectors, superconducting RF, ERL applications, etc. The talks will cover commissioning and operations experience, ERL applications and status presentations from different projects. There will be plenary sessions and the possibility to display posters.

Important dates and other useful information are available on the workshop website:
`https://www.helmholtz-berlin.de/events/erl19/index_en.html`

The website will be updated (regularly) in the course of preparation for the workshop.

Early registration is currently open and will end on June 30$^{\text{th}}$, 2019. Regular registration starts July 1$^{\text{st}}$, 2019

6.5 ICFA mini-Workshop on Mitigation of Coherent Beam Instabilities in Particle Accelerators, MCBI2019

CONTACT: Elias Métral, Tatiana Pieloni and Giovanni Rumolo, IOC Chairs MCBI2019

Following the ICFA mini-Workshop on "Electromagnetic Wake Fields and Impedances in Particle

Accelerators" held in April 2014 in Erice, Sicily, and the ICFA mini-Workshop on "Impedances and Beam Instabilities in Particle Accelerators", held in September 2017 in Benevento, Italy, a third workshop in the series will be organised jointly between CERN and EPFL and will take place from September 23rd to 27th, 2019 in Zermatt, Switzerland.

This workshop will focus on mitigation methods for coherent beam instabilities, reviewing in detail the theories (and underlying assumptions), simulations and measurements on the one hand, and on the other hand trying to compare the different mitigation methods (e.g. with respect to other effects such as beam lifetime) to provide the simplest and most robust solutions for day-to-day operation of the machines.

Further details are available at the workshop web-site: `https://indico.cern.ch/e/MCBI2019` which will be regularly updated to include the latest information as it becomes available.

6.6 22nd International Conference on Cyclotrons and their Applications, CYC2019

CONTACT: Lowry Conradie, CYC2019 International Organizing Committee Chair, and Muneer Sakildien, CYC2019 Local Organizing Committee Chair

The 22nd International Conference on Cyclotrons and their Applications (CYC2019) will be hosted in Cape Town, South Africa from the 22nd of September to the 27th of September, 2019.

The conference takes place every three years with the most recent events being held in Zurich/Switzerland (2016), Vancouver/Canada (2013) and Lanzhou/China (2010). The conference returns to the African continent after being hosted here in 1995 and opened then by one of the greatest sons of our continent, Dr Nelson Rolihlahla Mandela.

Cape Town is located on the southwest coast of South Africa at the foot of the majestic Table Mountain. The city is world-renowned for its breath-taking scenery and attractions such as the Kirstenbosch Botanical Gardens, Stellenbosch Wine Routes and the splendid beaches.

CYC2019 will offer plenary sessions of invited and contributed oral presentations from Monday morning through Friday noon. Poster sessions are scheduled for the Monday and Tuesday afternoons. The scientific program will cover six themes namely:

* Cyclotron Technologies
* Theory, Models and Simulations
* Operations and Upgrades
* Cyclotron Applications
* Cyclotron Concepts, FFA and New Projects
* Session for Young Scientists

The conference website is now online at: `https://indico-jacow.cern.ch/event/14/`
The deadline for abstract submission is Saturday, June 15th, 2019 (GMT+2).
The early bird registration deadline is Friday, May 31st, 2019 (GMT+2).
For more information and assistance, contact: cyc2019@tlabs.ac.za.

7. ANNOUNCEMENTS FROM THE BEAM DYNAMICS PANEL

7.1 ICFA Beam Dynamics Newsletter

7.1.1 Aim of the Newsletter

The ICFA Beam Dynamics Newsletter is intended as a channel for describing unsolved problems and highlighting important ongoing work, and not as a substitute for journal articles and conference proceedings that usually describe completed work. It is published by the ICFA Beam Dynamics Panel, one of whose missions is to encourage dissemination of information and international collaboration in beam dynamics. Normally the Newsletter is published every April, August and December. The deadlines are 15^{th} March, 15^{th} July and 15^{th} November, respectively.

7.1.2 Categories of Articles

The categories of articles in the newsletter are the following:

1. Announcements from the panel.
2. Reports of beam dynamics activities carried out by an ICFA-BD group.
3. Reports on workshops, meetings and other events related to beam dynamics.
4. Announcements of future beam dynamics-related international workshops and meetings.
    - Those who wish to use a newsletter to announce their workshops are welcome to do so. Articles should typically fit within half a page and include descriptions of the subject, date, place, web site and other contact information.
5. Review of beam dynamics problems.
    - This is a place to bring attention primarily to progress in solving problems or developing a field rather than just to report about completed work. Clear and short highlights on the problem are encouraged.
6. Letters to the editor
    - A forum open to everyone, anybody can express his/her opinion on beam dynamics and related activities, by writing to one of the editors. The editors reserve the right to reject contributions they judge to be inappropriate, although they have rarely had cause to do so. The editors may request an article following a recommendation by panel members. However anyone who wishes to submit an article is strongly encouraged to contact any Beam Dynamics Panel member before starting to write.

7.1.3 How to Prepare a Manuscript

The editors' preference is to prepare the Newsletter in LaTeX, although articles in Microsoft Word will also be accepted. Contact information for the Editor-in-Chief and the Issue Editor is provided on the Beam Dynamics Panel web site:

http://www.icfa-bd.org

Articles in LaTeX can be prepared using any standard class file or using the template for authors on the web page. The text and associated figures should be in separate files and sent to the editors together with a PDF file to indicate how the finished article is expected to appear.

Those using Word should download the appropriate template from the web site. Send the article to the editors as above, also including a PDF indicating how the finished article should appear.

In both cases the templates will evolve with time, so please make sure you use the latest version.

Each article should include the title, authors' names and affiliations. If agreeable the e-mail address of the lead author will also appear. However, personal data is subject to the provisions of data protection laws and it is within the rights of authors to request that details (such as their email address) are not published in the Newsletter.

Authors are reminded to respect the terms of copyright when submitting articles. If any part of an article has been previously published in a refereed journal or in conference proceedings, the author should check that it is permissible to reproduce it in the newsletter. Copyright terms can vary from journal to journal, conference to conference. The Chair of JACoW (chair@jacow.org) will normally grant permission for any part of a paper from a JACoW conference to be reproduced if an acknowledgement is made. Please consult him for the appropriate wording.

7.1.4 Distribution

The Newsletter is published in both html and (downloadable) PDF format. Readers who sign-up to the electronic mailing list via `http://www.icfa-bd.org` will receive an email notification whenever a new issue is released.

The Panel's web site provides access to the Newsletters, information about future and past workshops, and other information useful to accelerator physicists.

An archive of issues of this newsletter from 1987-2016 is available at

http://icfa-usa.jlab.org/archive/newsletter.shtml.

Except in a few exceptional cases, printed copies of the ICFA Beam Dynamics Newsletters are no longer issued.

7.1.5 Regular Correspondents

The Beam Dynamics Newsletter particularly encourages contributions from smaller institutions and countries where the accelerator physics community is small. Since it is impossible for the editors and panel members to survey all beam dynamics activity worldwide, we have some Regular Correspondents. They are expected to find interesting activities and appropriate persons to report them and/or report them by themselves. We hope that we will have a "compact and complete" list covering all over the world eventually. The present Regular Correspondents are as follows:

Liu Lin	Liu@ns.lnls.br	South America
Sameen Ahmed Khan	Rohelakhan@yahoo.com	Middle East and Africa
Suzie Sheehy	suzanne.sheehy@unimelb.edu.au	Australasia

Additional volunteers as Regular Correspondents would be welcome.

7.2 ICFA Beam Dynamics Panel Members

Name	eMail	Institution
Rick Baartman	baartman@lin12.triumf.ca	TRIUMF, 4004 Wesbrook Mall, Vancouver, BC, V6T 2A3, Canada
Marica Biagini	marica.biagini@lnf.infn.it	INFN-LNF, Via E. Fermi 40, C.P. 13, Frascati, Italy
John Byrd	jbyrd@anl.gov	Accelerator Systems Division, Argonne National Laboratory, 9700 S. Cass Ave Building 401-C4263, Argonne, IL 60439, U.S.A.
Yunhai Cai	yunhai@slac.stanford.edu	SLAC, 2575 Sand Hill Road, MS 26, Menlo Park, CA 94025, U.S.A.
Jie Gao	gaoj@ihep.ac.cn	Institute for High Energy Physics, P.O. Box 918, Beijing 100039, China
Ajay Ghodke	ghodke@rrcat.gov.in	RRCAT, ADL Bldg., Indore, Madhya Pradesh, 452 013, India
Eliana Gianfelice-Wendt	eliana@fnal.gov	Fermilab, Mail Station 312, PO Box 500, Batavia IL 60510-5011, U.S.A.
Ingo Hofmann	i.hofmann@gsi.de	High Current Beam Physics, GSI Darmstadt, Planckstr. 1, 64291 Darmstadt, Germany
Sergei Ivanov	sergey.ivanov@ihep.ru	Institute for High Energy Physics, Protvino, Moscow Region, 142281 Russia
In Soo Ko	isko@postech.ac.kr	Pohang Accelerator Lab, San 31, Hyoja-Dong, Pohang 790-784, South Korea
Elias Metral	elias.metral@cern.ch	CERN, CH-1211, Geneva 23, Switzerland
Peter Ostroumov	Ostroumov@frib.msu.edu	FRIB, National Superconducting Cyclotron Laboratory, Michigan State University, 640 S. Shaw Lane East Lansing, Michigan 48824, U.S.A.
Mark Palmer	mpalmer@bnl.gov	Brookhaven National Lab, Upton, NY 11973, U.S.A.
Chris Prior	chris.prior@stfc.ac.uk	STFC/RAL, Harwell Campus, Didcot, Oxon OX11 0QX, U.K.
Ji Qiang	jqiang@lbl.gov	Lawrence Berkeley National Laboratory (LBNL), MS 71J-100a, One Cyclotron Road, Berkeley, California, CA 94720-8211 U.S.A.
Yuri Shatunov	Yu.M.Shatunov@inp.nsk.su	Akad. Lavrent'eva, Prospekt 11, 630090 Novosibirsk, Russia
Yoshihiro Shobuda	yoshihiro.shobuda@j-parc.jp	J-PARC, Shirakata-Shirane 2-4, J-Tokai-Mura, Naka-Gun, Ibaraki-Ken 319-1195, Japan
Jiu-Qing Wang	wangjq@ihep.ac.cn	Institute for High Energy Physics, P.O. Box 918, 9-1, Beijing 100039, China
Rainer Wanzenberg	rainer.wanzenberg@desy.de	DESY, Notkestrasse 85, 22603 Hamburg, Germany

Zhentang Zhao	zhaozhentang@sinap.ac.cn	SINAP, Jiading campus: 2019 Jia Luo Road, Jiading district, Shanghai 201800, P.R. China; and Zhangjiang Campus: 239 Zhang Heng Road, Pudong New District, Shanghai 201203, P.R. China